

UNCLASSIFIED

REI

AD-A263 049

2

1a. REPORT SECURITY CLASSIFICATION  
Unclassified

DTI

■■■■■■■■■■

SECURITY CLASSIFICATION OF ABSTRACT

SELECT

2b. DECLASSIFICATION/DOWNGRADING SCHEDULE

1993

3. DISTRIBUTION/AVAILABILITY OF REPORT  
Approved for public release,  
distribution unlimited

4. PERFORMING ORGANIZATION REPORT NUMBER

5. MONITORING ORGANIZATION REPORT NUMBER(S)

AFOSR-TR- 03 0104

6a. NAME OF PERFORMING ORGANIZATION  
Dept. of Aeronautics and  
Astronautics6b. OFFICE SYMBOL  
(If applicable)  
31-264

7a. NAME OF MONITORING ORGANIZATION

See #8 AFOSR/NA  
Bolling AFB DC 20332-6448

6c. ADDRESS (City, State, and ZIP Code)

77 Massachusetts Ave.  
Cambridge, MA 02139

7b. ADDRESS (City, State, and ZIP Code)

See #8 AFOSR/NA  
Bolling AFB DC 20332-64488a. NAME OF FUNDING/SPONSORING  
ORGANIZATION  
AFOSR8b. OFFICE SYMBOL  
(If applicable)  
NA

9. PROCUREMENT INSTRUMENT IDENTIFICATION NUMBER

Grant AFOSR-90-0035

8c. ADDRESS (City, State, and ZIP Code)

AFOSR  
Bolling AFB, DC 20332

10. SOURCE OF FUNDING NUMBERS

PROGRAM  
ELEMENT NOPROJECT  
NOTASK  
NOWORK UNIT  
ACCESSION NO

61102F-2307

D 5

11. TITLE (Include Security Classification)

Unsteady Flow Phenomena in Turbomachines

12. PERSONAL AUTHOR(S)

E.M. Greitzer, A.H. Epstein M.B. Giles, J.E. McCune C.S. Tan

13a. TYPE OF REPORT  
Final Technical13b. TIME COVERED  
FROM 10/20/89 TO 10/19/9214. DATE OF REPORT (Year, Month, Day)  
January 20 199315. PAGE COUNT  
180

16. SUPPLEMENTARY NOTATION

17. COSATI CODES

FIELD GROUP SUB-GROUP

18. SUBJECT TERMS (Continue on reverse if necessary and identify by block number)

Computational Fluid Mechanics Unsteady Flows in Turbo-  
machines Vortex Vakes. Compressor Stability Transonic  
Compressors

19. ABSTRACT (Continue on reverse if necessary and identify by block number)

This report describes work carried out at the Gas Turbine Laboratory at MIT during the period 10/20/89 - 10/19/92, as part of our multi-investigator effort on basic unsteady flow phenomena in turbomachines. Within the overall project four separate tasks are specified. These are, in brief: I. The Influence of Inlet Temperature Nonuniformities on Turbine Heat Transfer and Dynamics; II. Assessment of Unsteady Losses in Stator/Rotor Interactions; III. Unsteady Phenomena and Flowfield Instabilities in Multistage Axial Compressors; IV. Vortex Wake-Compressor Blade Interaction in Cascades: A New Rapid Method for Unsteady Separation and Vorticity Flux Calculations.

220 003

98 3 31 067

93-06629

■■■■■■■■■■

181PP

20. DISTRIBUTION/AVAILABILITY OF ABSTRACT

☒ UNCLASSIFIED/UNLIMITED ☐ SAME AS RPT. ☐ DTIC USERS

21. ABSTRACT SECURITY

22a. NAME OF PERSON/ORGANIZATION

MAJOR D. FANT

22b. TITLE (Include Security Classification)

202-767-0471

22c. OFFICE SYMBOL

AFOSR/NA

UNCLASSIFIED

*Gas Turbine Laboratory  
Department of Aeronautics and Astronautics  
Massachusetts Institute of Technology  
Cambridge, MA 02139*

Final Technical Report

on

Grant AFOSR-90-0035

entitled

**UNSTEADY FLOW PHENOMENA IN TURBOMACHINES**

for the period

October 20, 1989 to October 19, 1992

submitted to

**AIR FORCE OFFICE OF SCIENTIFIC RESEARCH**

Building 410

Bolling Air Force Base, DC 20332

Attention: Major D. Fant

**DTIC QUALITY INSPECTED 4**

**PRINCIPAL  
INVESTIGATOR:**

Edward M. Greitzer  
H.N. Slater Professor and Director,  
Gas Turbine Laboratory

**CO-INVESTIGATORS:**

Professor Alan H. Epstein  
Professor Michael B. Giles  
Professor James E. McCune  
Dr. Choon S. Tan

January 1993

Accession For	
NTIS CRA&I	<input checked="" type="checkbox"/>
DTIC TAB	<input checked="" type="checkbox"/>
Unannounced	<input checked="" type="checkbox"/>
Justification	
By	
Distribution /	
Availability Codes	
Dist	Avail and/or Special
A-1	

**TABLE OF CONTENTS**

<b><u>Section</u></b>	<b><u>Page No.</u></b>
1. Introduction and Research Objectives	2
2. Status of the Research Program	3
Task I: The Influence of Inlet Temperature Nonuniformities on Turbine Heat Transfer and Dynamics	3
Task II: Assessment of Unsteady Losses in Stator/Rotor Interactions	97
Task III: Unsteady Phenomena and Flowfield Instabilities in Multistage Axial Compressors	119
Task IV: Vortex Wake-Compressor Blade Interaction in Cascades: A New Rapid Method for Unsteady Separation and Vorticity Flux Calculations	155
3. Air Force Research in Aero Propulsion Technology (AFRAPT) Program	170
4. Publications and Presentations	172
5. Program Personnel	173
6. Interactions	174
7. Discoveries, Inventions, and Scientific Applications	178
8. Concluding Remarks	179

## **1. INTRODUCTION AND RESEARCH OBJECTIVES**

This is a final technical report on work carried out at the Gas Turbine Laboratory at MIT, in a multi-investigator effort on unsteady flow phenomena in turbomachines. Support for this program was provided by the Air Force Office of Scientific Research under Grant Number AFOSR-90-0035, Major D. Fant, Program Manager.

The present report gives a summary of the work for the period 10/89 - 10/92, but is not intended to be the primary source and the referenced reports and publications can be consulted for more detailed information and background. These describe the research in considerable depth.

Within the general area of turbomachinery fluid dynamics, four separate tasks were specified under this contract. These are, in brief:

- I. The influence of inlet temperature non-uniformities on turbine heat transfer and measurement.
- II. Development and application of computational techniques for unsteady flows and assessment of unsteady losses in rotor/stator *interactions*.
- III. Unsteady phenomena, inlet distortion and flow instabilities in multistage compressors, including experimental and analytical investigations of the structure of instability precursors, nature of rotating stall modes, and detailed blade passage aerodynamics and stall onset in advanced blading geometries.
- IV. Unsteady blade-vortex street interaction in transonic cascades including models to describe the vortex wake-compressor blade interactions.

In addition to these tasks, the multi-investigator contract encompassed the Air Force Research in Aero Propulsion Technology (AFRAPT) Program. The work carried out in each of the tasks will be described in the next section. Publications generated are given in the individual task descriptions, and an overall list of presentations and publications associated with the projects appears in Section 4.



## **TASK I: THE INFLUENCE OF INLET TEMPERATURE NONUNIFORMITIES ON TURBINE HEAT TRANSFER AND MEASUREMENT**

(Investigators: A.H. Epstein, G.R. Guenette, T. Shang, M. Graf)

### **1.0 Executive Summary**

This is a technical progress report on the research conducted on the turbine inlet temperature distortion cooperative research program through December 1992. The objectives of the program are to elucidate the role of inlet temperature nonuniformity and turbulence on turbine rotor heat transfer through detailed experiments and calculations. The sponsors are SNECMA, Rolls-Royce, Inc., US Air Force Office of Scientific Research, and NASA Lewis Research Center. The effort is focused about a set of experiments on the MIT Blowdown Turbine facility in which the effects of inlet temperature distortion on a transonic turbine stage will be directly measured. This data will then be compared with CFD and analytical results.

The activities to date have concentrated on the refurbishment of the test rig, the addition of turbulence grids, the upgrading of heat transfer and aerodynamic instrumentation, the adaptation of a 3-D, inviscid, unsteady code to the measurement geometry, final assembly of the aerodynamic instrumentation and its calibration, initial NGV-only testing, and the resolution of problems encountered during the initial tests. The test rig refurbishment includes cleaning of the temperature distortion generator and reconfiguration of the generator to simultaneously produce different radial and circumferential distortion in separate 120° sectors.

Instrumentation upgrading consists of reinstrumentation of the rotor blades with heat flux transducers, the addition of circumferential rake translators upstream and downstream of the turbine, and the design and construction of pressure and temperature rakes for the translators. The temperature instrumentation measures time-averaged total temperature, while both time-averaged and time-resolved rakes were fabricated for total pressure. Wall static pressure taps have been added at the inner and outer annulus wall downstream of both the NGV's and the rotor. New signal conditioning and data acquisition equipment to accommodate the 80 additional aerodynamic measurement transducers has also been procured or constructed.

The temperature and pressure rakes were assembled and calibration. Considerable noise and induced signals were observed on the exit temperature rake during traverse shakedown in vacuum. This problem was solved with an improved grounding scheme. The overall DC accuracy and stability appear to be within 0.2%, sufficient for the planned test program.

The instrumentation performed as designed during the first NGV-only blowdown tests. The inlet rake mapped the distortion generator exit flowfield and the turbine exit rake could readily resolved the NGV wake structure. During the first test, cabling from the turbine exit translator became entangled in it drive chain. The exit cabling arrangement was modified to resolve this problem.

Turbulence screens have been designed and fabricated which match the turbulence spectrum suggested by Rolls-Royce as being representative of engine scale. These screens have been tested in a wind tunnel with satisfactory results.

A 3-D, unsteady, Euler code written by Saxer and Giles is being adapted to the test geometry. The code will be run with three NGV's and five rotor passages to simulate the 36 NGV, 61 rotor blade count of the experiment.

Two problems were encountered with the temperature and distortion generator – inadequate circumferential distortion and particulate contamination. The low level of circumferential distortion achieved was traced to the storage matrix having 15 times more thermal conductivity in the circumferential direction compared to the radial one, due to poor fabrication. This has the effect of quickly washing out circumferential distortions. The approach adopted was to double the number of spot heaters and run them at very high current levels (just below burnout as established experimentally) immediately preceding the blowdown tests. The particle contamination of the distortion generator has been a continuing problem and efforts to clean the unit have not been successful. The approach adopted here was to fabricate and insert a particle filter at the distortion generator exit.

An operational problem has developed due to the ten-fold increase in the price of Freon-12, to about \$1200 per test – well beyond the budget. We plan on using Freon for the first tests only

for continuity and then converting to an argon-CO<sub>2</sub> gas mixture.

The current schedule is to do the NGV-only testing in January and start the full-stage testing in February 1993.

## **2.0 Introduction**

The objective of this work is to understand how turbine inlet distortion and turbulence influence turbine heat transfer and aerodynamics. It is centered on a set of detailed spatially and temporally resolved measurements of a high pressure ratio turbine stage in a short duration turbine test facility. Numerical simulation and analytical modelling will then be used to interpret these measurements and help draw conclusions of use to a turbine designer.

The experimental work will be carried out in the MIT Blowdown Turbine Facility. This rig can simulate all of the non-dimensional fluid mechanic parameters known to be important in turbine aerodynamics (Reynolds No., Rossby no., Mach No., gas-metal temperature ratios, Prandtl No., ratio of specific heats, etc.) for approximately 300 ms. Turbine corrected speed and weight flow are held constant to better than 0.5% over this period. During the test, approximately 20 million data points can be taken from a variety of heat transfer and aerodynamic instrumentation.

The program plan is to setup a temperature distortion generator to produce both circumferential (hot spots) and radial temperature distortions simultaneously in separate 120° sectors. The time resolution of the instrumentation will permit differentiation among the sectors. The test plan for this year is to first operate the tunnel without the rotor so as to permit aerodynamic mapping of the nozzle guide vane (NGV) exit flowfield. (Since the nozzles are choked, the flowfield may approximate that with the rotor in place.) The rotor will then be added and the heat transfer and stage aerodynamic data taken.

To date, the effort has concentrated on readying the facility and its instrumentation for these tests, and adaptation of numerical tools. For the sake of this report, we will divide this effort into categories – (1) facility refurbishment and addition of inlet and outlet rake translators; (2) design and testing of turbulence grids; (3) new aerodynamic instrumentation and signal conditioning

equipment; (4) new rotor blade heat flux instrumentation; (5) CFD code adaptation and checkout; (6) instrumentation preparation and calibration; (7) NGV-only testing; and (8) problems uncovered and their solutions. In the following sections, we examine each item in turn.

### **3.0 Facility Refurbishment and Modification**

Three major items are required to ready the facility for the distortion testing – refurbishment of the facility, cleaning and retrofitting of the distortion generator, and the addition of new upstream and downstream circumferential translation capability. The tunnel refurbishment consists of disassembly; cleaning; bearing, seal, and lubricant replacement; etc., as well as checkout of the control, heating, eddy brake, and safety systems.

#### **3.1 Distortion Generator**

The distortion generator was cleaned and reconfigured. The unit (0.5 m dia. x 1 m long) was cleaned in an ultrasonic cleaner to remove the particles which caused extensive instrumentation damage during the previous test series. These appeared to be 25  $\mu\text{m}$  diameter, clear particles, probably silica from grit blasting at the honeycomb manufacturer. The unit was cleaned repeatedly, the cleaning fluid filtered, and the particle number noted. The number of particles was reduced on each cleaning until none remained.

The heaters from one of three radial distortion sectors of the generator was removed and the unit rethreaded as a circumferential distortion generator (Fig. 1). In this segment, the heaters are 6 mm in circumferential extent and spaced 2 nozzle guide vane pitches apart to approximate combustor nozzle spacing. Thirty thermocouples measuring metal temperature were then spotted about the matrix to aid in pre-test setup. The heaters and thermocouples performed satisfactorily in air. The generator is ready to go.

Different temperature patterns will be generated by varying the time temperature history of the wire heaters. High currents for short times will generate “spiky” distortions, which will soak out over time, lessening the temperature modulation. This is illustrated conceptually in Fig. 2. As an aid in the setup of the patterns, a numerical conduction model of the generator is being written

and will be fit to the experimental data.

### 3.2 Instrument Translators

The explicit inclusion of circumferential distortions and the desire to take high accuracy aerodynamic data necessitated the addition of circumferential traversing capability to the MIT blowdown tunnel. Traversing is required at the stage inlet to document the turbine inflow for both heat transfer and aerodynamics. Stage performance measurements demand that the rotor outflow be measured as well. The inlet translator was a part of the baseline program, whereas the participation of SNECMA has permitted the addition of a unit at the rotor outlet.

The design goals were similar for both units:  $240^\circ$  of annular transverse in 300 ms (to survey both  $\theta$ TDF and RTDF sectors in the useful test time), constant speed (to aid in data reduction and interpretation), one revolution maximum travel (to permit any two of the three  $120^\circ$  sectors to be measured), ready installation and removal of the rake instrumentation (for calibration checks and sensor replacement, if necessary), and, of course, minimum technical risk and cost. We wished to position the upstream translator as close to the NGV leading edges as possible and spent considerable time working on designs which would be accommodated within the current test section. However, there was very little space to accommodate the unit, major modifications would be required, bearings were not available in the sizes needed, and the high inertia made the drive very large. Thus, fitting the unit within the test section at the current rake location was quite unattractive because of the engineering difficulty, cost, and risk.

The approach adopted instead was to fabricate an additional casing (pressure vessel) for the translator, which was inserted between the distortion generator and the test section (Fig. 3). A cross-section of the unit is shown in Fig. 4. In this implementation, the rakes are mounted to the inner annulus wall which is rotated by a gear arrangement. This lowers the angular moment of inertia, compared to rotating the outer annulus wall, reducing the drive requirements to about 5 KW. A computer controlled DC servo drive runs the translator (Fig. 5). The unit is water-cooled on the upstream side to restrict pre-test heating of sensors and bearings. The signals from the

transducers are brought out of the rotary system by coiled wires (thus the one revolution maximum travel) and out of the pressure vessel by a vacuum feedthrough. A measured time trace of the translator motion is shown in Fig. 6. The unit operates satisfactorily.

The rotor exit translator was a much more difficult task in that there was no choice but to fit it within the existing test section and the geometric constraints are severe. In this case, the deswirl vanes downstream of the rotor are replaced by the translator. The tunnel flow path is shown in Fig. 7, while the detail of the translator is given in Fig. 8. As for the upstream translator, the probes are mounted on the inner annulus flow path wall. This wall is mounted on thin line bearings and chain-driven (the chain is in the flow path). The ribbon cabling is used which is formed into a spring coil under the turbine exit throttle sleeve. A DC servo drive similar to the upstream unit is used with the addition of a gearbox to increase the torque. As of this date, the unit has performed satisfactorily mechanically. The instrumentation wiring has not been completed.

#### 4.0 Turbulence Generation

The influence of turbulence on rotor heat transfer will be explored by operating the facility with high and low levels of turbulence. The blowdown turbine naturally produces a very quiet inflow, with turbulence levels measured before the contraction into the NGV's of less than 1%. Engine levels are considerably more, and we must ask the question "What are appropriate intensities and scales?" Rolls-Royce has suggested that the work of Moss and Oldfield [1] is a suitable representation of engine conditions. We have been operating under this assumption in the work described below. More recently, at the April program review and in subsequent correspondence, Dr. Richard Rivir of the USAF Wright Laboratories has pointed out that his work shows considerably more energy at high spatial frequencies than does that of Moss and Oldfield. We are in the process of trying to understand this discrepancy and would appreciate the opinions of our partners.

Basing the design criteria on Moss and Oldfield data, we considered the suitability of grids to produce the desired spectrum. Meshes placed at two axial stations were considered: (1) at the

NGV leading edge, and (2) further upstream before the contraction at the boundary layer bleed lips (Fig. 9). A summary of the grid properties is given in Table 1 and the resultant spectrum given in Fig. 10. While the intensity generated by grids at the NGV leading edge is higher, it is mechanically difficult to fit the screens there in such a manner as to be readily removable. Thus, boundary layer bleed leading edge placement was chosen. The grid geometry selected is a coarse, square cross-section grid, stamped from plate (Fig. 11).

The grid was tested in a low speed wind tunnel and produced a spectrum approximately that of Moss and Oldfield. The details of this testing are given in the following sections.

**TABLE 1**  
**SUMMARY OF TURBULENCE GRID MESH PROPERTIES**

Axial Station	Sector	Mesh Size M (in)	Wire Dia. b (in)	Solidity s (%)	Tu (%)	$\frac{\Delta P}{1/2 \rho U^2}$
At NGV Inlet	1	0.25	.063	44.0	17.8	1.14
	2	0.10	.025	43.8	9.18	1.13
	3	0.05	.012	42.2	5.43	1.04
At B.L. Bleed	RR Design	0.75	.192	44.7	8.10	1.18

#### **4.1 Experimental Facilities**

For the testing of the turbulence grids, the MIT 12"x12" low speed wind tunnel was used (Fig. 12). The turbulence of this tunnel was found to have a negligible effect on the turbulence measurements. To take the velocity measurements behind the grid, a Thermo-Systems 1050 constant temperature anemometer was used, with a Thermo-Systems 1213-T1.5 hot wire. This hot wire has a diameter of 4  $\mu$ m and an overheat ratio of 1.8. The anemometer voltages were recorded using a Nicolet NIC-310 recording oscilloscope with 16 bit resolution. This provides a velocity resolution of 0.1 m/s. Taking into account the errors caused by the hot wire, pitot tube, and calibration curve, the accuracy of the measurements was calculated to be approximately  $\pm 0.5$

m/s.

The calibration of the tunnel was done using a pitot tube attached to a pressure transducer. The pitot tube also acted as a check on the accuracy of the hot wire during the tests. The calibration curve of anemometer output voltage versus velocity was then used to convert the test voltages to velocities. Although the tunnel was calibrated at the beginning of each test sequence, the drift of the calibration curve was checked to see if it would produce an appreciable error as the tests continued. Figure 13 shows that the curve remains approximately constant with time.

Two groups of tests were carried out in the tunnel. The first group measured the turbulence characteristics at a position half way between the turbulence grid and nozzle guide vanes, and at the position of the nozzle guide vanes. At these two streamwise locations, six measurements were taken at different transverse positions to the flow to check for changes in turbulent characteristics in the transverse direction. The object of this first group of tests was to compare the results with similar tests run in the past [2], to confirm the grid was producing the correct turbulent characteristics.

For the second half of the tests, a plexiglass nozzle section was added to the tunnel. This nozzle is the same dimensions as the nozzle section in the blowdown turbine facility. The locations of the test positions was the same as for the first half of the tests. With these results, the freestream turbulence characteristics entering the nozzle guide vanes is known for the blowdown turbine facility. These turbulence characteristics can then be compared with measurements from a typical gas turbine engine burner exit.

## 4.2 Data Analysis

When looking at the effect of turbulence on rotor heat transfer, it is found that two of the most important parameters which characterize turbulence are turbulence intensity, and the power spectral density. The turbulence intensity is defined as

$$Tu = \frac{\sqrt{u'^2}}{U}$$



The power spectral density, relating turbulent energy with wave number, can be found by squaring the finite fourier transform of the data (see Table 2). From the data, the one sided power spectral density can be found as follows

$$G(k) = \frac{1}{\pi U N \Delta t} |X(f)|^2$$

where

$$X(f) = \Delta t \sum_{n=0}^{N-1} u'(n) e^{-i2\pi f n \Delta t} \quad n = 0, 1, 2, \dots, N-1$$

TABLE 2  
NOMENCLATURE

$f$	Frequency (Hz)
$u'$	Velocity fluctuation (m/s)
$U$	Mean axial velocity (m/s)
$k$	Wavenumber ( $1/m$ ) = $2\pi f/U$
$G(k, U)$	One-sided power spectral density = $d(u'/U)/dk$
$Tu$	Turbulence Intensity
$N$	Number of samples = 4000
$\Delta t$	Time between sampling points (s)
$X(f)$	Fourier transform
$\Lambda$	Integral length scale

For the first half of the experiments, these calculated values for turbulence intensity and power spectral density can be compared with similar tests performed in the past [2]. From these past experiments, the turbulence intensity and power spectral density were found to be approximated by

$$Tu = 1.13 \left( \frac{x}{d} \right)^{-5/7}$$

where  $x$  and  $d$  are the grid dimensions defined in Fig. 14, and

$$G(k) = \frac{4(Tu)^2 \Lambda U}{[1 + (k\Lambda)^2]}$$

where

$$\Lambda = 0.2d \left( \frac{x}{d} \right)^{1/2}$$

### 4.3 Results

Due to the difference in Reynolds Number between the wind tunnel and blowdown turbine, the effect of Reynolds Number on turbulent characteristics was investigated. Figure 15 shows the effect of Reynolds Number on power spectral density. From this graph, it can be seen that the turbulent characteristics are independent of Reynolds Number, except for a small influence at high wave number.

The first turbulent characteristic of interest is the turbulence intensity. Both the measured and predicted values [1], [2] of turbulence intensity over the frequency range  $12.5\text{Hz} < f < 25,000$  Hz can be found in Table 3, where 25,000 Hz is the Nyquist frequency.

**TABLE 3**  
**TURBULENT INTENSITIES**

	Streamwise Position			
	No Nozzle		Nozzle	
	1/2 NGV	NGV	1/2 NGV	NGV
Tu	23.6	13.6	23.0	6.4
Theory	18.6	12.2	18.6	8.7

From Table 3, it can be seen that the measured values of turbulence intensity were higher than the predicted values, except at the NGV streamwise location with the nozzle installed. This is the position of importance, because this position corresponds to the position of interest in the blowdown turbine facility. At this position, the measured value of turbulence intensity was lower than the turbulence intensity that would occur at this position in a typical gas turbine engine.

The other turbulence characteristic of importance is the power spectral density. Figures 16 and 17 show the graphs of the power spectral density for the no nozzle case at the 1/2 NGV and NGV streamwise locations respectively.

These two figures show the measured values of turbulent energy at high wavenumber correspond nicely with theory, while the measured energy at low wave number is noticeably higher than predicted. A series of tests were run in which a low pass filter was used to filter out the high frequency contribution of energy to the power spectral density to show that this high energy level at low wavenumber was not caused by aliasing of the signal when the data was taken. In Fig. 18, the graph of the power spectral density at the NGV streamwise location is plotted with the nozzle installed.

In Fig. 18, the theory line [1] is measurements taken at the burner exit of a simulated gas turbine combustor. The turbulence energy measured in the wind tunnel matches the turbulence energy measured in the gas turbine rather well at high and low wavenumber, however the wind tunnel measurements of turbulence energy are noticeably lower in the intermediate wavenumber region. This lower energy region agrees with the lower value of turbulence intensity measured in the wind tunnel.

In order to check the effect of transverse positioning of the hot wire on turbulence characteristics, a number of measurements were carried out at various transverse positions, while keeping the streamwise position constant. The measurements were taken at the NGV streamwise position, with nozzle installed. Figure 19 shows the effect of transverse positioning in the direction parallel to the nozzle by looking at two positions 1/2 of one grid mesh apart in the direction parallel to the nozzle. Figure 20 shows the effect of transverse positioning in the direction of nozzle

contraction by looking at two positions 1/2 of one grid mesh apart in the direction of nozzle contraction.

Figure 19 shows that the parallel positioning of the hot wire in the nozzle has little effect on turbulence characteristics, while Fig. 20 shows that hot wire position has a considerable effect in the direction of nozzle contraction. When looking at the turbulence intensities at the NGV streamwise position, it was found that the turbulence intensities varied in the direction of nozzle contraction due to changes in the mean velocity across the nozzle. The root mean square values of the velocity fluctuations remained constant across the nozzle. Figure 21 shows the value of turbulence intensity in the direction of nozzle contraction at the NGV streamwise position.

#### 4.4 Conclusions

The turbulence characteristics of the turbulence grid to be used in the blowdown turbine facility have been presented. A number of interesting points have been presented.

1. The turbulent characteristics of the flow produced by the grid are independent of Reynolds Number in the range  $Re = 5 \times 10^3$  to  $1.5 \times 10^4$ , except for a small effect at high wavenumber.
2. For all cases, the measured value of turbulent intensity was larger than theory, except at the NGV streamwise position with the nozzle installed. In this case, the turbulence intensity was found to be lower than that measured by Moss and Oldfield.
3. At high and low wavenumber, the power spectral density was found to match rather well with the results obtained by Moss and Oldfield. At the middle wavenumbers however, the power spectral density measured behind the turbulence grids was found to be noticeably less. This result points out the lower amount of turbulent energy contained in the turbulence generated by the grid.

Assuming no change in the velocity perturbation through the NGV, the turbulence intensity at rotor entrance can be calculated. In the absolute frame of reference, the turbulence intensity was calculated to be 0.58%, while in the relative frame of reference, the turbulence intensity was calculated to be 0.97%.

## **5.0 Aerodynamic Instrumentation**

Prior to the start of this program, the aerodynamic instrumentation available on the blowdown turbine facility was limited to the steady state instrumentation in Table 4 and the time-resolved instrumentation in Table 5. In the context of the blowdown turbine, steady state is relative to the rotor blade passing frequency of approximately 6 kHz. For aero performance quality measurements, the steady state instrumentation requires frequency response of several hundred hertz to follow the tunnel transient (step input startup followed by a 20 second time constant exponential decay), and the temporal fluctuations produced by moving the measurement point through a spatially nonuniform flow field such as a turbine exit.

The baseline research program added an additional upstream circumferentially traversing total temperature rake between the exit of the distortion generator and the turbine inlet, and wall static taps on the NGV inner and outer annulus at the trailing edge. After SNECMA joined the program, we were able to add turbine exit translating time-averaged total pressure and temperature rakes, and a time-resolved exit total pressure rake. After the April program review meeting, an upstream inlet total pressure rake and exit inner annulus static tap were added. The new instrumentation is summarized in Table 6. In the following sections, we discuss the design of the rakes, the signal conditioning equipment, and instrument calibration plans.

### **5.1 Temperature Rakes**

The measurement of total gas temperature in the blowdown turbine represents unusual problems because of the relatively fast time response required (several hundred hertz) even for time-averaged measurements. The most important design constraint is the reduction of transient thermal conduction error due to heat conduction from the thermocouple to the supporting structure. The design of suitable probes was described in some detail in L. Cattafesta's thesis, in which several alternate approaches were evaluated.

The design philosophy was to adapt the basic probe flow geometry used at Rolls-Royce to the transient environment. This has the principal advantage of maintaining continuity with

**TABLE 4**  
**BASELINE BLOWDOWN TURBINE STEADY STATE AERODYNAMIC INSTRUMENTATION**

ID	Type	Location	Sensor(s)	Range	Comments
PT0A, PT0B	Stagnation Pressure	Supply Tank	Kulite XTE-190	0-150 psig	Redundant
PT2	Total Pressure Rake	B.L. Bleed	Kulite XCQ-093	0-100 psig	5 Station, Remote Transducers
P4S	Wall Static	Downstream, Rotor Exit	Kulite XTE-190	0-50 psig	Flush Mounted
PT4	Total Pressure	Downstream, Rotor Exit, Mid-Height	Kulite XTE-190	0-100 psig	Kiel Head, Remote Transducers
PT4R	Total Pressure Rake	Downstream, Rotor Exit	Kulite XCQ-093	0-50 psig	5 Station, Kiel Heads, Remote Transducers
PDMP	Stagnation Pressure	Dump Tank	Kulite XTE-190	0-50 psig	
TT0	Total Temperature	Supply Tank	T/C, Type K	270-550°K	For Initial Temp. Only, 4 Places
TT2	Total Temperature	B.L. Bleed	Beckman 300, T/C, Type K	270-550°K	5 Station, Kiel Head, Heated
TT4	Total Temperature	Downstream, Rotor Exit	Beckman 300, T/C, Type K	270-550°K	5 Station, Kiel Head, Heated

**TABLE 5**  
**BASELINE BLOWDOWN TURBINE TIME-RESOLVED INSTRUMENTATION**

<b>ID</b>	<b>Type</b>	<b>Measurements</b>	<b>Position</b>	<b>Net Freq. Response</b>	<b>Sensors</b>	<b>Transversing</b>	<b>Comments</b>
4-Way Probe	Cylinder	Total & Static Pressure, Radial & Tang. Flow Angle	Rotor Exit	15 kHz	Kulite XCQ-063	Radial or 2 NGV Pitch	Water Cooled
PTS	Impact	Total Pressure	Rotor Exit	25 kHz	Kulite XCQ-030	Radial or 2 NGV Pitch	Poor Stability
Hot Wire		~Velocity	Inlet	40 kHz	TSI or Dantek	Not Currently	For Turbulence
Aspirating Probe		Total Pressure & Total Temperature	Rotor Exit	20-25 kHz	Hot Wires	Radial or 2 NGV Pitch	Difficult to Use

**TABLE 6**  
**ADDITIONAL BLOWDOWN TURBINE AERODYNAMIC INSTRUMENTATION**

<b>ID</b>	<b>Type</b>	<b>Location</b>	<b>Sensor(s)</b>	<b>Range</b>	<b>Comments</b>
PT1R	Total Pressure	On Inlet Translator	Kulite XCQ-063	0-100 psig	11 Station, Kiel Head, Integral Transducers, on Inlet Translator
PT3L, PT30	Wall Static Pressure	NGV Exit Annulus	Kulite XCQ-093	0-100 psig	At NGV TE, Mid-Passage on Inner & Outer Annulus Walls, Remote Transducer
PT4N	Total Pressure	Downstream, Rotor Exit	Kulite XCQ-063	0-100 psig	8 Station, Kiel Head, Integral Transducers, on Exit Translator
P4I	Wall Static Pressure	Downstream, Rotor Exit	Kulite XCQ-063	0-100 psig	On Inner Annulus, on Exit Translator
PT4F	Total Pressure	Downstream, Rotor Exit	Kulite XCQ-063	0-100 psig	8 Station, High Frequency, Flush Transducers, on Exit Translator
TT4R	Total Temperature	Downstream, Rotor Exit	Beckman Special, T/C	Type K	8 Station, Kiel Head, Dual Sensors, on Exit Translator



measurements made on the same stage hardware at Derby. To that end, the basic probe is a vented, shield Kiel-type design. A "micro-disk" thermocouple ( $20\text{ }\mu\text{m}$  diameter x  $5\text{ }\mu\text{m}$  thick) is used for its high frequency response ( $300\sim 500\text{ Hz}$ ). The thermocouple is mounted on a  $75\text{ }\mu\text{m}$  diameter,  $4\text{ mm}$  long quartz standoff to minimize the thermal conduction from the T/C to probe body. The arrangement is illustrated in Fig. 22. The vent hole size is a tradeoff between a low velocity need to minimize recovery factor corrections and a high velocity which increases the heat transfer to the T/C support stem and thus reduces the transient thermal error. Hole sizes are varied to account for the mean Mach number of the external flow field and are  $1\text{ mm}$  and  $0.6\text{ mm}$  on the turbine inlet and exit probes respectively.

These measurements reduce the transient thermal conduction error due to the tunnel startup to  $1\sim 2^\circ\text{K}$ , a level sufficient for the support of heat transfer measurements ( $150^\circ\text{K}$  gas-to-wall temperature difference) but inadequate for aerodynamic performance determination. An additional transient error source is introduced when a probe is traversed through thermal gradients such as wakes. This effect was simulated by driving a time accurate conduction model of the temperature probe with the output of a 2-D viscous multi-blade row calculation of the flow in the turbine (Fig. 23). A measured blowdown tunnel transient is shown in the temperature time history of Fig. 24, in which the top trace (labeled "gas") is the output of the micro disk thermocouple. A second thermocouple was mounted at the bottom of the  $75\text{ }\mu\text{m}$  diameter quartz stem (labeled "stem bottom"). The gas trace illustrates the rapid temperature rise as the tunnel starts at  $80\text{ ms}$  and the slow decay as the supply tank blows down. The stem bottom trace reflects the temperature rise of probe support structure, which is non-negligible over the first  $500\text{ ms}$  of interest. The differences between the two traces is a measure of the driving temperature difference responsible for the transient conduction error. Given measurement of this temperature difference, the conduction error can be estimated and a correction made. The accuracy to which this procedure can be implemented must be established by calibration and will be discussed in a later section. The principal disadvantage of this approach is that twice as many sensors, signal conditioners, and data recording channels are required compared to just single thermocouple measurements.

### **5.1.1 Inlet Rake**

The inlet rake consists of 11 Kiel head measurement points (2 sensors each) arranged to sample equal areas in the 10 cm high annulus (Fig. 25). The unit is mounted on the inlet circumferential translator, angled to account for the probe rotation velocity. Thermocouple (Type K) wires are derotated by a coil and brought out through the pressure vessel wall. A "cold" junction connection to copper leads is then made in a dewar. Rather than keep the dewar at the ice point, the cold block temperature is measured with two 4-wire platinum resistance thermometer devices (RTD's).

### **5.1.2 Turbine Exit Rake**

The turbine exit rake consists of 8 Kiel head measurement points (2 sensors each) arranged to sample equal areas in the 3.7 cm high annulus (Fig. 26). The unit mounts to the turbine exit circumferential translator, which presented two severe design constraints. The first is that the rake must be readily removable from the blowdown tunnel with the rotor in place for calibration. The only access is through the three small instrumentation ports. This suggested placing the cold junction within the probe body itself so that all thermocouple wires and joints are included in the calibrations. The second constraint is space, since the turbine exit translator is retrofit to an area in which no provision had been made during the initial facility design. The final probe design houses a copper cold plate in a cylindrical housing below the flow path. The thermocouple wires transition to copper on solder pads on the cold plate. The cold plate temperature is monitored by two RTD's. There is sufficient thermocouple wire within the rake body to permit separation of the rake head and cold plate for calibration. The bottom of the rake assembly is a 41 pin electrical connector so that the entire unit simply plugs into the exit translator.

### **5.1.3 Temperature Rake Signal Conditioning**

Each of the rake sensors (11 upstream, 8 downstream) has two thermocouples and thus requires two signal conditioners and two A/D channels. The principal requirements for the conditioners are low noise (compared to the thermocouple output) and long-term stability (since the amplifiers must remain stable between calibrations, hopefully several weeks). Analog devices

2B31H instrumentation signal conditioners were selected. They are operated at a gain of approximately 800 and the internal two pole filters are set at 500 Hz. The same units are also used as RTD signal conditioners for the cold junction references. Forty-two channels have been built.

The data acquisition system has been expanded with the addition of an Analogic 64-channel, 16-bit, PC-based A/D subsystem. The maximum aggregate sampling rate for the unit is 200 kHz. Software has been written so that this unit mimics the functionality of the existing blowdown turbine data system (41 channels at 200 kHz per channel plus 128 channels at 16 kHz may rate per channel). The new unit is required because of inadequate stability for aero performance of the older low speed channels as well as lack of capacity.

#### **5.1.4 Temperature Rake Calibration**

Three calibration steps are required to establish the rake accuracy. The first is a steady state voltage output versus temperature calibration. This will be performed in a stirred silicon oil bath over the 300-500°K range of interest. A secondary standard (0.01°K) platinum RTD is the temperature reference. The second step is to establish the long-term stability of the sensors, signal conditioners, and A/D, which will be established by multiple calibrations. The third and final step is determining the overall accuracy of the rake in measuring gas temperature, which will include the transient conduction and recovery factor corrections.

The final aerodynamic calibration of the rakes requires that: (a) the freestream temperature be uniform and known to the necessary accuracy (0.1~0.3°K); (b) the freestream Mach number be variable to match the turbine inlet and exit conditions; and (c) the flow turn on with approximately the same time constant as the blowdown tunnel (30~50 ms). To accomplish this, we have built a 75 mm diameter blowdown test tunnel using blowdown turbine components (Fig. 27). The heated gas supply is the blowdown turbine supply tank (~11 m<sup>3</sup> volume). The flow is turned on and off using the 75 mm diameter, fast-acting (15 ms) coolant supply valve. An orifice at the test section discharge is used to establish the Mach number. The test tunnel is closely coupled to the supply tank to keep the thermal boundary layers thin at the probe location. The supply tank gas is homogenized prior to the test by three fans. The temperature distribution is established by 11

platinum RTD's spotted through the tank (Fig. 28). The RTD's are bath-calibrated against a secondary standard before installation. Figure 29 is data taken from the tank sensors and shows that the temperature is uniform to about 0.2°K.

The tank RTD's and fans have been removed from the supply tank for the turbine testing. The plan is to bath calibrate the temperature rakes, run the turbine tests, and then, in the late summer-early fall time frame, set up the test tunnel and run the calibration checks.

## **5.2 Total Pressure Rakes**

Three translating total pressure rakes are planned for these tests: two exit rakes described at the April review meeting, and a new inlet rake as suggested at the meeting. The inlet rake and one exit rake are designed to measure time-averaged total pressure and look externally the same as the total temperature rakes in Figs. 25 and 26. They are vented Kiel head designs with short (75-100 mm) pressure tubes leading to transducers mounted in the rake housing under the flow path. This is to insulate the pressure transducers from the temperature transient of the tunnel operation and maintain stability over the first 500 ms to the end of the test time. One Kulite XCQ-063 transducer is used per rake position (11 at inlet, 8 at outlet). The pressure tubes extend to the transducer faces, so that there is no "dead" volume and thus frequency response is maximized. The differential transducers are used with the reference tube brought out to the laboratory. During the test time, the transducers are referenced to vacuum. Just prior to and after each, the transducers are calibrated by changing the reference pressure. Thus, the transducers need not remain stable for more than a minute or two. This results in stable and accurate DC pressure readings. The pressure rakes are interchangeable with the temperature rakes.

The third pressure rake is designed to measure time-resolved total pressure so the transducers (Kulite XCQ-063) are mounted in the eight rake Kiel heads, protected by a screen. Because the transducers are now exposed to the flow, their temperature change and thermal drift are expected to be greater than for the rakes with the protected and insulated transducers. If drift is a problem, then the DC values for these transducers will be corrected with the readings from the

steady-state rake.

### **5.3 Static Pressure Taps**

Wall static pressure taps have been added to the inner and outer annulus walls at the NGV trailing edge (mid-passage), and at the inner annulus at the turbine exit translator at the rake axial station. All three consist of short tubes (50~100 mm) fed through Kulite XCQ-093 transducers.

### **6.0 Rotor Blade Heat Flux Instrumentation**

Since a principal output of this research program is a set of detailed rotor blade heat transfer measurements, the rotor blade instrumentation is the single most important part of the facility preparation. It is also the most time consuming and expensive by far, with more than one half the program resources to date being expended in this area. For this program, the instrumentation has been entirely redone, including the manufacture of transducers, their mounting and wiring, and blade calibration.

Three blades have been produced, each instrumented about their chord with the spanwise location differing among blades. A composite of the three blades is shown in Fig. 30, which illustrates the heat flux gauges' locations. Thirty-nine gauges are fully functioning. An additional five have just the top sensor operational, in which case essentially all information can be retrieved with some additional data reduction effort. On three additional sensors, only the bottom sensors are working, in which case little information can be extracted. Two additional gauges are mounted on the blade platform near midpassage at the leading edge plane. Resistance thermometers are mounted to the underside of the blade platforms to serve as pre- and post-test temperature references which facilitate scale factor and drift determination.

The wiring for each of the three blades is shown schematically in Fig. 31. The signals from each transducer is brought out by slip rings. The signals are then fed through 34 bridge amplifiers (DC-50 kHz bandwidth) and into individual data acquisition channels (200 kHz sampling rate for the top sensors, 16 kHz for the bottom sensors).

The blades have been completed and the 94 amplifiers required checked out. Blade

calibration will be done as the NGV-only testing is ongoing in order to free up manpower for readying the facility.

## 7.0 CFD Activities

The principal CFD tool to be used at MIT on this program is the three-dimensional, unsteady, multi-blade row Euler code written by Saxer and Giles, UNSFLO3. This is an explicit time-marching, node-based, Ni-Lax-Wendroff algorithm implemented on an unstructured grid. Non-reflecting boundary conditions are applied at the inlet and outlet and at the stator-rotor interface.

This code had been run on the experiment's NGV and rotor blade geometries by Saxer but at equal NGV-rotor pitches rather than the 36 NGV's, 61 rotor blades of the rig. The grid geometry has been modified to calculate 3 NGV passages and 5 rotor passages (i.e., 36 NGV, 60 rotor blade count) as illustrated in Fig. 32. This grid is currently set up with about 256,000 node points ( $56 \times 36 \times 21$  in each of 3 NGV passages and  $56 \times 22 \times 21$  in each of 5 rotor passages). A coarser version of the grid (only 9 rather than 21 radial planes) has been run to convergence as an initial checkout. Rotor blade temperature contours are shown in Fig. 33. The finer grid is currently running.

The inlet boundary conditions have been set up so that quite general radial temperature and pressure distortions can be specified. Periodicity, however, constrains hot spot placement to one every 3 NGV pitches where the experiment is set up as one hot spot for every 2 NGV pitches (Fig. 34). After we gain some experience with the code, the blade count can be enlarged to 6 NGV's and 10 rotor blades to permit the experiment's periodicity to be modelled. This is at the expense of doubling the run time, of course. The grids have been interfaced to the MIT 3-D visualization codes.

In addition to UNSFLO3, the two-dimensional Euler version and a 2-D thin shear layer viscous version are available at MIT and have been checked out with the experimental geometry. Also available is John Denton's MULTISTAGE 3-D, steady, multi-blade row, Euler code.

Discussions are ongoing with NASA Lewis Research Center about using John Adamczyk's 3-D viscous code.

## **8.0 Rig Preparations**

Rig preparations included completion and installation of the new rake translators; refurbishment and repair of tunnel subsystems, installation and programming of new data acquisition equipment, and instrumentation calibrations and cables. The inlet and outlet rake translators were completed and installed in the rig. The units performed as designed during vacuum testing.

Several of the rig subsystems required refurbishment and repair, which was not surprising considering that the rig is 10 years old and had not been operated for about 3 years. The Freon boiler in the gas mixing system failed pressure testing and was replaced as were numerous leaking valves. The vacuum system valves and vacuum pumps were overhauled. When the test section was disassembled to mount the rotor exit translator, it was discovered that a wire on one of the eddy brake magnet coils was broken. This explains the sudden shift in brake calibration noted during the previous test series. The eddy brake was removed for repair and will be re-installed with the rotor.

## **8.1 Data Acquisition**

Two new data acquisition systems have been added to supplement the current unit and serve as backup (the current system is 11 years old). Sixty-four low speed channels have been added. These units have 16-bit resolution (about 14 of which are usable given the noise levels at the rig), and 3 kHz per channel maximum data rate. The unit is mounted in a '486 PC. These low noise, high resolution channels have been allocated primarily to the temperature rake outputs. Additional high bandwidth channels have been added as well. Thirty-two channel (24 arrived, 8 on order), 12-bit, 330 kHz per channel A/D's have been added in a second '486 PC. This unit was purchased by the laboratory and will be shared with other experiments. This brings the total channel capacity of the blowdown turbine facility to approximately 68 high speed analog channels

(200+ kHz per channel) and 192 low speed analog channels (3+ kHz per channel).

Both the new low and high speed data acquisition systems (A/D's plus computers) required considerable custom cabling and programming. The units were programmed to interface to the current data handling systems and are mostly transparent to the user.

## 8.2 Instrumentation Calibration

Upon completion of the A/D systems, the temperature and pressure rakes were DC calibrated. The temperature rakes are of a pitot-type configuration with two type K thermocouples at each head position, one to measure gas temperature, the other to measure the temperature of the new stem on which the first is mounted, to permit corrections for conduction errors. The rakes are designed with local reference hot junctions rather than standard remote cold junctions (Fig. 35a). This arrangement facilitates rapid recalibration of the rakes without necessitating teardown of the test section, as would be the case if thermocouple leads were run out to external cold junctions. (The rakes can be removed through windows in the test section while leaving the cabling in place.) The hot junctions consists of an insulated copper block on which the thermocouple to copper wire connections are made. The block is instrumented with two resistance thermometers (RTD's). Calibration consisted then of two steps – calibration of the reference junction sensors followed by calibration of the thermocouples. Both were done in a stirred bath of silicon oil against a secondary standard platinum RTD stable to 0.01°C. The calibrations were performed through the entire data chain – sensor, cabling, signal conditioners, data acquisition system. Transducers agreed with each other to 0.1°C. Repeatability of calibration was within 0.2°C.

The pressure transducers in the rakes (Fig. 35b) are readily calibrated since each is a differential transducer with a reference pressure which is brought out of the rake and through the translator. In practice, the transducers are calibrated in place immediately before and after each test. The pressure transducers were checked for temperature sensitivity by calibrating them in an oven at temperatures up to 100°C. All transducers are stable to better than 1% over the temperature range.



### 8.3 Instrumentation Performance on Translators

The rake instrumentation was installed in the translators (Fig. 35c) which were then run in vacuum as an operational check. The pressure rakes' operation was satisfactory in that no extraneous signal or noise was observed on the pressure transducer outputs during the translator motion (Fig. 6). The temperature outputs, however, did show artifacts due to both translator motion and operation of the DC servo systems driving the two translators. A signal related to the motion can be seen on the output from an inlet rake thermocouple in Fig. 36, starting at about 200 msec (same time scale as in Fig. 6). The signal is similar in shape and magnitude on all 22 thermocouples on the inlet rake. The signals are clearly related to the probe motion in that they do not appear on the reference RTD signals (Fig. 37) which are mounted in the stationary frame for the inlet rake. The magnitude of this unwanted signal, about  $0.2^{\circ}\text{C}$ , is sufficiently low that it does not serve as a hindrance to this research program but, at this level, it is a major component of the upstream gas temperature measurement uncertainty.

The level of unwanted signal is much greater on the outlet temperature rake, as can be seen in Fig. 38, in which the 'noise' amplitude is about  $3^{\circ}\text{C}$ . As with the inlet rake, the signal is similar on all the thermocouples on the rake to a remarkable degree (Fig. 39). Unlike the inlet rake, however, the outlet temperature reference RTD's are on the rotating system and these exhibit a signal amplitude similar to that of the thermocouples, Fig. 40. (The plotted 'reduced' thermocouple temperature traces incorporate the RTD signals since these are reference sources which are differenced with the raw thermocouple temperature.)

The level of temperature uncertainty represented by the level of interfering signal on the outlet temperature rake ( $3^{\circ}\text{C}$ ) is clearly unacceptable for aeroperformance measurements and marginal for reducing heat transfer measurements. Therefore, considerable effort was put into understanding this problem. Sources of the interference considered included some combination of magnetic pickup on the rotating system, cross-talk between layers of cabling, grounding problems, etc. The presence of this signal on the outlet RTD's (which were operated in a 4-wire configuration to eliminate common signals induced in the leads) and its absence on the pressure

rakes (4-wire bridge configuration) which share the same cabling was particularly puzzling. Comparison of these signals, as in Fig. 41, was interesting but unenlightening. Circuit modelling and bench testing were unsuccessful in reproducing or explaining the problem. Mu metal shielding was added to the cabling to exclude magnetic fields with no avail. Finally, the grounding scheme of the rakes was modified in an *ad hoc* manner. This succeeded in reducing the induced signal on the exit rake by more than an order of magnitude (Figs. 42 and 43), to less than  $0.15^{\circ}\text{C}$ . Only minor improvement was observed in the upstream rake output (Fig. 44). At its current level, these unwanted signals will not adversely affect the current research program. We fixed things without understanding why and will now retire from the field of battle clothed in graceful victory and ignorance.

## **9.0 Initial NGV-Only Blowdown Testing**

Two blowdown tests were run within the NGV-only configuration – with the rotor removed, and with the outlet rakes moved upstream to the NGV exit (Fig. 45). Several problems were encountered during the runs but data was nevertheless taken. In the following sections, we will first examine the data and then discuss the problems which arose and their resolution.

### **9.1 Initial NGV Test Data**

The primary purpose of these tests is checkout and evaluation of the facility and its instrumentation. Two tests were run – test 150 with both radial and circumferential distortions, and test 151 with radial distortions only (the circumferential distortion heat burned out, as will be discussed later). A pressure history from the inlet total pressure rake (Fig. 46) illustrates tunnel operation. The mainflow valve is commanded to open at 0 milliseconds (ms). The pressure begins to rise in the test section at 60 ms and peaks at 95 ms. The 20 second experimental decay time constant of the facility then can be seen in the decay of the mean pressure level from 100 to 600 ms. Superimposed on this is a ringing of the cavity formed by the inlet valve to the NGV throat, driven by the startup fast rise. This ringing has substantially dried out by 250 ms, the start of the useful test time which runs until 550 ms into the test. (The data acquisition systems operate

at their highest rate, 200 kHz per channel, during this 250 to 550 test time.) This time trace also illustrates the radial flow uniformity at the tunnel inlet and thermal drift limits of the transducer. All six of the radial stations agree to within one percent, and five of the six to 0.5%. We believe that the sixth transducer's performance can be improved with additional calibration.

Performance of the low frequency response turbine exit pressure rake and the wall static taps is shown in Fig. 47. The sawtooth signals are the NGV wakes through which the rake is being translated. The sudden steps in two signals are due to a wiring failure which will be discussed later. An example of the pressure rake signal during the 250-550 ms test time can be seen in Fig. 48 in which the NGV exit flow structure can be clearly seen superimposed on the DC pressure decay of the facility. A similar plot is shown in Fig. 49 for a high frequency response total pressure rake midspan position. We infer from an examination of this data that the pressure rake performance is satisfactory and as planned.

The response of the upstream temperature rake during the circumferential traverse in a blowdown test is illustrated in Fig. 50 for the midspan location. The initial upspike at 90~100 ms is compressional heating during the startup transient. The three downspikes at 250 ms, 390 ms, and 550 ms are the thermal wakes of the struts separating the three sectors of the temperature distortion generator. The data from all eleven sensors along the span was used to construct the contour plot of gas temperature in Fig. 51. The circumferential<sup>1</sup> translator is accelerating until about 120 ms (resulting in the close contour lines), but is travelling at constant velocity during the 250-550 ms test time. Thus, the time axis can be considered to be circumferential position during the test time. That period replotted in Fig. 52 shows the traverse of two 120° segments of the annulus, a  $\theta$ TDF sector from 250 to 390 ms, and an RTDF sector from 390 to 550 ms. The strut wake can be seen at 390 ms. The radial temperature distortion is seen to be uniform circumferentially between 450 and 510 ms (about a 45 degree sector or 4-5 NGV spacings).

The output from the midspan exit total temperature rake sensor as it is traversed about the circumference at the NGV exit is illustrated in Fig. 53. The compressional startup spike is evident at 90 ms. The cold wakes of the NGV's can be seen between 200 and 300 ms. From 300 to 500

ms, the rake is traversing through the  $\theta$ TDF sector, whose heater was burned out during this test, so that the temperature is quite low. After examining the temperature data, we conclude that the temperature instrumentation is operating as designed and that its performance is satisfactory for this research project.

## **9.2 Exit Rake Translator Wiring Problems**

During the first NGV-only blowdown tests, the wiring which runs from the translator to the stationary frame was seriously damaged. The wiring consists of three 50-conductor ribbon cables sandwiched between four layers of 75  $\mu$ m stainless steel shim spring stock. The multi-layer cable is 3/4 of a meter long and arranged in a hairpin with one end fastened to the rotating translator and the other fixed to the stationary test section. The cable is located at the rear of the turbine exit flow path in a protective shroud. This loop arrangement (Figs. 8 and 54) facilitates 360 degree travel during the test. The shims both protect the ribbon conductors and provide the restoring force needed when the translator is reset between tests. Unfortunately, the ribbon blew out under its containment shroud and became entangled in the chain drive (Fig. 55) approximately 250 ms into the first test.

Several solutions were considered, including a rotary seal on the protective shroud and various modifications to the laminated ribbon assembly. The geometric constraints of the test section proved very restricting. A full-scale mockup was constructed to evaluate various schemes. The approach adopted was (a) to stiffen up the ribbon assembly by replacing the outer two 75  $\mu$ m thick shims with 150  $\mu$ m shims, and (b) the addition of a rotating containment ring at the inner radius of the stationary protective shroud. This ring increases the moment of inertia of the rotating system, slowing the translator acceleration.

## **10.0 Temperature Distortion Generator**

The temperature distortion generator used for these tests is the honeycomb storage matrix unit originally designed for RTDF tests. It uses electric heating wires at midspan as a heat source and oil cooling jackets on the inner and outer flow path walls to serve as heat sinks, thus generating

a parabolic temperature profile across the annulus during the pretest heatup period. The unit was modified for  $\theta$ TDF testing by spacing the heating wires along the circumference in one  $120^\circ$  sector to generate hot spots, one hot spot per two NGV pitches (Fig. 1).

Previous testing had shown that the generator was contaminated with fine particles during manufacturing which destroyed the rotor blade heat flux instrumentation. Therefore, a 1000 liter ultrasonic cleaner was constructed so that the generator could be immersion cleaned. After each cleaning, the water was drained and filtered and the particles counted. The cleaning was repeated until no particles could be discerned.

### **10.1 Circumferential Distortion Heatup Difficulties**

The design of the distortion generator was based on the original design estimates of the thermal diffusivity of the stainless steel honeycomb matrix. Variations in hot spot amplitude and extent were to be achieved by adjusting the current time history into the electric heaters as illustrated in Fig. 2. During the first tests, it was observed that circumferential temperature gradients were small relative to those in the radial direction. Thermocouples spotted about the matrix permitted explicit measurement of relative thermal diffusivities (Fig. 56). Figure 57 shows the difference between the radial and circumferential temperature gradients to step changes in heat input. The matrix equilibrates in the radial direction in about an hour, while only five minutes is needed in the circumferential direction. This implies that circumferential distortions will quickly "wash out" compared to radial ones.

To quantify this difference, a two-dimensional transient conduction model of the distortion generator was written. The thermal diffusivities in the radial and circumferential directions were estimated by fitting the model to time-temperature histories of thermocouples spotted about the matrix. The model fits the data well (Fig. 58), giving confidence in the results. The conclusion is that the thermal conductivity is 15 times greater in the circumferential direction than in the radial one. The cause of this large a nonuniformity is not clear (poor brazing?) but the implication is that  $\theta$ TDF can be held for only short periods of time and that large amplitude hot spots will be difficult

to achieve. This is illustrated in Fig. 59, which shows the result of a transient heat calculation of a sector with two hot spots. At heater current levels compatible with past practice, a 60 to 80°C hot spot is achieved in two minutes. After an additional two hours of heating, these relatively small hot spots are now superimposed on a large radial temperature profile. This pattern is quite similar to that in an engine (good) but not so convenient as pure  $\theta$ TDF for simple analysis (bad).

One solution to this problem is very fast, high current spikes applied immediately (1~3 minutes) before the start of a test. The constraint is the current level which can be put into the heater before mechanical failure (burnout) of either the heater wire or its termination. This was investigated experimentally on a test rig in vacuum, and it appears that  $\theta$ TDF's of 20% can be generated before either the heater wire burns out or the brazed matrix is damaged.

The solution adopted was to double the number of heater wires at each spot from 2 to 4, thus doubling the heat input. The  $\theta$ TDF wires are operated at currents of 30 amps (as opposed to 10 amps in the RTDF sector), increasing the heating rate by nine times. This high heat rate is applied five minutes immediately prior to the blowdown test and should produce hot spots of approximately 50°C. Vacuum tests with thermocouples in the matrix indicated this to be a viable approach. As of this time, one half pressure test has been run at low current (20 amps) as a mechanical checkout. Its results are inconclusive insofar as  $\theta$ TDF levels achievable.

## 10.2 Distortion Generator Contamination

Although the generator was thoroughly cleaned before testing, aluminum witness cylinders were placed in the flow path at the NGV exit. Microscopic examination after the first test showed significant impact, equivalent to about  $10^5$  particles per test if the sampled area is extrapolated over the entire flow annulus. This level of contamination is unacceptable.

Particles were collected and examined. Two types were noted – clear spheres of about 50-100  $\mu$ m diameter, and brown cubes of similar size. Since clear spheres did not dissolve in any acid other than hydrofluoric, they are thought to be glass sandblast beads. The brown particles did not dissolve in any acid. They closely resemble and are thought to be aluminum oxide abrasive

particles, also used for sandblasting.

The question is, of course, how to remove the particles. The ultrasonic cleaning removed all the particles that ultrasonic cleaning will remove. What to do about the rest? Mechanical cleaning techniques considered included shaking the unit on a 100 g shaker used for satellite prelaunch testing, repeated heating and blowing cycles, and steam cleaning. Chemical means of dissolving the particles were also considered. Tests indicated that the procedure outlined in Table 7 might be effective. The question with all of these alternatives is how to remove the particles but not damage the brazed stainless steel matrix. Since we know that the matrix brazing is substandard, all of these options entail considerable risk of damaging the matrix.

**TABLE 7**  
**ONE CHEMICAL CLEANING OPTION**

<p>High pressure steam clean, followed by H<sub>2</sub>O          8-hour immersion in ammonium bifluoride and HCL          8-hour immersion in sulfuric acid at 140°F          Neutralize in NaOH          High pressure steam, followed by H<sub>2</sub>O          Clean gas flow</p>
--

The solution of replacing the distortion generator with one of a different design or from a more reliable vendor is not a serious option due to cost and schedule constraints. The solution adopted was to fabricate a particle filter for the distortion generator option. The engineering design criteria for the filter includes filter efficiency (99%+ of particles 50  $\mu$ m diameter and larger), low pressure drop at 25 kg/sec mass flow, low thermal inertia (to prevent attenuation of the distortion pattern), mechanical integrity, and rapid, relatively low cost fabrication. The final design incorporates a sintered stainless steel filter mesh rated as a nominal 20  $\mu$ m particle filter, backed up by a 45% porosity, three millimeter thick perforated stainless steel plate for mechanical support. The filter in the rig is illustrated in Fig. 7. Because the filter extends the rig length by about 3 cm, realignment of the supply tank and modification of several auxiliary systems was required.

At this time, one blowdown test has been run at one-half pressure with the filter in place. No mechanical problems were encountered. The trapping of particulates was evident when the filter was disassembled for inspection after the test. Thus, this problem appears solved.

### **11.0 Gas Availability and Test Costs**

Since the blowdown turbine facility was last operated, the cost of Freon-12 has risen tenfold, from \$1/lb to \$10/lb. With allowance for leakage and aborted tests, this translates to \$1200 per test for Freon, a cost level which is not in the current budget. There are several possible alternative approaches to this problem, including:

- a) Running fewer tests
- b) Testing with the Freon-12 replacement, HC-134a
- c) Recycling the gas mixture
- d) Testing in air at  $\gamma = 1.4$
- e) Testing with an argon and CO<sub>2</sub> mixture at the proper  $\gamma$
- f) Some combination of the above.

Each of these approaches has some advantages and serious disadvantages which are discussed below.

(a) Obviously, running fewer tests is the most unattractive since the entire point of the project is to take data; the data, however, must be relevant, i.e. properly scaled conditions.

(b) The Freon-12 replacement, Hc-134a, is 20% more expensive so it does not represent a useful alternative.

(c) Recycling the gas mixture is technically feasible but somewhat complicated since the gas mixture is used at a pressure above that for condensation of Freon-12 at room temperature. Also, a relatively large amount of gas (20~50 kg) is used. Initial estimates are that such a recycling system would cost between \$50,000 and \$100,000 and take 4-6 months to get working. Thus, this solution is not compatible with the current project budget and schedule.

(d) Running tests in air is inexpensive but requires a 25% increase in rotor speed to



maintain constant corrected speed. This represents a 50% increase in rotor (no problem) and instrumentation (may be a problem) stress levels. This speed increase is in addition to the 20% increase over the original tunnel design speed needed to operate at the  $-10^\circ$  rotor incidence angle that is now the standard operating condition. This places the rotor speed at 8,000+ RPM, very near the dynamic limit of the current rotating system. Also, of course,  $\gamma$  is 1.4 rather than 1.28.

(e) Gas mixtures other than argon-Freon have been considered. One of the most benign is argon and  $\text{CO}_2$  mixed to the proper  $\gamma$  of 1.28. This has a molecular weight of 42 and a speed of sound 114% of that of argon and Freon. Thus, it represents a low cost alternative with a less extreme increase in rotor speed and stress levels.

None of these options are all that attractive but we are unaware of any other alternatives. The current plan for the NGV-only testing is to (a) run most tests in air, (b) run a set with argon- $\text{CO}_2$  for comparison, and (c) run two Freon tests for reference and comparison with previous running. For the rotor tests, the first few tests will be with the standard argon-Freon mixture. The principal concern here is to avoid stressing of and damage to the rotor instrumentation until a baseline set of tests have been completed (or the budget is exhausted). Testing will then switch to argon- $\text{CO}_2$ .

## 12.0 Near-Term Plans

The plan for this winter is to conduct the NGV-only tests at the end of December and in January. The rotor instrumentation will be calibrated in January and the rotor installed. The full-stage testing should begin before February and continue through the spring.

## 13.0 References

1. Moss, R.W., and Oldfield, M.L.G., "Measurements of Hot Combustor Turbulence Spectra," Rolls-Royce, plc, 1990.
2. Roach, P.E., "The Generation of Nearly Isotropic Turbulence by Means of Grids," *Int. J. of Heat and Fluid Flow*, Vol. 8 (2), 1986.

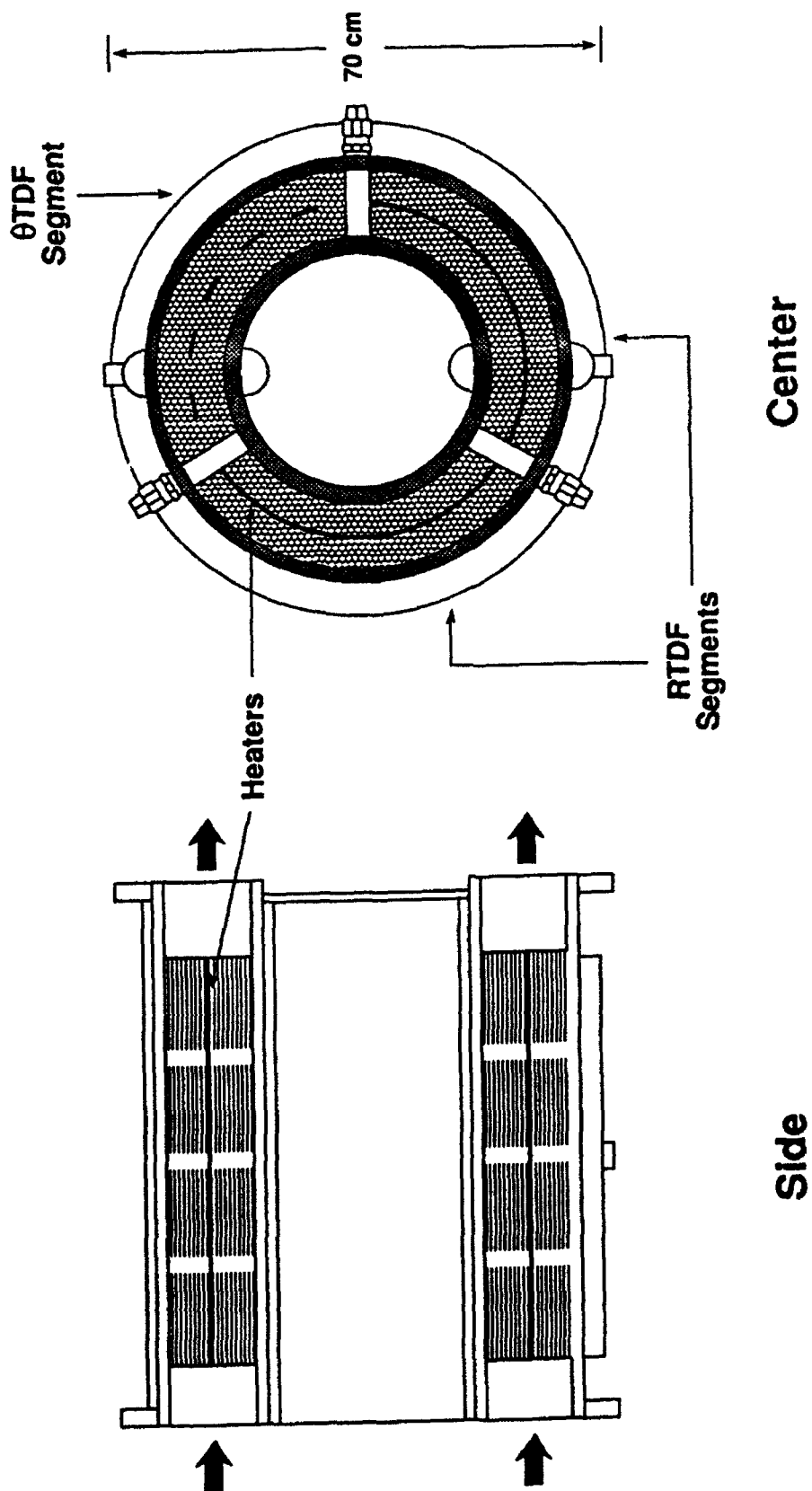
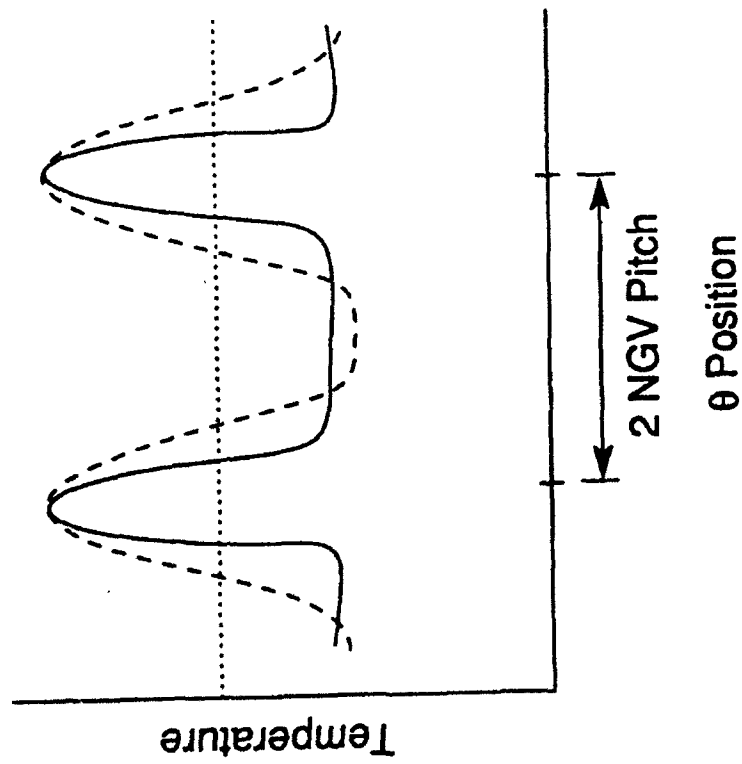


Fig. 1: Distortion generator modified for simultaneous radial and circumferential patterns

### Vary Time for Extent



### Vary Power Input for Peak

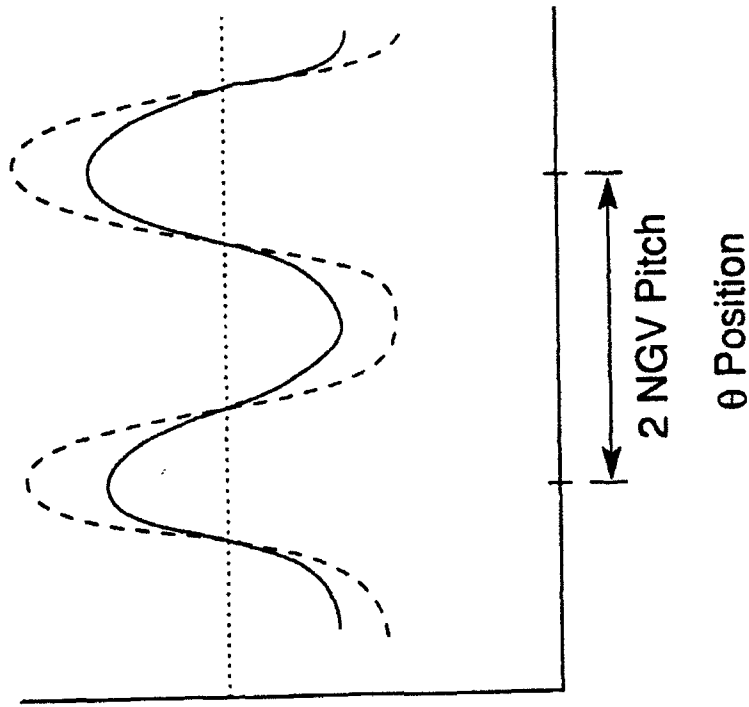


Fig. 2:  $\theta$ TDF temperature profiles will be set up by varying the time x power history into generator

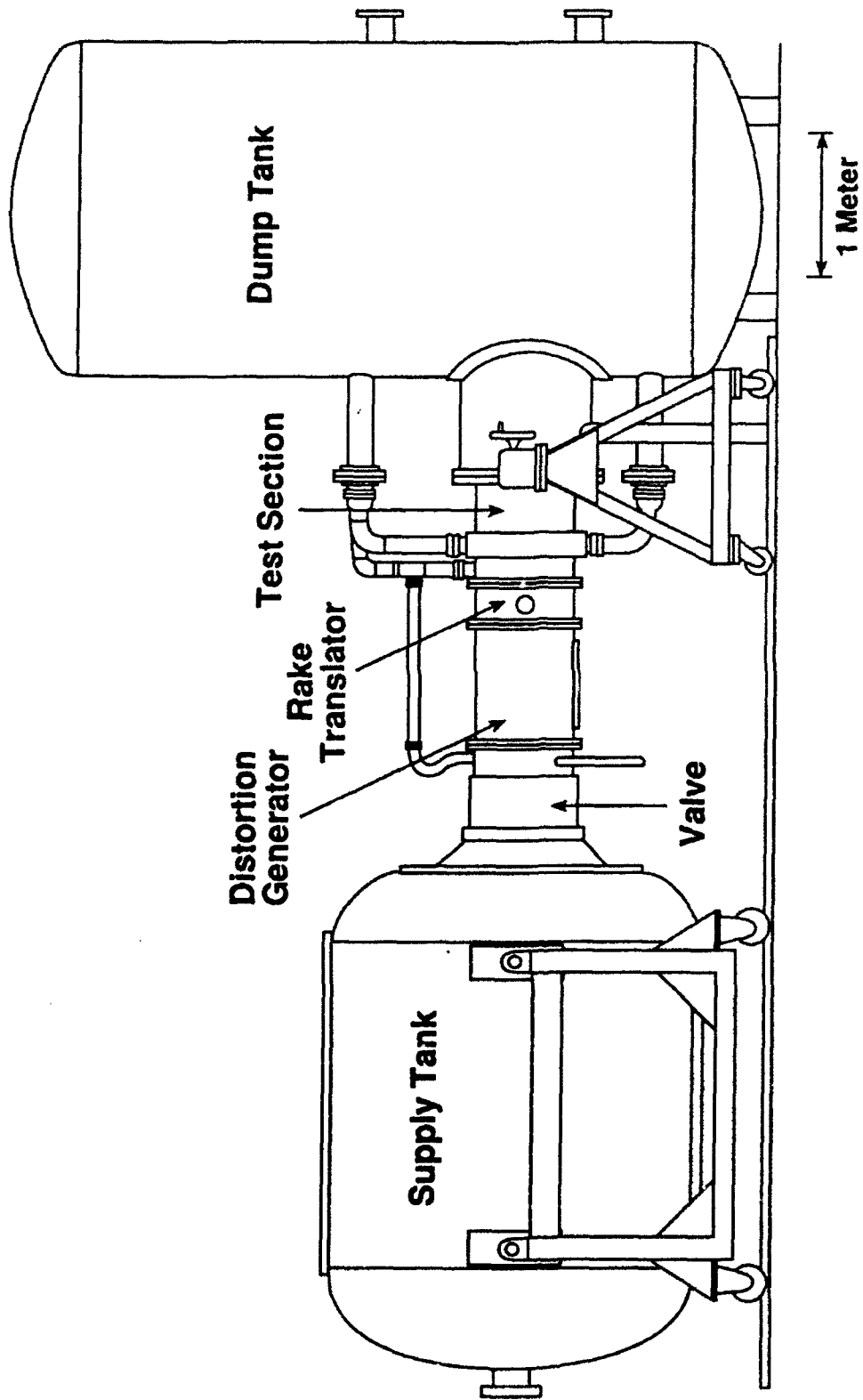


Fig. 3: Blowdown turbine facility with distortion generator and upstream rake translator installed

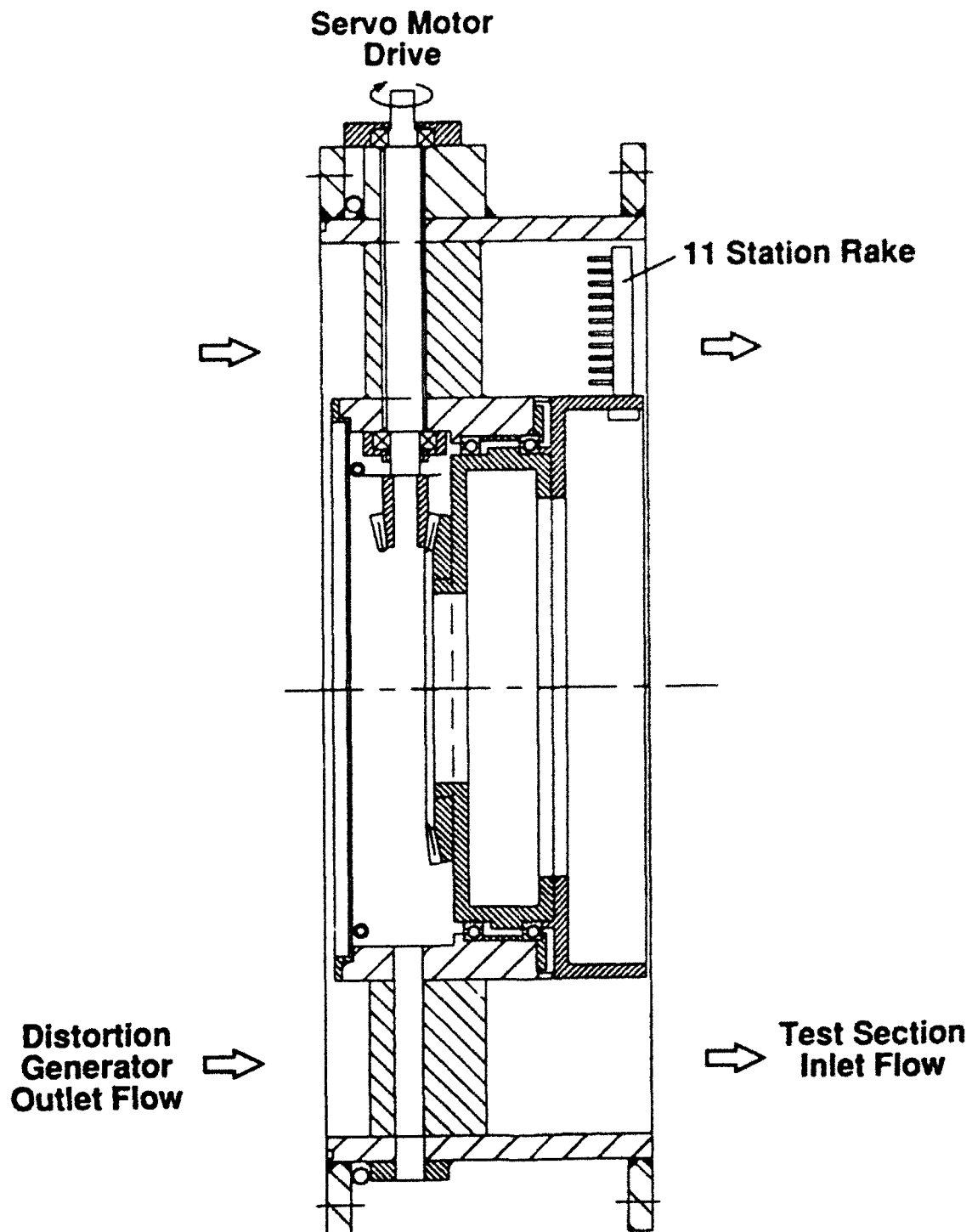


Fig. 4: Inlet rake translator

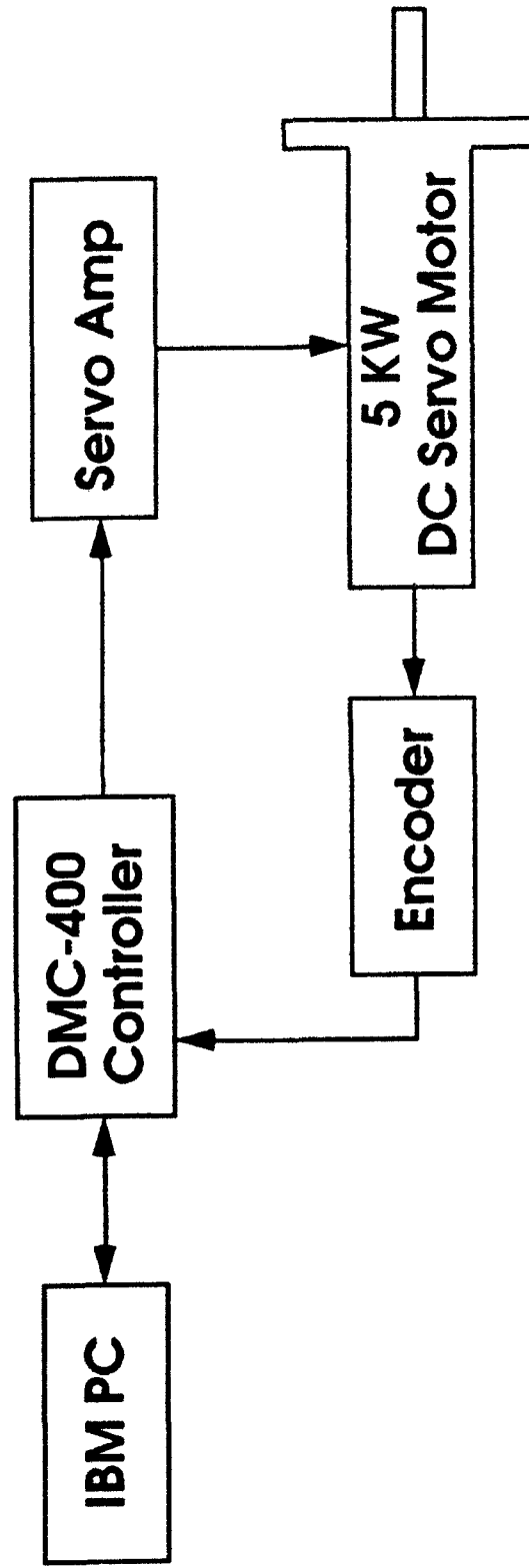


Fig. 5: Computer-controlled translator drive gives programmed acceleration schedule and position control

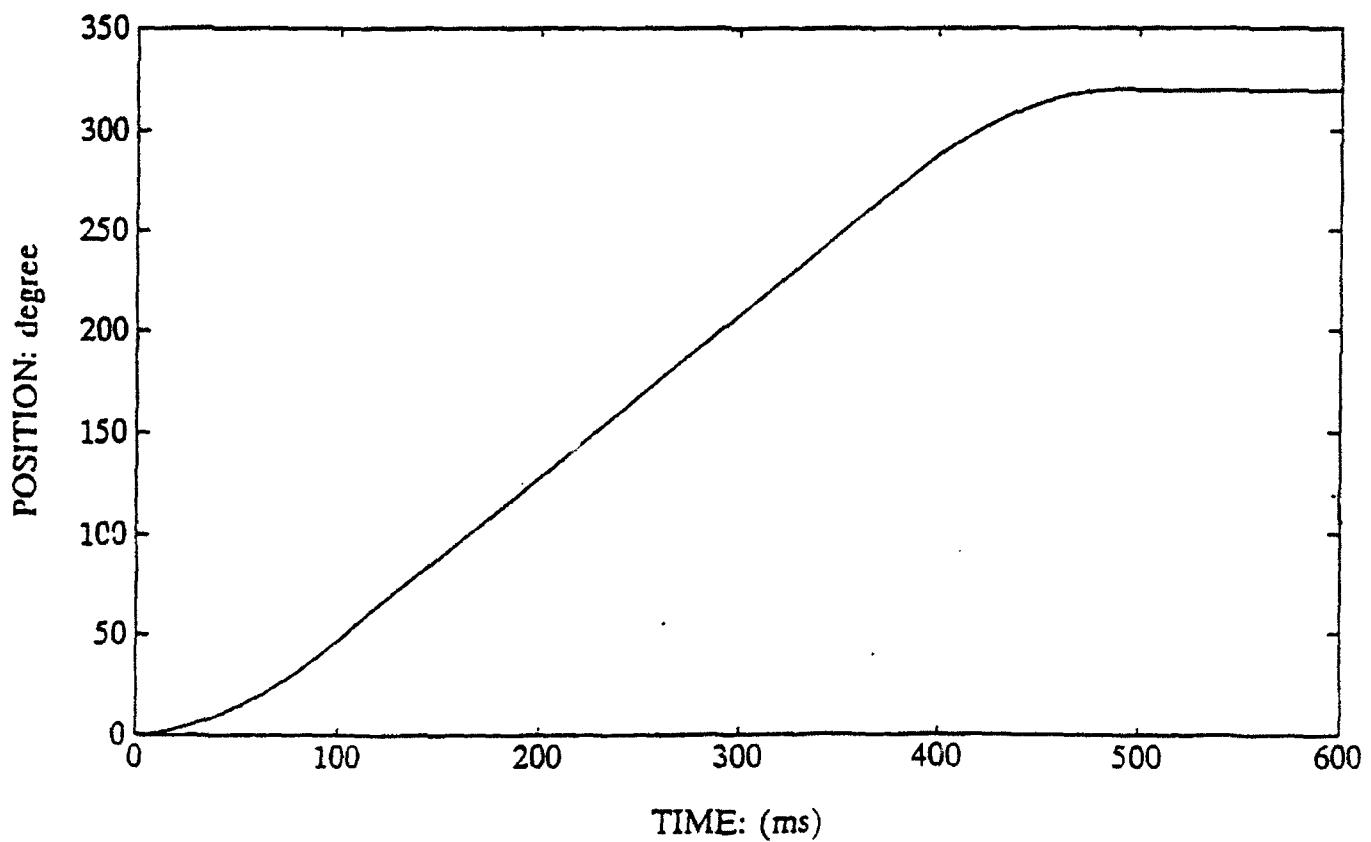
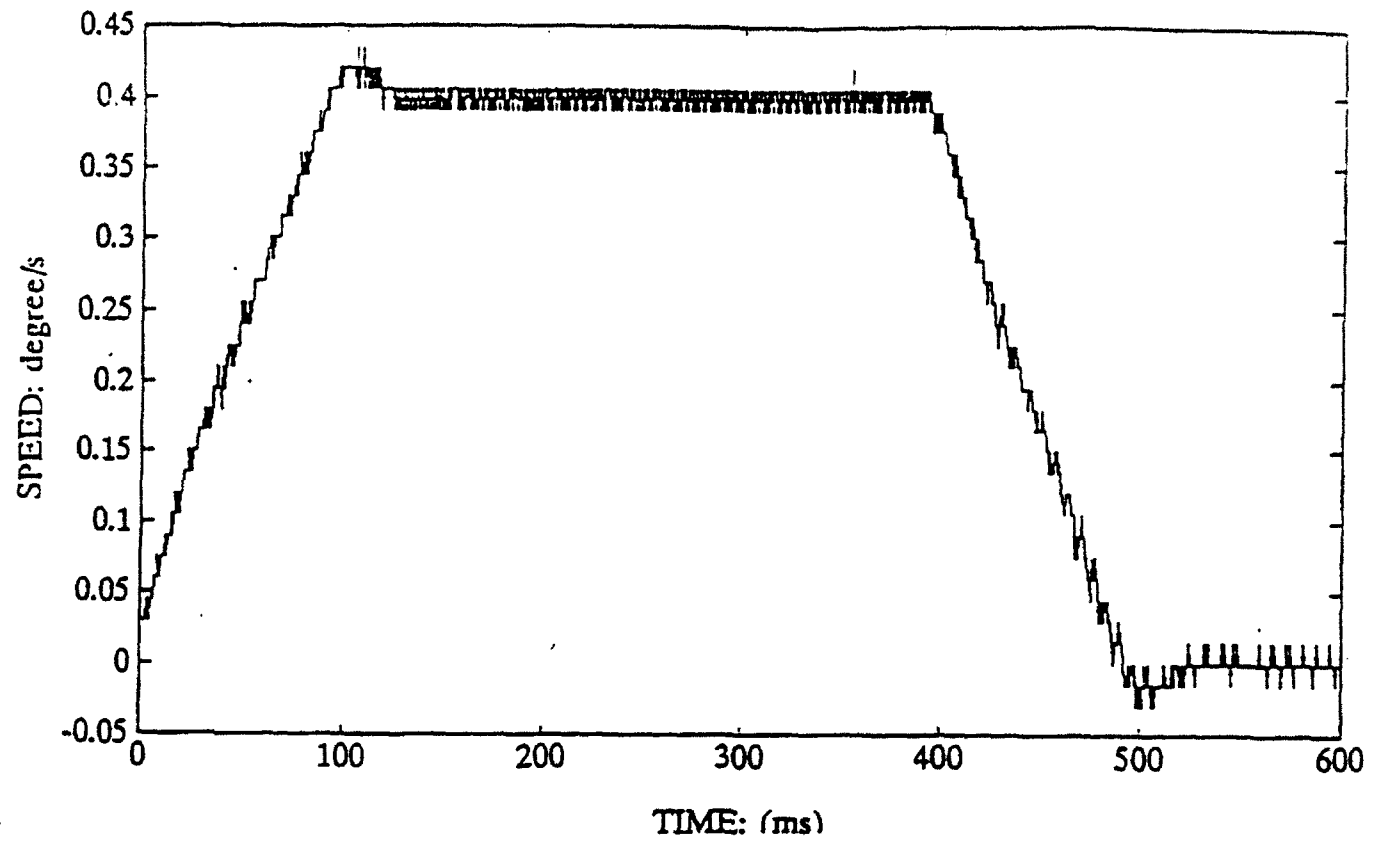


Fig. 6: Measured performance of unstream rake translator

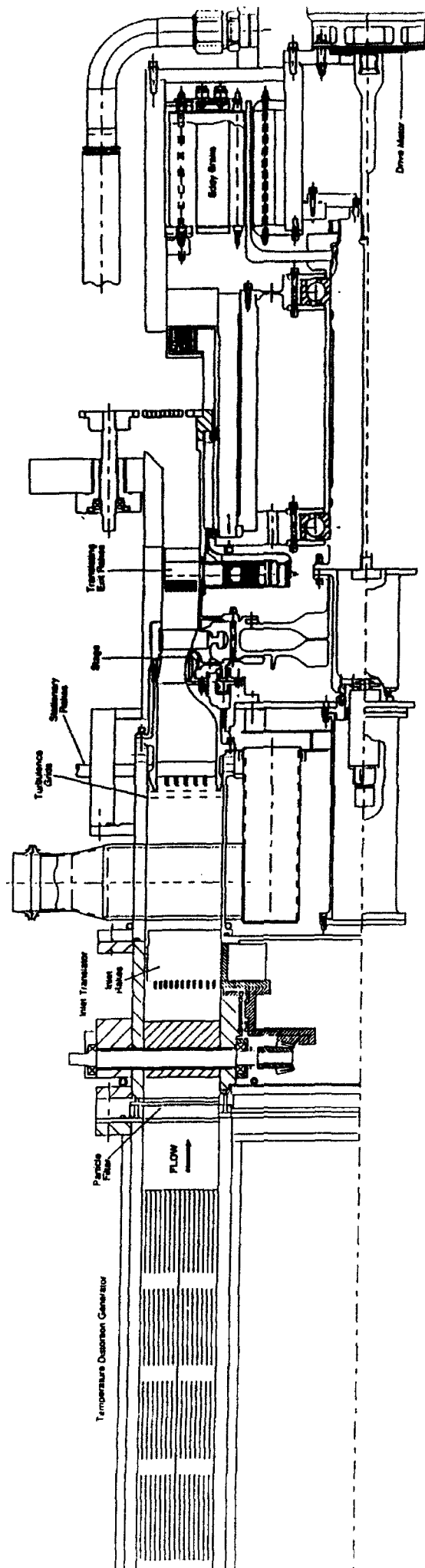


Fig. 7 : Blowdown turbine cross-section including particle filter.



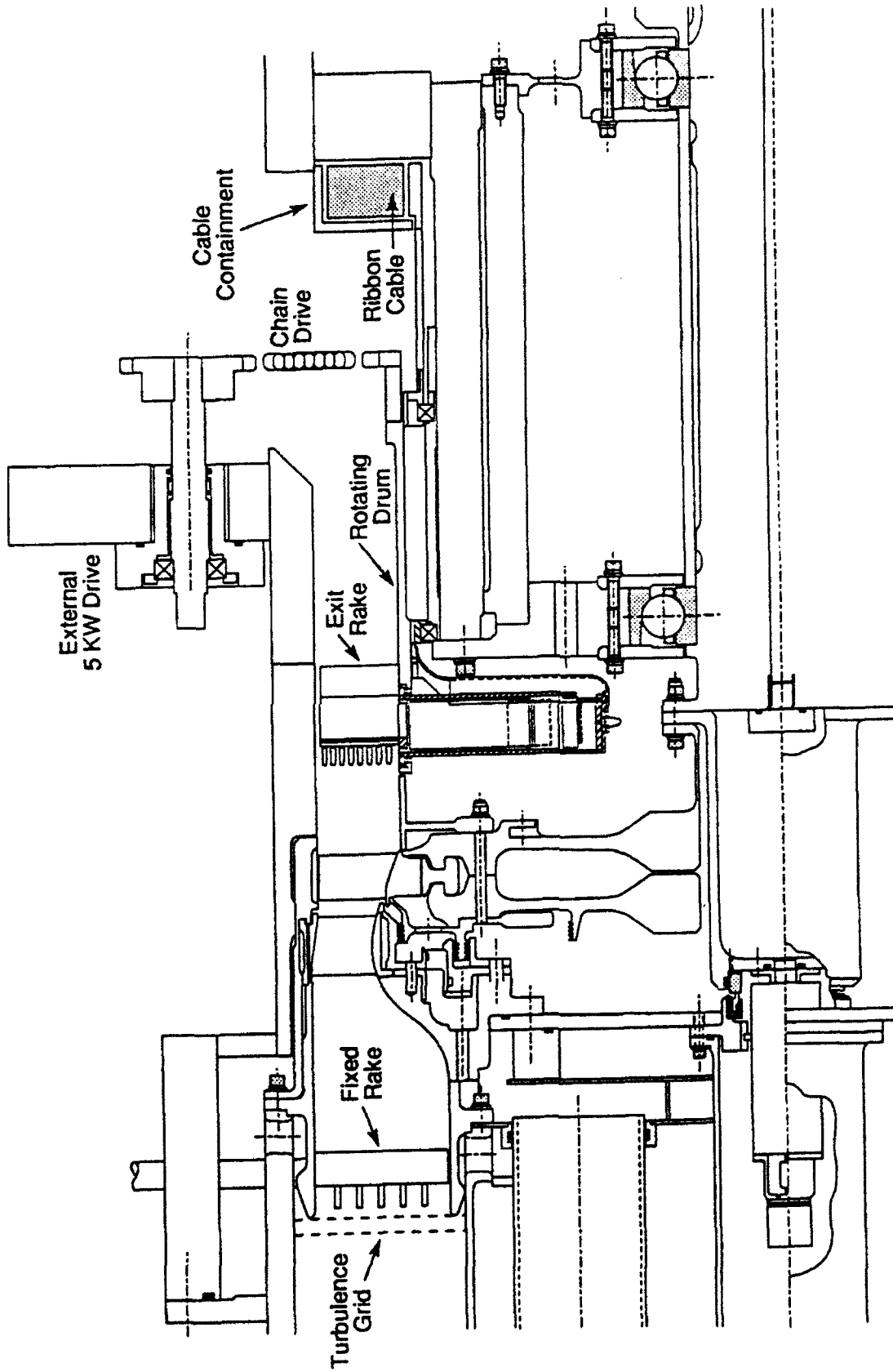


Fig. 8: The exit rake translator installation in the test section.

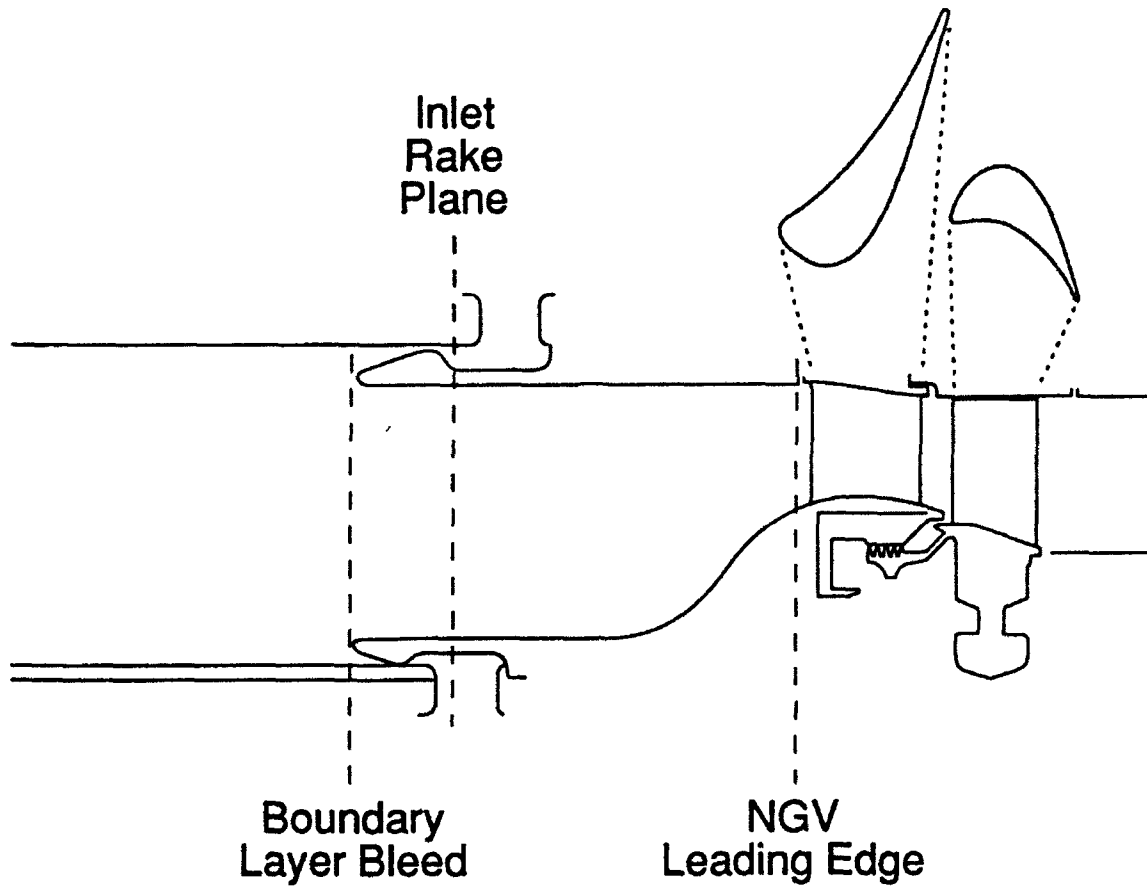


Fig. 9: Alternate locations considered for turbulence grid placement

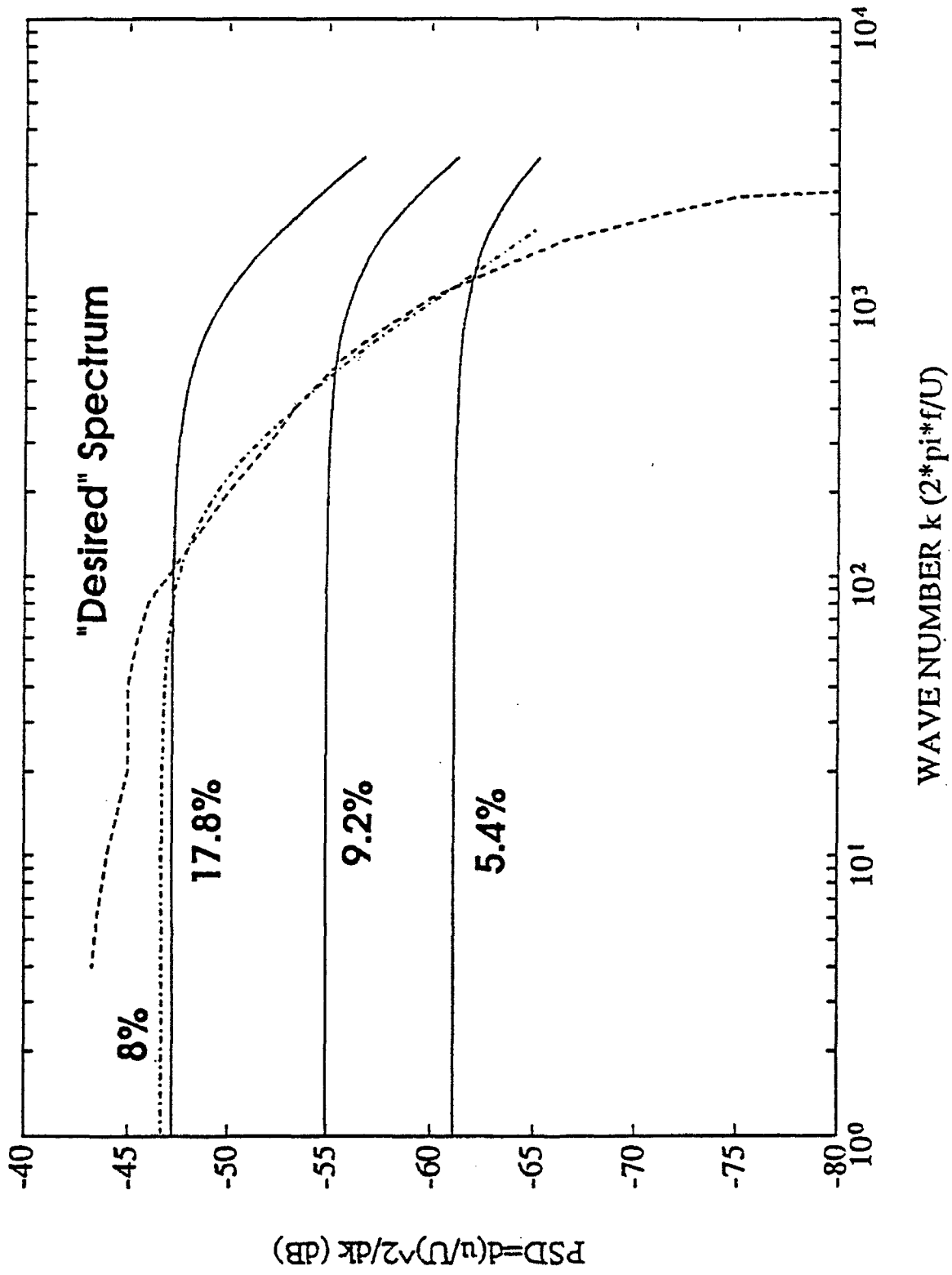
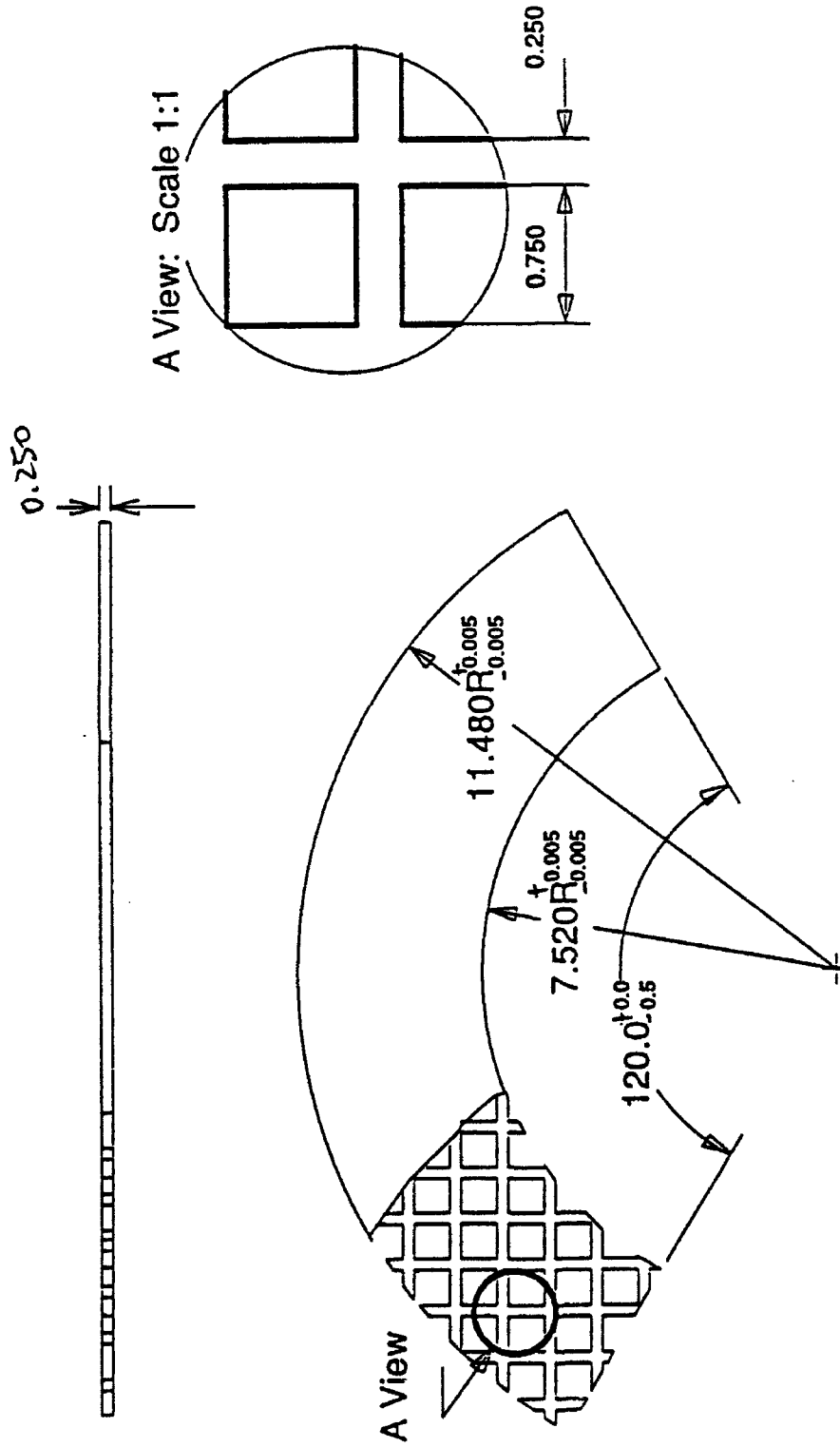


Fig. 10: Turbulence energy spectrum



**Fig. 11: Grid geometry for blowdown. Grid is placed at boundary layer bleed lip.**

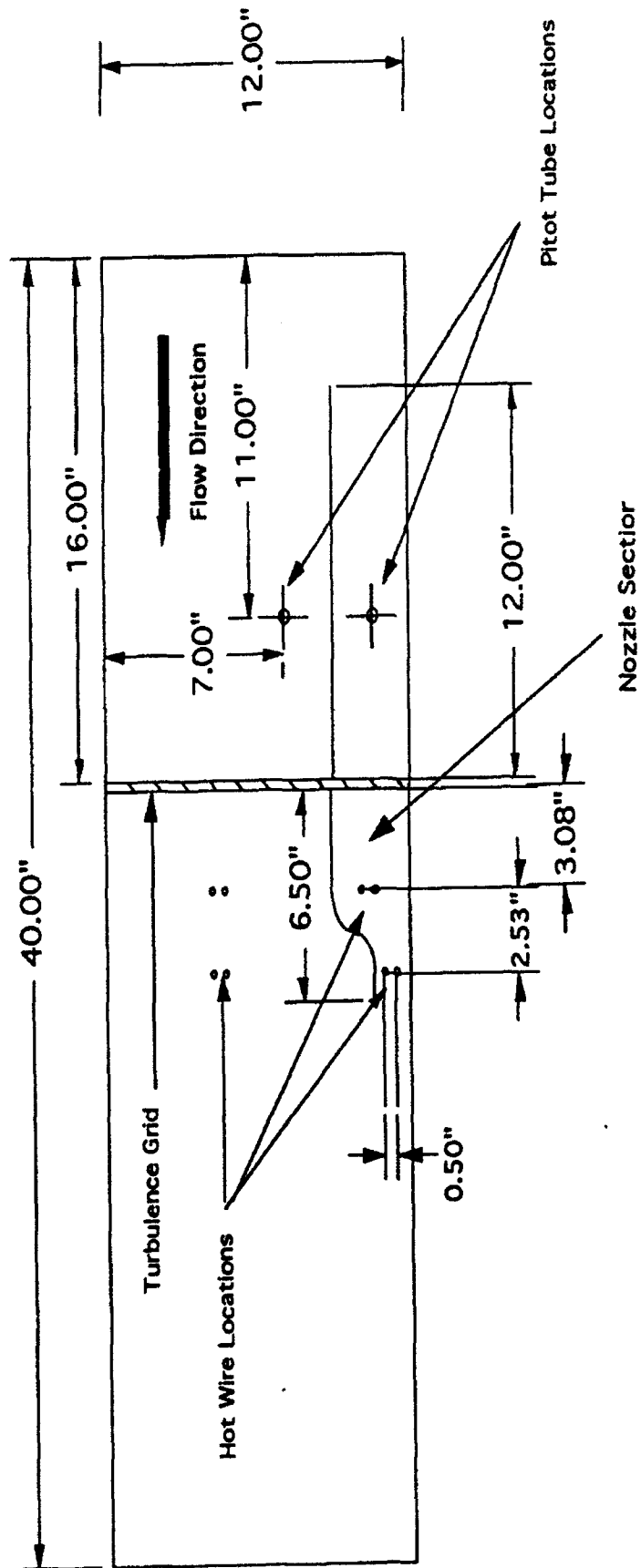


Figure 12: Tunnel layout

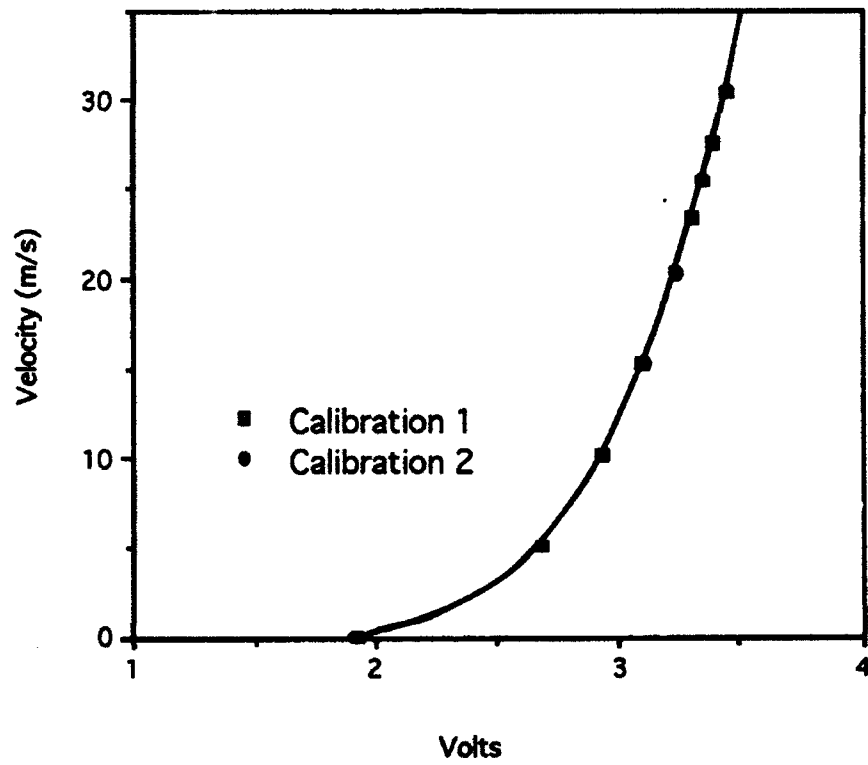


Figure 13: Hot wire calibration graphs

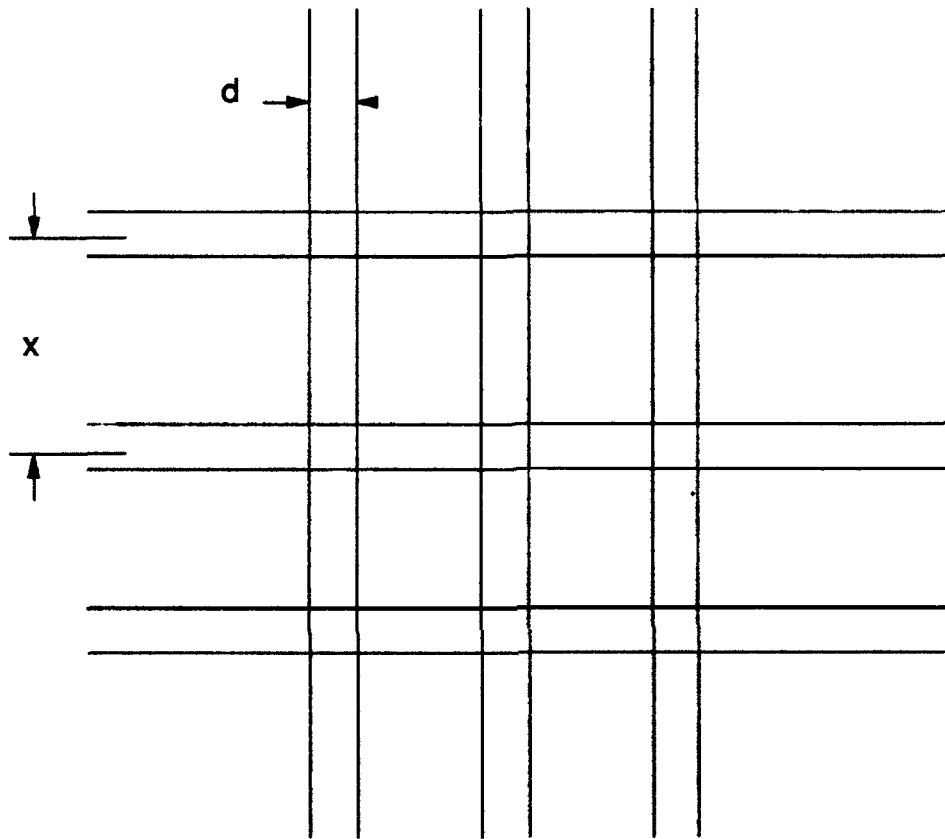


Figure 14: Turbulence grid dimensions

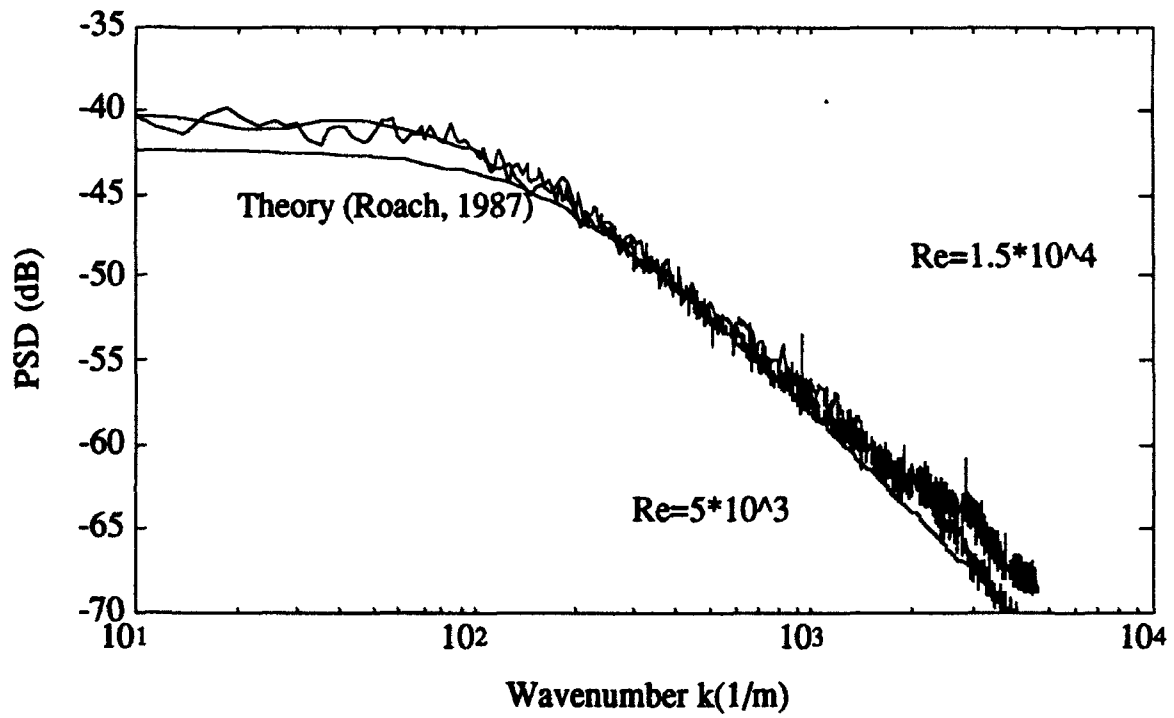


Figure 15: Reynolds number effect



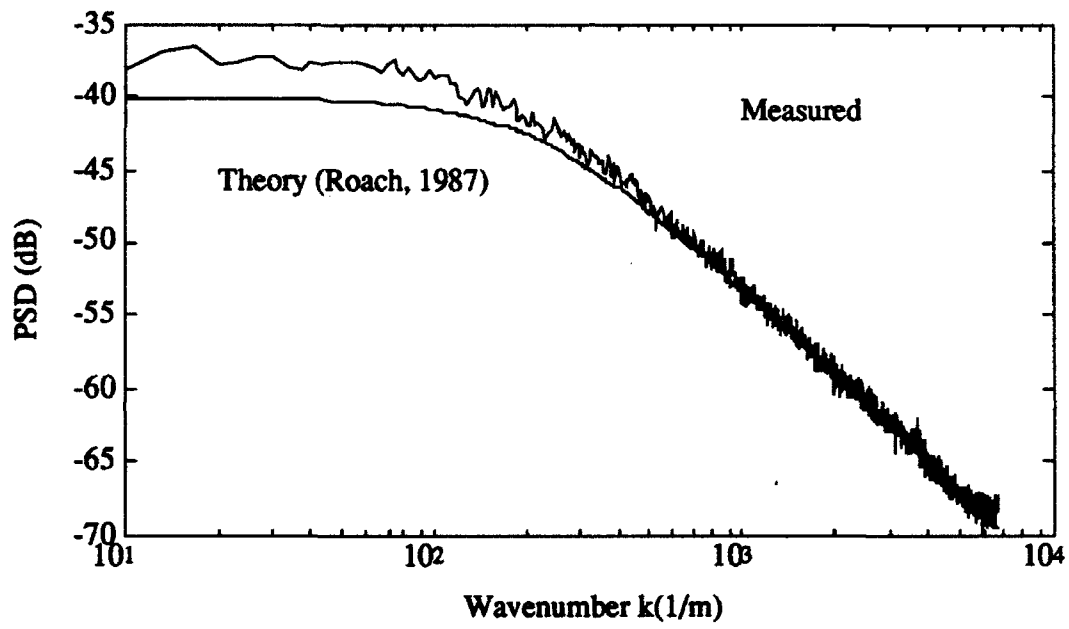


Figure 16: PSD; 1/2 NGV location

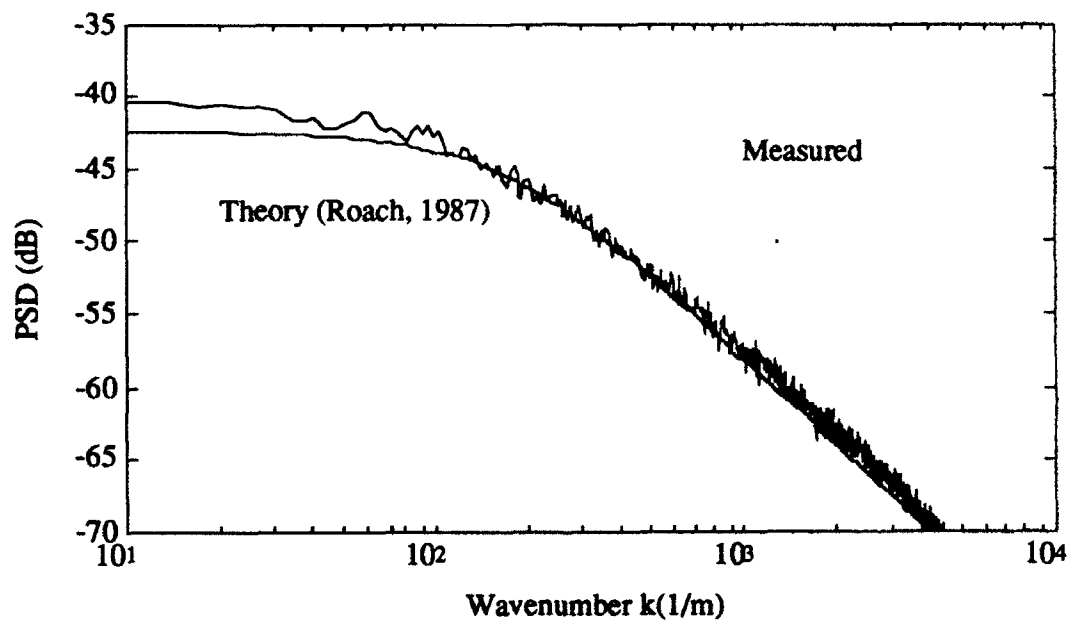


Figure 17: PSD; NGV location

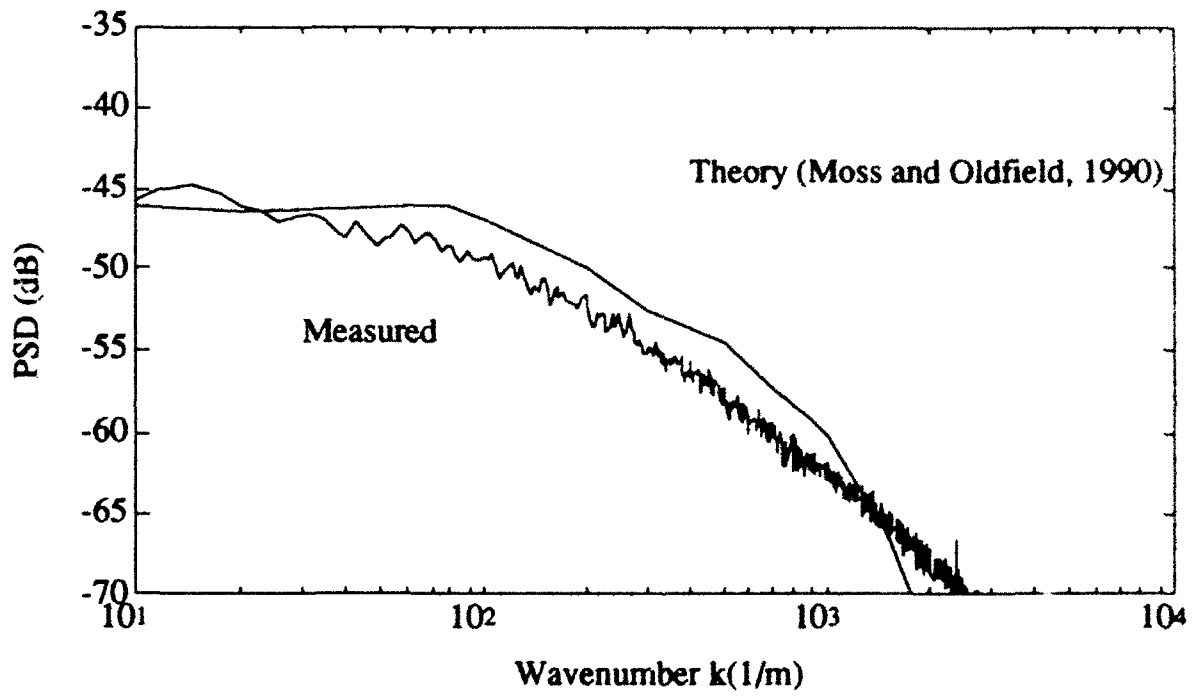


Figure 18: PSD nozzle case NGV location

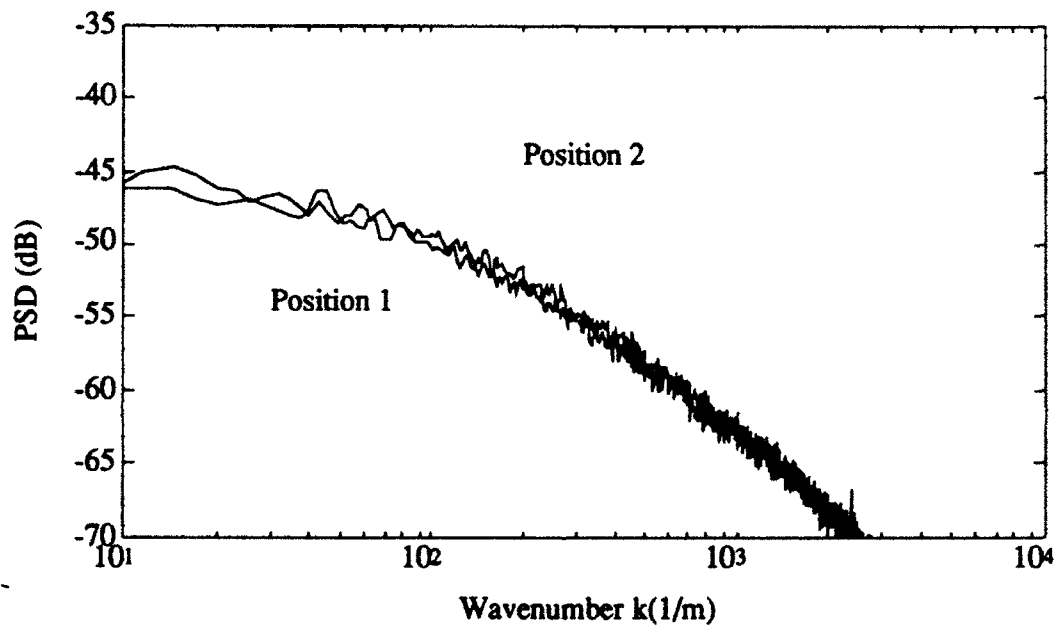


Figure 19: Positioning effect parallel to nozzle

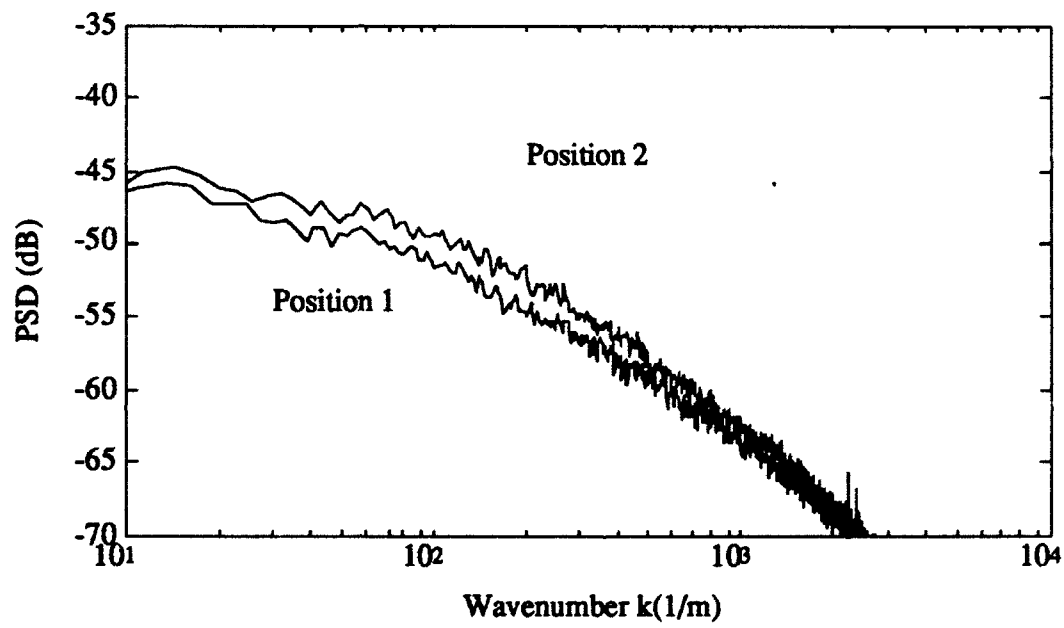


Figure 20: Positioning effect in direction of nozzle contraction

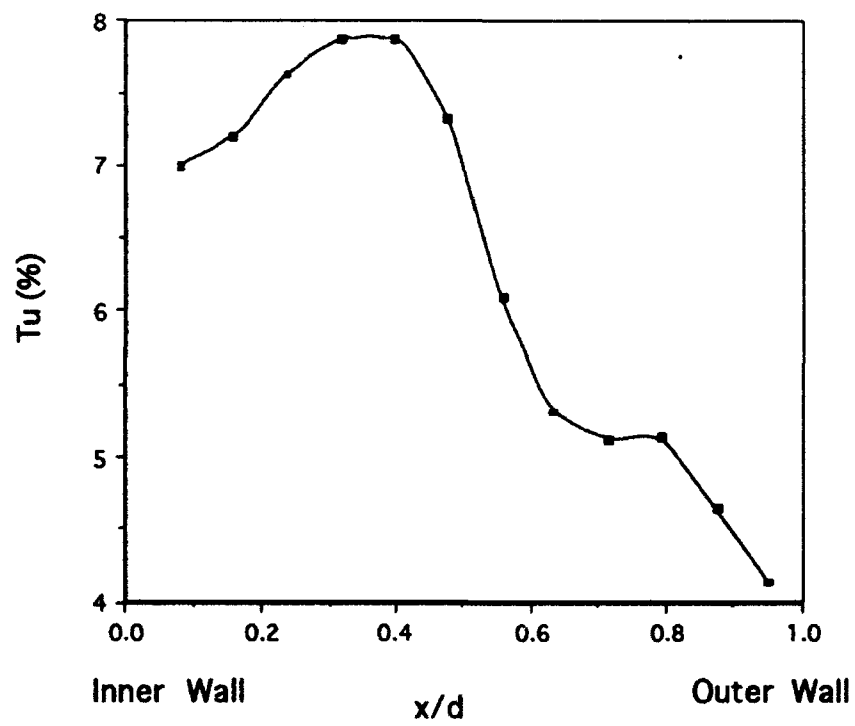


Figure 21: Turbulence intensity variation

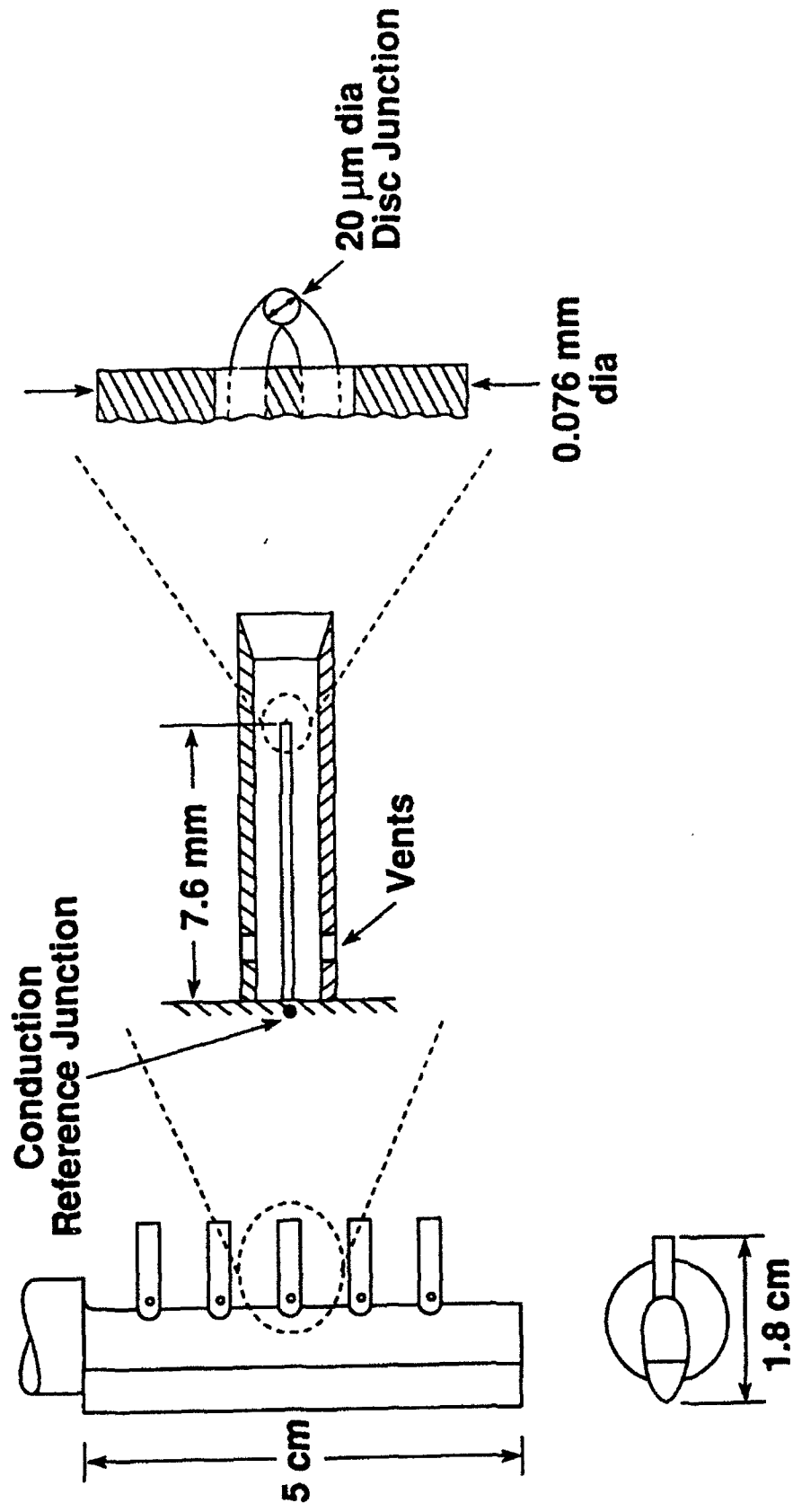


Fig. 22: The general arrangement of the fixed MIT fast response total temperature rake. The new units are similar but the insulators are 3.8 mm rather than 7.6 mm long.

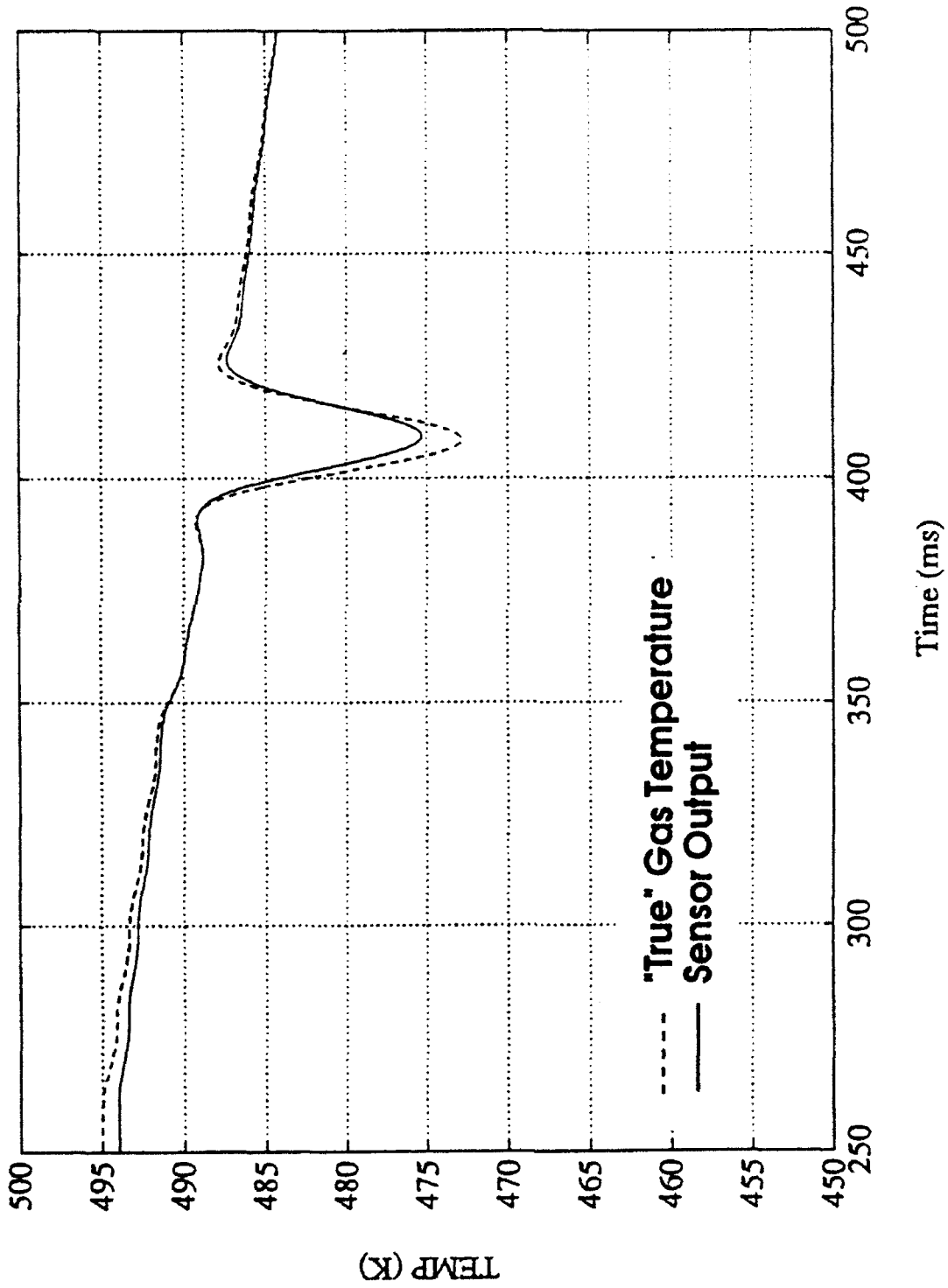


Fig. 23: Simulated sensor traverse behind NGV without corrections



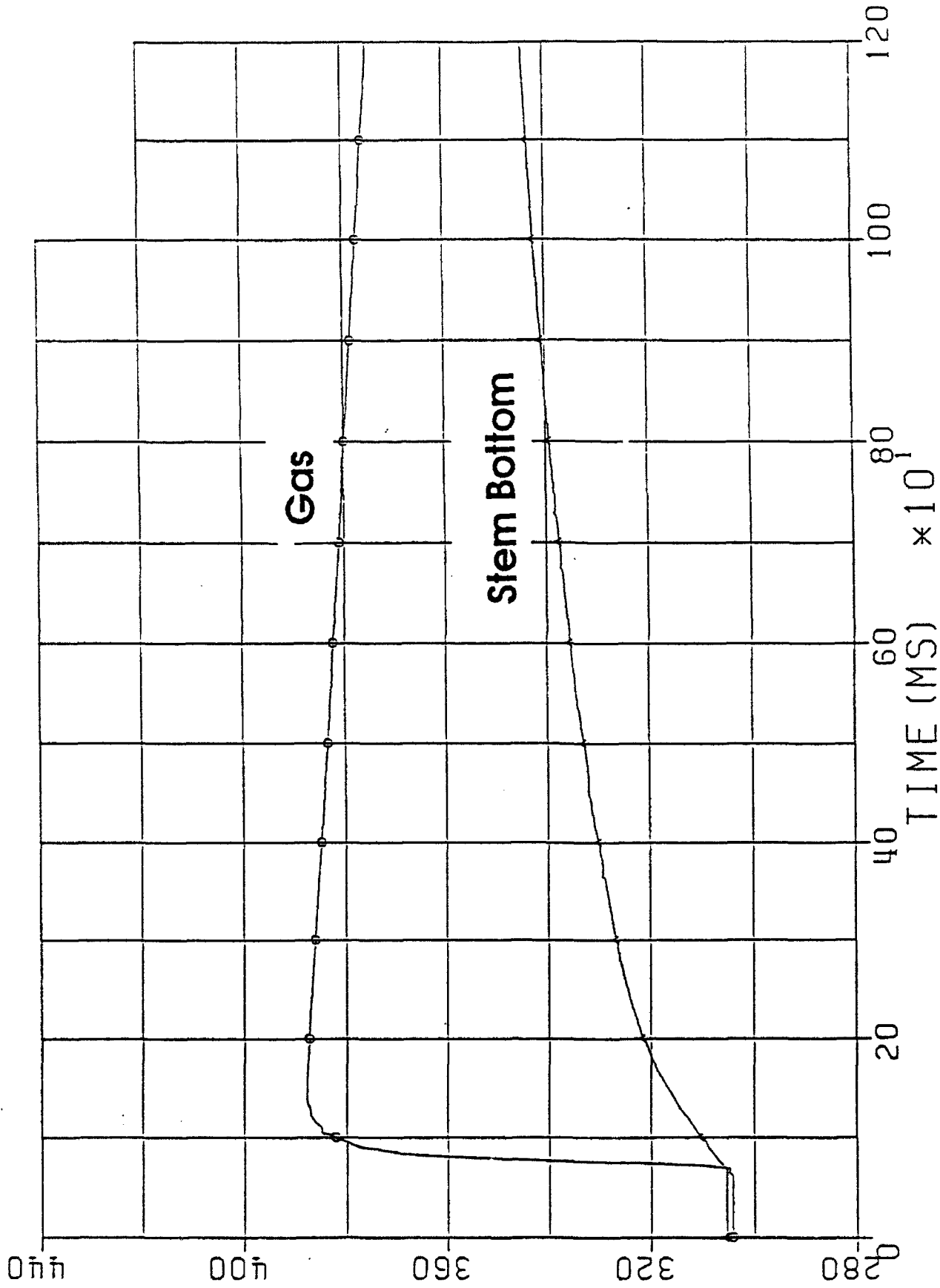


Fig. 24: Time history of the exposed (gas) thermocouple output and that buried at the bottom of the support stem. Test time is from 250 to 550 ms.

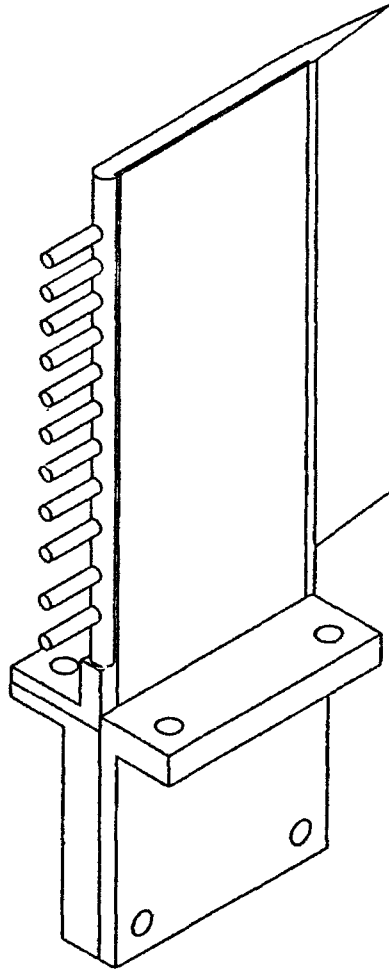


Fig. 25: Inlet temperature rake. Each of the 11 sensors is a vented design similar to Fig. 22.

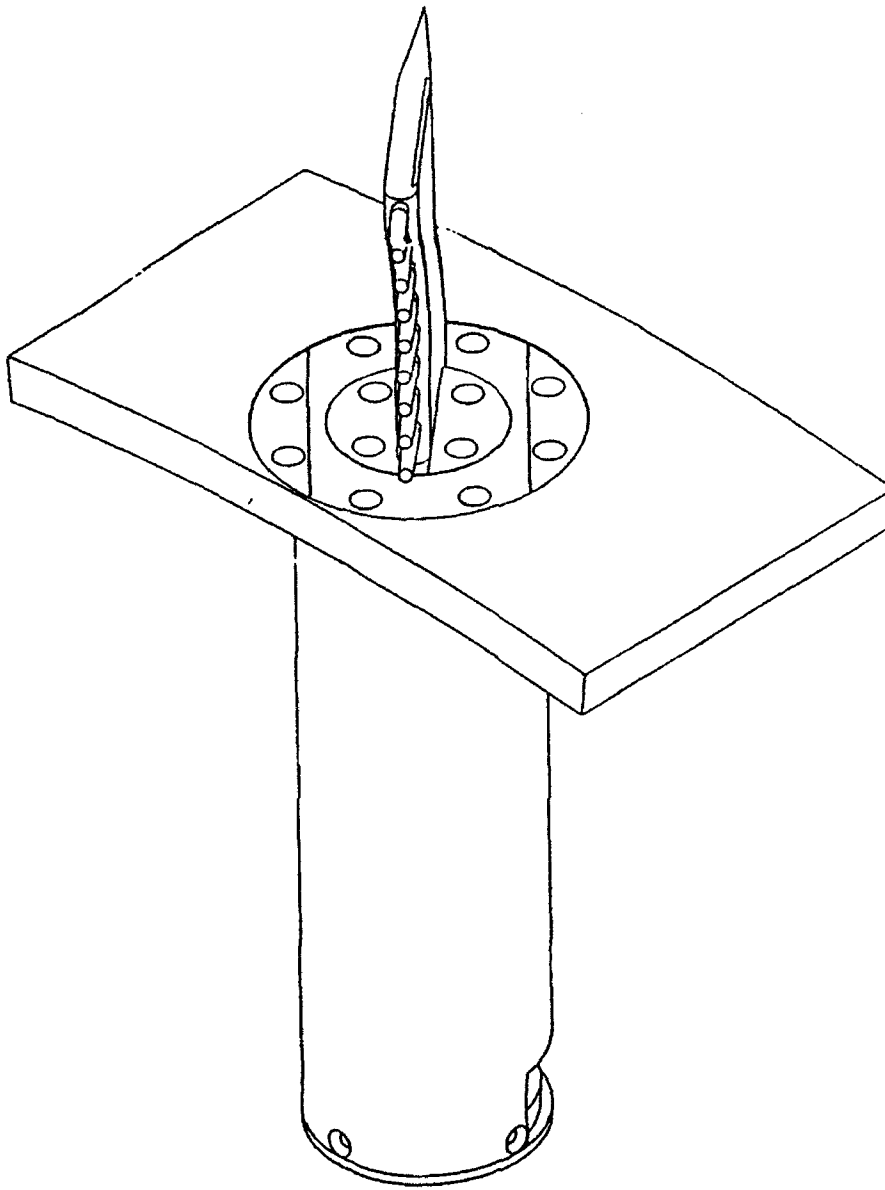


Fig. 26: Turbine exit rake shown mounted in downstream circumferential translator.  
Cold junction is in cylindrical body below rake.

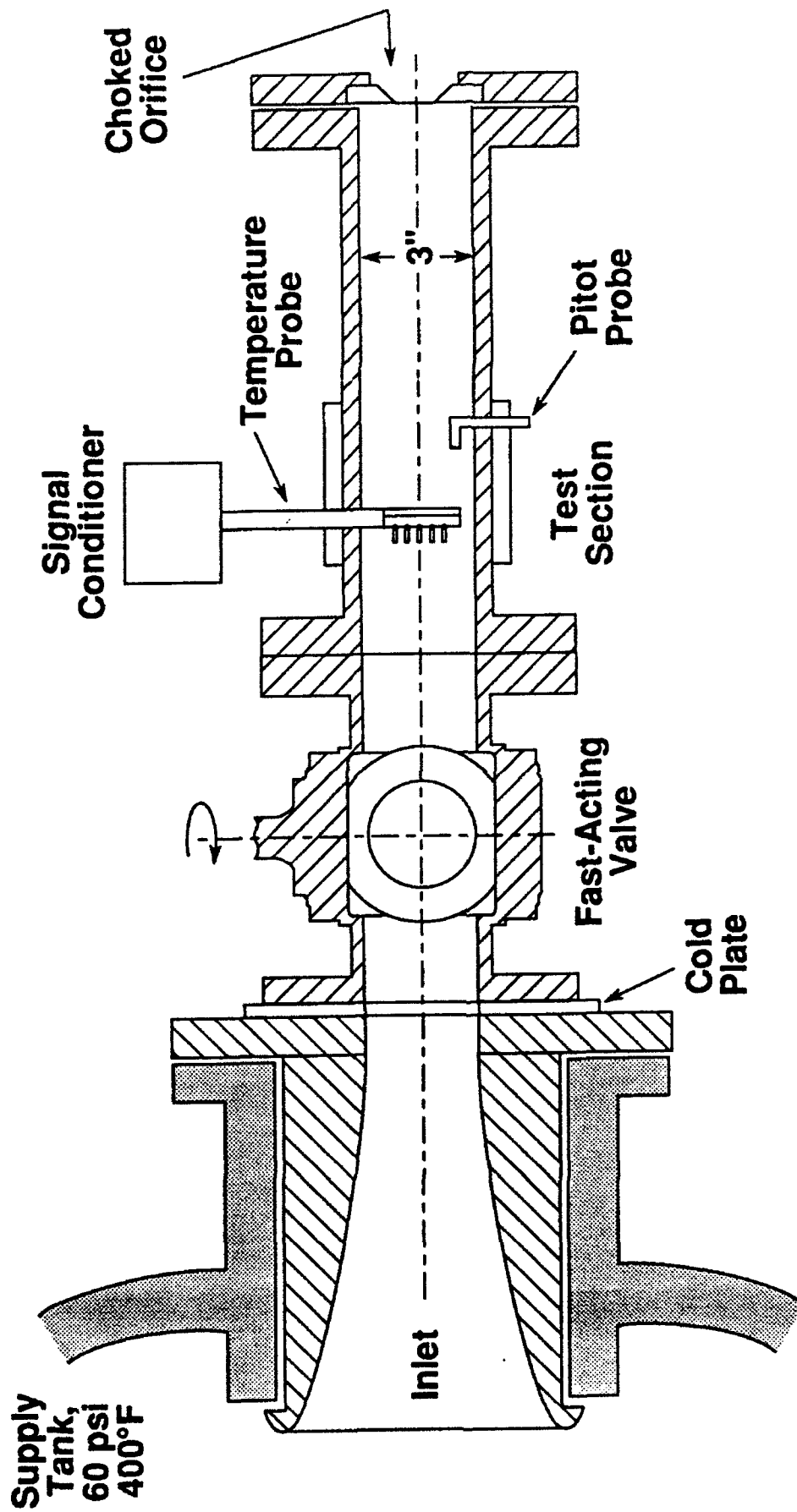
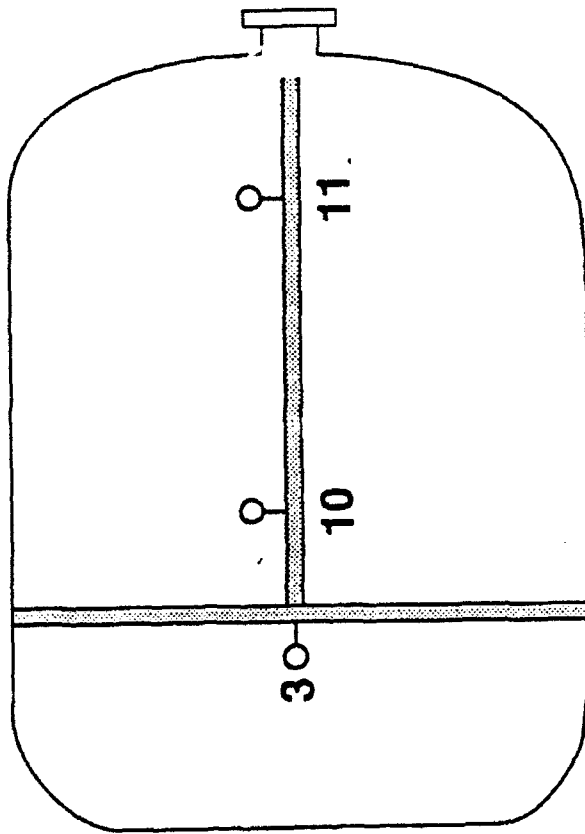
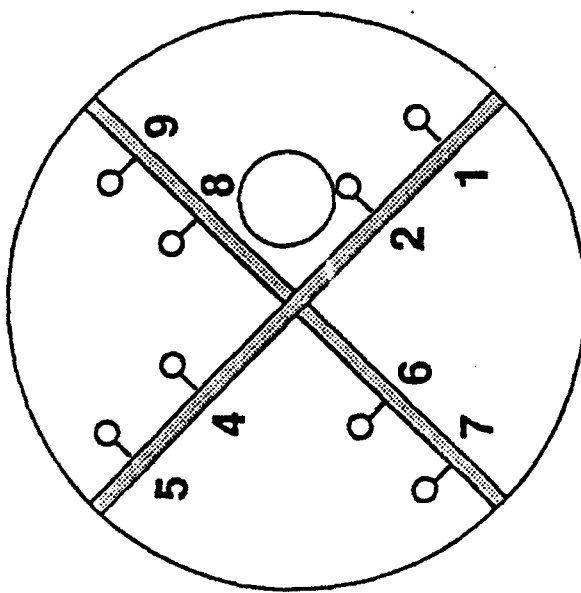


Fig. 27: Rake calibration tunnel



Side



Front

Fig. 28 : Temperature sensor distribution in turbine supply tank

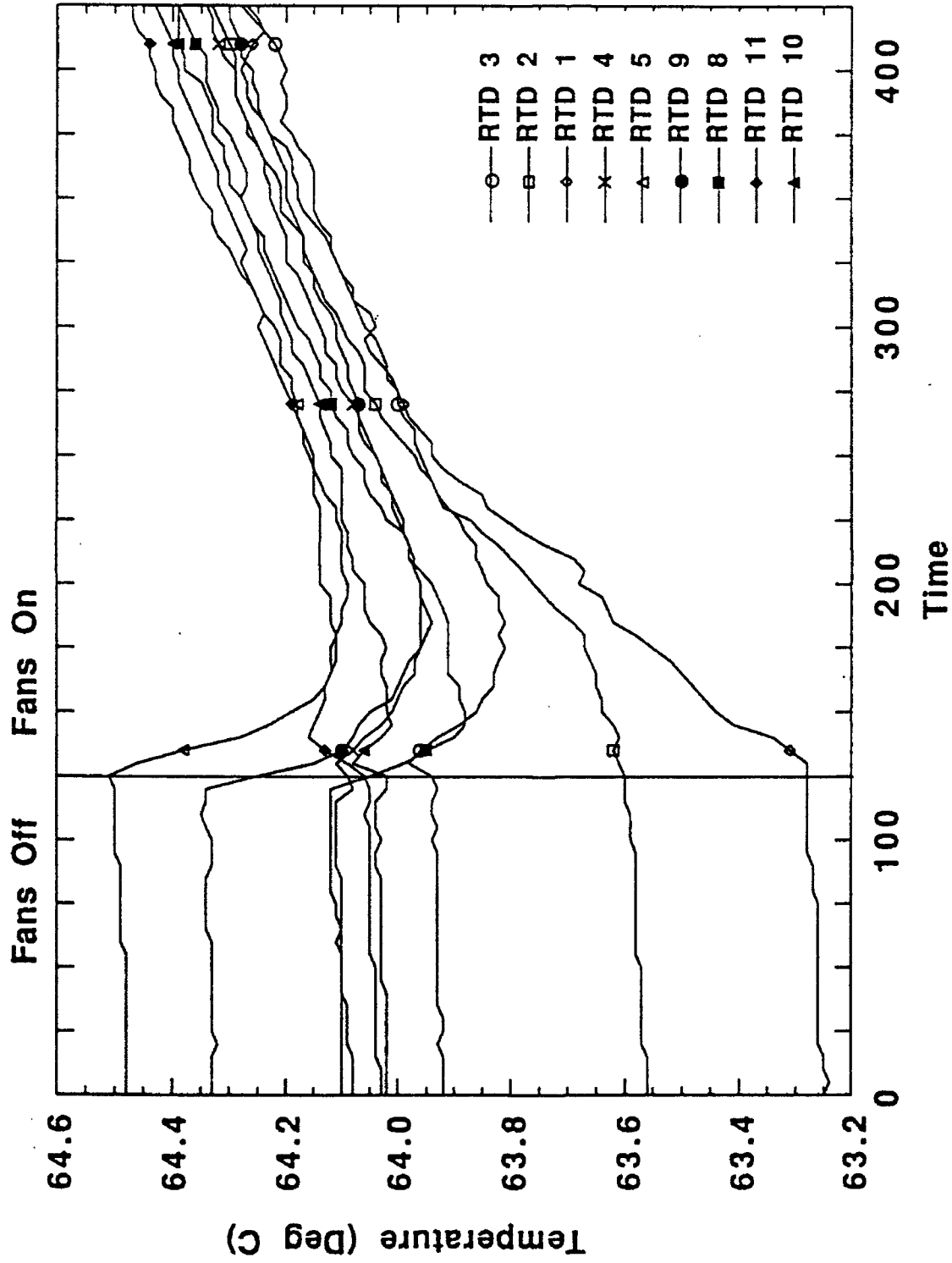
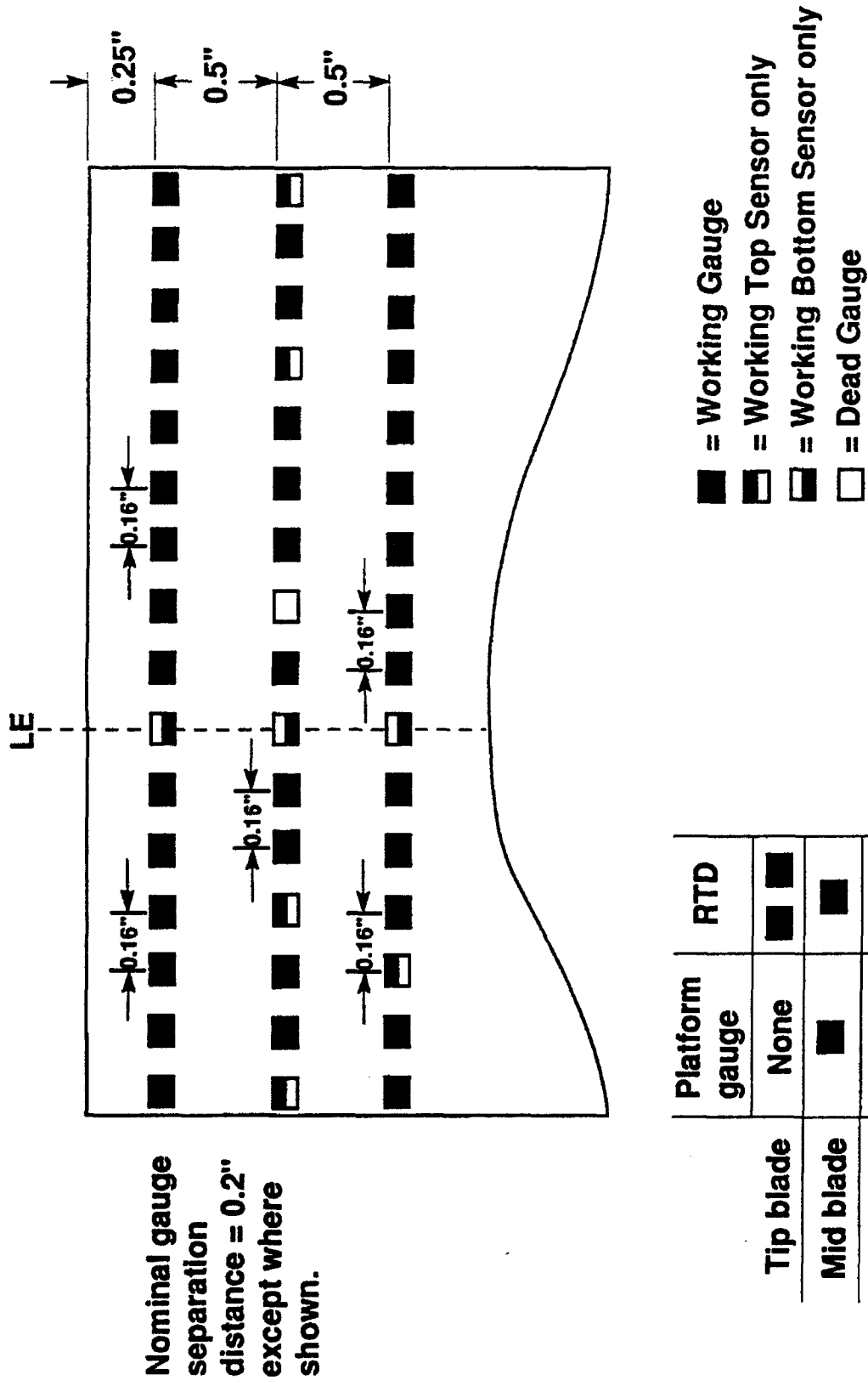


Fig. 29: Influence of fans on supply tank temperature distribution



**Fig. 30: Composite of rotor blade heat flux instrumentation projected onto a plane. Each chordwise row is on a separate blade.**

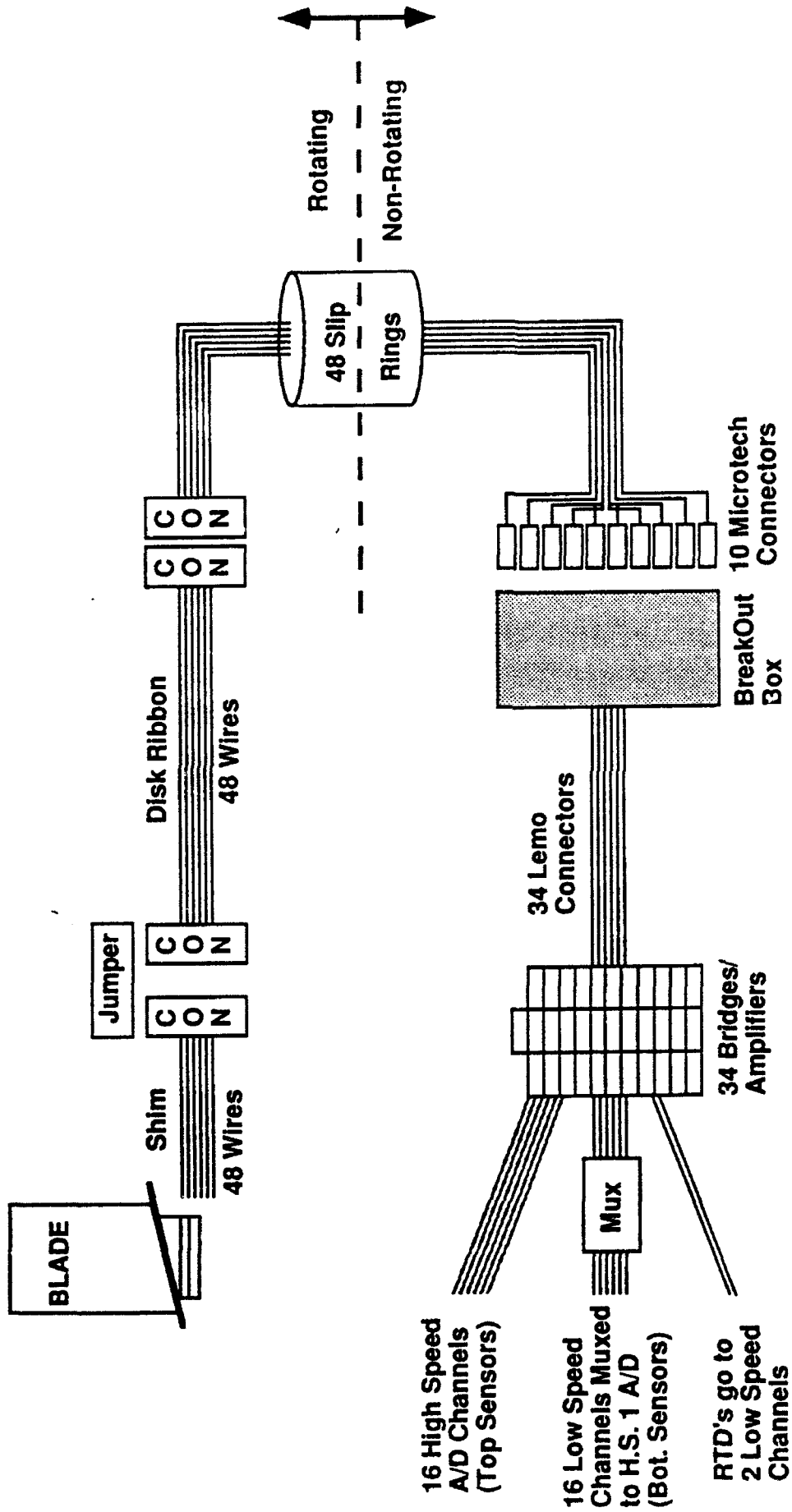


Fig. 31: Wiring diagram for a single rotor blade, with 16 high frequency heat flux gauges and 2 RTD's



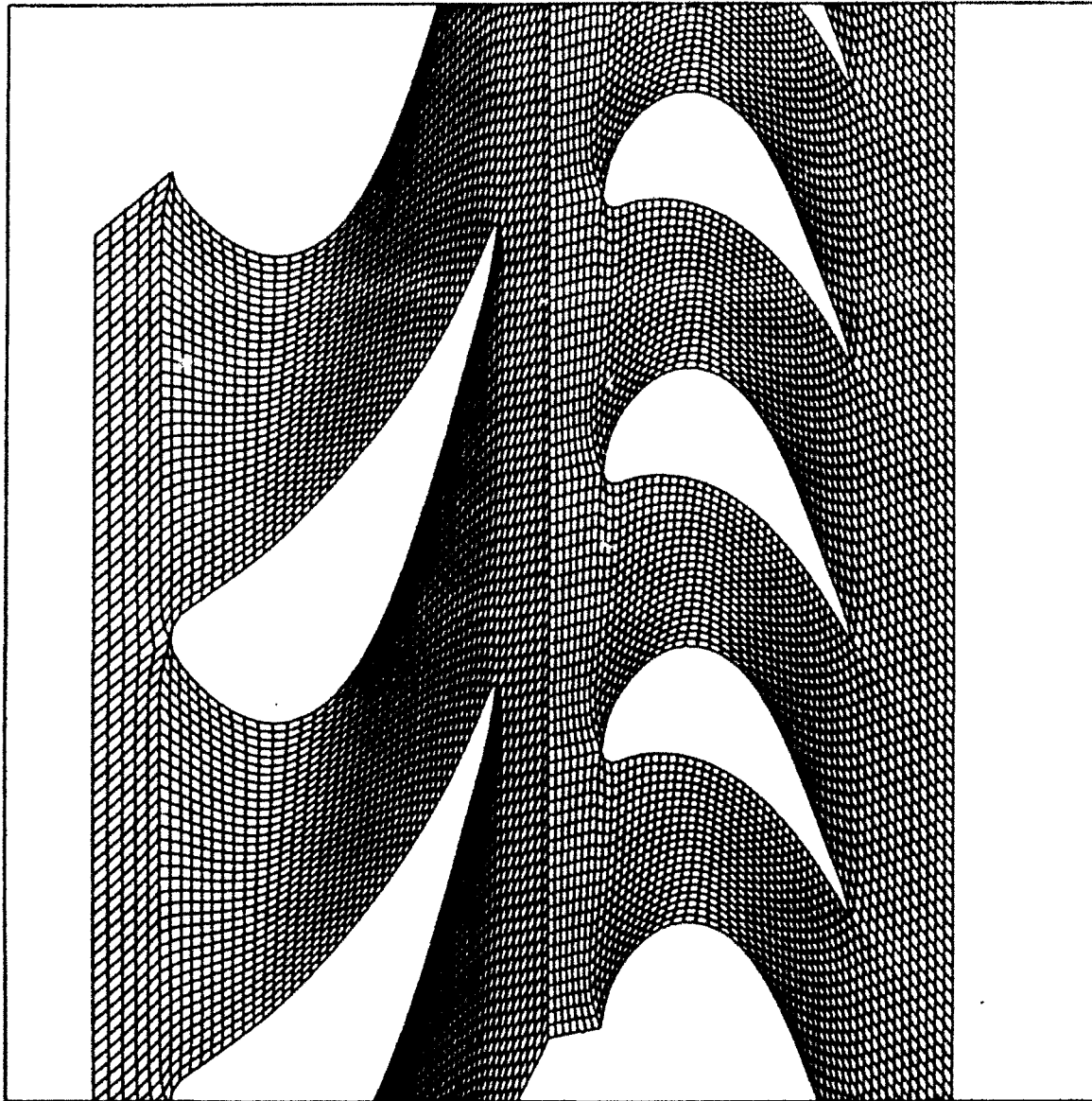


Fig. 32: 3 NGV, 5 rotor blade grid geometry illustrated for the hub plane

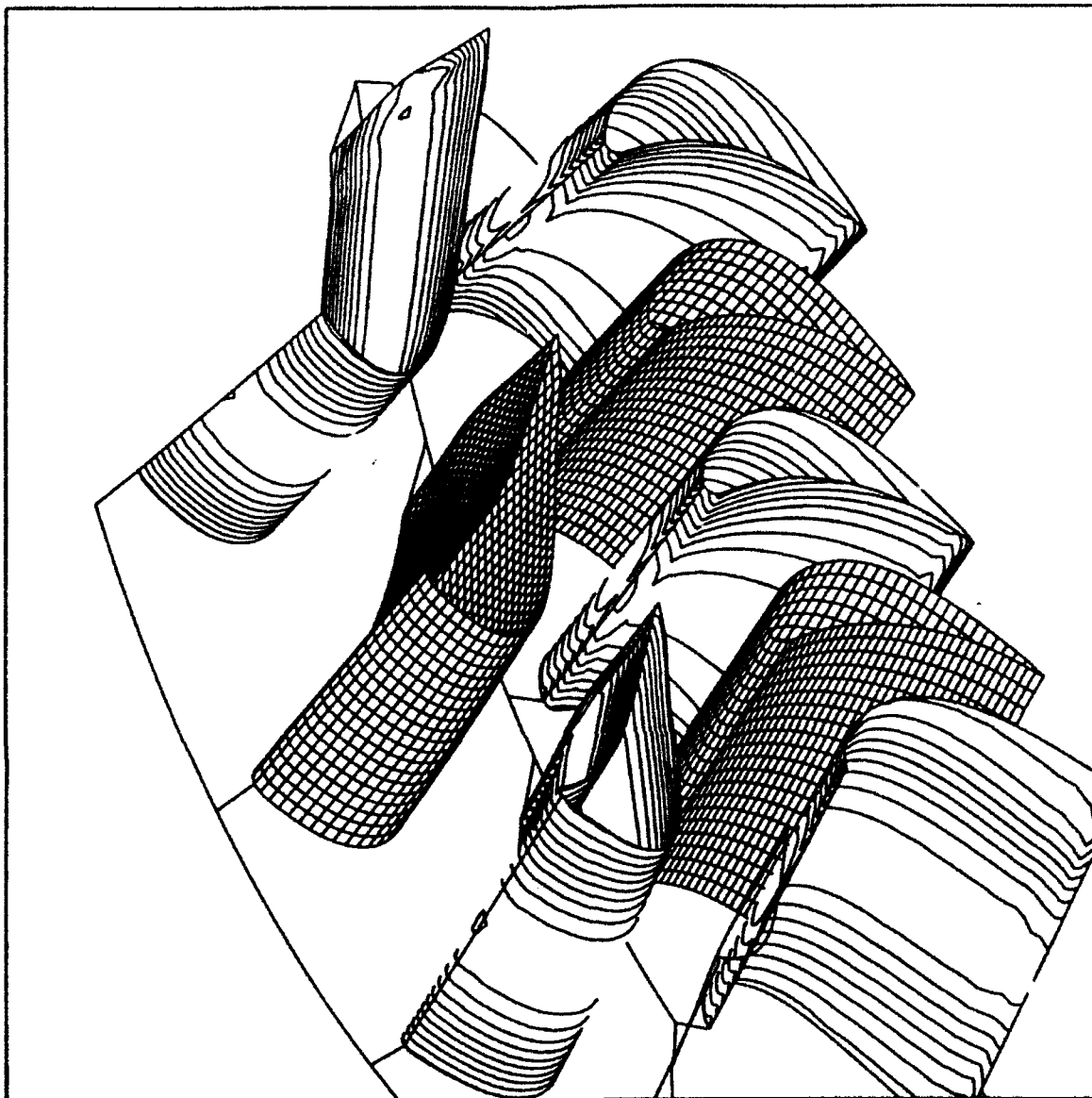


Fig. 33: Computational domain with total temperature contours illustrated on blade surfaces. There are  $56 \times 36 \times 21$  nodes in each NGV passage and  $56 \times 22 \times 21$  in each rotor passage.

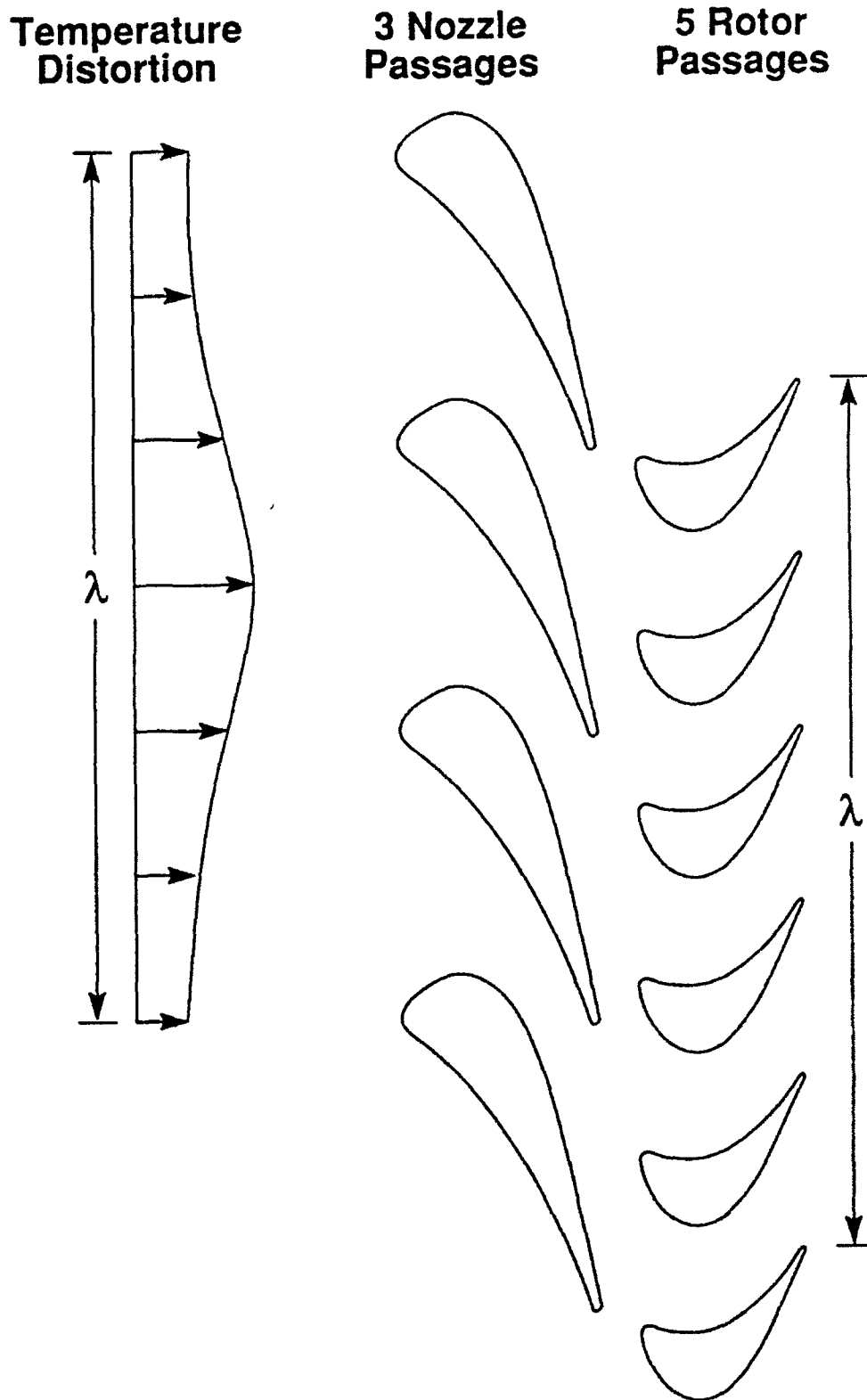


Fig. 34: The circumferential period,  $\lambda$ , of the inlet temperature distortion must match the 3 NGV-5 rotor grid geometry

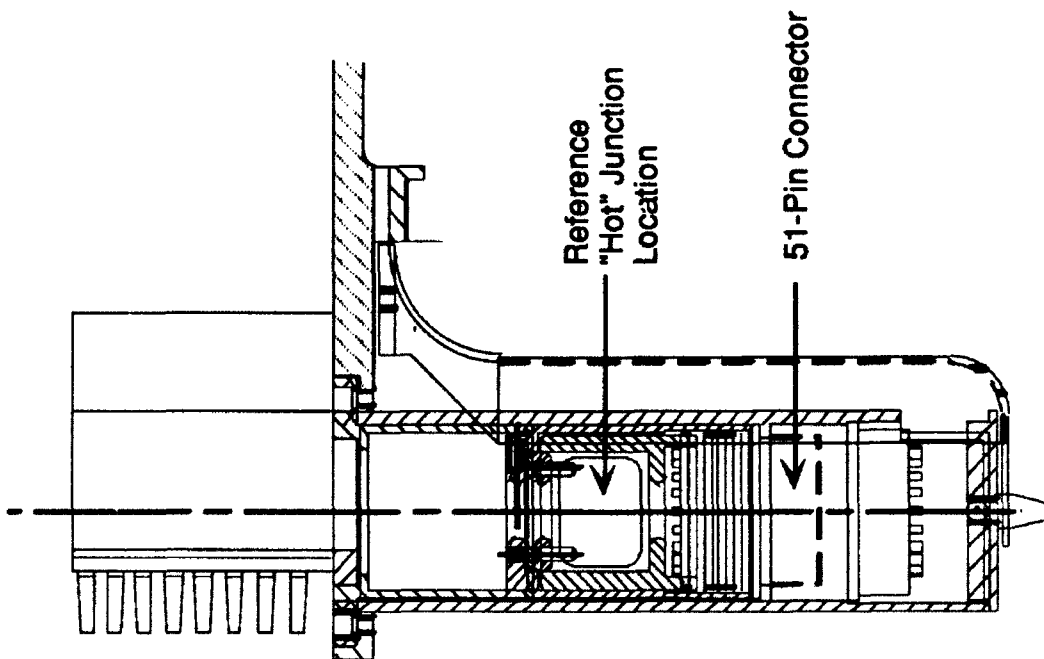
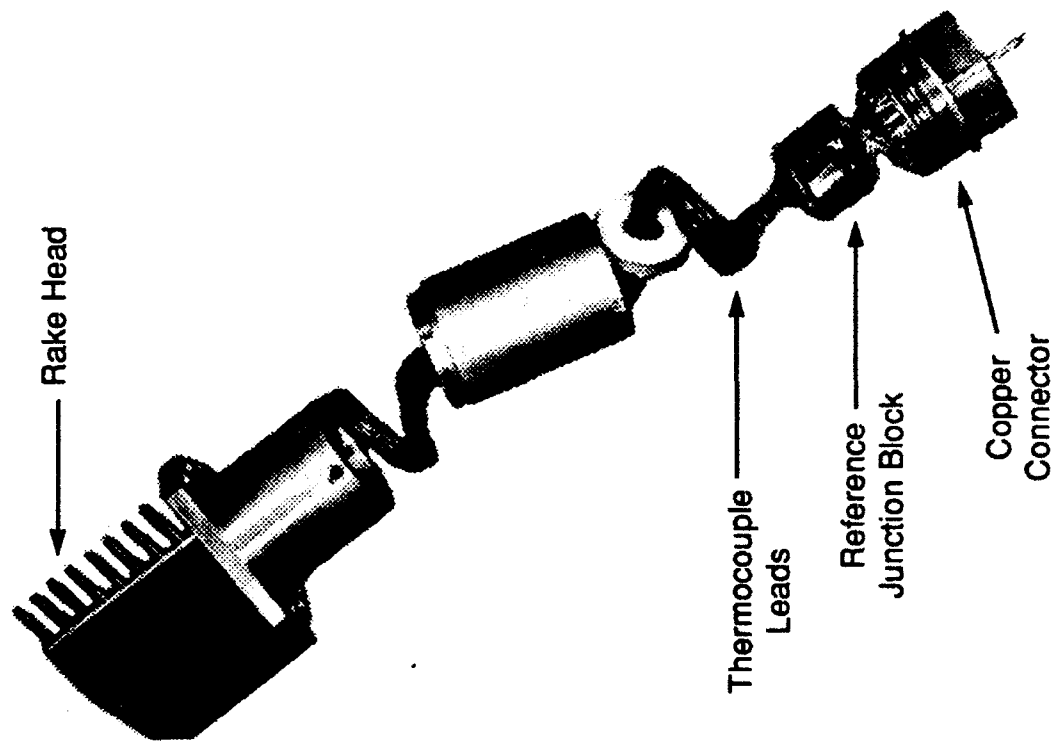
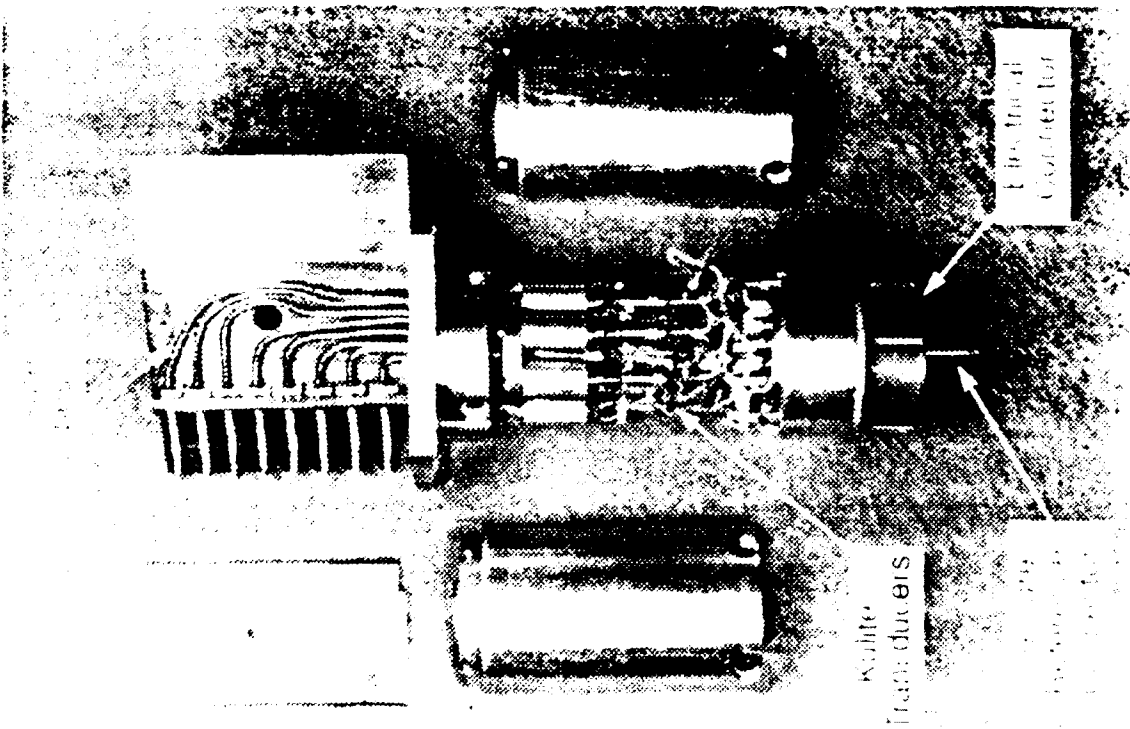
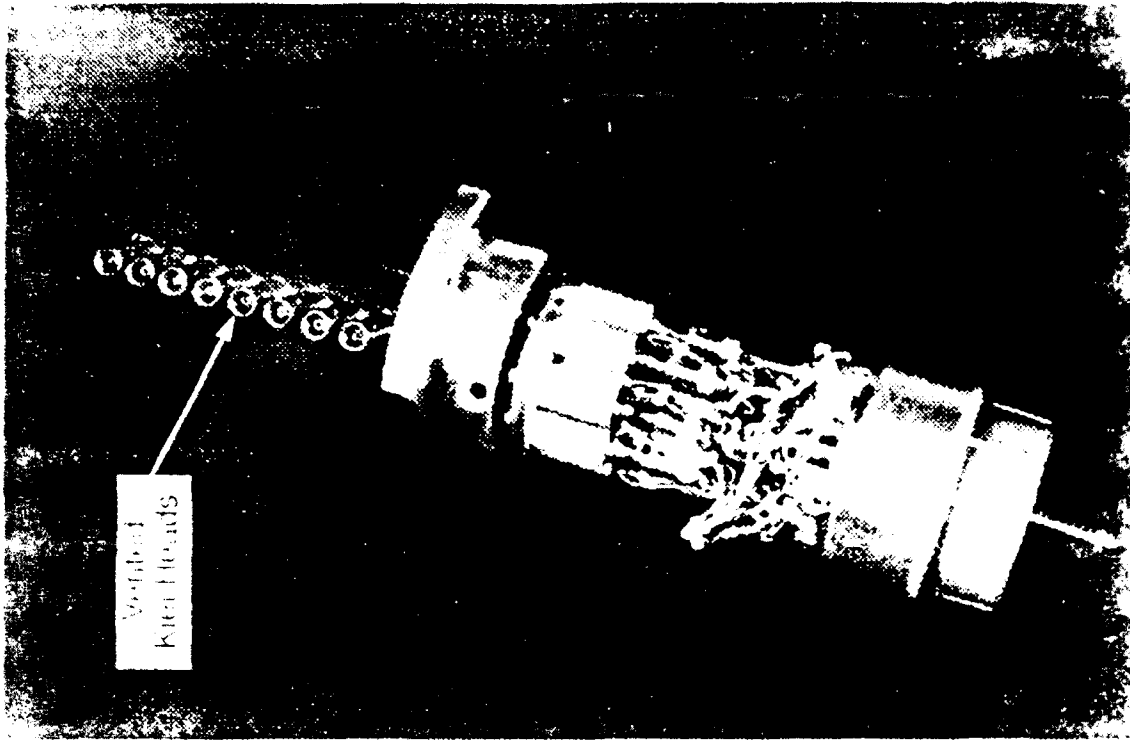


Fig. 35a: Turbine exit traversing rake. The thermocouple reference junctions are mounted in the rake body.



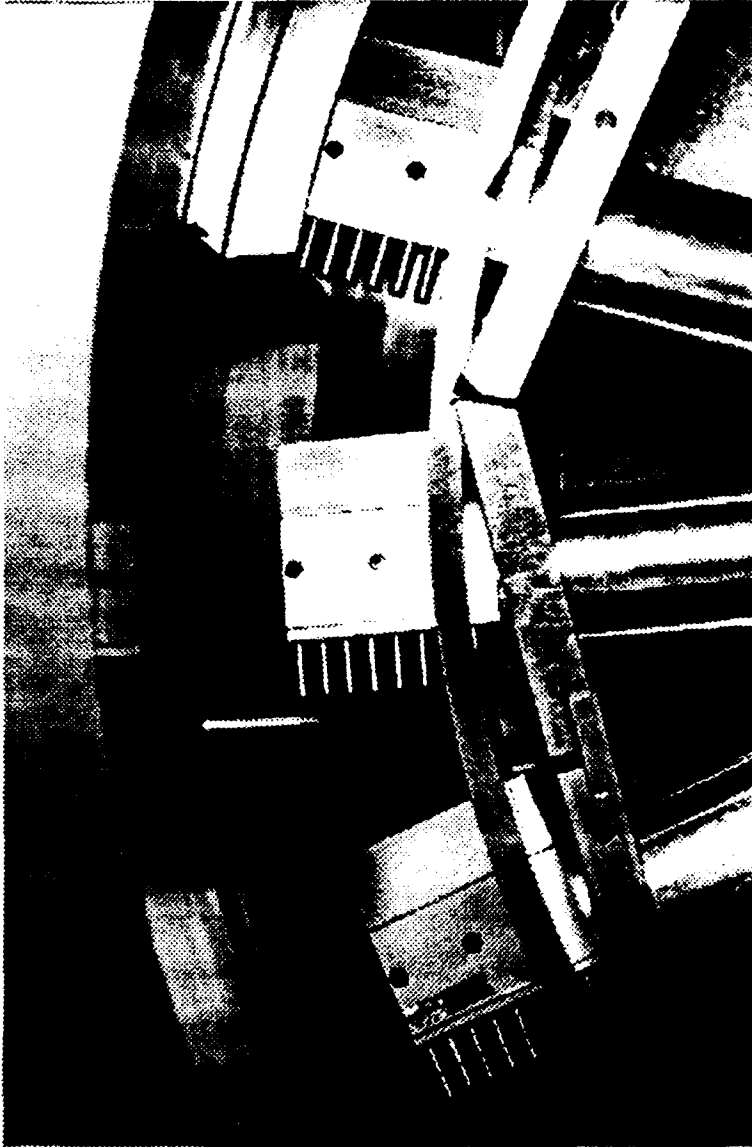


Fig. 35c: Total temperature, high frequency total pressure, and low frequency total pressure rakes mounted at NGV exit station on rotating drum (looking downstream).

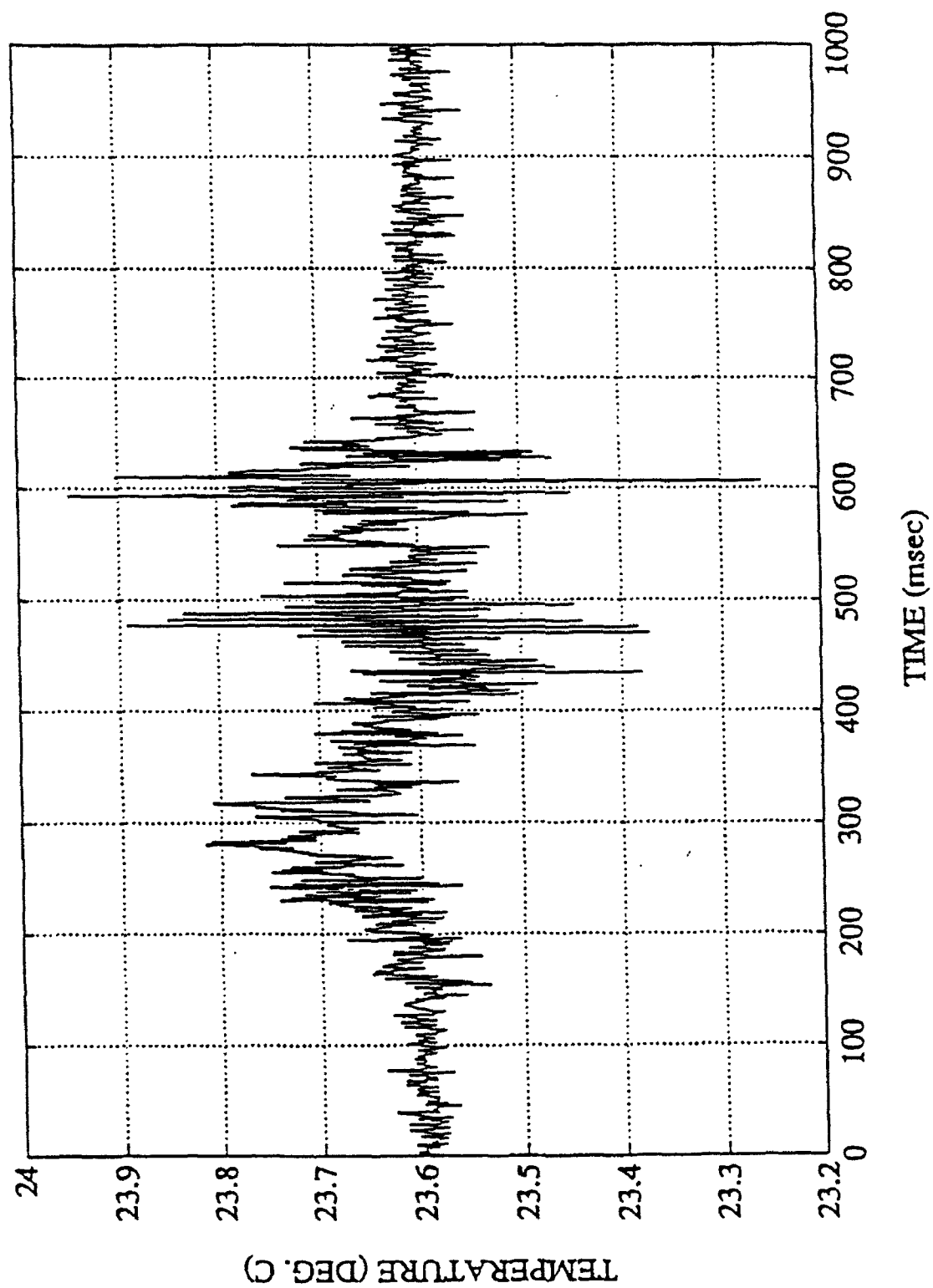


Fig. 36:Time history of inlet midspan thermocouple during traverse in vacuum.

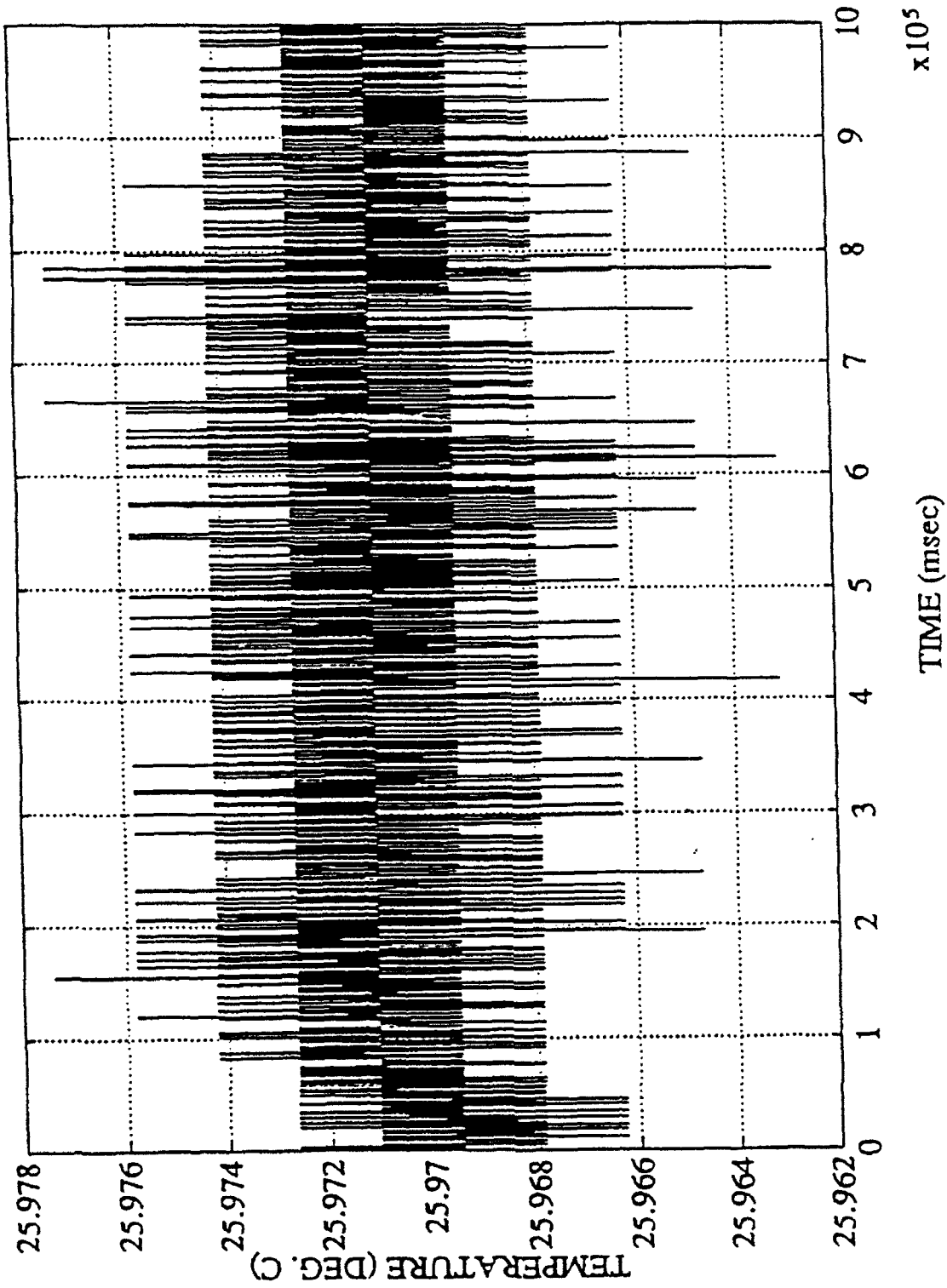


Fig.37 : Time history of inlet rake reference junction during traverse in vacuum.



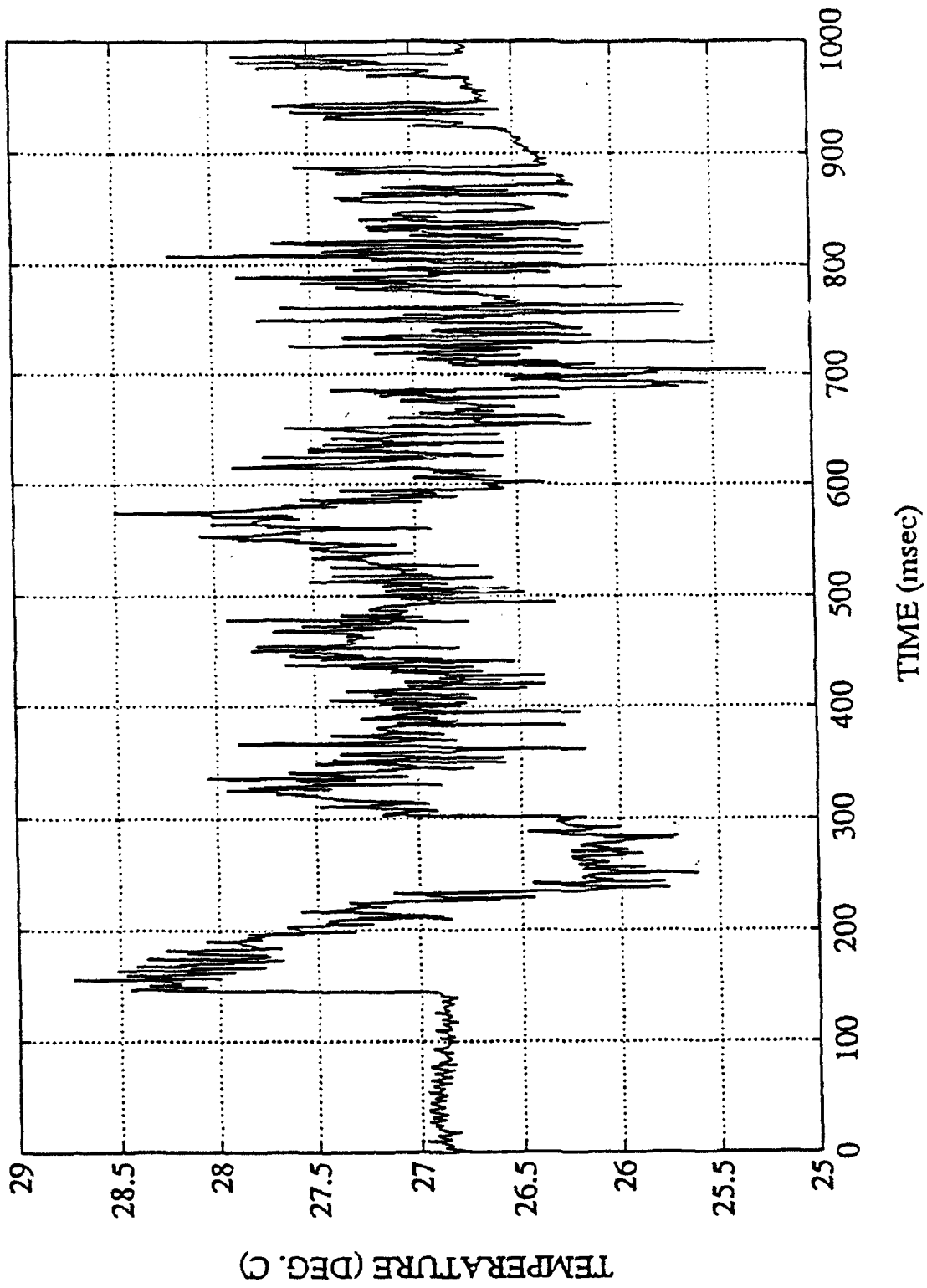


Fig. 38: Time history of exit tip thermocouple during traverse in vacuum.

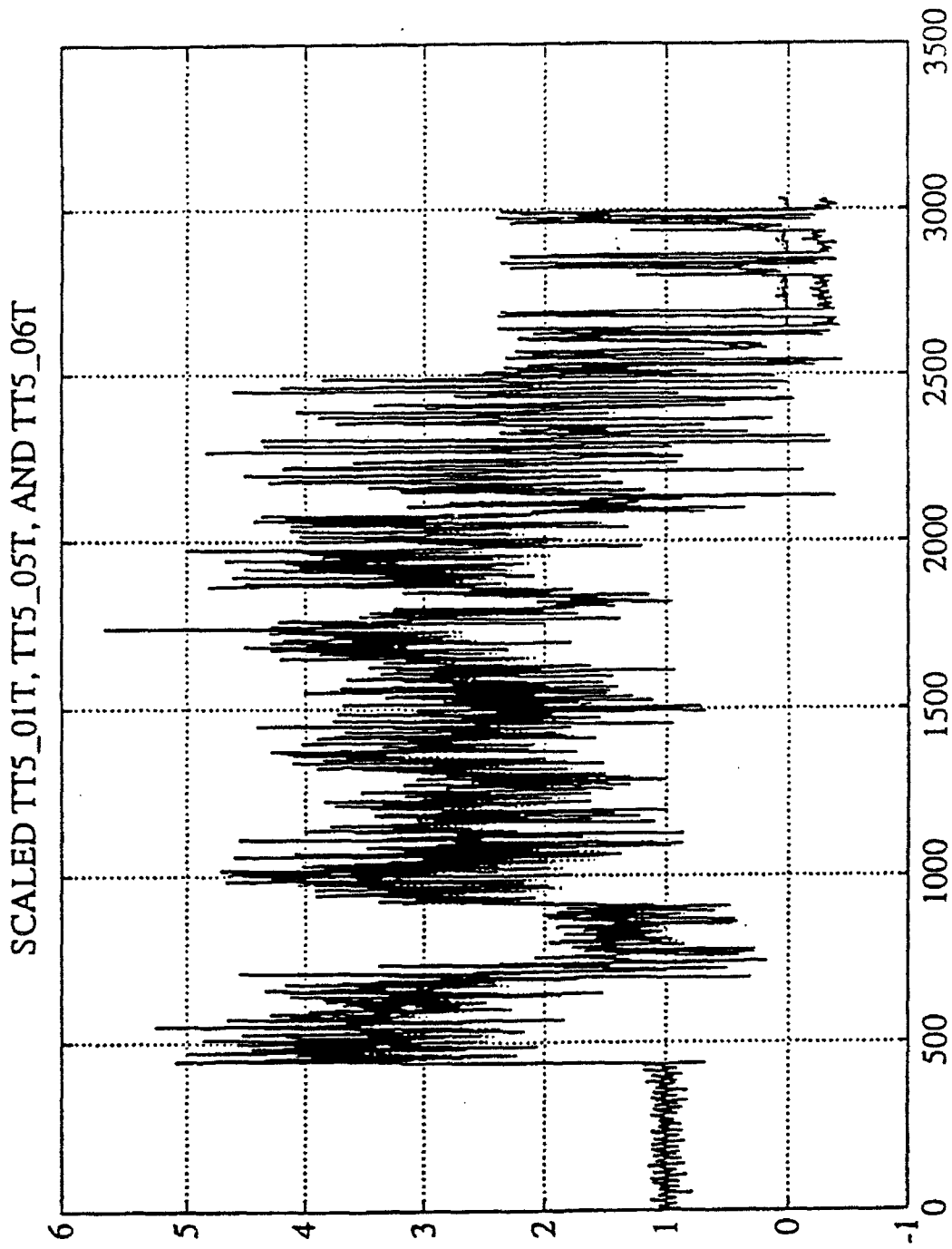


Fig.39 : Time histories of three exit rake thermocouples during traverse in vacuum.  
The three outputs closely line up.

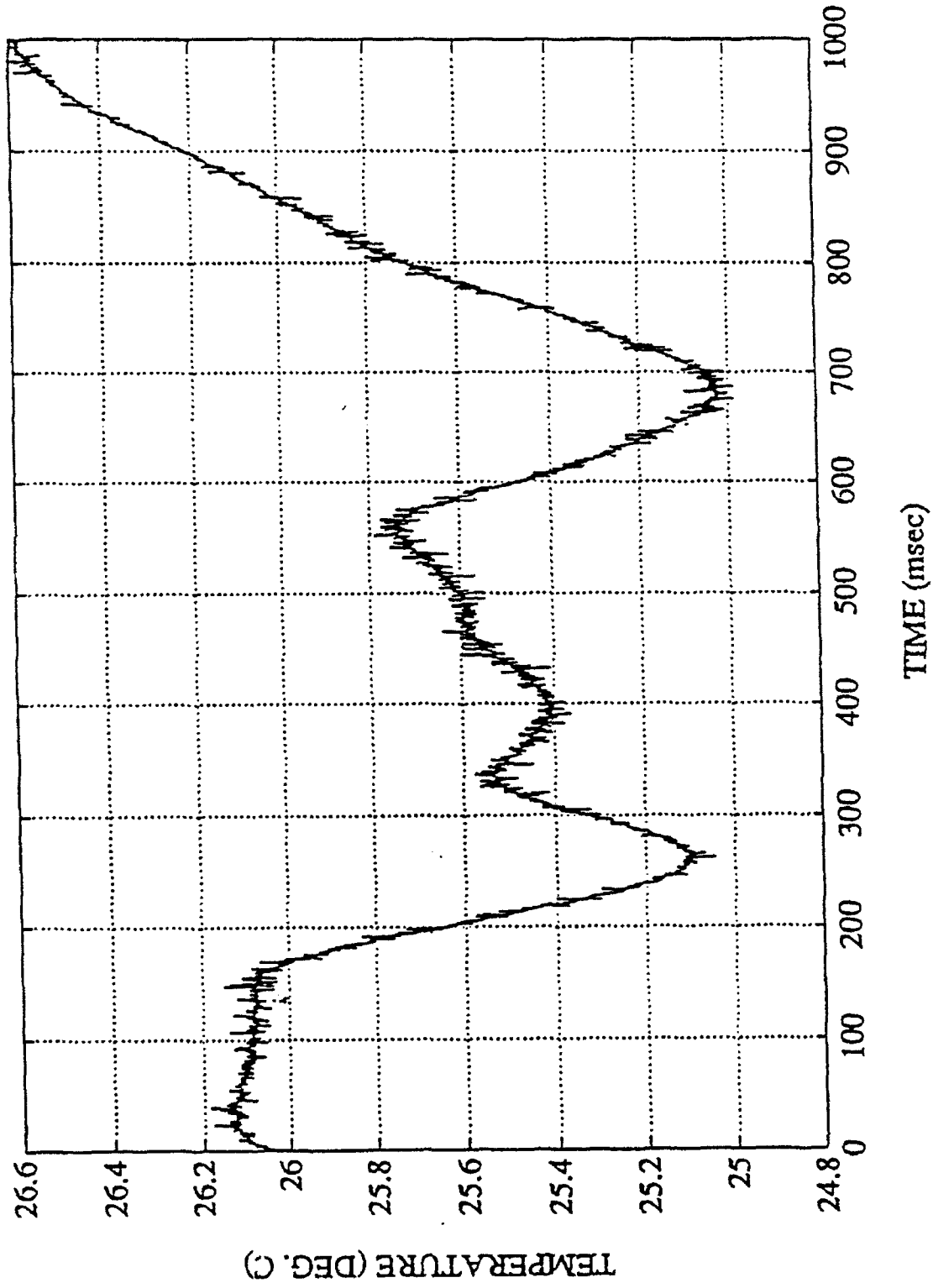


Fig. 40: Time history of exit rake temperature reference output during traverse in vacuum.

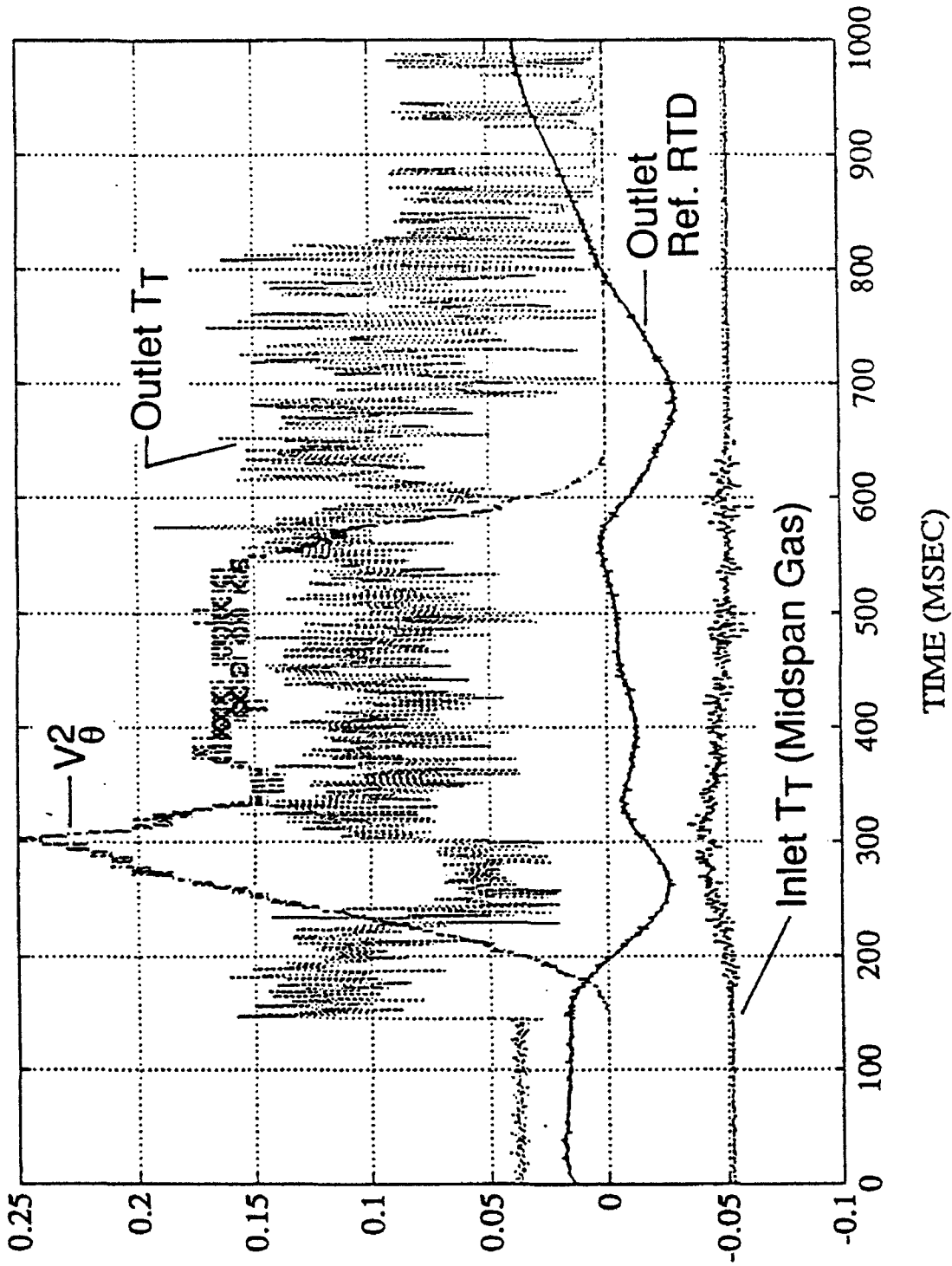


Fig.4.1: Inlet and outlet T/C's and RTD plotted with angular velocity squared ( $V_{\theta}^2$ ) during a vacuum traverse.

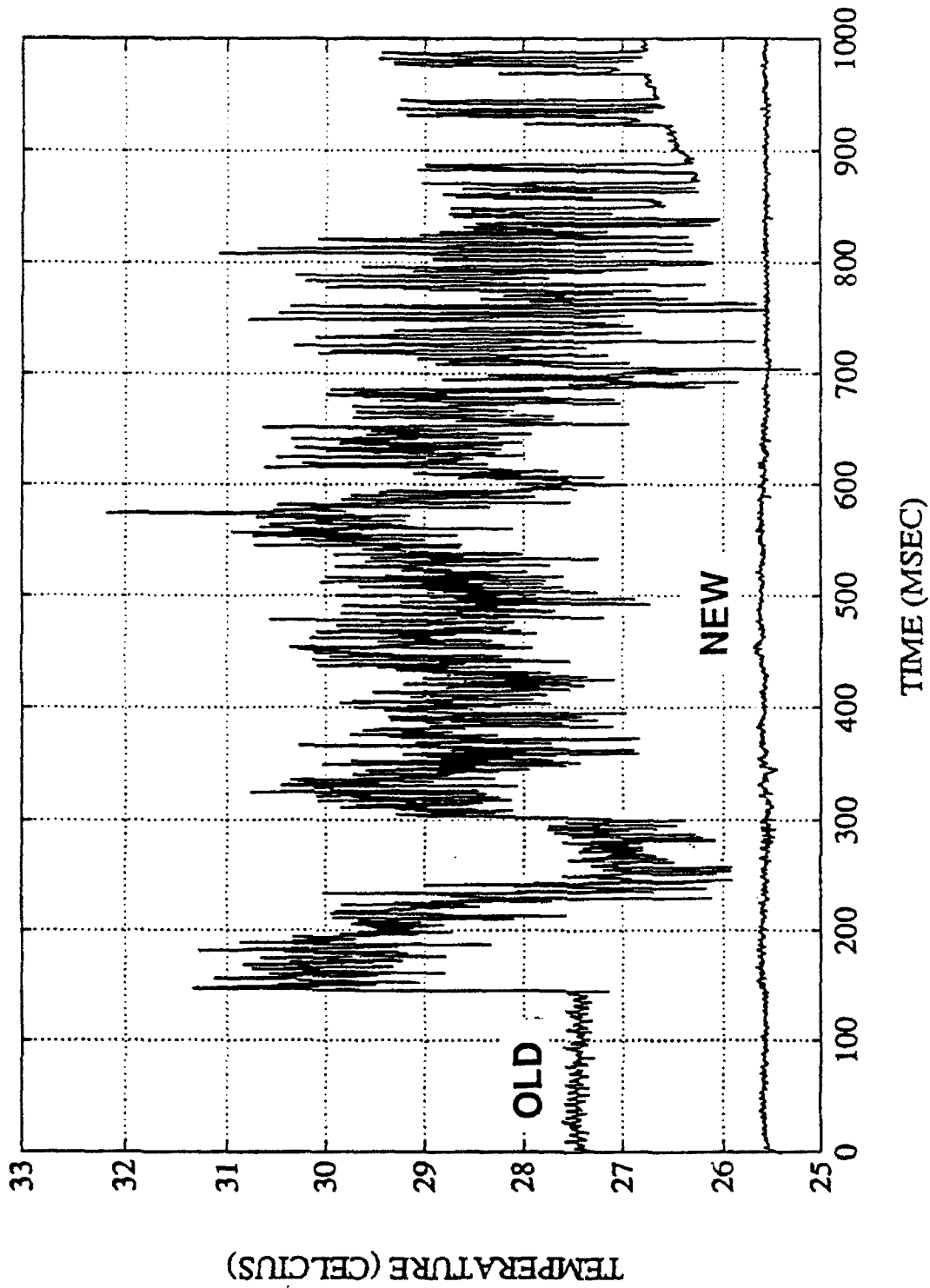


Fig.4.2 : New grounding scheme (bottom trace) greatly reduces induced signals compared to original circuit during a traverse in vacuum.

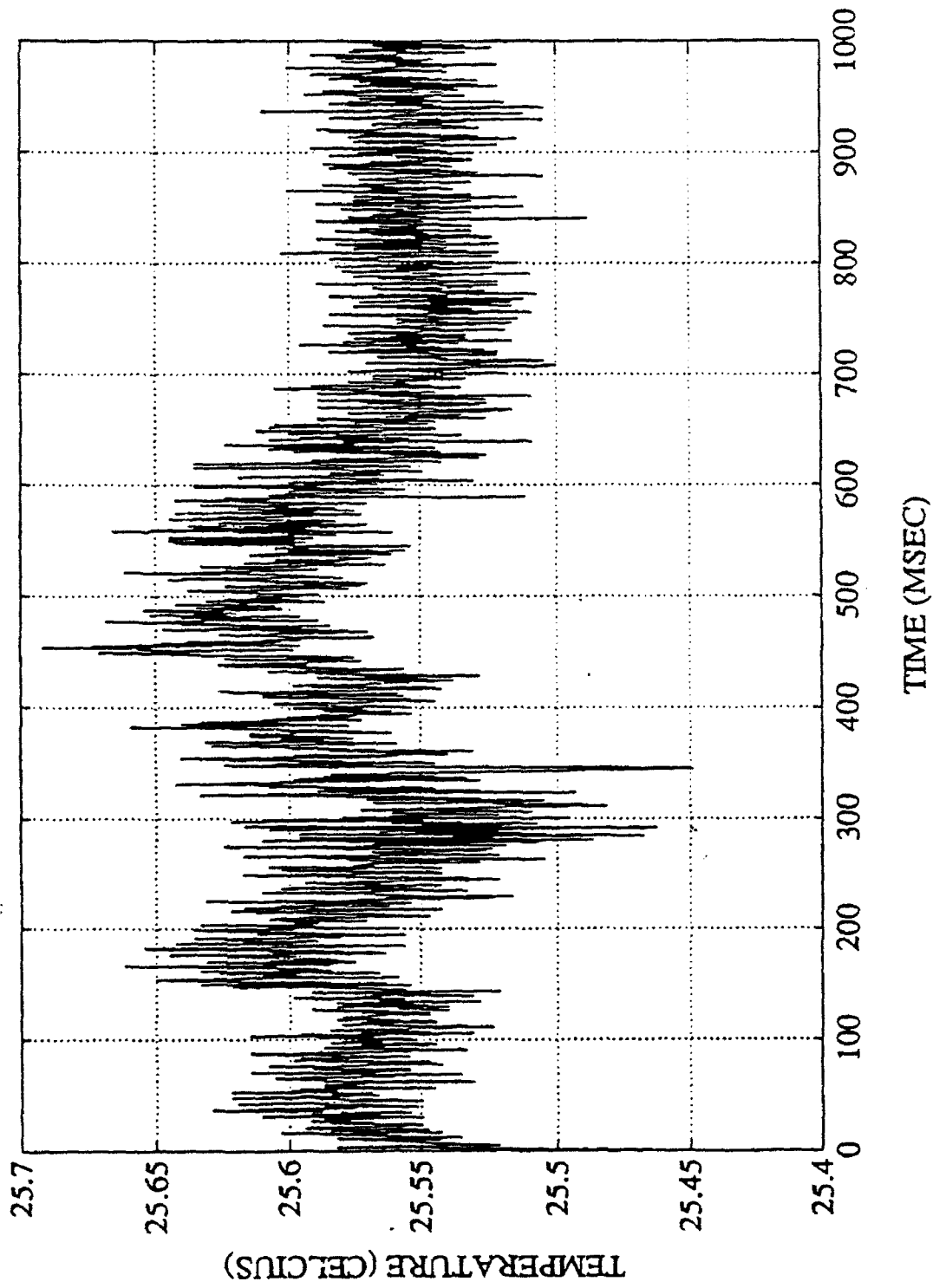


Fig. 43 : The unwanted induced signals on the exit rake are less than 0.2°C with the new grounding scheme.

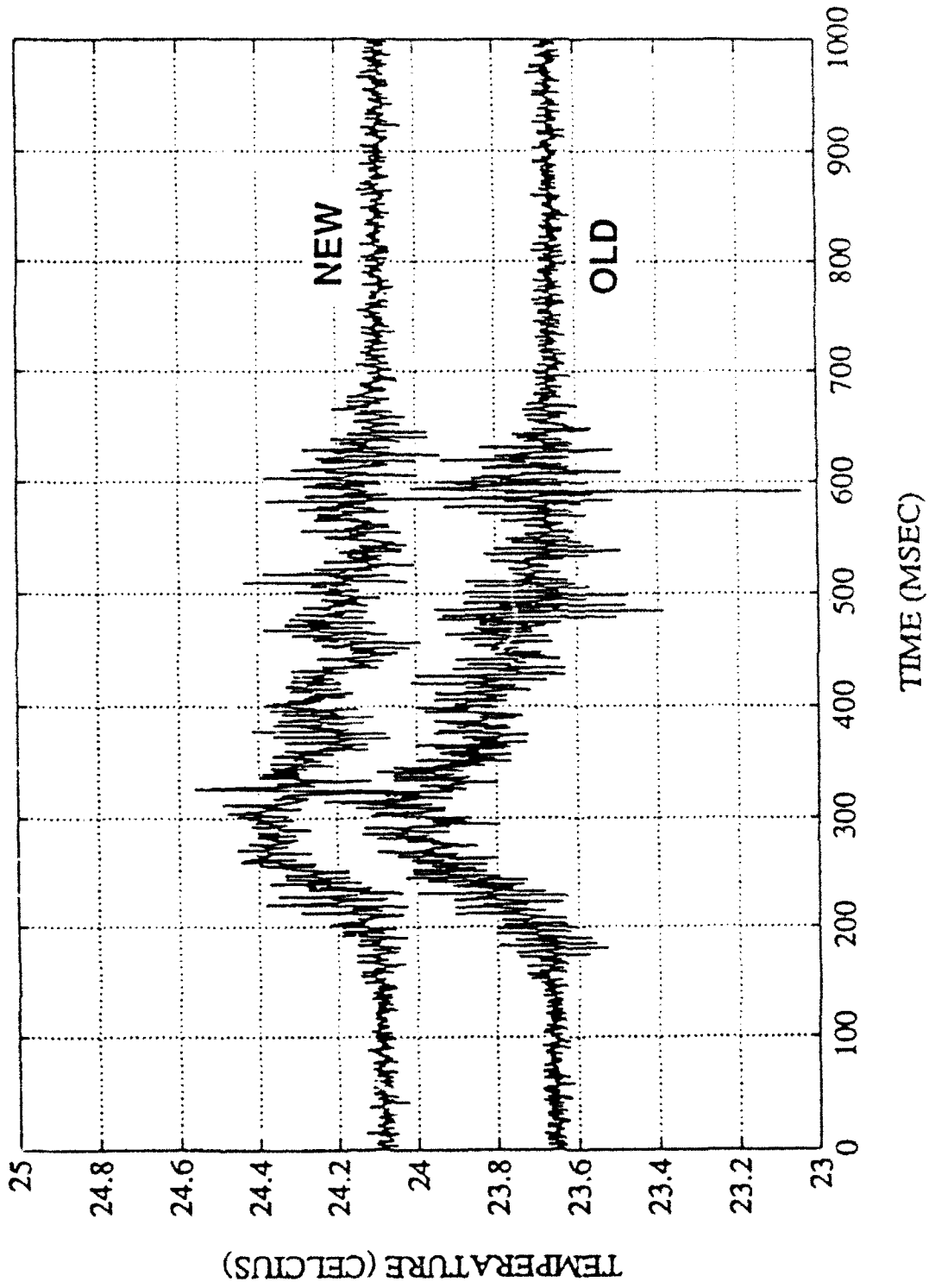


Fig. 44: The new grounding scheme does little to reduce the noise on the inlet rake.

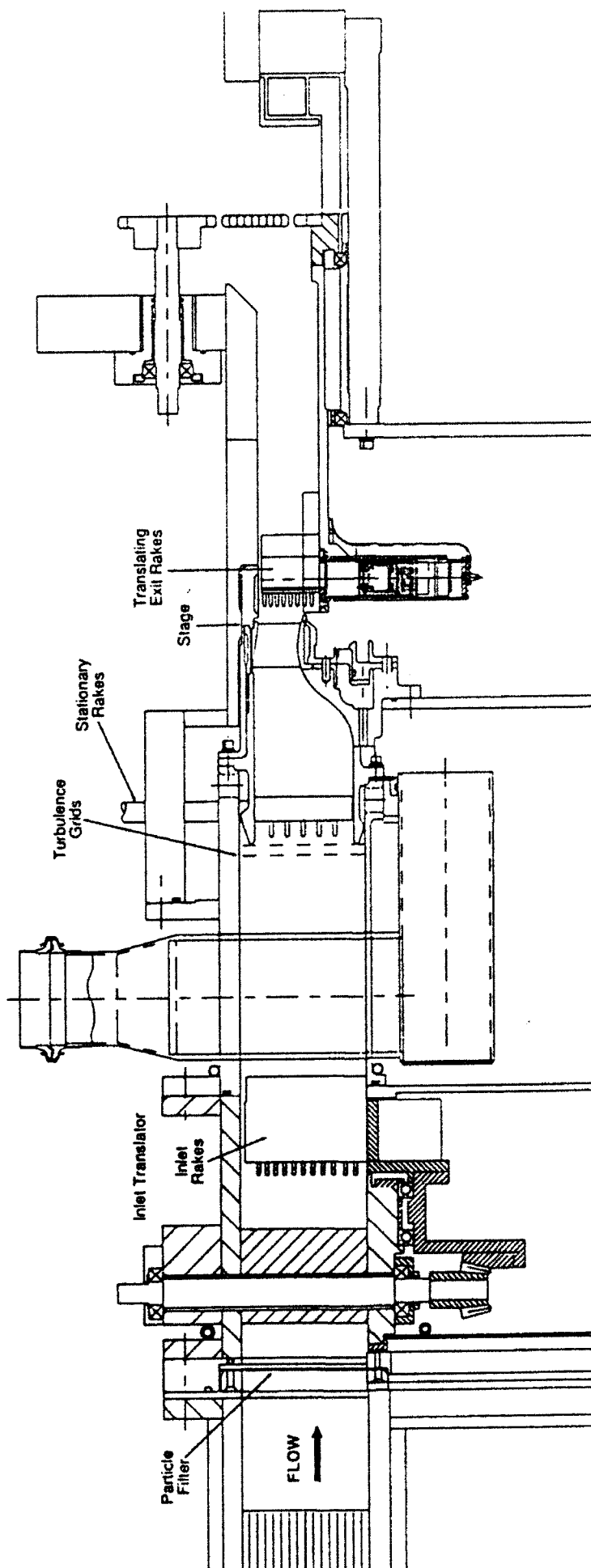


Fig. 4.5 : Test section arrangement for NGV-only testing



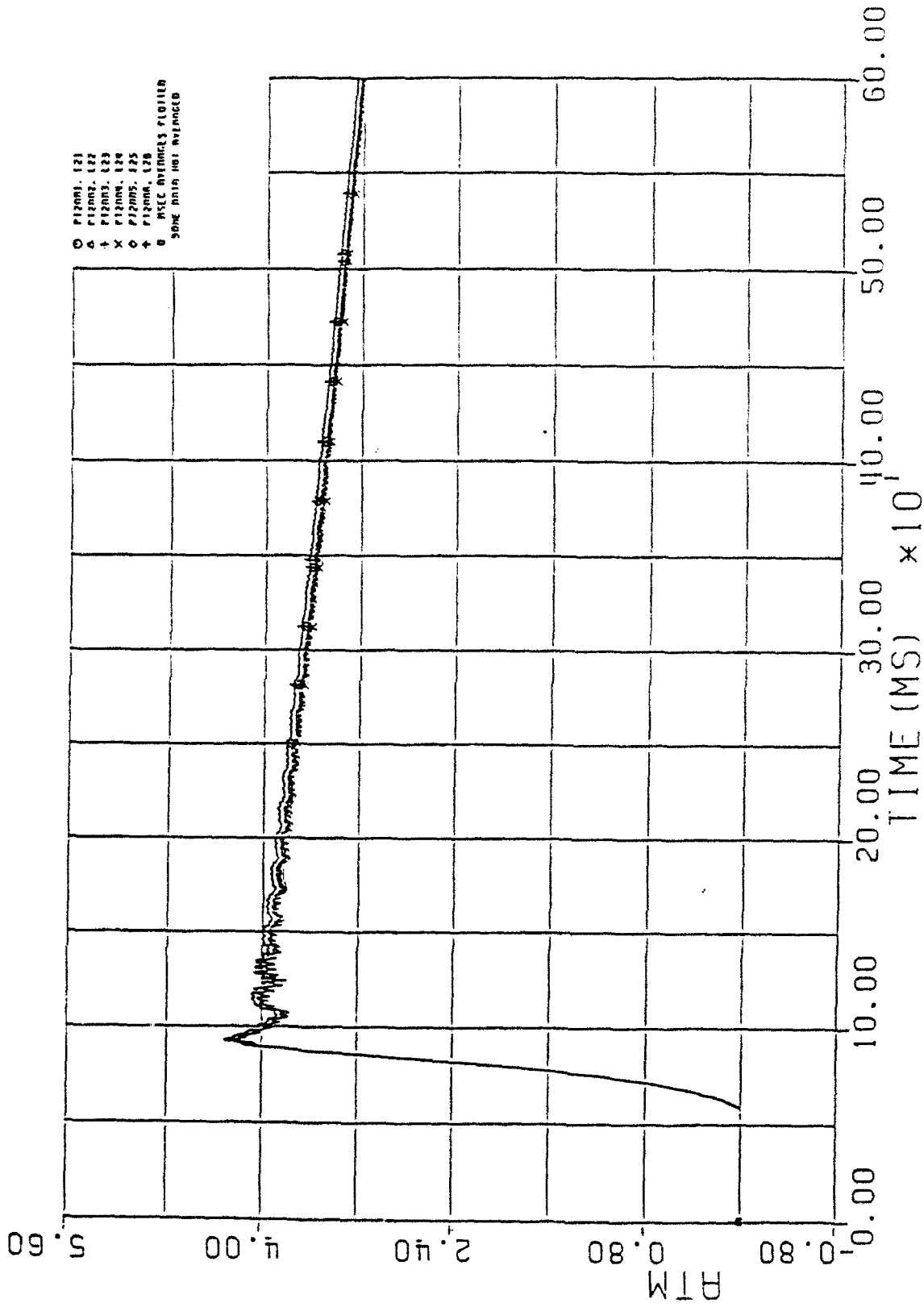


Fig. 46 : Time history of the six transducers from stationary inlet total pressure rake during a blowdown test.

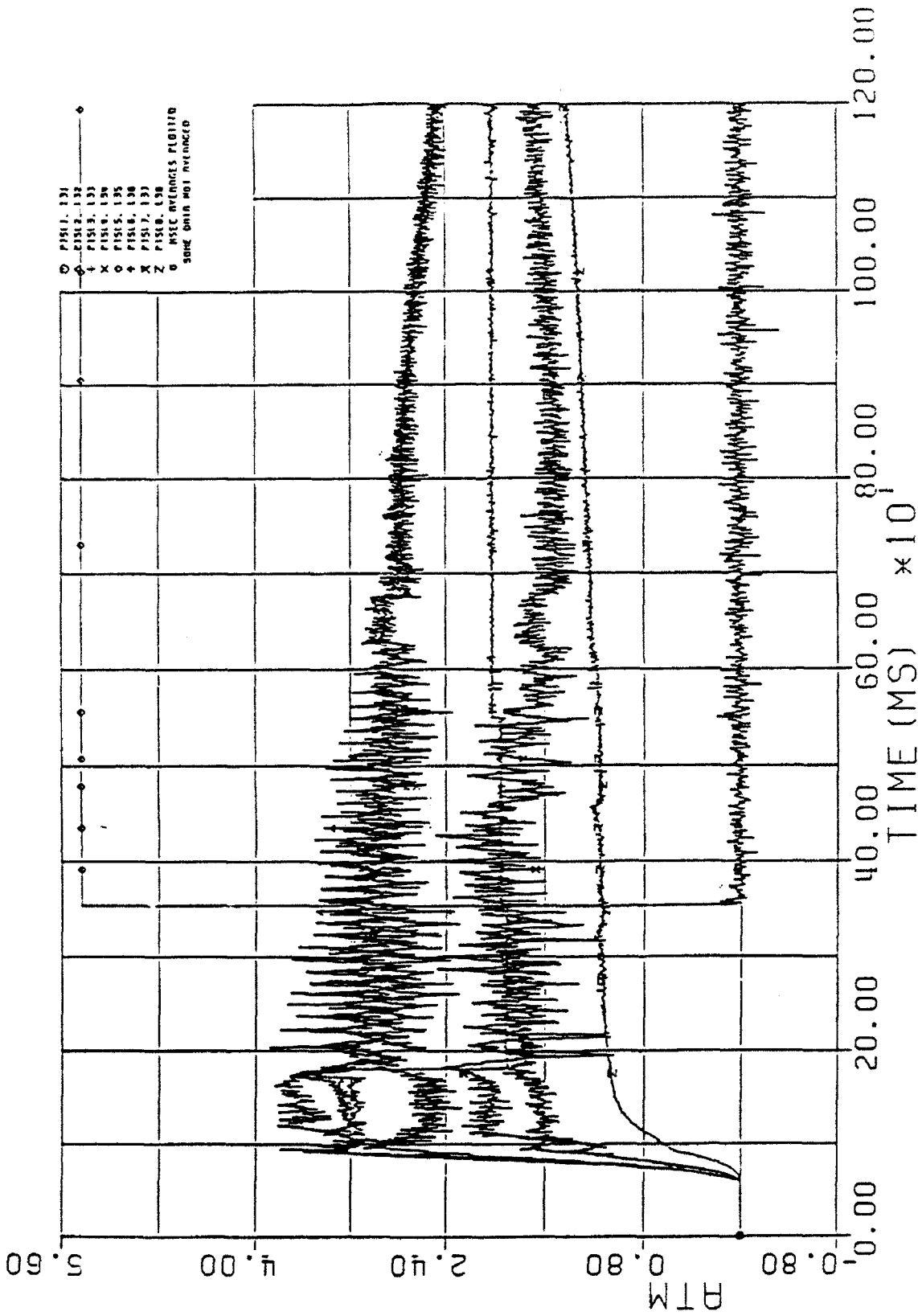


Fig. 47 : Performance of low frequency response exit total pressure rake and wall static transducers during an NGV-only test. The useful test time is 250-550 ms.

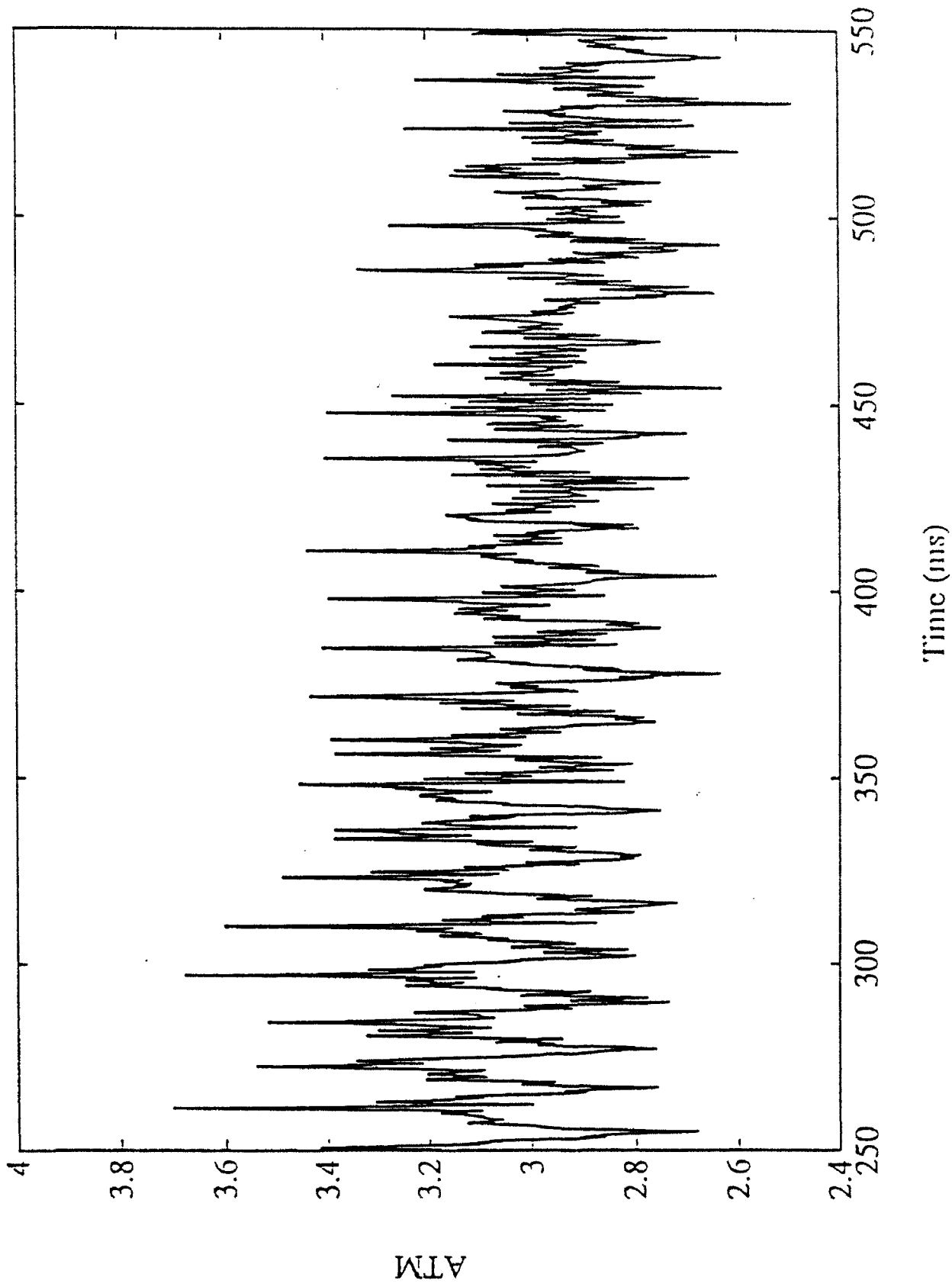


Fig. 48 : The periodicity of the NGV exit flow is evident as the exit rake is traversed behind the NGV's.

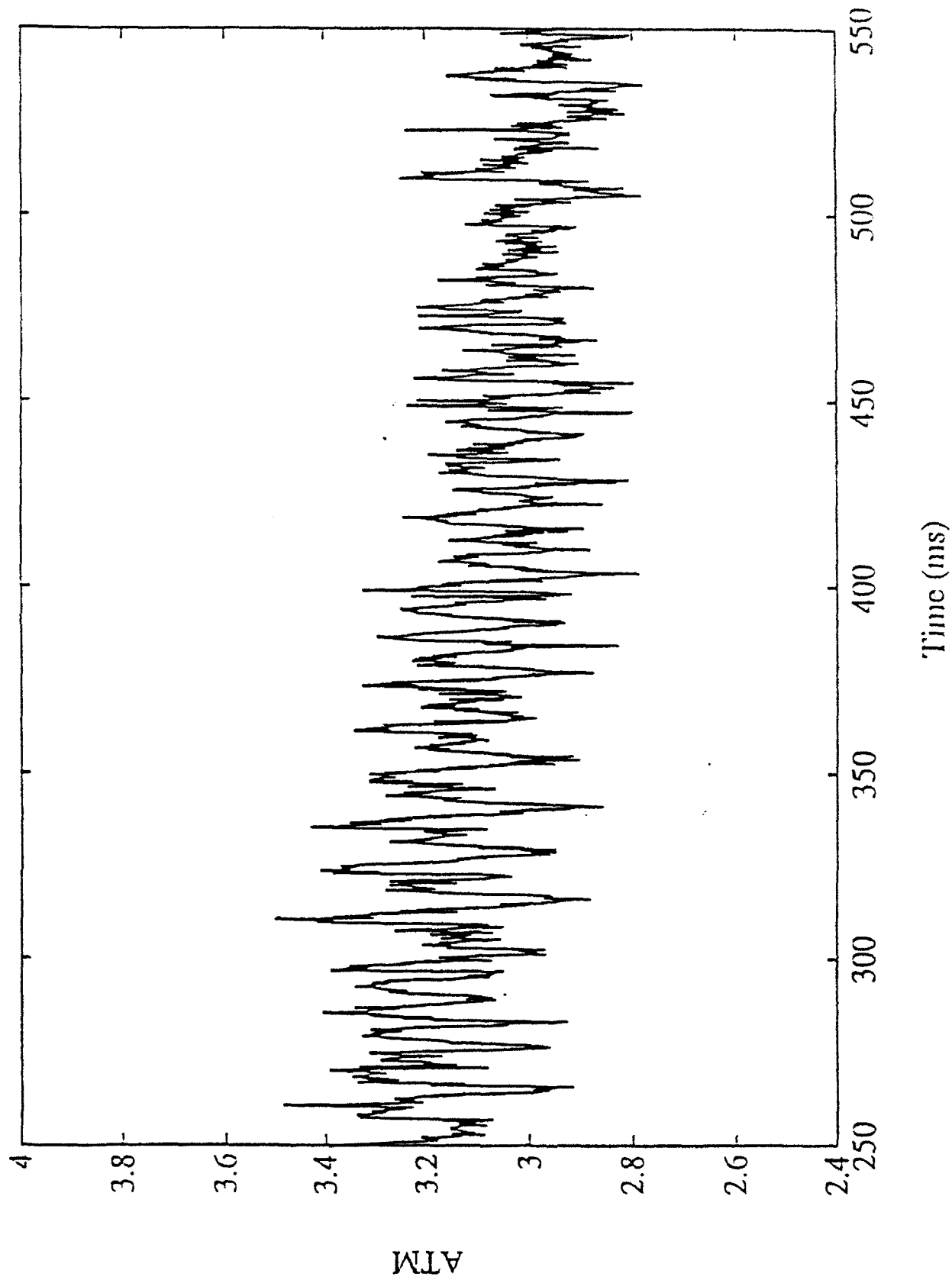


Fig. 49 : The high frequency response exit total pressure rake shows the NGV exit flow field during a test traverse.

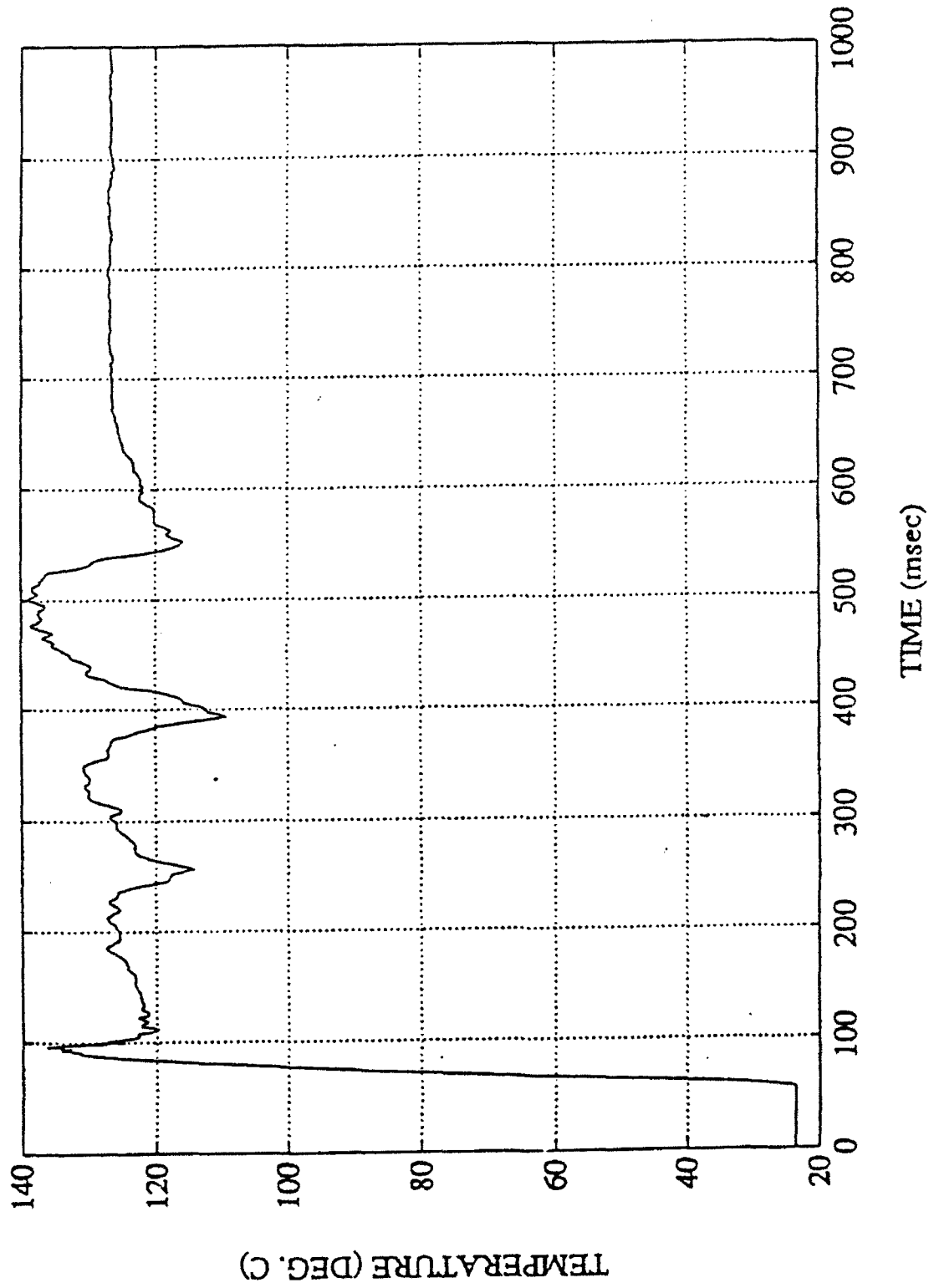


Fig. 50: A circumferential traverse of the inlet rake midspan station. The downspikes at 250, 390, and 550 ms are the strut wakes from the distortion generator.

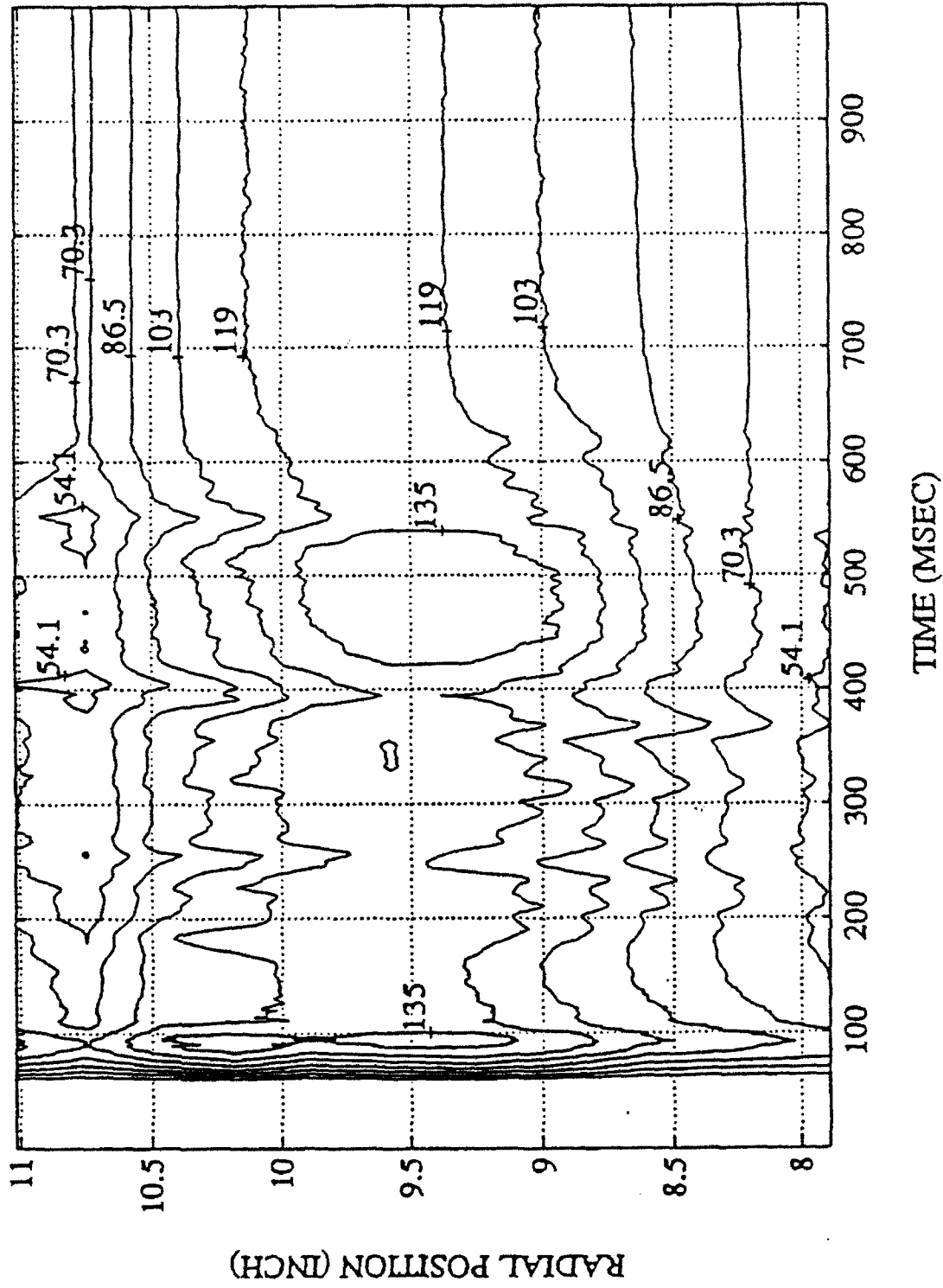


Fig. 51: A contour map of the turbine inlet flow made from the 11 rake T/C's as they are traversed about the annulus.

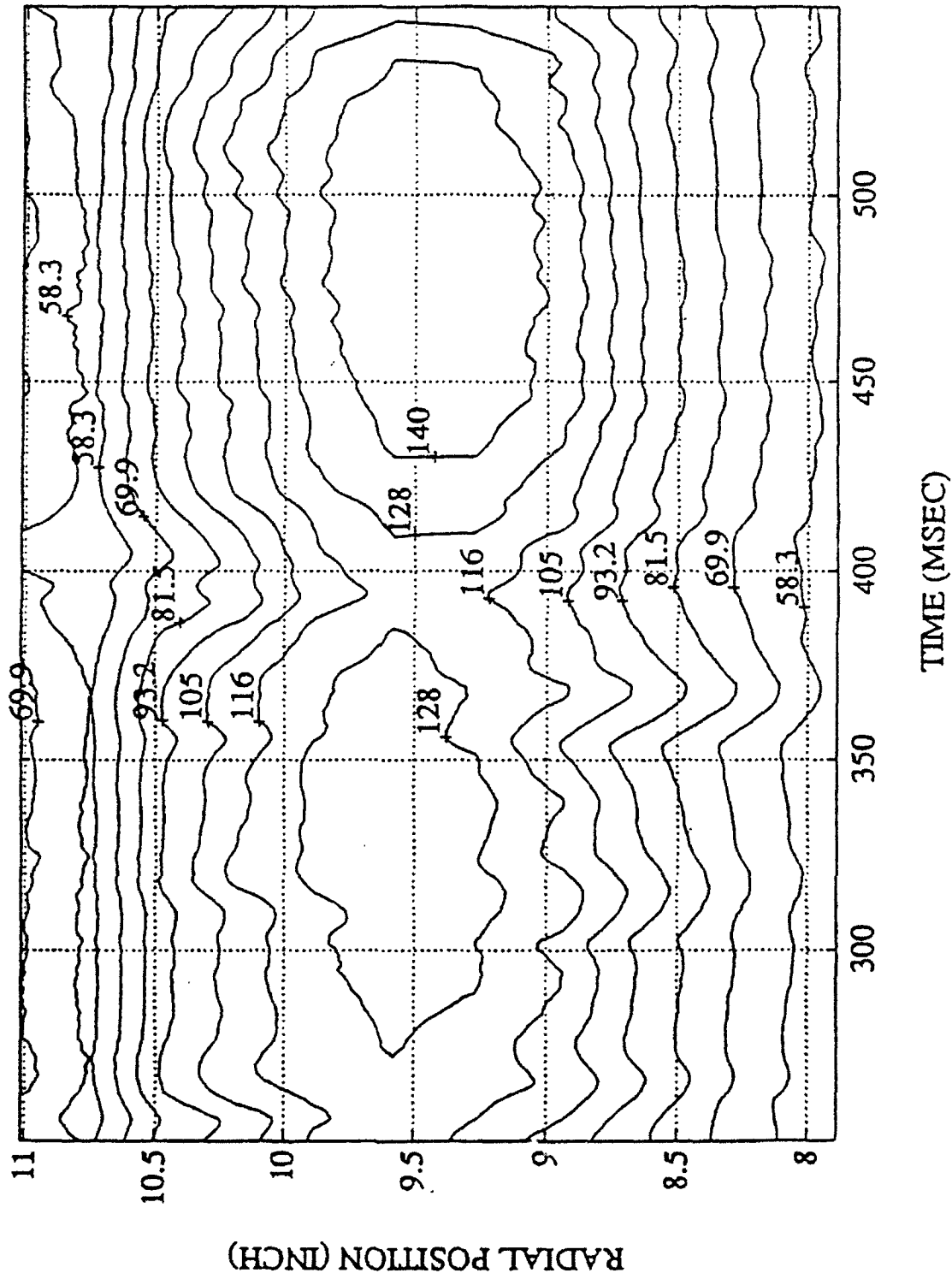


Fig. 52: A contour map of inlet total temperature during the test time. The traverse is travelling at constant velocity so that the horizontal axis translates linearly into  $240^\circ$  of angular position.

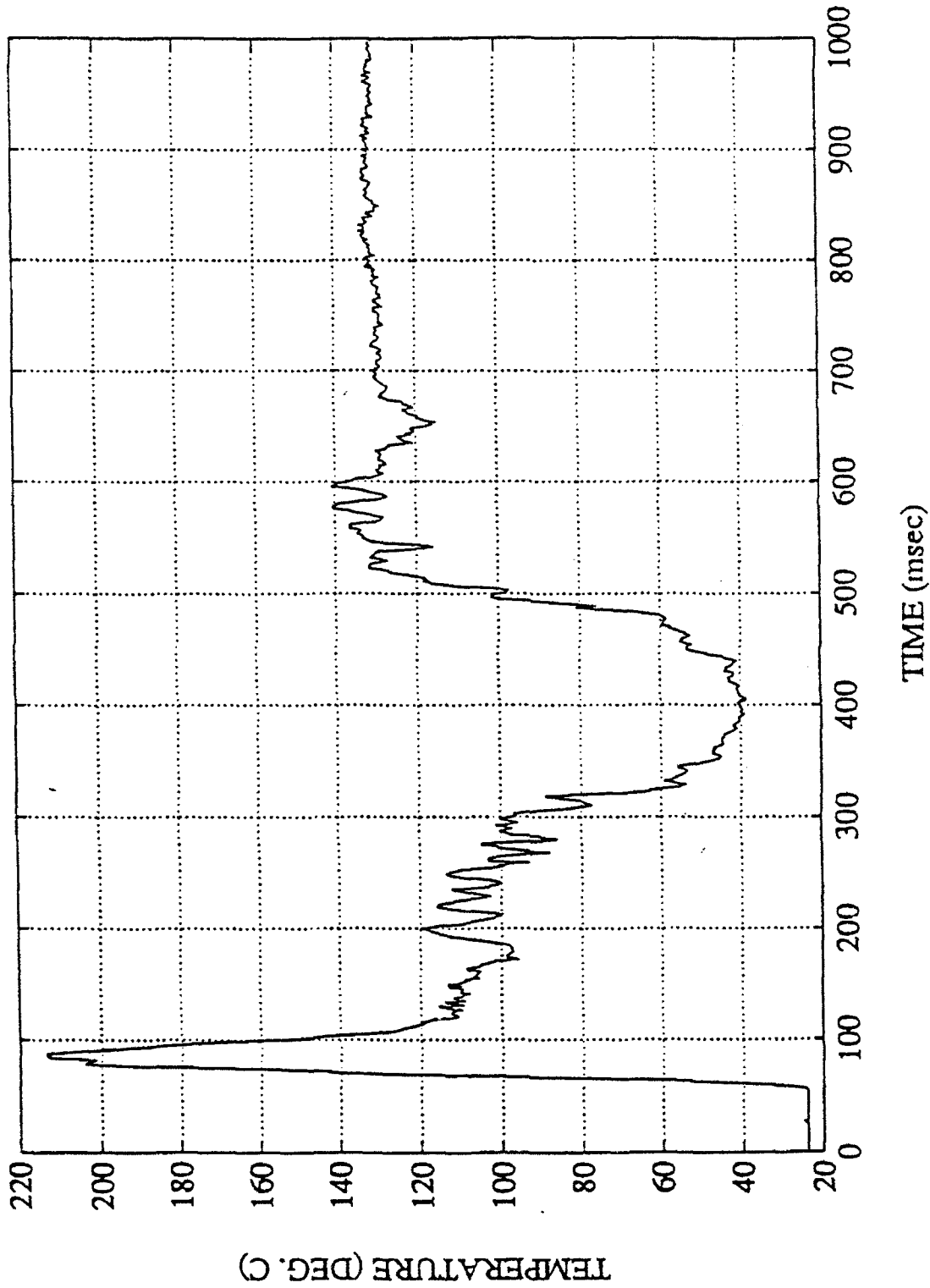


Fig. 53: Midspan NGV exit total temperature as the rake is traversed. NGV wakes are apparent between 200-300 ms and an unheated sector of the distortion generator between 300-500 ms.



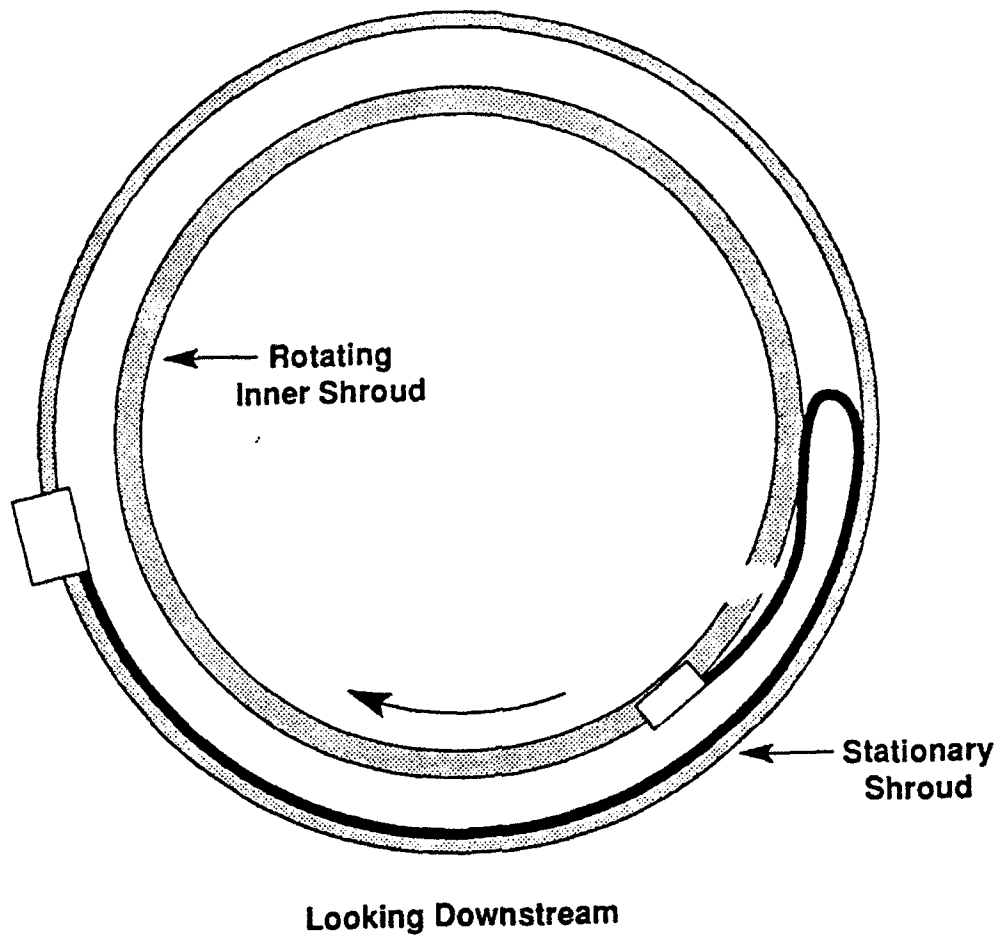


Fig. 54: Rotating multilayer ribbon arrangement on exit translator.  
Shown in starting position, travel is  $350^\circ$ .

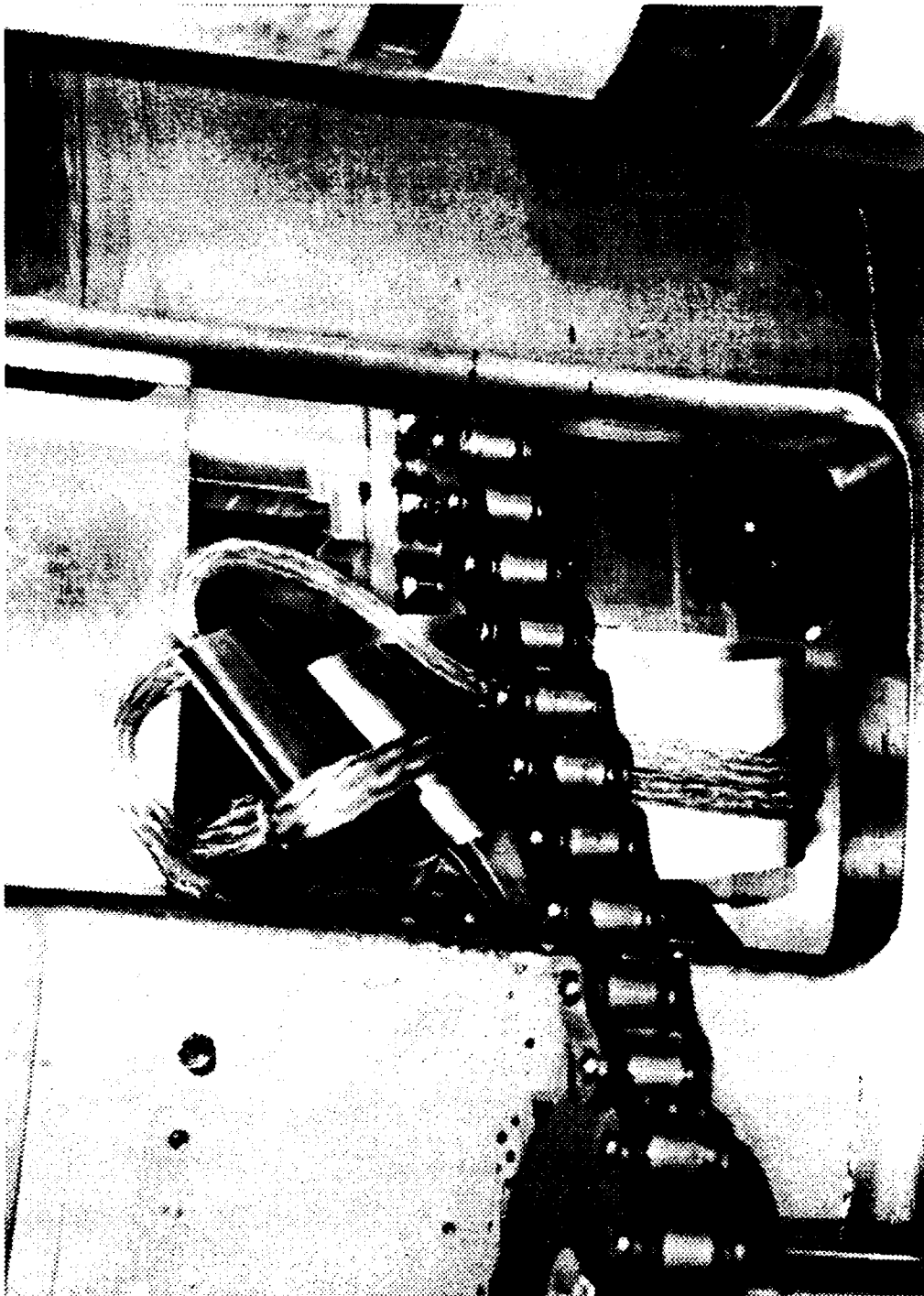


Fig. 55: The exit rake cabling became entangled in the translator chain drive during the first test.

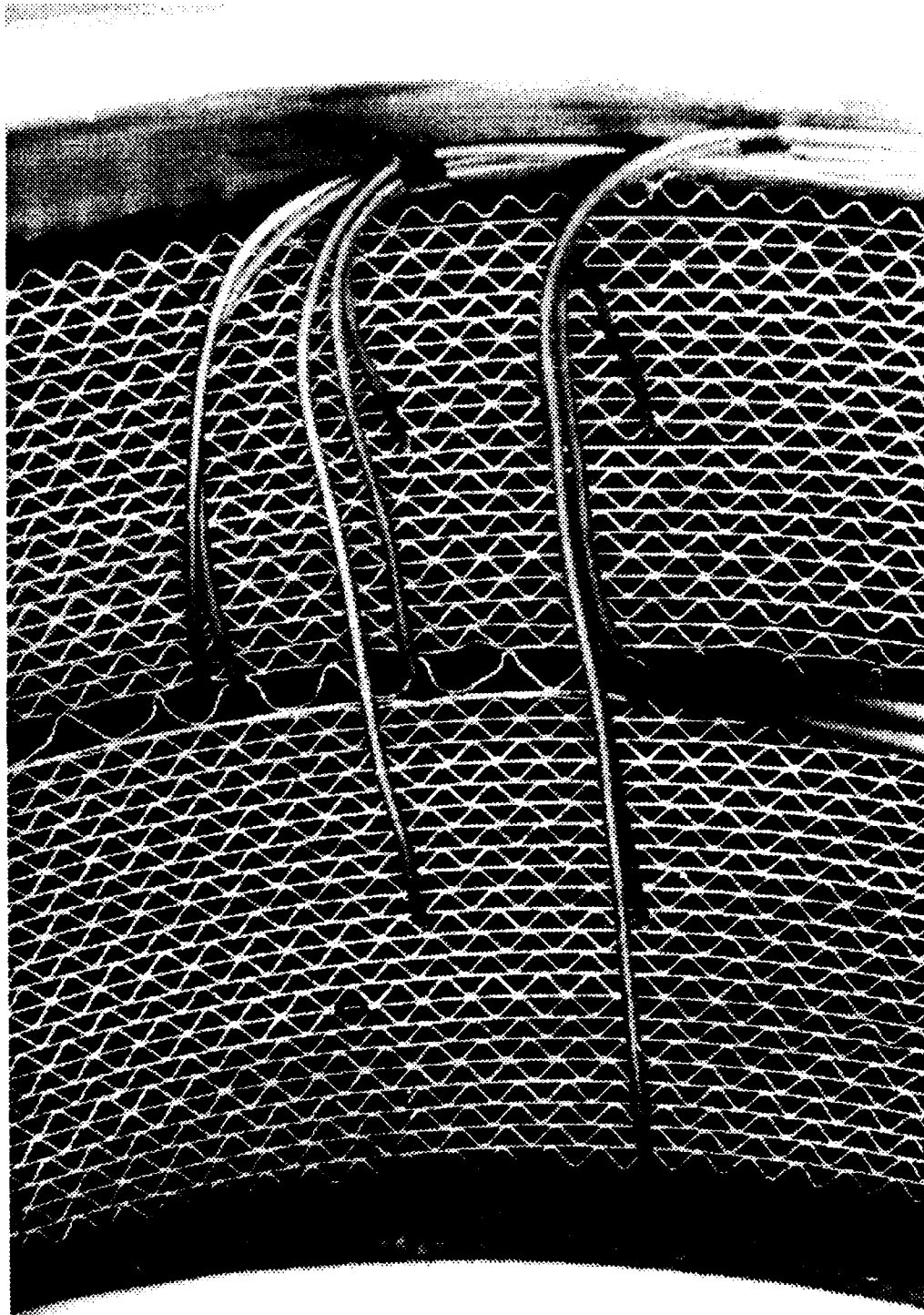
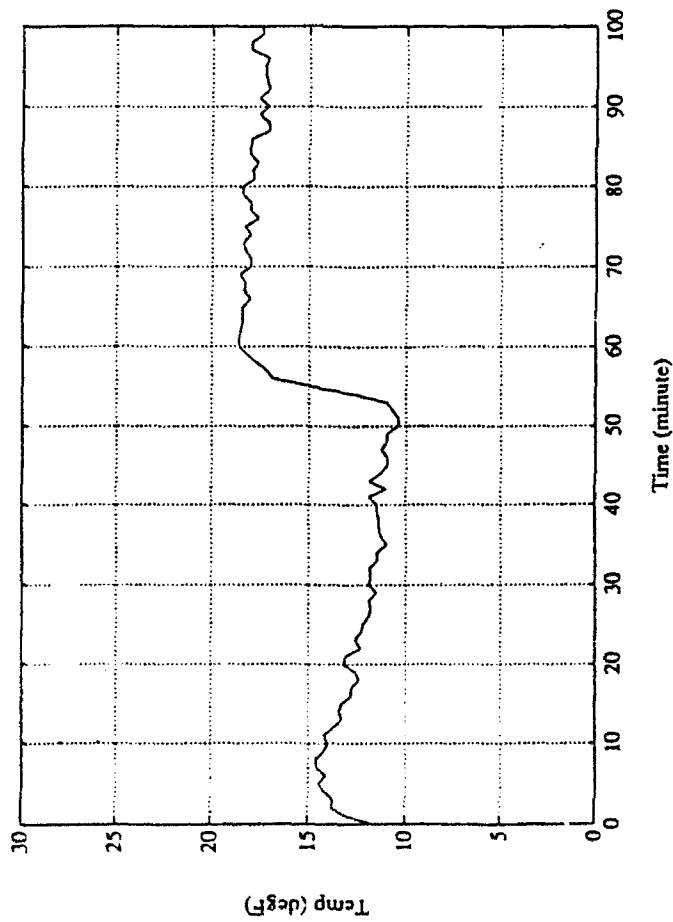


Fig. 56: Upstream end of the  $\theta$ TDF sector of the distortion generator showing matrix, heater (thick wire), and thermocouples (numerous smaller wires).

### Circumferential $\Delta T$



### Radial $\Delta T$

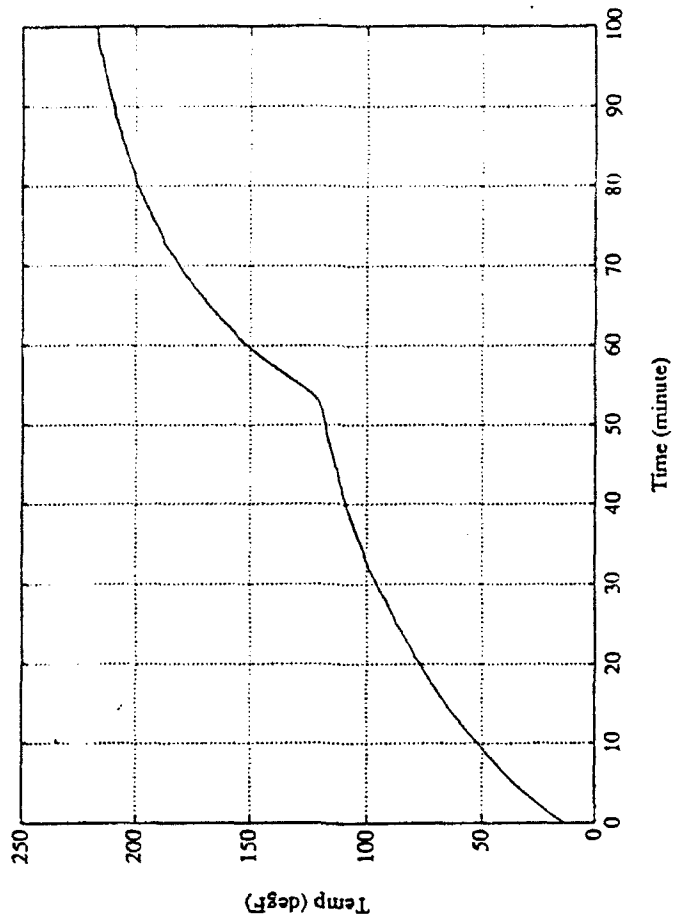
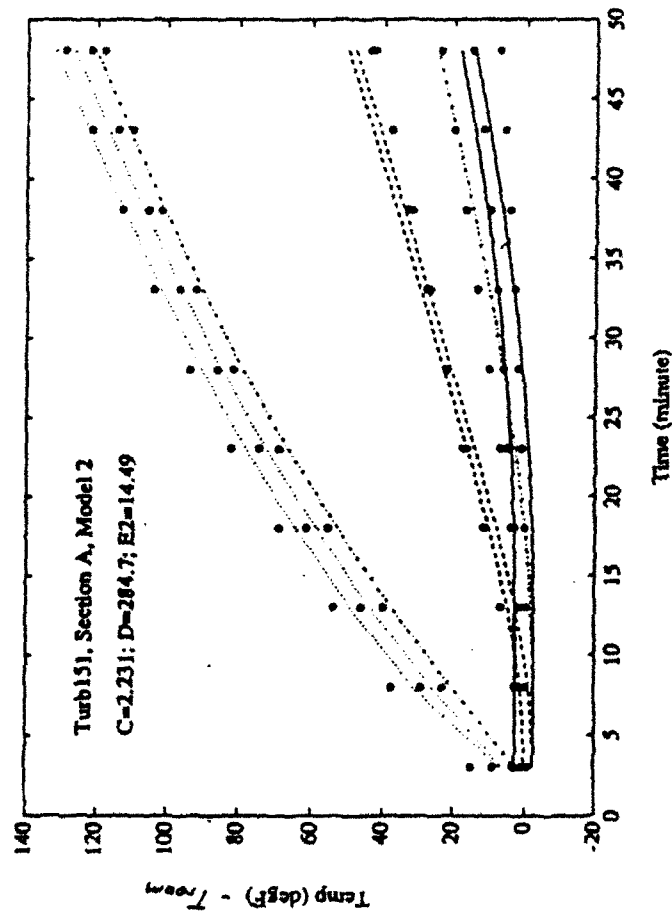


Fig. 57 : 0TDF sector response to step heat inputs.

## RIDF Sector



## θIDF Sector

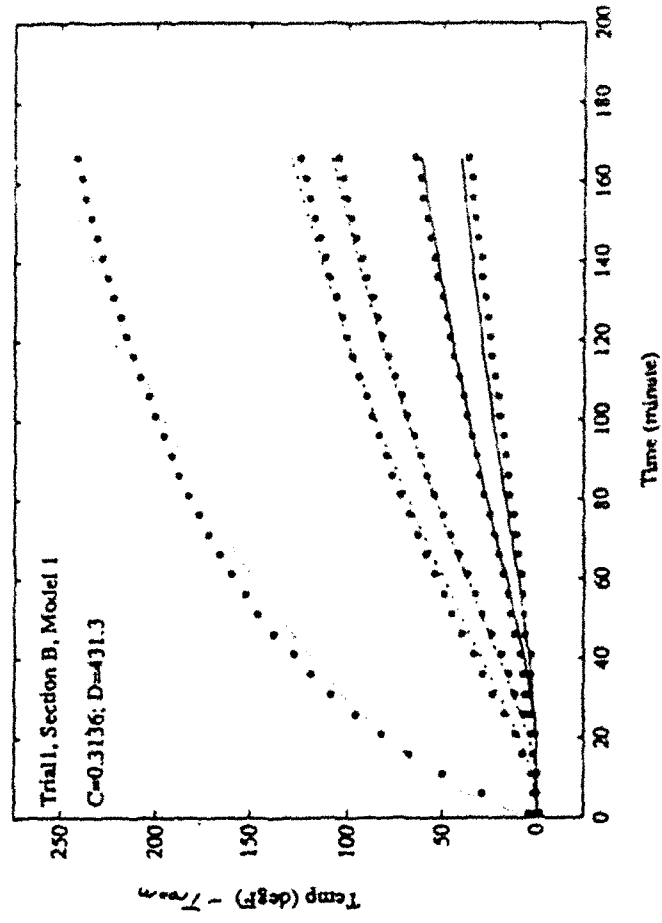
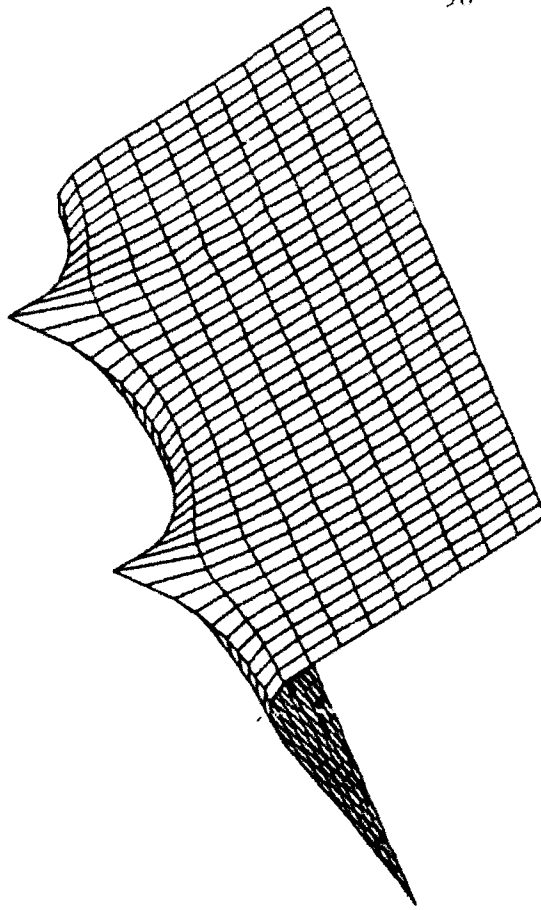
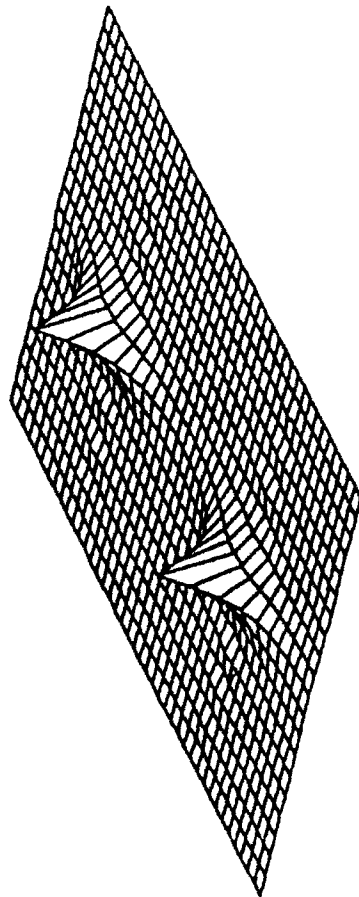


Fig. 58: Fit of transient conduction parameters (lines) to data (symbols) during vacuum heatup of distortion generator.



**$\theta$ TDF Profile**  
**Current = 10A, Power on 180 minutes**



**$\theta$ TDF Profile**  
**Current = 10A, Power on 2 minutes**

Fig. 59: Model predictions of  $\theta$ TDF generator performance showing two hot spots. Height is temperature.

## **TASK II: ASSESSMENT OF UNSTEADY LOSSES IN STATOR/ROTOR INTERACTIONS**

(Investigators: M.B. Giles, G. Fritsch)

Gerd Fritsch, the graduate student who was working on this project, completed his Ph.D. thesis in May 1992. The thesis was subsequently prepared as an MIT Gas Turbine Laboratory Report (GTL Report No. 210, "An Analytical and Numerical Study of the Second-Order Effects of Unsteadiness on the Performance of Turbomachines") and is available on request. In June, a paper was presented at the ASME Gas Turbine Conference in Cologne. This focussed on the loss mechanism due to the unsteady Stokes sublayer, as discussed in previous annual reports. A copy of the paper is given as an Appendix. A second paper based on Fritsch's work is now in preparation for the 1993 ASME Gas Turbine Conference in Cincinnati. This addresses the analysis of time-averaged and space-averaged mixing loss which was discussed in last year's annual report.

Overall, Fritsch's research has made an important contribution towards the growing understanding of the impact of unsteadiness in turbomachinery flow. He has shown that the loss due to unsteady circulation is very small and can be disregarded in future research. He has explained and analyzed the mechanism of the unsteady Stokes layer loss. Unfortunately, he has not been able to accurately assess its magnitude under typical engine conditions but even in this he has made the important contribution of showing the limitations of existing CFD methods in addressing this important question. Finally, his analytical work on the mixing loss ties together and expands upon the work done by others and shows the separation of the loss due to different forms of unsteady wave. It also highlights the loss that is introduced in steady-state multistage CFD analyses using mixing plane coupling.

Also presented in last year's report were ideas for continuing this work in the future using a combined asymptotic analysis of unsteady multistage flow fields. In the analysis, the base level is a steady-state multi-row calculation using mixing plane coupling at all stator/rotor interfaces. The next part is a calculation of the unsteady flow field using a linear perturbation assumption. The

third stage calculates the change in the time-averaged flow field due to quadratic terms associated with the linear unsteady flow field. A paper was presented on this idea at the ASME Gas Turbine Conference in Cologne (also included in the Appendix). A number of related issues were also discussed at a Workshop on Unsteady Losses held at NASA Lewis in May. This brought together researchers in NASA, academia and industry to discuss the key aspects of unsteady flow in turbomachinery, to review our current understanding and the issues that need to be resolved. Discussion of this is given in the section on Interactions.

Work on the multi-stage analysis will be continued by Dr. Giles at Oxford University, to which he moved in June.





The Society shall not be responsible for statements or opinions advanced in papers or in discussion at meetings of the Society or of its Divisions or Sections, or printed in its publications. Discussion is printed only if the paper is published in an ASME Journal. Papers are available from ASME for fifteen months after the meeting.  
Printed in USA.

## Second-Order Effects of Unsteadiness on the Performance of Turbomachines

GERD FRITSCH  
MICHAEL GILES

Department of Aeronautics and Astronautics  
Massachusetts Institute of Technology  
Cambridge, MA 02139

### Abstract

A 2D, linearized approach is used to investigate second-order effects of unsteadiness on the time-mean efficiency of turbomachinery. The objective is to quantify unsteady losses with a nonzero time-mean and to examine numerical simulations with respect to the modeling of unsteady flow fields and loss mechanisms. Results of simulations constitute the input to the analytical models employed.

Two unsteady loss mechanisms, one of inviscid and the other of viscous nature, are considered. The unsteady circulation losses, i.e., the transfer of kinetic energy into the unsteady part of the flow field through vorticity shed at the trailing edge of a blade, was first considered by Keller (1935) and later by Kemp and Sears (1956). The vorticity is shed in response to an unsteady blade circulation and determined from Kelvin's circulation theorem which is valid in compressible homentropic flow. Use of a numerical simulation to obtain circulation amplitudes avoids the limitations of thin-airfoil theory and yields results more realistic for modern turbomachinery. For the unsteady viscous loss mechanism, i.e., the dissipation in an unsteady boundary layer on the blade surface, Lighthill's high-reduced-frequency limit (1955) is used to obtain the local velocity distribution in the laminar sublayer and the corresponding time-mean unsteady dissipation. The input to the model is the time-harmonics of the pressure gradient along a blade surface obtained from a simulation. A numerical study of the errors introduced by a departure from the high-reduced-frequency limit is presented. Losses from both sources are found to be small.

### Nomenclature

#### Latin Symbols

$a$	speed of sound
$c$	blade axial chord
$c_p$	specific heat at constant pressure
$h_t$	total specific enthalpy of a fluid
$k, k_r$ and $k_m$	wave number, reduced frequencies

$\bar{k}e$	average kinetic energy in a convected frame
$n$	coordinate normal to a blade surface
$p$	pressure
$s$	entropy, surface coordinate, surface length
$t$	time
$u/v$	velocity in the direction $x, \hat{x}$ , or $s / y, \hat{y}$ or $n$
$x, \hat{x}$	axial/streamwise coordinate, convected $x$ -coord.
$y, \hat{y}$	coordinate normal to $x, \hat{x}$

$I_i, I_r$	incident and reflected acoustic intensity
$\bar{M}, \bar{M}_\infty$	mean Mach numbers $(U/\bar{a}), (U_\infty/\bar{a}_\infty)$
$P, \hat{P}$	pitch, pitch in a convected frame ( $\hat{P} = P \cos \alpha$ )
$\Re(\ )$	real part of a quantity
$Re$	Reynolds number based on chord,
$Re_s, Re_\delta$	$Re$ based on surface length, momentum thickness
$\Delta S$	average nondimensional entropy rise
$U, U_s$	mean convection velocity, velocity at the b.l. edge
$V_R$	rotor speed

#### Greek Symbols

$\alpha$	angle between mean flow and axial direction
$\beta$	inter-blade phase angle, attenuation factor
$\hat{\beta}$	inter-wake phase angle in convected frame
$\gamma$	ratio of specific heat, vortex street strength
$\bar{\delta}, \delta_f$	steady and unsteady boundary layer thickness
$\delta_l$	laminar sublayer thickness in turbulent flow
$\mu, \nu, \kappa$	viscosity, kinematic viscosity, conductivity
$\pi_t$	total pressure ratio
$\epsilon$	smoothing coefficient
$\eta_s$	isentropic efficiency
$\rho$	density
$\sigma, \tau$	normal stress, shear stress
$\phi$	perturbation potential
$\theta$	angle between wave vector and surface normal
$\lambda_m, \lambda_f$	a reduced frequency $\lambda_m = \frac{1}{2} k_m \bar{c}$ , wavelength
$\omega, \omega_f$	angular frequency, blade passing frequency

$\Gamma$	circulation
$\Delta$	difference, grid spacing
$\Phi$	dissipation function

## Subscripts

$e$	at the boundary layer edge
$i$	integrated
$in$	steady uniform fluid state far-upstream
$mized$	mixed-out state far-downstream of the rotor
$out$	unsteady nonuniform state at the rotor outflow
$s$	isentropic
$w$	at the wall

$D, T$	design, turbine
$HFL$	high-frequency limit

$1, 2$	first/second-order (perturbation)
--------	-----------------------------------

## Superscripts

$\sim$	unsteady quantity
$\wedge$	complex amplitude
$-$	time-mean, time-mean and space-mean

## Introduction

Flow fields in turbomachinery are inherently unsteady. In a turbine, the first blade row will be subject to a nonuniform distribution of velocity and total temperature due to incomplete mixing in the combustion chamber. The relative motion of two adjacent blade rows, in conjunction with the spatially nonuniform pressure field locked to a loaded blade, leads to an unsteady pressure distribution through potential interaction. A blade row may move through and interact with the shock system originating at the trailing edges of the upstream blade row. Stator wake/rotor interaction causes unsteadiness in the rotor frame of reference because the rotor is moving through and chopping the wakes. Similarly, secondary flow effects like horse shoe vortices, passage vortices, and tip clearance vortices contribute to flow unsteadiness. The viscous flow past a blunt turbine trailing edge results in vortex shedding; trailing edge vortex shedding has also been found in compressors operating in the transonic or supersonic regime. Finally, there is unsteadiness induced by the motion of the blades themselves, i.e., blade flutter.

Nevertheless, the standard aerodynamic design tools for turbomachinery are steady state codes both inviscid and viscous, and steady cascade experiments. Designing a single stage or blade row with steady state tools amounts to placing the stator and rotor infinitely far apart thus eliminating the effects of blade row interaction and the interaction of convected disturbances with the downstream blade rows. Unsteadiness, however, contributes additional losses with nonzero time-mean. First, the energy associated with the unsteady part of the flow field is usually not recovered in the blade passage or in downstream blade rows; it will eventually be lost to viscous dissipation. Second, the interaction of the unsteadiness with boundary layers and shock structures can trigger additional dissipation (Hodson, 1983; Ng and Epstein, 1985). In a steady viscous simulation, the effects of unsteadiness and unsteady viscous dissipation on the efficiency are not captured. An unsteady nonlinear simulation is still prohibitively expensive for routine design purposes and will likely remain so for the foreseeable future, in particular for multi-stage turbomachinery. Furthermore, the weakest point of any numerical simulation, steady or unsteady, is the accurate prediction of losses and heat loads due to the unavailability of adequate turbulence and transition models. Testing of a stage or

a whole turbine under unsteady operating conditions, reproducing the whole range of unsteady effects, will remain impractical for routine design purposes.

One of the main impulses for this investigation was the development of the CFD-code UNSFLO by Giles (1987, 1990, 1991a) and the visualization package VISUAL2 by Giles and Haines (1991b), which provides a detailed picture of unsteady flow phenomena. Those include wake/blade row interaction, unsteady shock wave structures, unsteady boundary layers, unsteady heat transfer, and unsteady vortex shedding. There is a need to understand the physical nature of these phenomena, to quantify their effect on the time-mean efficiency of turbomachinery, and to examine the modeling accuracy of CFD-codes with respect to these phenomena.

An alternative to nonlinear unsteady simulations, which is receiving increased attention, are linear perturbation methods. A nonlinear steady state is found and the unsteady portion of the flow field superimposed upon it as a small perturbation. Second-order terms, i.e., terms quadratic in unsteady quantities, are neglected since the perturbations are assumed to be small. Linear perturbation codes have been found to give accurate results up to a surprisingly high level of unsteadiness (Hall and Crawley, 1987; Lindquist and Giles, 1991) and will be more widely used in the future. Linear codes, like steady codes, cannot capture unsteady losses. The time-mean of the first-order unsteady dissipation is zero; only terms second-order in unsteadiness have a nonzero time-mean dissipation.

The turbomachinery community is moving towards the consensus that increased losses under unsteady operating conditions are primarily due to nonlinear effects like the alteration of the boundary layer characteristics through their effect on transition (Hodson, 1983), the variation of secondary flow generation in downstream blade passages and their effect on separation or reattachment. Nevertheless, the magnitude of effects that can be treated in a linear framework, remains undetermined. While the corresponding unsteady losses are small by definition, their exact magnitude is of importance to the design process. Small changes in the aerodynamic performance figure significantly over the lifetime of an engine. In a turbine, for example, efficiencies often exceed 90% and improvements will be incremental.

This paper treats two aspects in a 2D, linearized framework. In the first part, it revisits the Unsteady Circulation Losses first examined by Keller (1935) and later by Kemp and Sears (1956). Keller estimated the unsteady circulation amplitude to arrive at the average kinetic energy in the unsteady part of the flow field induced by the vorticity shed at the trailing edge. Sears and Kemp used thin-airfoil theory to obtain the unsteady circulation amplitude. This approach, while enabling them to calculate the circulation amplitudes, limited them to incompressible flow, blades of zero thickness and camber with the mean flow nearly in the blade direction, i.e., lightly loaded blades. Thus, the airfoils are more representative of compressor blades than turbine blades. Furthermore, they had to specify the steady lift distribution on the blade. In this paper, the fluctuation amplitudes are the result of CFD-simulations, which allows one to obtain fluctuation amplitudes for arbitrary blade and stage geometries, steady lift distributions, and Mach numbers. Kelvin's circulation theorem, upon which Keller's work rests, is valid even in compressible homentropic flows. Eliminating the need to estimate the fluctuation amplitudes or to deduce them from

thin-airfoil theory, results in a more realistic measure for the secondary kinetic energy in modern turbomachines and the losses associated with its dissipation. The dissipated energy is related to the efficiency through a control volume argument and the linearization of the unsteady isentropic efficiency. Examples are given for several blade rows and stages.

The second part considers Unsteady Viscous Losses, that is, dissipation in unsteady boundary layers on the blade surfaces. Using linearization, Fourier-decomposition in time, and Lighthill's high-reduced-frequency limit, the momentum equation, driven by the harmonics of the pressure gradient obtained from a simulation, yields the local velocity distribution in the laminar sublayer. While a numerical simulation has difficulties in accurately predicting the losses, the pressure distribution is predicted accurately in attached flows. The second-order dissipation function with nonzero time-mean is calculated from the induced velocity distribution and the corresponding entropy increase integrated over the blade surface. The analysis can be regarded as a viscous complement to Johnson et al. (1988), who studied the surface heat transfer fluctuations in response to shock wave passing. The results of a numerical study to check the errors introduced by a departure from the high-frequency limit are discussed. The model is applied to a transonic turbine stage. Comparing the entropy rise due to unsteady viscous losses to the total entropy rise in the simulation, it is seen that unsteady viscous losses account only for a small part of the increased losses under unsteady operating conditions. A simple analytical model for the propagation of pressure waves in a CFD-simulation is used to show that the principal loci of unsteady dissipation in a simulation may not be in unsteady boundary layers as in real flows. Due to the action of numerical smoothing, dissipation within the blade passage can dominate.

## Unsteady Circulation Losses

### Theory

Figure 1 shows a cascade in which every blade is experiencing an unsteady circulation due to the presence of and interaction with the upstream blade row in an elementary stage. The derivation proceeds along the lines of Keller (1935). The coordinate system has been chosen such that the mean velocity  $\bar{U}$  far downstream is in the  $x$ -direction; the vortex sheet shed from the  $n$ th blade is located at  $y = n\hat{P}$ .  $P$  is the blade pitch,  $\hat{P}$  the rotated pitch defined as  $(P \cos \alpha)$ , and  $\alpha$  the angle between the direction of the convected vortex sheet and the axial direction.

The circulation of the  $n$ th blade is given by

$$\Gamma_n(t) = \bar{\Gamma} + \sum_m \Gamma_m \exp \{-i(\omega_m t - n\beta_m)\} \quad (1)$$

with  $\beta_m$  being the inter-blade phase angle for the  $m$ th mode. The frequencies  $\omega_m$  correspond to the blade passing frequency  $\omega_j$  and its harmonics. The real part of any physical quantity is implied by complex notation. The strength of the unsteady vortex sheet shed at the trailing edge is determined by the condition that the sum of bound and shed vorticity remain constant. This is a consequence of Kelvin's circulation theorem, which is valid for any compressible, inviscid, and barotropic fluid with conservative body forces acting on it. The strength of a vortex sheet

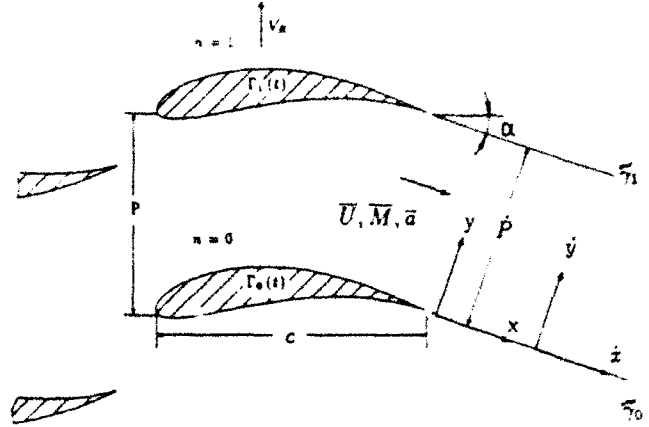


Figure 1: A cascade with unsteady lift and circulation

$\tilde{\gamma}_n(x, t)$  convected with the mean flow is related to the rate of change of the circulation by

$$\tilde{\gamma}_n(x, t) = -\frac{1}{\bar{U}} \frac{d}{dt} \left[ \Gamma_n \left( t - \frac{x - nP \sin \alpha}{\bar{U}} \right) \right] \quad (2)$$

With equation (1) and the convected coordinate  $\hat{x} = x - \bar{U}t$ , this can be expressed in the form

$$\tilde{\gamma}_n(\hat{x}) = i \sum_m k_m \frac{\Gamma_m}{c} \exp \left\{ i \left( k_m \frac{\hat{x}}{c} + n\beta_m \right) \right\} \quad (3)$$

in the convected coordinate system  $(\hat{x}, \hat{y})$ . The reduced frequency  $k_m = \omega_m c / \bar{U}$  is defined with the blade axial chord  $c$ ;  $\beta_m$  denotes the inter-wake phase angle of the  $m$ th mode. In the stationary frame, the linearized equation for the perturbation potential  $\tilde{\phi}$  describing the vortex sheet far downstream of the trailing edge, is

$$\nabla^2 \tilde{\phi} - \frac{1}{\bar{a}^2} \left( \frac{\partial}{\partial t} + \bar{U} \frac{\partial}{\partial x} \right)^2 \tilde{\phi} = 0, \quad (4)$$

where  $\bar{a}$  denotes the speed of sound. It does not describe perturbations convected through the blade row. The unsteady and convective contributions are eliminated by a shift to the convected frame of reference; all that remains is

$$\frac{\partial^2 \tilde{\phi}}{\partial \hat{x}^2} + \frac{\partial^2 \tilde{\phi}}{\partial \hat{y}^2} = 0. \quad (5)$$

In the convected frame, the perturbation potential satisfies the equation for steady irrotational flow. Due to the linear nature of equation (5), one temporal mode can be treated at a time. The periodicity condition for the  $m$ th mode is

$$\tilde{\phi}_m(\hat{x}, \hat{y} + \hat{P}) = \tilde{\phi}_m(\hat{x}, \hat{y}) \exp \{ i\beta_m \}. \quad (6)$$

The potential for  $0 \leq \hat{y} \leq \hat{P}$ , is of the form

$$\tilde{\phi}_m(\hat{x}, \hat{y}) = \left[ \hat{A}_m \cosh \left( k_m \frac{\hat{y}}{c} - \lambda_m \right) + \hat{B}_m \sinh \left( k_m \frac{\hat{y}}{c} - \lambda_m \right) \right] \exp \left\{ i \left( k_m \frac{\hat{x}}{c} + \frac{\beta_m}{2} \right) \right\} \quad (7)$$

where  $\lambda_m$  is defined by  $\lambda_m = \frac{1}{2} k_m \frac{\hat{P}}{c}$ . The values of the complex amplitudes  $\hat{A}_m$  and  $\hat{B}_m$  are determined from the matching

conditions at  $\dot{y} = 0$ . First, the jump in the streamwise velocity perturbation  $\tilde{u}_m$  at  $\dot{y} = n\dot{P}$  must equal the strength of the  $n$ th vortex sheet. Second, there must be no jump in the normal velocity perturbation  $\tilde{v}_m$  across it. Using the periodicity condition (6) to relate the velocities at  $(\dot{z}, 0^-)$  to those at  $(\dot{z}, \dot{P}^-)$ , the perturbation potential becomes

$$\tilde{\phi}_m = \frac{-\Gamma_m/2}{\sin^2 \frac{\dot{P}_m}{2} + \sinh^2 \lambda_m} \left[ i \cosh \lambda_m \sin \frac{\dot{\beta}_m}{2} \cosh \left( k_m \frac{\dot{y}}{c} - \lambda_m \right) + \sinh \lambda_m \cos \frac{\dot{\beta}_m}{2} \sinh \left( k_m \frac{\dot{y}}{c} - \lambda_m \right) \right] \exp \left\{ i \left( k_m \frac{\dot{z}}{c} + \frac{\dot{\beta}_m}{2} \right) \right\}. \quad (8)$$

## Efficiency Drop

The average kinetic energy per unit mass associated with the convected vortex sheet is

$$\begin{aligned} \bar{k}e_m &= \frac{1}{\dot{P}} \int_0^{\dot{P}} \frac{k_m}{2\pi c} \int_0^{\frac{2\pi}{k_m}} \frac{1}{2} \left[ \Re(\tilde{u}_m)^2 + \Re(\tilde{v}_m)^2 \right] d\dot{y} d\dot{z} \\ &= \frac{1}{4} \frac{\Gamma_m^2}{\dot{P}^2} \frac{\lambda_m \sinh \lambda_m \cosh \lambda_m}{\sin^2 \frac{\dot{P}_m}{2} + \sinh^2 \lambda_m}, \end{aligned} \quad (9)$$

which coincides with the result of Keller (1935).  $\Re$  denotes the real part of a complex quantity. Questions relating to cross-induced contributions in the kinetic energy from disturbances convected through the blade row, which were brought up by Kemp and Sears (1956), are addressed in Fritsch (1992). They will not be discussed here because they do not bear heavily on the conclusions drawn.

It is assumed that the kinetic energy associated with the unsteady vortex sheet cannot be recovered downstream. If this kinetic energy is lost to viscous dissipation in a constant area duct, the average entropy rise per unit mass for an ideal gas with constant specific heats  $\gamma$  is

$$\Delta \bar{S} = \frac{(\rho u s)_{mixed} - (\overline{\rho u s})}{c_p (\rho u)_{mixed}} = (\gamma - 1) \sum_m \frac{\bar{k}e_m}{\bar{a}^2}. \quad (10)$$

The subscript 'mixed' in equation (10) denotes the uniform state after mixing; the overbar implies a mass-average taken before the mixing process that dissipates the kinetic energy. Equation (10) holds regardless of the mean-flow Mach number  $\bar{M}$  and in the presence of unsteady waves other than vorticity waves, like pressure waves or entropy waves. The entropy rise associated with dissipation of the kinetic energy (9) is

$$\Delta \bar{S}_m = \frac{(\gamma - 1)}{4} \left( \frac{\Gamma_m}{\dot{P} \bar{a}} \right)^2 \frac{\lambda_m \sinh \lambda_m \cosh \lambda_m}{\sin^2 \frac{\dot{P}_m}{2} + \sinh^2 \lambda_m}. \quad (11)$$

In spatially nonuniform unsteady flow, it is the mass-averages of total pressure and total temperature at inflow and outflow that are needed to determine the isentropic efficiency. As mixing occurs downstream of the rotor (or stator) exit, more losses are generated and the mixed-out uniform and steady state leads to a lower total pressure. If the energy associated with unsteadiness is not recovered then it is the appropriate state to use in the isentropic efficiency. The isentropic efficiency for unsteady nonuniform flow in an elementary turbine stage with adiabatic blades is

$$\eta_{s,T} = \frac{(\rho u h_t)_{in} - \int_0^1 (\rho u h_t)_{out} d\left(\frac{y}{\dot{P}}\right)}{(\rho u h_t)_{in} - \int_0^1 (\rho u h_t)_{out,s} d\left(\frac{y}{\dot{P}}\right)}. \quad (12)$$

The subscript 'in' refers to a uniform and steady state far upstream of the stator while 'out,s' and 'out' refer to the unsteady spatially nonuniform rotor outflow in an (hypothetical) isentropic expansion and in the actual expansion, respectively. Linearization of (12), calculus of small variables, and definition of an isentropic 'design point efficiency' between the steady and uniform states 'in' and 'mixed',

$$\eta_{s,T,D} = \frac{(\rho u h_t)_{in} - (\rho u h_t)_{mixed}}{(\rho u h_t)_{in} - (\rho u)_{mixed} h_{t,in} \pi_{t,D}^{\frac{\gamma-1}{\gamma}}}, \quad (13)$$

lead to the result

$$\frac{\Delta \eta_{s,T}}{\eta_{s,T,D}} \approx - \frac{\pi_{t,D}^{\frac{\gamma-1}{\gamma}}}{1 - \pi_{t,D}^{\frac{\gamma-1}{\gamma}}} \Delta \bar{S}. \quad (14)$$

The 'design total pressure' ratio  $\pi_{t,D}$  is defined as  $(p_{t,mixed}/p_{t,in})$ . Equation (14), in conjunction with (11), tells how much of the departure of the isentropic efficiency from unity can be ascribed to the dissipation of unsteady vorticity downstream of the rotor outflow. An analogous result can be derived for a compressor stage. Details of the derivation for both turbine stages and compressor stages are found in Fritsch (1992).

## Results - Unsteady Circulation Losses

The model described in the previous section was applied to a number of blade rows and stages. The amplitudes of the unsteady circulation were calculated with the CFD-code UNSFLO by Giles (Giles, 1987, 1990; Giles and Haines, 1991a). It uses an explicit Lax-Wendroff scheme to solve the unsteady compressible Euler equations in 2D on an unstructured grid composed of triangular and/or quadrilateral cells. Its quasi-3D capability accounts for a varying streamtube thickness; arbitrary pitch ratios are handled by a time-inclined computational domain. The simulations were run until the flow was periodic; then 50 instantaneous flow solutions equally spaced in time were stored, from which the circulation amplitudes have been determined.

### Single blade row simulations

This section combines the results of simulations for three different rotor blade rows with incoming wake disturbances modeled at the inflow boundary. The wake parameters were chosen from the experimental data for the respective stages; no effort was made to account for the viscous decay of the wakes in the experiment. Potential disturbances were also simulated, but their effect was found to be comparably small due to the Mach numbers and axial gaps in the corresponding experiments. The numerical implementation of wake models and potential disturbance models is treated in Giles (1988).

Hodson (1984b) conducted measurements of wake-generated unsteadiness in the rotor of a large-scale, low-speed, single-stage, air-driven turbine. The 51 rotor blades are separated from 36 stator blades by an axial gap of about one rotor axial chord. A corresponding inviscid simulation of the 2D wake/rotor interaction has been presented by the same author (Hodson, 1984a); the incoming wake was modeled after the experiment (Hodson, 1984b). The wake model in the simulation for this case, case

A of table 1, was identical to his and the maximum velocity defect and the wake width were chosen such as to replicate the maximum velocity deficit and the momentum deficit in the experiment.

Case B is a simulation of the flow through the rotor of a large-scale, axial-flow turbine model investigated experimentally by Joslyn et al. (1983). It is a one and one-half stage turbine model consisting of 22 first vanes, 28 first blades, and 28 second vanes, representing the first three blade rows of the high pressure turbine of a high-bypass-ratio aircraft turbine. The Reynolds number as well as the absolute and relative flow angles are typical for current high-pressure-turbine airfoils. The wake profile at the rotor inflow boundary was Gaussian (Giles, 1988). Wake width and maximum velocity defect were chosen to match the maximum velocity defect and the momentum defect measured at midspan downstream of the first vane.

Binder (1985) used the L2F-technique to measure the flow in a cold-air turbine. The stage has 20 stator blades, 31 rotor blades, and an axial gap of 113% rotor axial chord; it is a scaled version of the first stage of a helicopter gas turbine. The flow in the low-aspect ratio, high hub-to-tip ratio stage is weakly transonic and the experiments showed a wake with a velocity defect of 6.5% at midspan 50% rotor axial chord upstream of the rotor leading edge. Based on the measured velocity distribution at the rotor inlet plane, a sinusoidal wake model (Giles, 1988) with a maximum velocity defect of 6.5% in the stator frame was chosen for the simulation of the flow through the rotor (case C).

Parameter	Case A	Case B	Case C
inflow angle	2.1°	48.9°	46.7°
outflow angle $\alpha$	-66.8°	-65.5°	-62.0°
inflow Mach number	0.14	0.12	0.43
outflow Mach number	0.40	0.20	0.65
rotor speed $V_R$	0.31	0.11	0.58
reduced frequency $k_1$	3.45	2.92	4.25
wake velocity defect	4.6%	15%	6.5%
Wake width/stator pitch	30%	10%	— — —
circulation $\Gamma_1/\Gamma_0$	0.67%	0.57%	2.83%
entropy rise $\Delta S$	$1.7 \cdot 10^{-6}$	$1.2 \cdot 10^{-6}$	$3.6 \cdot 10^{-4}$
efficiency drop $\Delta \eta_{s,T}/\eta_{s,T,D}$	-0.04%	-0.11%	-0.24%

Table 1: Results for single blade row simulations

The results are summarized in table 1. Mach numbers and flow angles are mixed-out averages in the rotor frame. Unlisted higher harmonics of the circulation are a factor 10 or more smaller than the first harmonic.

#### Single stage simulations

Two inviscid simulations are presented here; one for a turbine stage and one for a compressor stage. In contrast to the previous three cases, the unsteadiness acting on the downstream blade row is not prescribed but the result of blade row interaction in the simulation. Viscous wakes and their subsequent interaction with the downstream blade row, some aspects of which could be modeled inviscidly, are not included.

The turbine case considered is a highly loaded transonic high-pressure turbine stage, often referred to as the ACE turbine stage, which was tested at MIT (Guenette et al., 1988). A 2D-

version of the rotor profile was investigated at Oxford University (Ashworth et al., 1985; Johnson et al., 1988). In the simulation, stator and rotor row are separated by an axial gap of 40% rotor axial chord and the rotor operates near the design inflow angle of 58°. The outflow of rotor and stator row are supersonic, producing weak oblique shocks at the trailing edges. A detailed computational account of the inviscid stator/rotor interaction for almost identical input parameters was presented by Giles (1990). The oblique shock wave originating at the nozzle guide vane trailing edge first hits the downstream rotor around the crown of the suction surface and is reflected from there. Subsequently, it moves forward to the leading edge with the reflected portion impinging on the pressure surface of the adjacent blade and being reflected to the suction surface once more. Upon lifting off the rotor blade, the primary shock wave grows in length until the relative motion of the blade rows causes it to strike the next rotor blade. In the mean time its reflection off the rotor leading edge has impinged on and reflected from the nozzle guide vane suction side. Comparatively large unsteady amplitudes for this strong interaction are expected and have been reported for this turbine stage (Giles, 1990). The increased importance of higher harmonics is a consequence of the discontinuous nature of the shock waves.

Parameter	ACE	Stage 67
stator inflow angle	0°	-44.7°
stator outflow angle	73.5°	3.5°
rotor inflow angle	56.7°	59.9°
rotor outflow Angle	-67.6°	39.7°
stator inflow Mach number	0.14	0.67
stator outflow Mach number	1.13	0.46
rotor inflow Mach number	0.59	1.11
rotor outflow Mach number	1.16	0.62
rotor speed $V_R$	0.55	0.83
reduced Frequency $k_1$	2.38 (rotor)	21.5 (stator)
circulation $\Gamma_1/\Gamma_0$	2.19%	0.90%
$\Gamma_2/\Gamma_0$	1.02%	0.80%
$\Gamma_3/\Gamma_0$	0.20%	0.49%
$\Gamma_4/\Gamma_0$	0.25%	0.14%
entropy rise $\sum_m \Delta S_m$	$1.1 \cdot 10^{-3}$	$4.0 \cdot 10^{-4}$
efficiency drop $\Delta \eta_s/\eta_{s,D}$	-0.30%	-0.03%

Table 2: Results for single stage simulations

The compressor stage is known as NASA stage 67. It is a low-aspect ratio, single-stage, transonic, axial-flow compressor designed and experimentally investigated at the NASA Lewis Research Center (Hathaway et al., 1987). The stage consists of 22 rotor blades separated from 34 stator blades by an axial gap of 78% rotor axial chord. At a rotor tip Mach number of 1.38, strong shocks are present in the rotor passage. Shang (1989) used UNSFLO to calculate the flow through the stage at midspan with the input parameters inferred from the experiments at NASA Lewis. The case considered here is a full stage with purely potential interaction between the blade rows. The magnitude of the potential interaction strongly depends on the size of the axial gap separating the blade rows. A wide range of gap sizes exists in compressors and the gap itself varies hub to tip. For the case presented here, the gap was 10% of the rotor axial chord. The shock position is roughly 30% rotor axial chord downstream of the rotor leading edge and there is no significant

interaction between the shock system and the downstream stator blade row. As a consequence, the unsteady circulation and the losses are significantly smaller than for the ACE turbine stage.

### Summary

The magnitude of the unsteady circulation amplitude, estimated at 5% of the mean by Keller (1935), typically was of the order of 1% with larger values reserved for highly loaded blade rows with high turning. In their incompressible considerations within the limits of thin-airfoil theory, Kemp and Sears (1956) had concluded that the amplitude fluctuations are, generally, substantially smaller than 5%. The values found here suggest that 5% can be considered an upper bound for the unsteady circulation amplitude.

The amount of kinetic energy associated with the shed vorticity, which is proportional to the square of the unsteady circulation amplitude, is small. Keller (1935) deduced a magnitude of 0.4 to 1% of the power consumed or delivered by the rotor for circulation amplitudes of 5%. The values reported in this paper are smaller with a maximum efficiency drop of 0.3% for the ACE turbine stage which shows a strong shock wave/blade row interaction. The effect of incoming wake disturbances can be of the same order of magnitude.

Potential interaction was found to be of minor significance for the cases considered.

## Unsteady Viscous Losses

### Conceptual Model

Unsteady viscous losses are losses with a nonzero time-mean due to viscous dissipation of energy associated with or induced by the unsteady part of the flow field, primarily on the blade surfaces.

The unsteady velocity distribution induced by a wall oscillating harmonically with frequency  $\omega_f$  in a fluid at rest, Stokes' second problem, is shown in figure 2. On the left, the velocity distribution seen in a stationary frame of reference has been sketched for two particular instants during a period. The length scale characterizing the extent to which unsteady viscous effects spread away from the wall during a period is  $\delta_f = \sqrt{\nu/\omega_f}$ . On the right, the unsteady velocity distribution is shown in a frame of reference fixed to the wall. The same velocity distribution as on the right is obtained with a harmonically varying static pressure gradient, if the characteristic length of the pressure disturbance is much larger than the thickness of the unsteady boundary layer it induces.

On a turbomachinery blade, figure 3, both a steady and an unsteady boundary layer are present together with a mean flow pressure gradient. The pressure disturbance can be a pressure wave, the potential field of another blade row, or a weak shock wave. Far from the wall, the unsteady velocity distribution in the boundary layer, driven by the harmonically varying pressure gradient, differs from the one in Stokes' second problem. It is influenced by a nonzero, transitional or turbulent, mean flow and compressibility effects. In the immediate neighborhood of the wall, where the unsteady dissipation is concentrated, the

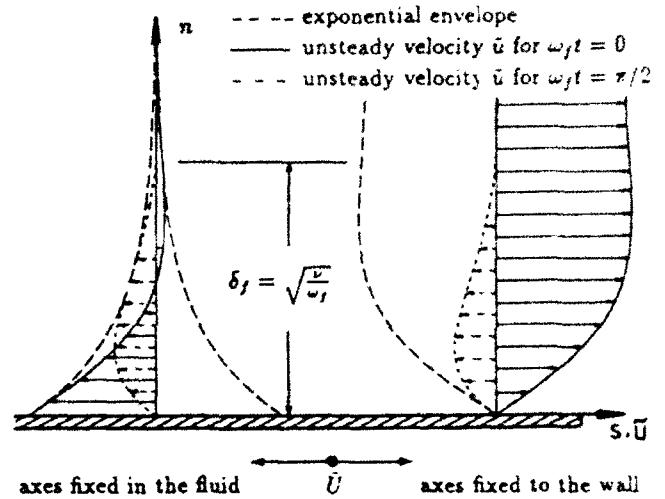


Figure 2: Unsteady boundary layer on an oscillating wall

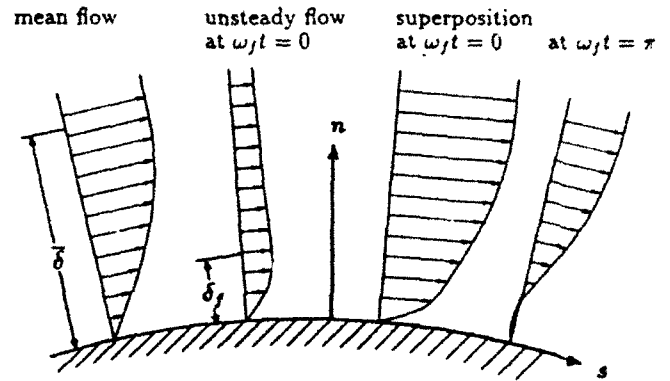


Figure 3: Unsteady boundary layer on a blade

pressure disturbance still induces a velocity distribution as found in Stokes' second problem for sufficiently high reduced frequency.

The energy associated with the unsteady flow field is dissipated either in the free stream or in unsteady boundary layers at the blades, the hub and the tip. To compare the relative importance of the two dissipation loci in laminar flow, the following order-of-magnitude argument is instructive. In the free stream the velocity gradient is set by the magnitude of the unsteady velocity  $\tilde{u}_e$ , and the characteristic length  $l_f$ , of the disturbance.

$$|\nabla \tilde{u}| \sim \frac{|\tilde{u}_e|}{l_f} \quad (15)$$

For a pressure wave traveling in or against the free stream direction, the characteristic length  $l_f$  becomes the wavelength  $\lambda_f$ .

$$\frac{\lambda_f}{c} = \frac{2\pi}{k_e} \frac{(1 \pm \overline{M}_e)}{\overline{M}_e} \quad (16)$$

The reduced frequency is defined in terms of the blade passing frequency  $\omega_f$ , the local mean velocity in the free stream (at the boundary layer edge)  $\overline{U}_e$ , and the axial chord  $c$  as  $k_e = \omega_f c / \overline{U}_e$ . At the wall, the pressure wave gives rise to an unsteady boundary layer with a thickness characterized by  $\delta_f$  and a velocity gradient of order

$$\left| \frac{\partial \tilde{u}}{\partial n} \right| \sim \frac{|\tilde{u}_e|}{\delta_f} \quad (17)$$

The local average rate of unsteady viscous dissipation is proportional to the square of the velocity gradient. The extent of the free stream, characterized by the axial chord, is much larger than the unsteady boundary layer thickness. To obtain the integrated effect of dissipation in the free stream and the unsteady boundary layer, these different scales have to be accounted for. Dissipation in the free stream is negligible if

$$\left(\frac{\delta_f}{l_f}\right)^2 \left(\frac{c}{\delta_f}\right) \ll 1. \quad (18)$$

With the definition of  $\delta_f$  and equation (16), (18) is rewritten as

$$\frac{1}{4\pi^2} k_e \sqrt{\frac{k_e}{Re}} \frac{M_e^2}{(1 \pm M_e)^2} \ll 1, \quad (19)$$

where the Reynolds number is defined in terms of mean free stream quantities as  $Re = \bar{\rho}_e \bar{U}_e c / \bar{\mu}_e$ . For the Reynolds numbers encountered in turbomachinery, this inequality is always satisfied and dissipation in unsteady boundary layers dominates over dissipation in the free stream. Unless the level of the turbulent viscosity in the freestream far exceeds the one characterizing the boundary layer, inequality (19) also holds in turbulent flow.

### Theory - Unsteady Viscous Losses

The initial step in the analytical approach is to linearize the governing viscous equations around their time-mean. Taking the first-order perturbation equations to their asymptotic high-frequency limit, the momentum equation yields the unsteady streamwise velocity distribution. From the unsteady velocities in the boundary layer, the time-mean of the dominating term in the second-order unsteady dissipation function  $\bar{\Phi}_2$  can be calculated and related to a change in the time-mean isentropic efficiency.

The problem is described in a Cartesian coordinate system  $(s, n)$  where the coordinate  $n$  is aligned with the local surface normal. The governing equations are the continuity equation, the streamwise momentum equation in conjunction with the stress-strain relations,

$$\frac{\partial u}{\partial t} + u \frac{\partial u}{\partial s} + v \frac{\partial u}{\partial n} = \frac{1}{\rho} \left( -\frac{\partial p}{\partial s} + \frac{\partial \sigma_{ss}}{\partial s} + \frac{\partial \tau_{sn}}{\partial n} \right), \quad (20)$$

$$\sigma_{ss} = \frac{2}{3} \mu \left( 2 \frac{\partial u}{\partial s} - \frac{\partial v}{\partial n} \right), \quad \tau_{sn} = \mu \left( \frac{\partial u}{\partial n} + \frac{\partial v}{\partial s} \right), \quad (21)$$

the energy equation in conjunction with the definition of the dissipation function  $\Phi$ ,

$$\rho c_p \left( \frac{\partial T}{\partial t} + u \frac{\partial T}{\partial s} + v \frac{\partial T}{\partial n} \right) = \frac{\partial p}{\partial t} + u \frac{\partial p}{\partial s} + v \frac{\partial p}{\partial n} + \frac{\partial}{\partial s} \left( \kappa \frac{\partial T}{\partial s} \right) + \frac{\partial}{\partial n} \left( \kappa \frac{\partial T}{\partial n} \right) + \Phi, \quad (22)$$

$$\Phi = \mu \left[ 2 \left( \frac{\partial u}{\partial s} \right)^2 + 2 \left( \frac{\partial v}{\partial n} \right)^2 + \left( \frac{\partial v}{\partial s} + \frac{\partial u}{\partial n} \right)^2 - \frac{2}{3} \left( \frac{\partial u}{\partial s} + \frac{\partial v}{\partial n} \right)^2 \right], \quad (23)$$

and the equation of state. Due to the boundary layer character of the problem, the normal momentum equation is replaced by the assumption  $(\partial p / \partial n = 0)$ .

Linearizing the kinematic and the thermodynamic variables around their time-mean (and nondimensionalizing them by the local mean velocity and density in the free stream, the blade passing frequency, and the blade axial chord), the first-order perturbation equations of the streamwise momentum equation and the stress-strain relations take the form

$$k_e \frac{\partial \bar{u}}{\partial t} + \bar{u} \frac{\partial \bar{u}}{\partial s} + \bar{u} \frac{\partial \bar{u}}{\partial s} + \bar{v} \frac{\partial \bar{u}}{\partial n} + \bar{v} \frac{\partial \bar{u}}{\partial n} = -\frac{1}{\bar{\rho}} \frac{\partial \bar{p}}{\partial s} + \frac{1}{\bar{\rho}} \left( \frac{\partial \bar{\sigma}_{ss}}{\partial s} + \frac{\partial \bar{\tau}_{sn}}{\partial n} \right) + \frac{\bar{p}}{\bar{\rho}^2} \frac{\partial \bar{p}}{\partial s} - \frac{\bar{p}}{\bar{\rho}^2} \left( \frac{\partial \bar{\sigma}_{ss}}{\partial s} + \frac{\partial \bar{\tau}_{sn}}{\partial n} \right), \quad (24)$$

$$\bar{\sigma}_{ss} = \frac{2}{3} \frac{1}{Re} \left( 2 \frac{\partial \bar{u}}{\partial s} - \frac{\partial \bar{v}}{\partial n} \right), \quad \bar{\tau}_{sn} = \frac{1}{Re} \left( \frac{\partial \bar{u}}{\partial n} + \frac{\partial \bar{v}}{\partial s} \right). \quad (25)$$

The laminar viscosity  $\mu$  has been assumed constant. The second-order unsteady dissipation function  $\bar{\Phi}_2$  which, unlike its first-order counterpart, has a nonzero time-mean, is

$$\bar{\Phi}_2 = \frac{1}{Re} \left[ 2 \left( \frac{\partial \bar{u}}{\partial s} \right)^2 + 2 \left( \frac{\partial \bar{v}}{\partial n} \right)^2 + \left( \frac{\partial \bar{v}}{\partial s} + \frac{\partial \bar{u}}{\partial n} \right)^2 - \frac{2}{3} \left( \frac{\partial \bar{u}}{\partial s} + \frac{\partial \bar{v}}{\partial n} \right)^2 \right]. \quad (26)$$

The high-frequency limit is characterized by a reduced frequency

$$k_e \gg 1. \quad (27)$$

As a consequence,

$$\delta_f / \bar{\delta} \ll 1, \quad (28)$$

$$\lambda_f / c \ll 1, \quad (29)$$

$$\text{and } \delta_f / \lambda_f \ll 1 \quad (30)$$

hold in the high-frequency limit. Inequality (28) implies that normal derivatives of unsteady quantities dominate over normal derivatives of steady quantities, because the unsteady boundary layer thickness is much less than the thickness of its steady counterpart. Inequality (29) allows one to neglect streamwise mean flow derivatives because the wavelength of the disturbance is much less than the axial chord which characterizes mean flow gradients. In other words, parallel mean flow is assumed and the streamwise evolution of the steady boundary layer is neglected. Inequality (30) implies that the wavelength of the disturbance is far greater than the unsteady boundary layer thickness. It allows for the neglect of unsteady streamwise derivatives in the presence of unsteady normal derivatives; it always holds for the large Reynolds numbers found in turbomachinery.

Taking the momentum equation (24) and the stress-strain relations (25) to their asymptotic high-frequency limits, the following terms drop out:

$$k_e \frac{\partial \bar{u}}{\partial t} + \bar{u} \frac{\partial \bar{u}}{\partial s} + \bar{u} \frac{\partial \bar{u}}{\partial s} + \bar{v} \frac{\partial \bar{u}}{\partial n} + \bar{v} \frac{\partial \bar{u}}{\partial n} = -\frac{1}{\bar{\rho}} \frac{\partial \bar{p}}{\partial s} + \frac{1}{\bar{\rho}} \left( \frac{\partial \bar{\sigma}_{ss}}{\partial s} + \frac{\partial \bar{\tau}_{sn}}{\partial n} \right) + \frac{\bar{p}}{\bar{\rho}^2} \frac{\partial \bar{p}}{\partial s} - \frac{\bar{p}}{\bar{\rho}^2} \left( \frac{\partial \bar{\sigma}_{ss}}{\partial s} + \frac{\partial \bar{\tau}_{sn}}{\partial n} \right) \quad (27)$$

$$+ \frac{1}{\bar{\rho}} \left( \frac{\partial \bar{\sigma}_{ss}}{\partial s} + \frac{\partial \bar{\tau}_{sn}}{\partial n} \right) + \frac{\bar{p}}{\bar{\rho}^2} \frac{\partial \bar{p}}{\partial s} - \frac{\bar{p}}{\bar{\rho}^2} \left( \frac{\partial \bar{\sigma}_{ss}}{\partial s} + \frac{\partial \bar{\tau}_{sn}}{\partial n} \right) \quad (29) \quad (28)$$

$$\bar{\tau}_{sn} = \frac{1}{Re} \left( \frac{\partial \bar{u}}{\partial n} + \frac{\partial \bar{v}}{\partial s} \right) \quad (30)$$

Numbers above the arrows refer to inequalities (27) to (30) and give the rationale for the neglect of individual terms. Inequality (27) leaves the unsteady term dominant on the left-hand side of the momentum equation. On the right-hand side, the driving unsteady pressure term and the unsteady shear term remain. Substituting the stress-strain relation into the high-frequency limit of the momentum equation, the velocity distribution near the wall is described by the differential equation

$$k_s \frac{\partial \tilde{u}}{\partial t} - \frac{1}{Re} \frac{1}{\bar{\rho}_w} \frac{\partial^2 \tilde{u}}{\partial n^2} = -\frac{1}{\bar{\rho}_w} \frac{\partial \tilde{p}}{\partial s} \quad (31)$$

Since (31) is a linear constant-coefficient equation, any disturbance can be decomposed into its temporal Fourier-modes. For the  $m$ th mode, the solution near the wall is

$$\tilde{u}_m = \frac{-i}{mk_s \bar{\rho}_w} \left( 1 - \exp \left\{ (i-1) \sqrt{\frac{m}{2}} \frac{n}{\delta_f} \right\} \right) \frac{\partial \tilde{p}_m}{\partial s} \exp \{-imt\} \quad (32)$$

where  $\tilde{p}_m$  denotes the complex magnitude of the  $m$ -th harmonic of the pressure disturbance. Figure 4 compares this solution to the exact solution for an upstream propagating pressure wave over a flat plate with a laminar boundary layer. In the Stokes

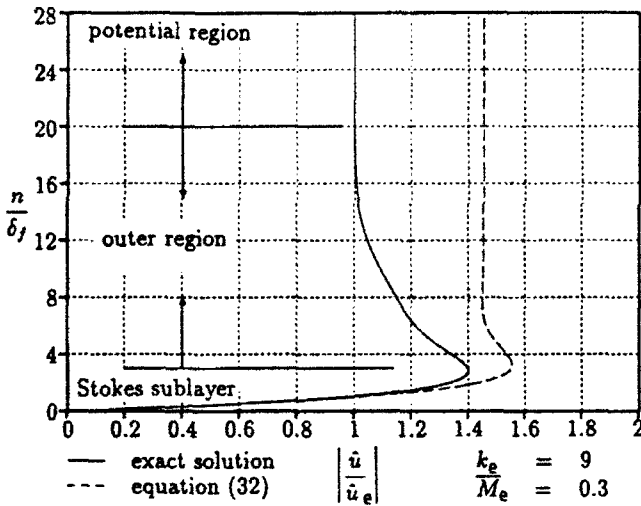


Figure 4: Unsteady velocity distribution as a function of  $(n/\delta_f)$

sublayer near the wall, the velocity distribution is well represented by equation (32). The agreement increases with the ratio  $\delta/\delta_f$  (which is proportional to  $\sqrt{k_s}$  for a laminar flat plate boundary layer). It decreases with the Mach number because (32) assumes negligible mean flow at the edge of the unsteady boundary layer and incompressible flow. Due to the neglect of free stream convection it asymptotes to the wrong velocity magnitude in the free stream.

The dominating term of the unsteady dissipation function  $\tilde{\Phi}_2$  in the asymptotic high-frequency limit is obtained from (26) with inequalities (28) to (30). Taking its time-mean gives

$$\begin{aligned} \bar{\Phi}_2 &\approx \frac{1}{Re} \int_0^1 \left[ \sum_{m_1} \Re \left( \frac{\partial \tilde{u}_{m_1}}{\partial n} \right) \right] \left[ \sum_{m_2} \Re \left( \frac{\partial \tilde{u}_{m_2}}{\partial n} \right) \right] dt = \\ &= \frac{1}{Re} \int_0^1 \sum_m \left[ \Re \left( \frac{\partial \tilde{u}_m}{\partial n} \right) \right]^2 dt \quad (33) \end{aligned}$$

due to the orthogonality of sines and cosines. The time-mean of the unsteady dissipation is calculated mode by mode and summed subsequently. For the  $m$ -th mode, the dissipation per unit volume is

$$\bar{\Phi}_{2,m} = \frac{1}{2mk_s \bar{\rho}_w} \left| \frac{\partial \tilde{p}_m}{\partial s} \right|^2 \exp \left\{ -\sqrt{2m} \frac{n}{\delta_f} \right\} \quad (34)$$

The dissipation is largest in the region of steep gradients near the wall where the agreement between high-frequency limit and exact solution is best. Therefore, equation (34) is integrated from the wall into the free stream to obtain the dissipation per unit surface area.

$$\bar{\Phi}_{2,m} = \frac{1}{2mk_s \bar{\rho}_w} \sqrt{\frac{1}{2mk_s \bar{\rho}_w Re}} \left| \frac{\partial \tilde{p}_m}{\partial s} \right|^2 \quad (35)$$

The difference in the integrated dissipation  $\bar{\Phi}_2$ , between the exact solution and the high-frequency-limit solution of figure 4 is about 10% of the exact solution. The effects of turbulent boundary layers, mean flow pressure gradients, and mean flow Mach number are addressed later.

Unlike in the Unsteady Circulation Losses, the energy is not dissipated downstream of the last blade row but in the blade passage. The mean flow state along the blade varies and the entropy rise per unit dissipated energy is not constant. Integration around the blade surface and division by the mass flux  $\dot{m}$  yield the average specific entropy rise in the blade passage due to unsteady viscous dissipation. In dimensional quantities it is

$$\Delta \bar{S} = \frac{(\gamma-1)}{\dot{m}} \sum_m \int \frac{d\bar{\Phi}_{2,m}}{a_w^2} \quad (36)$$

The average specific entropy rise is again related to an efficiency drop, as in equation (14).

## Results - Unsteady Viscous Losses

The model has been applied to the ACE-turbine stage described in the results section of the Unsteady Circulation Losses. The input required for the model is the time harmonics of the local pressure gradient along the blade surfaces. Those can be the result of a viscous or an inviscid unsteady simulation. The dominating unsteady effect of rotor blade row/shock wave interaction is captured in an inviscid simulation. The parameters of the simulation were similar to the ones used before except that UNSFLO was run in the viscous mode (Giles and Haines, 1991a), the rotor speed was increased, and the back pressure was lowered slightly. This resulted in stronger stator trailing edge shock waves and reduced the mean rotor incidence angle to 48°, matching the experiments of Johnson et al. (1988). In experiments (Ashworth et al., 1985), the rotor boundary layer was laminar over most of the suction surface for low levels of free stream turbulence and in the absence of wakes and shock waves. The pressure surface boundary layer was transitional. Bar passing experiments to simulate the stator wakes and shock waves showed that widely spaced wakes and shock waves temporarily trip the boundary layer, which will relax back to a laminar state after the disturbance has passed. For a bar spacing resembling engine conditions, the boundary layer is transitional or turbulent. In the simulation, the flow was prescribed turbulent from the leading edge on.



Figure 5 shows the specific entropy rise due to unsteady viscous dissipation on a rotor blade surface. A value of  $s=0$  corresponds to the rotor leading edge; positive and negative values correspond to pressure and suction surface, respectively. The losses are concentrated on the suction surface between rotor leading edge and crown, where the pressure gradient fluctuates in response to shock wave passing. The integrated entropy rise for a rotor blade is  $\Delta \bar{S} = 2.8 \cdot 10^{-4}$ ; this translates into an efficiency drop of  $\Delta \eta_{s,T}/\eta_{s,T,D} = -0.09\%$ . These numbers are subject to errors examined in the following section. Of the total, 64% is at blade passing frequency and 14% in the first harmonic.

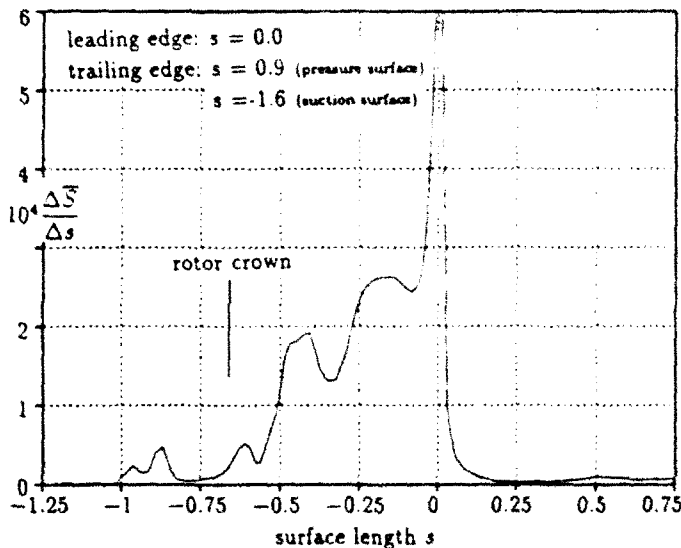


Figure 5: Entropy rise per unit surface length

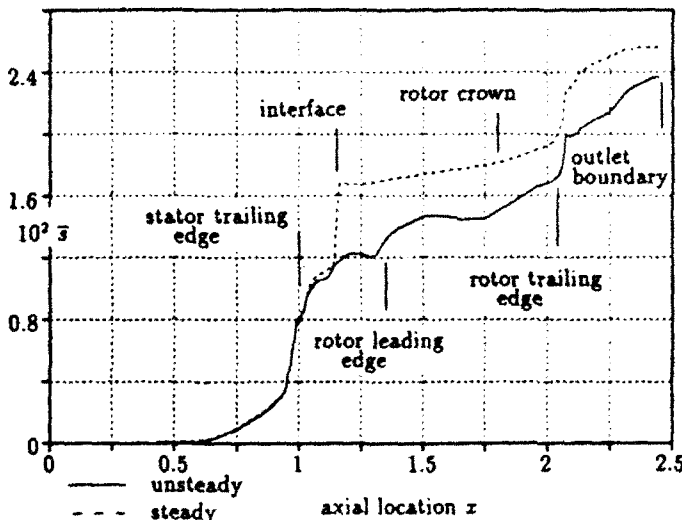


Figure 6: Entropy rise in the steady and the unsteady simulation

Figure 6 shows the time-mean mass-averaged entropy rise through the turbine stage in the simulations. The axial coordinate  $x$  is nondimensionalized by the stator axial chord; the stator leading edge is located at  $x=0$ . Three observations can be made. First, the steady simulation, in which case the conservation variables are averaged at the interface, has a higher

entropy rise through the stage than the unsteady simulation. In the steady case, the fluxes of mass, momentum and energy are averaged at the stator outflow boundary to provide uniform and steady rotor inflow conditions. The (nonphysical) entropy rise at the interface, accounts for about 20% of the total. As a consequence, the isentropic stage efficiency is 0.4% less in the steady simulation. Since the unsteadiness does not propagate beyond the steady interface, the entropy rises much slower in the rotor passage than in the unsteady simulation. Second, the entropy rise between rotor leading edge and crown, the region where the unsteady losses are concentrated, is about  $10^{-3}$  for the steady case and  $3 \cdot 10^{-3}$  for the unsteady case. The difference is much larger than the entropy rise that has been ascribed to unsteady viscous losses. Third, the entropy rise between crown and trailing edge as well as between trailing edge and outlet boundary is significantly in the unsteady simulation. Baring turbulence modeling in the boundary layer as a reason for the steeper rise, numerical smoothing acting on the unsteadiness in the blade passage remains as the only explanation.

## Modeling Accuracy

### Loss model

The derivation of the unsteady viscous losses involved four approximations, each of which introduced errors. The first two, the boundary layer approximation and the linearization thereof, will not be examined. The errors introduced in the last two steps, the invocation of the high-frequency limit and the assumption of laminar flow, dominate.

In laminar flow, the two main effects not modeled in the high-frequency limit are the compression of the boundary layer and the free stream convection. Even larger errors are due to the presence of a turbulent mean flow. To estimate the errors, a 1D code was written to solve the linearized equations for a flat plate boundary layer, figure 7, subject to a pressure wave propagating at an arbitrary nonzero angle  $\theta$  relative to the surface normal. The parallel flow assumption was retained because the evolu-

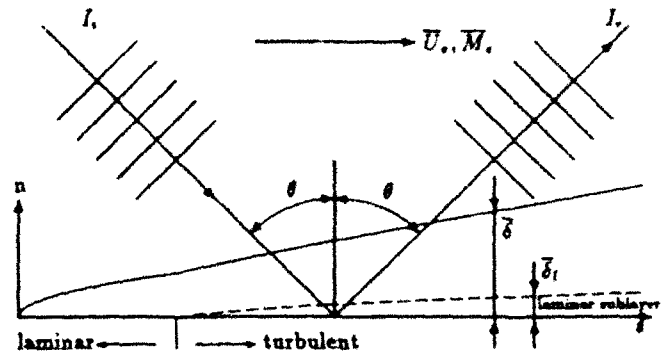


Figure 7: Model problem for numerical error evaluation

tion of the mean flow boundary layer takes place over a length scale much larger than the steady or the unsteady boundary layer thickness. This assumption combined with a small steady and unsteady boundary layer thickness (compared to the wavelength), reduces the problem to one dimension. The boundary was modeled as an adiabatic wall.

All mean velocity profiles were taken to be identical to the corresponding profiles in steady flow. Only very large disturbance amplitudes (and frequencies close to the turbulent bursting frequency) lead the mean flow profiles to deviate from the corresponding profiles in steady flow (Karlsson, 1959; Parikh et al., 1982). In laminar flow, the velocity profiles were obtained as the solution of the Falkner-Skan equations. In turbulent flow, a three layer model with the inner law in Spalding's formulation (Spalding, 1961) and a law of the wake in Coles' formulation (Coles, 1956) was used. Both the laminar and the turbulent velocity profile are strictly valid for incompressible flow only, but were used regardless of the free stream Mach number. The mean temperature and density profiles were obtained from the velocity profiles with the assumption of a unit Prandtl number.

The laminar part of the code was verified by comparison to Lighthill's analytical work (1954) on oscillatory boundary layers in an incompressible mean flow. The turbulent part was first checked against the laminar solution for very high frequencies and then against experiments by Cousteix et al. (1977).

The numerical error evaluation is summarized in figures 8 to 10. Figure 8 assumes laminar mean flow and pressure waves propagating parallel to the boundary. It shows the ratio of the

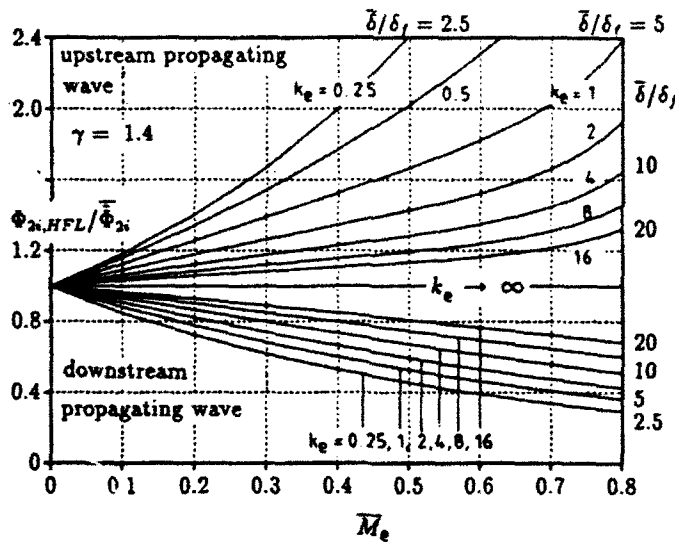


Figure 8: High-frequency-limit dissipation and full linearized laminar model dissipation

integrated dissipation  $\bar{\Phi}_{2i}$  calculated in the high-frequency limit (HFL) to the one calculated with the full linearized equations. In the limit ( $M_e \rightarrow 0$ ) or ( $k_e \rightarrow \infty$ ), the HFL model gives the correct dissipation. The lower the reduced frequency for a nonzero free stream Mach number, the greater the deviation. This is a consequence of the unsteady boundary layer spreading away from the wall into the steady boundary layer where convective terms in (24) become important. Depending on the direction of propagation, the HFL yields an integrated dissipation greater or less than the full linearized model.

The flows in turbomachinery are almost always transitional or turbulent and the unsteady boundary layer extends beyond the laminar sublayer. In figures 9 and 10 errors due to the assumption of laminar mean flow in the HFL model appear superimposed on errors due to finite reduced frequencies. They show

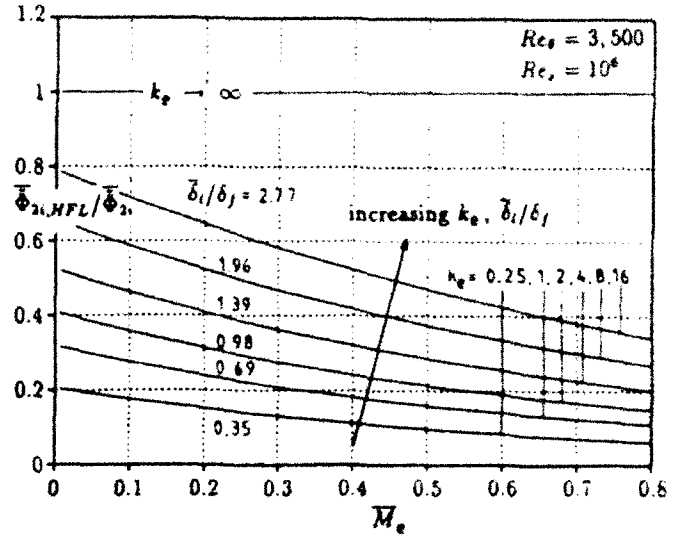


Figure 9: High-frequency limit dissipation and full turbulent model dissipation - downstream propagating wave

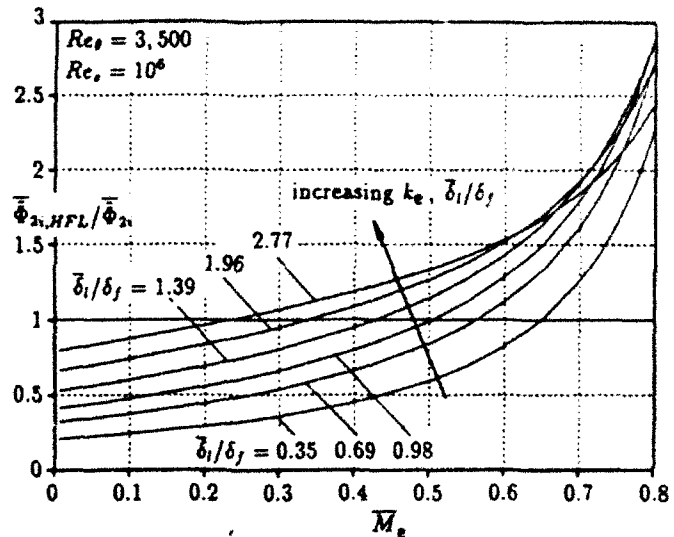


Figure 10: High-frequency limit dissipation and full turbulent model dissipation - upstream propagating wave

the ratio of the integrated dissipation calculated in the HFL to the full turbulent dissipation for a Reynolds number  $Re_\tau = 10^6$ . As opposed to the case in laminar flow, the HFL is not exact in the limit ( $M_e \rightarrow 0$ ). This is because the turbulent nature of the mean flow introduces additional errors into the HFL model which is an inherently laminar model. For high reduced frequencies, the turbulent dissipation again approaches the value of the HFL model although this is not evident within the range of reduced frequencies displayed. The parameter ( $\delta_i/\delta_f$ ) is the ratio of the thickness of the laminar sublayer of the mean flow, defined as  $30y^+$  in wall coordinates, to the thickness of the unsteady boundary layer. For frequencies such that ( $\delta_i/\delta_f$ )  $\gg 1$ , the unsteady boundary layer is confined to the laminar sublayer and the HFL model gives accurate results.

The ratio ( $\bar{\Phi}_{2i,HFL}/\bar{\Phi}_{2i}$ ) for a downstream propagating wave in turbulent flow behaves in a similar fashion to the corresponding ratio in laminar flow. With higher reduced frequency and

lower Mach number, the HFL is more accurate. The behavior of  $(\bar{\Phi}_{21,HFL}/\bar{\Phi}_{21})$  for an upstream propagating wave, however, differs significantly from the behavior in laminar flow. In the limit  $(M_\infty \rightarrow 0)$ , the ratio is less than unity and matches the value for a downstream propagating wave. The laminar HFL model underpredicts the velocity gradients (and uses the laminar viscosity) and thus arrives at too low an integrated dissipation for finite reduced frequencies (or  $\bar{\delta}_1/\delta_f$ ). As the Mach number increases, this ratio rises above unity because the HFL overpredicts the unsteady velocity magnitude in the free stream; it is the relative magnitude of these two effects that governs the behavior of  $(\bar{\Phi}_{21,HFL}/\bar{\Phi}_{21})$  in figure 10.

The flow through the rotor of the ACE stage is turbulent and there is a strong favorable mean pressure gradient in the region of unsteady viscous losses. Calculating the laminar sublayer thickness from the wall shear of the simulation, gives a ratio  $\bar{\delta}_1/\delta_f \approx 1.2$ . The free stream Mach number in the rotor frame is  $(M_\infty \approx 0.65)$  in the main region of unsteady viscous losses. Therefore, figures 9 and 10 suggest that the unsteady viscous losses calculated for the ACE turbine stage ( $\Delta\eta_{s,T}/\eta_{s,T,D} = 0.09\%$ ) are at most a factor 1.5 too large and could be up to five times larger.

### Numerical smoothing

Consider a pressure wave propagating through an unloaded flat plate cascade with uniform mean flow  $U_\infty$ . The incident pressure wave of figure 7, propagating at an angle  $\theta$  relative to the surface normal, is described by its wave amplitude

$$\bar{p} = \bar{p} \exp \{ i k (s \sin \theta - n \cos \theta) - i t \}. \quad (37)$$

where  $k$  denotes the wavenumber. Upon reflection at the blade surface, the wave will lose a small fraction  $\beta$  of its amplitude to dissipation in an unsteady boundary layer. The time-mean rate of energy dissipation per unit surface area is given by equation (35) with the pressure gradient determined from (37). The time-mean rate of acoustic energy incident on the wall is given by the acoustic intensity

$$\bar{I}_i \approx \frac{1}{2} |\bar{p}\bar{v}| \approx \frac{1}{2} |\bar{p}|^2 M_\infty \cos \theta. \quad (38)$$

The rate of acoustic energy reflected is

$$\bar{I}_r \approx \frac{1}{2} (1 - \beta)^2 |\bar{p}\bar{v}| \approx \frac{1}{2} (1 - \beta)^2 |\bar{p}|^2 M_\infty \cos \theta. \quad (39)$$

The above acoustic intensities, strictly valid only for  $M_\infty = 0$ , are used for simplicity. Since the objective is an order-of-magnitude argument, these simplification do not compromise the subsequent conclusions. The streamwise velocity distribution in the unsteady boundary layer induced by the incident and the reflected wave are nearly in phase because of inequality (30). The rate of unsteady viscous dissipation per unit surface area is

$$\bar{\Phi}_{21} = \frac{(2 - \beta)^2}{2k_\infty} \sqrt{\frac{1}{2k_\infty Re}} \left| \frac{\partial \bar{p}}{\partial s} \right|^2, \quad (40)$$

where incompressible mean flow was assumed. Balancing incoming intensity, reflected intensity, and unsteady dissipation gives an estimate for the attenuation factor  $\beta$  of

$$\beta_1 = M_\infty \sqrt{2k_\infty / Re} \tan \theta \sin \theta, \quad (41)$$

where the relation  $(k/k_\infty)^2 \approx M_\infty^2$ , valid in the limit  $(M_\infty \rightarrow 0)$ , has been used. Alternatively, (41) can be expressed as

$$\beta_1 = \sqrt{2(M_\infty / Re)} (2\pi/\lambda_f) \tan \theta \sin \theta. \quad (42)$$

The longest wave in a turbomachine typically has a nondimensional wavelength  $\lambda_f$  of order unity. Assuming Reynolds and Mach numbers typical of turbomachinery (and  $\tan \theta \sin \theta$  of order one),  $O(10^3)$  reflections should occur before the wave amplitude is halved. In an inviscid simulation of the flow through the ACE turbine stage no more than three reflections of weak shock waves/pressure waves are discernible. The approximations made in the derivation of the HFL model and in the above order-of-magnitude argument can not account for a difference of two orders of magnitude. This suggests that numerical smoothing in the free stream dominates over dissipation in unsteady boundary layers.

The propagation of a pressure wave in the uniform free stream can be modeled numerically by the convection-diffusion equation

$$\frac{\partial \bar{p}}{\partial t} + (1 \pm M_\infty \sin \theta) \frac{\partial \bar{p}}{\partial z} = \epsilon_2 \Delta \frac{\partial^2 \bar{p}}{\partial z^2} - \epsilon_4 \Delta^2 \frac{\partial^4 \bar{p}}{\partial z^4}, \quad (43)$$

where  $z$  is a coordinate in the direction of wave propagation;  $\Delta$  denotes the mesh spacing. The time  $t$  has been nondimensionalized by the axial chord and the speed of sound. Numerical smoothing, necessary to stabilize the code, has been added on the right-hand side. The time-rate of decay of a wave amplitude due to second-order smoothing for shock wave capturing is

$$\beta_2 \sim \epsilon_2 k^2 \Delta. \quad (44)$$

In smooth-flow regions, second-order smoothing is turned off. There, the time-rate of decay due to fourth-order smoothing is

$$\beta_4 \sim \epsilon_4 k^4 \Delta^2. \quad (45)$$

Assuming that a wave typically travels one axial chord between successive reflections, the time between reflections is  $t \approx 1$  for moderate Mach numbers. Therefore,  $\beta_2$  and  $\beta_4$  also represent the amplitude attenuation caused by numerical smoothing between reflections. Alternatively, they can be written as

$$\beta_2 \sim \epsilon_2 \Delta (2\pi/\lambda_f)^2 \quad \text{and} \quad \beta_4 \sim \epsilon_4 \Delta^2 (2\pi/\lambda_f)^4 \quad (46)$$

which shows the strong bias of fourth-order smoothing towards short wavelengths. Typical values of the smoothing coefficients are ( $\epsilon_2 = 10^{-1}$ ) and ( $\epsilon_4 = 10^{-2}$ ). A standard value of the mesh spacing is  $\Delta = 3 \times 10^{-2}$ . For the longest wave with a wavelength of order unity, fourth-order smoothing in between successive reflections results in an amplitude attenuation that is an order of magnitude smaller than the attenuation caused by viscous dissipation in an unsteady boundary layer. For shorter wavelengths, numerical smoothing starts to dominate. The attenuation coefficient  $\beta_4$  of the sixth harmonic approaches unity for the above choice of  $\Delta$  and  $\epsilon_4$ . This implies, that numerical smoothing dissipates waves prematurely in the free stream unless the wavelength is on the order of an axial chord or more.

The weak shock waves, whose interaction with the blade rows is the primary cause of unsteadiness in the ACE turbine stage, are subject to strong numerical dissipation, even in the absence of second-order smoothing. The pressure gradients driving the unsteady boundary layer are diminished by numerical smoothing, lowering the level of the predicted unsteady viscous losses.

## Conclusions

This paper has studied two unsteady loss mechanisms for geometries, Mach numbers and loading realistic for modern turbomachinery. The results of numerical simulations were used as input to the 2D, linearized, analytical loss models. Losses from both mechanisms are small compared to other (nonlinear) sources that increase the losses under unsteady operating conditions, like a change in the transition point, and compared to the uncertainty in measured efficiencies. Since this paper is 2D, it does not account for possibly important 3D effects.

The Unsteady Circulation Losses, which are due to viscous dissipation of kinetic energy associated with vorticity shed in response to circulation variations, resulted in an isentropic efficiency drop of 0.3% for the ACE turbine stage. The ACE turbine stage operates at a comparably high level of unsteadiness but is representative of current and future high-pressure turbine designs.

The Unsteady Viscous Losses, i.e., the additional time-mean dissipation in unsteady boundary layers, that were calculated for the ACE turbine stage, are much smaller and caused a drop of 0.09% in the isentropic efficiency. Their exact magnitude is uncertain due to the limitations of the model used and the effect of numerical smoothing in the simulation. With the bounds found in a numerical error study, they can be of the same magnitude as the Unsteady Circulation Losses for this stage.

In unsteady simulations, numerical smoothing can shift the locus of dissipation from unsteady boundary layers into the blade passages. Pressure waves, which are the input to the viscous loss model, are diminished prematurely in the passage. In steady simulations, the entropy rise at the stator/rotor interface, which is an numerical artifact, can account for a significant part of the total losses in a stage.

## References

- D. A. Ashworth, J. E. LaGraff, D. L. Schultz, and K. J. Grindrod, 1985. 'Unsteady Aerodynamic and Heat Transfer Processes in a Transonic Turbine Stage', *Journal of Engineering for Gas Turbine and Power*, Vol. 107, pp. 1022-1030.
- A. Binder, 1985. 'Stationäre Strömungsvorgänge im Laufrad einer Turbine', Doctoral Thesis, RWTH Aachen.
- D. E. Coles, 1956. 'The Law of the Wake in the Turbulent Boundary Layer', *Journal of Fluid Mechanics*, Vol. 1, pp. 191-226.
- J. Cousteix, A. Desopper, R. Houdeville, 1977. 'Structure and Development of a Turbulent Boundary Layer in an Oscillatory Outer Flow', *Proceedings of the First Symposium on Turbulent Shear Flows*, Penn State University, pp. 154-171.
- G. Fritsch, 1992. 'An Analytical and Numerical Study of the Second-Order Effects of Unsteadiness on the Performance on Turbomachines', Ph.D. Thesis, MIT, June 1992.
- M. B. Giles, 1987. 'Calculations of Unsteady Wake/Rotor Interaction', AIAA Paper 87-0006.
- M. B. Giles, 1988. 'UNSFLO: A Numerical Method for Unsteady Inviscid Flow in Turbomachinery', GTI-Report #195, MIT, Gas Turbine Laboratory.
- M. B. Giles, 1990. 'Stator/Rotor Interaction in a Transonic Turbine', *Journal of Propulsion and Power*, Vol. 6, pp. 621-627.
- M. B. Giles and R. Haines, 1991a. 'Validation of a Numerical Method for Unsteady Flow Calculations' ASME-Paper 91-GT-271.
- M. B. Giles and R. Haines, 1991b. 'Advanced Interactive Visualization For CFD', *Computing Systems in Engineering*, Vol. 1, pp. 51-62.
- G. R. Guenette, A. H. Epstein, M. B. Giles, R. Haines, and R. J. G. Norton, 1988. 'Fully Scaled Transonic Turbine Rotor Heat Transfer Measurements', ASME Paper 88-GT-171.
- K. C. Hall, and E. F. Crawley, 1987. 'Calculation of Unsteady Flows in Turbomachinery Using the Linearized Euler Equations', *Fourth Symposium on Unsteady Aerodynamics and Aeroelasticity of Turbomachines and Propellers*, Aachen, Germany.
- M. D. Hathaway, T. H. Okiishi, A. J. Strazisar, and J. J. Adamczyk, 'Measurements of the Unsteady Flow Field within the Stator Row of a Transonic Axial Flow Fan', ASME Papers 87-GT-226 and 87-GT-227.
- H. P. Hodson, 1983. 'Boundary Layer and Loss Measurements on the Rotor of an Axial-Flow Turbine', ASME Paper 83-GT-4.
- H. P. Hodson, 1984a. 'An Inviscid Blade-to-Blade Prediction of a Wake-Generated Unsteady Flow', ASME Paper 84-GT-43.
- H. P. Hodson, 1984b. 'Measurements of Wake-Generated Unsteadiness in the Rotor Passages of Axial Flow Turbines', ASME Paper 84-GT-189.
- A. B. Johnson, M. J. Rigby, M. L. G. Oldfield, R. W. Ainsworth, and M. J. Oliver, 1988. 'Surface Heat Transfer Fluctuations on a Turbine Rotor Blade due to Upstream Shock Wave Passing', ASME Paper 88-GT-172.
- H. D. Joslyn, R. P. Dring, and O. P. Sharma, 1983. 'Unsteady Three-Dimensional Turbine Aerodynamics', *Journal of Engineering for Power*, Vol. 105, pp. 322-331.
- S. K. F. Karlsson, 1959. 'An Unsteady Turbulent Boundary Layer', *Journal of Fluid Mechanics*, Vol. 5, pp. 622-636.
- C. Keller, 1935. 'Energy Losses on High Speed Turbomachine Resulting from Irregular Flow to the Runner Wheel', *Escher-Wyss News*, March/April 1935.
- N. H. Kemp and W. R. Sears, 1956. 'On the Wake Energy of Moving Cascades' *Journal of Applied Mechanics*, Vol. 23, pp. 262-268.
- M. J. Lighthill, 1954. 'The Response of Laminar Skin Friction and Heat Transfer to Fluctuations in the Stream Velocity', *Proceedings of the Royal Society A*, Vol. 224, pp. 1-23.
- D. R. Lindquist, 1991. 'On the Validity of Linearized Unsteady Euler Equations with Shock Capturing', AIAA Paper 91-1598-CP.
- W. F. Ng, and A. H. Epstein, 1985. 'Unsteady Losses in Transonic Compressors', *Journal of Engineering for Power*, Vol. 105.
- P. G. Parikh, W. C. Reynolds, and R. Jayaramon, 1982. 'Behavior of an Unsteady Turbulent Boundary Layer', *AIAA Journal*, Vol. 20, pp. 769-775.
- T. Shang, 1989. 'Blade Row Interaction Effects on Compressor Measurements', Master's Thesis, MIT, 1989.
- D. B. Spalding, 1961. 'A Single Formula for the Law of the Wall', *Journal of Applied Mechanics*, Vol. 28, pp. 455-457.



The Society shall not be responsible for statements or opinions advanced in papers or in discussion at meetings of the Society or of its Divisions or Sections, or printed in its publications. Discussion is printed only if the paper is published in an ASME Journal. Papers are available from ASME for fifteen months after the meeting.  
Printed in USA.

## An Approach for Multi-Stage Calculations Incorporating Unsteadiness

MICHAEL GILES

Department of Aeronautics and Astronautics  
Massachusetts Institute of Technology  
Cambridge, MA 02139

### Abstract

This paper describes a mathematical approach to the calculation of unsteady flow in multi-stage turbomachinery. An asymptotic formulation is used, with the small asymptotic parameter being the level of unsteadiness in each blade row. The baseline flow is the nonlinear steady flow that is computed by many existing multi-stage calculation methods. The first order linear perturbation is the unsteady flow field arising from stator/rotor interactions between neighboring blade rows. The second order correction contains the information about the time-averaged effect of unsteadiness on the mean flow. The advantage of this asymptotic approach is that it leads to a set of equations which can be solved numerically very much more cheaply than the full nonlinear unsteady flow equations, while still retaining the key features of the flow.

### Introduction

During the last ten years many researchers have developed numerical methods for calculating nonlinear unsteady flows (Chen, 1988, Erdos, 1977, Fourmaux, 1986, Giles, 1988, 1990, He, 1991, Hodson, 1984, Rai, 1987, 1989, Siden, 1991). The capabilities of the codes which have been developed vary widely. Some are two-dimensional, some have quasi-three-dimensional extensions, and some are fully three-dimensional. Some assume inviscid flow and use the Euler equations, while others adopt the Reynolds-averaged Navier-Stokes equations with turbulence modeling. Some are able to treat arbitrary number of blades in each blade row using techniques due to Erdos (1977) or Giles (1988) but most treat only very simple integer ratios, such as 2:3. Most can analyze stator/rotor interaction in which the unsteadiness is due to the relative blade motion. Some can also treat unsteadiness due to prescribed blade vibration (He, 1991, Siden, 1991, Giles, 1991) incoming wakes (Hodson, 1984, Giles, 1988) or potential disturbances (Giles, 1991).

These codes are now very useful practical tools for the investigation of important unsteady flow phenomena in turbomachinery. This is clear from the growing number of papers concentrating not on the mathematical formulation of the methods but on their use as 'numerical wind tunnels'. Sometimes this use is in conjunction with detailed experimental work, in which case the computation is used to understand the experimental results more fully (Abhari, 1991, Epstein, 1989, Dorney, 1991, Johnson, 1990). The experimental data is usually limited to a few variables (e.g. pressure, total temperature) in a few locations, whereas the computational results supply all variables at all locations. In other cases, the confidence in numerical methods is sufficiently great that computations are performed in the complete absence of experimental data due to the difficulty or cost of performing the experiments (Paulon, 1991). This is particularly true for parametric design studies (Rangwalla, 1991, Korakianitis, 1991).

Despite the impressive capabilities of these nonlinear time-marching methods there is a major limitation for industrial engineering application, which is the cost and compute times associated with these codes. Inviscid, two-dimensional, unsteady computations can be performed in minutes on a CRAY, or less than an hour on today's new generation of very fast workstations. At the other extreme however, viscous three-dimensional unsteady calculations can require several days of CRAY time. These computational costs can be justified when trying to identify and correct design problems. They are also justifiable when the codes are used as a research tool to increase our understanding of unsteady flows in turbomachinery, so that our increased knowledge can lead to improved designs with fewer problems. However, axial gas turbine engines are multi-stage in nature, and if one considers multi-stage calculations, possibly even the calculation of the flow through an entire engine, then nonlinear time-marching methods seem to be totally impractical for the foreseeable future.

It is not simply that the computational work scales linearly with the number of stages. It may in fact grow faster than linearly because of the possibility of slower convergence due to the increasing inflow-outflow-inflow round-trip signal propagation time in unchoked engines. The main complicating factor

leading to extraordinarily large computing times is the problem of the periodic boundary conditions. In single-stage computations there is a time-lagged spatial periodicity condition which can be treated numerically by one of two approaches (Erdos, 1977; Giles, 1988). As soon as there is more than one stage in the calculation there is an unavoidable problem. Consider a  $1\frac{1}{2}$  stage calculation in which the first and second stator rows have different numbers of blades. If there is no common factor in the numbers of blades then each of the second stator row blades will experience a different unsteady force depending on its circumferential position relative to the blades in the first stator row. There is no mathematically correct way around this problem. Some researchers have performed calculations by modifying geometries to achieve very simple ratios in the numbers of blades (e.g. 1:1,2:3,3:4) but these modifications change the flow field being calculated, and involve larger and larger errors as more stages are included in the calculation. Ultimately, the only correct nonlinear time-marching treatment is to analyze the entire annulus in each blade row. This is simply too computationally expensive to consider for many years.

The question then is how one can best perform multi-stage flow calculations in a manner which includes the prediction of unsteady effects. Before offering an answer to this, it is appropriate to first discuss what one would hope to get out of such calculations. The focus in this work is on the development of a tool that can be used by designers as part of the regular design system. From the designer's point of view one of the principal objectives is an accurate prediction of mean flow properties such as mass flow, turning, work and efficiency. This is the aim of research work by Adamczyk, who in the early 1980's pointed out the impracticality of multi-stage unsteady Navier-Stokes calculations. His point is that the unsteady components of the flow are important only in as much as they change the mean flow. Therefore, he formulated a system of 'passage-averaged' equations in which the effect of deterministic periodic unsteadiness on the mean flow is included through terms which are similar in nature to the Reynolds stresses in the Reynolds-averaging of turbulent flow equations (Adamczyk, 1985). The implementation of these equations in a multi-stage flow code has been very successful in predicting the mean flow in both turbines (Adamczyk, 1989) and compressors (Mulac, 1991). In particular, his approach has correctly predicted flow features which are not captured by steady-state multi-stage flow calculations which do not include unsteady flow effects. These ideas of Adamczyk have played a major role in stimulating the ideas for the quadratic terms in the approach in this paper.

The other major concerns with flow unsteadiness are the possibility of bending or torsional flutter, and the magnitude of unsteady loads and forced response due to various kinds of unsteady interactions. Flutter is by definition a linear problem since it is concerned with the possible growth of infinitesimal unsteady perturbations. A growing body of evidence suggests that the forced response problem is also largely linear. Comparisons between linear and nonlinear calculations, for levels of unsteadiness typical of engine conditions, show that the linear calculations predict the forced response to within 5% (Hall, 1989; Sudhoo, 1991). This level of accuracy is perfectly adequate for all practical engineering design purposes and is probably within the level of other modeling errors. This has motivated the development of linear Euler methods for forced response prediction. In

these methods, the unsteadiness is assumed to be a small perturbation to a steady nonlinear flow field obtained from a solution of the Euler equations. Some preliminary research on a linear Euler method was performed in 1975 by Ni (1975) but the recent research activity began with the PhD thesis of Hall (1987). Hall's research involved the development of a two-dimensional finite element method for the calculation of linear unsteady flows in cascades, plus shock-fitting for unsteady flows in ducts (Hall, 1989). By comparing to results of unsteady, nonlinear Euler time-marching calculations he demonstrated the validity of the linear approximation up to large levels of unsteadiness. Later, Giles proposed an alternative pseudo-time-marching approach to solving the linear Euler equations (Giles, 1989) based on an idea of Ni (1975). Lindquist and Giles have also proved that with careful treatment shock capturing can be valid for linear unsteady calculations (Lindquist, 1991). Pseudo-time-marching shock-capturing linear Euler methods are also being developed by Hall (1991) and Holmes (1991).

This paper combines the ideas of Adamczyk with the recent developments in linear unsteady flow modeling, to formulate an asymptotic approach to multistage unsteady flow calculations. First, one calculates a steady multi-stage flow field in a manner similar to that used by Denton (1985, 1990) and Dawes (1990). Next, one calculates the unsteady flow assuming that its magnitude is sufficiently small that it may be analyzed using the linearized form of the unsteady Euler equations. In the third step, changes to the steady-state flow field due to the time-averaged effect of the unsteadiness are related to source terms whose magnitude is quadratic in the level of unsteadiness. This is similar to the modeling of Reynolds stresses in turbulent flow, except that in this case the unsteady flow perturbations have been calculated using the linear Euler analysis and so the construction of the quadratic source terms is a purely algebraic exercise.

## 1 Asymptotic analysis

### 1.1 Unsteady Euler equations

The starting point for the entire analysis is the nonlinear unsteady Euler equations describing the motion of an inviscid, compressible gas in three dimensions in a frame of reference rotating with angular velocity  $\Omega$  about the  $z$ -axis.

$$\frac{\partial U}{\partial t} = - \left( \frac{\partial F_x}{\partial x} + \frac{\partial F_y}{\partial y} + \frac{\partial F_z}{\partial z} \right) + S, \quad (1)$$

where the state vector  $U$  is a five-component vector,

$$U = \begin{pmatrix} \rho \\ \rho u_x \\ \rho u_y \\ \rho u_z \\ \rho E \end{pmatrix}, \quad (2)$$

the three flux vectors,  $F_x$ ,  $F_y$  and  $F_z$ , are given by

$$F_x = \begin{pmatrix} \rho u_x \\ \rho u_x^2 + p \\ \rho u_x u_y \\ \rho u_x u_z \\ u_x(\rho E + p) \end{pmatrix}, \quad F_y = \begin{pmatrix} \rho u_y \\ \rho u_x u_y \\ \rho u_y^2 + p \\ \rho u_y u_z \\ u_y(\rho E + p) \end{pmatrix}, \quad F_z = \begin{pmatrix} \rho u_z \\ \rho u_x u_z \\ \rho u_y u_z \\ \rho u_z^2 + p \\ u_z(\rho E + p) \end{pmatrix}. \quad (3)$$

and the source term  $S$  containing both centrifugal and coriolis effects is

$$S = \begin{pmatrix} 0 \\ 0 \\ \rho(\Omega^2 y + 2\Omega u_x) \\ \rho(\Omega^2 z - 2\Omega u_y) \\ 0 \end{pmatrix}. \quad (4)$$

The total energy  $E$  is related to the pressure, density and velocities through the equation of state for an ideal gas.

$$E = \frac{p}{(\gamma-1)\rho} + \frac{1}{2}(u_x^2 + u_y^2 + u_z^2) - \frac{1}{2}\Omega^2 r^2 \quad (5)$$

Integrating over a static control volume gives the integral form of the equations of motion.

$$\frac{d}{dt} \iiint_V U dV = - \iint_{\partial V} F_x dA_x + F_y dA_y + F_z dA_z + \iiint_V S dV. \quad (6)$$

It is this equation which is used as the basis for the discretization in most numerical time-marching methods.

## 1.2 Asymptotic expansions

The approach which is proposed uses the first three terms in an asymptotic expansion in which the level of unsteadiness is the small asymptotic parameter. It is very closely related to the mathematical techniques used to analyze a phenomenon known as 'acoustic streaming', in which unsteady sinusoidal perturbations of a stationary fluid can generate a small second order mean flow (Batchelor, 1967, Schlichting, 1979).

The flow variables are represented by an asymptotic expansion in  $\epsilon$ .

$$U(x, t) = U^{(0)}(x) + \epsilon U^{(1)}(x, t) + \epsilon^2 U^{(2)}(x, t) + O(\epsilon^3). \quad (7)$$

The next step is to construct the asymptotic form of all flow variables using Taylor series expansion. For an arbitrary scalar function  $A(U)$ ,

$$\begin{aligned} A(U^{(0)} + \epsilon U^{(1)} + \epsilon^2 U^{(2)}) \\ = A(U^{(0)}) + \frac{\partial A}{\partial U_j} (\epsilon U_j^{(1)} + \epsilon^2 U_j^{(2)}) + \frac{1}{2} \frac{\partial^2 A}{\partial U_j \partial U_k} (\epsilon U_j^{(1)})(\epsilon U_k^{(1)}) + O(\epsilon^3) \\ = A(U^{(0)}) + \epsilon \frac{\partial A}{\partial U_j} U_j^{(1)} + \epsilon^2 \left( \frac{\partial A}{\partial U_j} U_j^{(2)} + \frac{1}{2} \frac{\partial^2 A}{\partial U_j \partial U_k} U_j^{(1)} U_k^{(1)} \right) + O(\epsilon^3). \end{aligned} \quad (8)$$

Note that the second order term has two pieces, one due to the linear sensitivity to second order changes in  $U$  (which will be referred to as the second order linear perturbation) and the other due to the quadratic sensitivity to the first order changes in  $U$  (which will be referred to as the quadratic perturbation).

To avoid the use of superscripts, the superscript  $(0)$  will be dropped unless it is needed for clarity. In addition, the following notation is introduced.

$$\begin{aligned} \bar{A} &\equiv \frac{\partial A}{\partial U_j} U_j^{(1)} \\ \bar{\bar{A}} &\equiv \frac{\partial A}{\partial U_j} U_j^{(2)} \\ \bar{\bar{\bar{A}}} &\equiv \frac{1}{2} \frac{\partial^2 A}{\partial U_j \partial U_k} U_j^{(1)} U_k^{(1)} \end{aligned} \quad (9)$$

The overlining on the r.h.s of these definitions denotes a time-average. The reason for introducing the time-averages is that it is only the mean second-order effects which are considered to be important in the analysis because they affect quantities such as the mean efficiency and mass flow. The unsteady component of the second order terms is assumed to give only a small change in the unsteady loading on the blades and is therefore neglected.

After some algebra one finds that the linear perturbations to the velocities and pressure are

$$\begin{aligned} \bar{u}_x &= \rho^{-1}(\bar{\rho} \bar{u}_x - u_x \bar{\rho}) \\ \bar{u}_y &= \rho^{-1}(\bar{\rho} \bar{u}_y - u_y \bar{\rho}) \\ \bar{u}_z &= \rho^{-1}(\bar{\rho} \bar{u}_z - u_z \bar{\rho}), \end{aligned} \quad (10)$$

$$\bar{p} = (\gamma-1) \left( \bar{\rho} \bar{E} - \bar{\rho} \left( E - \frac{p}{(\gamma-1)\rho} \right) - \rho(u_x \bar{u}_x + u_y \bar{u}_y + u_z \bar{u}_z) \right), \quad (11)$$

and hence the perturbations to the flux vectors are

$$\bar{F}_x = \begin{pmatrix} u_x \bar{\rho} + \bar{u}_x \rho \\ u_x \bar{\rho} u_x + \bar{u}_x \rho u_x + \bar{p} \\ u_x \bar{\rho} u_y + \bar{u}_x \rho u_y \\ u_x \bar{\rho} u_z + \bar{u}_x \rho u_z \\ u_x (\bar{\rho} \bar{E} + \bar{p}) + \bar{u}_x (\rho E + p) \end{pmatrix} \quad (12)$$

$$\bar{F}_y = \begin{pmatrix} u_y \bar{\rho} + \bar{u}_y \rho \\ u_y \bar{\rho} u_x + \bar{u}_y \rho u_x \\ u_y \bar{\rho} u_y + \bar{u}_y \rho u_y + \bar{p} \\ u_y \bar{\rho} u_z + \bar{u}_y \rho u_z \\ u_y (\bar{\rho} \bar{E} + \bar{p}) + \bar{u}_y (\rho E + p) \end{pmatrix} \quad (13)$$

$$\bar{F}_z = \begin{pmatrix} u_z \bar{\rho} + \bar{u}_z \rho \\ u_z \bar{\rho} u_x + \bar{u}_z \rho u_x \\ u_z \bar{\rho} u_y + \bar{u}_z \rho u_y \\ u_z \bar{\rho} u_z + \bar{u}_z \rho u_z + \bar{p} \\ u_z (\bar{\rho} \bar{E} + \bar{p}) + \bar{u}_z (\rho E + p) \end{pmatrix}, \quad (14)$$

and the perturbation to the source term is

$$\bar{S} = \begin{pmatrix} 0 \\ 0 \\ \Omega^2 \bar{\rho} y + 2\Omega \bar{\rho} \bar{u}_x \\ \Omega^2 \bar{\rho} z - 2\Omega \bar{\rho} \bar{u}_y \\ 0 \end{pmatrix}. \quad (15)$$

The relationship between the second order linear perturbation  $\bar{A}$  and  $\bar{U}$  is exactly the same as the relationship between the first order perturbation  $\bar{A}$  and  $\bar{U}$ .

After considerable algebra the quadratic velocity perturbations are found to be

$$\begin{aligned} \bar{\bar{u}}_x &= -\rho^{-1} \bar{\rho} \bar{\bar{u}}_x \\ \bar{\bar{u}}_y &= -\rho^{-1} \bar{\rho} \bar{\bar{u}}_y \\ \bar{\bar{u}}_z &= -\rho^{-1} \bar{\rho} \bar{\bar{u}}_z, \end{aligned} \quad (16)$$

and the quadratic pressure perturbation is

$$\bar{\bar{p}} = -\frac{1}{2}(\gamma-1)\rho (\bar{\bar{u}}_x^2 + \bar{\bar{u}}_y^2 + \bar{\bar{u}}_z^2). \quad (17)$$

The quadratic perturbations to the flux vectors are

$$\bar{\bar{F}}_x = \begin{pmatrix} 0 \\ \bar{\bar{u}}_x \rho u_x + \bar{u}_x \bar{\rho} u_x + \bar{\bar{p}} \\ \bar{\bar{u}}_x \rho u_y + \bar{u}_x \bar{\rho} u_y \\ \bar{\bar{u}}_x \rho u_z + \bar{u}_x \bar{\rho} u_z \\ \bar{\bar{u}}_x (\rho E + p) + u_x \bar{\bar{p}} + \bar{u}_x \bar{\rho} E + \bar{u}_x \bar{p} \end{pmatrix} \quad (18)$$

$$\bar{F}_y = \begin{pmatrix} 0 \\ \bar{u}_y \rho u_x + \bar{u}_y \rho \bar{u}_x \\ \bar{u}_y \rho u_y + \bar{u}_y \rho \bar{u}_y + \bar{p} \\ \bar{u}_y \rho u_z + \bar{u}_y \rho \bar{u}_z \\ \bar{u}_y (\rho E + p) + u_y \bar{p} + \bar{u}_y \rho E + \bar{u}_y \bar{p} \end{pmatrix} \quad (19)$$

$$\bar{F}_z = \begin{pmatrix} 0 \\ \bar{u}_z \rho u_x + \bar{u}_z \rho \bar{u}_x \\ \bar{u}_z \rho u_y + \bar{u}_z \rho \bar{u}_y \\ \bar{u}_z \rho u_z + \bar{u}_z \rho \bar{u}_z + \bar{p} \\ \bar{u}_z (\rho E + p) + u_z \bar{p} + \bar{u}_z \rho E + \bar{u}_z \bar{p} \end{pmatrix} \quad (20)$$

and the quadratic perturbation to  $S$  is zero.

### 1.3 Steady-state equations

The steady-state equations are obtained by substituting the asymptotic expansions of the fluxes  $F_x, F_y, F_z$  and the source term  $S$  into the nonlinear equations of motion, and retaining only those terms which are  $O(1)$ . Dropping the superscript  $(0)$ , the equations are identical to the standard nonlinear steady-state Euler equations.

$$\iint_{\partial V} F_x dA_x + F_y dA_y + F_z dA_z = \iiint_V S dV. \quad (21)$$

As an iterative numerical procedure to solve these equations it is convenient to add back in an unsteady term

$$\frac{d}{dt} \iiint_V U dV + \iint_{\partial V} F_x dA_x + F_y dA_y + F_z dA_z = \iiint_V S dV, \quad (22)$$

and integrate in time until a steady-state solution is achieved. This can be accelerated by neglecting time accuracy and using techniques such as local time-stepping and multigrid.

### 1.4 Linear equations

The linear perturbation of the unsteady integral equation of motion is obtained from the terms which are  $O(\epsilon)$ .

$$\frac{d}{dt} \iiint_V \bar{U} dV + \iint_{\partial V} \bar{F}_x dA_x + \bar{F}_y dA_y + \bar{F}_z dA_z = \iiint_V \bar{S} dV. \quad (23)$$

The fact that this equation is linear and all of the coefficients depend on  $U$  and geometric terms, which do not vary in time, means that there are harmonic solutions of the form  $\bar{U}(x) \exp(-i\omega t)$ . The most general periodic solution can be expressed as the real part of a linear superposition of such solutions for a number of different real positive frequencies  $\omega$ , all satisfying the necessary periodicity constraints.

$$\bar{U} = \mathcal{R} \left( \sum_{\omega} \bar{U}_{\omega} \exp(-i\omega t) \right). \quad (24)$$

A useful idea due to Ni (1975) is to formulate the harmonic equation by retaining a time dependence in  $\bar{U}$ . Substituting

$$\bar{U} = \bar{U}(x, t) \exp(-i\omega t) \quad (25)$$

gives the unsteady, harmonic equation

$$\frac{d}{dt} \iiint_V \bar{U} dV + \iint_{\partial V} \bar{F}_x dA_x + \bar{F}_y dA_y + \bar{F}_z dA_z = \iiint_V (\bar{S} + i\omega \bar{U}) dV. \quad (26)$$

The advantage of retaining the time-dependent term is that numerical integration of this equation until a 'steady-state' solution is achieved will result in the desired harmonic solution. This allows one to employ any of a set of standard numerical time-marching methods with the usual acceleration techniques.

### 1.5 Quadratic equations

The quadratic equations come from taking the terms which are  $O(\epsilon^2)$  and then time-averaging.

$$\iint_{\partial V} \bar{F}_x dA_x + \bar{F}_y dA_y + \bar{F}_z dA_z - \iiint_V \bar{S} dV = \text{QST} \quad (27)$$

The quadratic source terms (QST) are

$$\text{QST} = - \iint_{\partial V} \bar{F}_x dA_x + \bar{F}_y dA_y + \bar{F}_z dA_z. \quad (28)$$

Eq. (27) is a linear equation in  $\bar{U}$ ; the quadratic source terms are the inhomogeneity that drives this second order flow perturbation.

Again using Ni's idea of adding a pseudo-unsteady term to allow the use of numerical time integration schemes, one obtains

$$\frac{d}{dt} \iiint_V \bar{U} dV + \iint_{\partial V} \bar{F}_x dA_x + \bar{F}_y dA_y + \bar{F}_z dA_z - \iiint_V \bar{S} dV = \text{QST} \quad (29)$$

In this form, it is equivalent to the linear harmonic equation with zero frequency and the addition of the quadratic source terms. Thus it can be solved numerically with only trivial changes to the numerical procedure.

An alternative approach is to define a time-averaged state

$$\bar{U} = U + \epsilon^2 \bar{\bar{U}} \equiv \overline{U^{(0)} + \epsilon U^{(1)} + \epsilon^2 U^{(2)}}, \quad (30)$$

and recombine the steady-state equation with the second order equation to form

$$\frac{d}{dt} \iiint_V \bar{U} dV + \iint_{\partial V} \bar{F}_x dA_x + \bar{F}_y dA_y + \bar{F}_z dA_z - \iiint_V \bar{S} dV = \epsilon^2 \text{QST}. \quad (31)$$

This effectively introduces into the nonlinear steady-state equation the time-averaged effect of the linear unsteadiness through the simple inclusion of the quadratic source terms.

A final issue is the evaluation of the quadratic source terms for linear unsteady solution  $\bar{U}$  which is represented as the real part of a sum of harmonic solutions of different frequencies.

$$\bar{U} = \mathcal{R} \left( \sum_{\omega} \bar{U}_{\omega} \exp(-i\omega t) \right) \quad (32)$$

It turns out that this is very simple. For an arbitrary scalar function  $A(U)$ ,

$$\begin{aligned} \bar{\bar{A}} &= \frac{1}{2} \frac{\partial^2 A}{\partial U_j \partial U_k} \overline{U_j^{(1)} U_k^{(1)}} \\ &= \frac{1}{2} \frac{\partial^2 A}{\partial U_j \partial U_k} \mathcal{R} \left( \sum_{\omega} \bar{U}_{j,\omega} \exp(-i\omega t) \right) \mathcal{R} \left( \sum_{\omega} \bar{U}_{k,\omega} \exp(-i\omega t) \right) \\ &= \frac{1}{4} \frac{\partial^2 A}{\partial U_j \partial U_k} \sum_{\omega} \mathcal{R}(\bar{U}_{j,\omega} \bar{U}_{k,\omega}^*). \end{aligned} \quad (33)$$



Thus, the quadratic source terms can be expressed as a sum of the quadratic source terms for each distinct harmonic frequency

$$\text{QST} = \sum_{\omega} \text{QST}_{\omega}, \quad (34)$$

and each of the harmonic components is easily evaluated knowing  $\hat{U}$ .

## 2 Boundary conditions

### 2.1 Steady flow

The boundary conditions on blade surfaces and endwalls is simply that there is no mass flux across the boundary, or equivalently that the normal component of the velocity is zero.

If the calculation is performed for a single blade-blade passage in a blade row with multiple blades, then the periodic boundary condition is that

$$U_p(x, \theta, r) = U_p(x, \theta + \Delta\theta), \quad (35)$$

where  $\Delta\theta$  is the angular pitch and the 'primitive' variable vector  $U_p$  in cylindrical coordinates is defined as

$$U_p = \begin{pmatrix} \rho \\ u_x \\ u_\theta \\ u_r \\ p \end{pmatrix}. \quad (36)$$

At inflow and outflow boundaries, steady-state non-reflecting boundary conditions can be constructed (Saxer, 1991). In these, one specifies at the inflow circumferentially averaged values of total temperature, total pressure and flow angles as functions of radius. At the outflow circumferentially averaged values of pressure are specified, consistent with radial equilibrium. Circumferential harmonics of  $U_p$  are not set to zero but are allowed to evolve to values which are consistent with the existence of an infinite annular duct upstream or downstream of the computational domain.

At stator/rotor interfaces a very similar treatment is used, but the circumferentially averaged values of  $U_p$  are determined instead by the constraint that the total flux of mass, momentum and energy across the interface must match. Defining the axial flux in cylindrical coordinates as

$$F_{x\theta} = \begin{pmatrix} \rho u_x \\ \rho u_x^2 + p \\ \rho u_x u_\theta \\ \rho u_x u_r \\ u_x(\rho E + p) \end{pmatrix}, \quad (37)$$

with all quantities being in the absolute frame, then the matching condition between blade rows 1 and 2 is that

$$\overline{F_{x\theta}}^{\text{row 1}} = \overline{F_{x\theta}}^{\text{row 2}}, \quad (38)$$

with the notation  $\overline{\phantom{x}}$  denoting a circumferential average over one blade passage. This flux-conservation treatment was first used by Denton and can cause a small entropy rise due to the implicit mixing process (Denton, 1985).

### 2.2 Linear unsteady flow

The boundary conditions on blade surfaces and endwalls are again that there is no mass flux across the boundary. When this condition is linearized it produces the requirement that the normal component of the velocity perturbation is zero.

The periodic boundary condition is slightly more complicated than for the steady state flow due to the inclusion of the interblade phase angle  $\phi$ .

$$\hat{U}_p(x, \theta, r) = \exp(i\phi) \hat{U}_p(x, \theta + \Delta\theta, r) \quad (39)$$

This is still a very much simpler boundary condition to implement numerically than the lagged periodic boundary condition in single stage nonlinear stator/rotor calculations (Erdos, 1977, Giles, 1988). Also, linearity allows one to superimpose two solutions with different interblade phase angles due to differing number of blades in upstream and downstream blade rows.

The most interesting boundary conditions are the inflow and outflow conditions used to model unsteady stator/rotor interaction in a linear sense. Consider two neighboring blade rows, labeled 1 and 2, rotating with speeds  $\Omega_1$  and  $\Omega_2$ . The key idea is that a stationary circumferential variation in one blade row becomes a rotating unsteady perturbation in the other blade row due to the relative rotation of the two rows. The steady-state primitive flow variables in cylindrical coordinates in blade row 1 can be expressed as the sum of an axisymmetric part plus circumferential harmonic terms.

$$U_p(x, \theta_1, r) = \bar{U}_p(x, r) + \mathcal{R} \left\{ \sum_{m \neq 0} U_{pm} \exp \left( \frac{2\pi m i \theta_1}{\Delta\theta_1} \right) \right\} \quad (40)$$

The angle  $\theta_2$  in neighboring blade row 2 is related through

$$\theta_1 + \Omega_1 t = \theta_2 + \Omega_2 t. \quad (41)$$

Hence,

$$\frac{2\pi m \theta_1}{\Delta\theta_1} = \frac{2\pi m (\theta_2 - (\Omega_1 - \Omega_2)t)}{\Delta\theta_1}. \quad (42)$$

and so the stationary  $m^{\text{th}}$  mode in blade row 1 is equivalent to an unsteady mode in blade row 2 with the frequency

$$\omega_2 = \frac{2\pi m (\Omega_1 - \Omega_2)}{\Delta\theta_1}. \quad (43)$$

The harmonic boundary terms that go with this mode are

$$\hat{U}_p(x, \theta_2, r) = \exp \left( -\frac{i \theta_2 \phi_2}{\Delta\theta_2} \right) U_{pm}(x, r) \quad (44)$$

where the inter-blade phase angle is

$$\phi_2 = -\frac{2\pi m \Delta\theta_2}{\Delta\theta_1} \quad (45)$$

A slight complication is the desire to keep all frequencies  $\omega$  positive. If the above description gives a value for  $\omega_2$  which is negative then the problem is avoided by noting that a harmonic solution with frequency  $\omega$  and inter-blade phase angle  $\phi$  is the complex conjugate of another solution with frequency  $-\omega$  and interblade phase angle  $-\phi$ .

### 2.3 Quadratic equations

The solid wall and periodic boundary conditions are exactly the same as for the steady flow analysis. The inflow and outflow boundary conditions are also similar in that the circumferential harmonics are again specified by steady-state non-reflecting boundary condition theory. At stator/rotor interfaces, the circumferentially averaged values of the second order flow perturbations are set by the requirement that the average fluxes (averaged both in time and circumferentially) must match. Substituting the asymptotic expansion of the flux and then time-averaging gives the following equation.

$$\overline{F_{z\theta} + \epsilon^2(\bar{\bar{F}}_{z\theta} + \bar{\bar{F}}_{z\theta})}_{\text{row 1}} = \overline{F_{z\theta} + \epsilon^2(\bar{\bar{F}}_{z\theta} + \bar{\bar{F}}_{z\theta})}_{\text{row 2}} \quad (46)$$

Canceling the  $O(1)$  terms which match in the steady-state equations, yields

$$\overline{\bar{\bar{F}}_{z\theta} + \bar{\bar{F}}_{z\theta}}_{\text{row 1}} = \overline{\bar{\bar{F}}_{z\theta} + \bar{\bar{F}}_{z\theta}}_{\text{row 2}} \quad (47)$$

Alternatively, if one adopts the other approach to the second order analysis by adding  $\bar{\bar{U}}$  to  $U$  to form the time-average  $\bar{U}$ , then one obtains the matching condition

$$\overline{\bar{F}_{z\theta} + \epsilon^2\bar{\bar{F}}_{z\theta}}_{\text{row 1}} = \overline{\bar{F}_{z\theta} + \epsilon^2\bar{\bar{F}}_{z\theta}}_{\text{row 2}} \quad (48)$$

In this form, the matching condition is similar to a mathematical constraint derived by Adamczyk to ensure the correct transfer of time-averaged, circumferentially averaged vorticity across the interface (Adamczyk, 1991).

## 3 Possible Applications

The purpose of this section is to discuss the variety of different phenomena which can be analyzed using the approach outlined in this paper.

### 3.1 Wake and hot streak migration

In a compressor, rotor wakes migrate towards the pressure surface of the stators downstream (Kerrebrock, 1970). Similarly, in a turbine first stage, hot streaks coming from spatial nonuniformities in the combustor migrate towards the pressure surface of the rotor leading to elevated heat transfer (Butler, 1986). In both cases the mechanism is essentially the same. The unsteady velocity of the wake or hot streak relative to the mean flow drives the fluid across the passage towards the pressure surface. The time-averaged effect is quadratic in the level of unsteadiness. For example, the elevated surface temperature in the turbine is proportional to both the unsteady velocity and the unsteady perturbation in temperature.

Such phenomena will be captured by the second order analysis using the quadratic source terms. In the case of the hot streaks, the quadratic term in the energy flux which reflects the migration effect is of the form  $\bar{u}_y \bar{T}$ .

### 3.2 Time-averaged total temperature variations

In fans and compressors an unsteady rotor/stator interaction can lead to a circumferential variation in time-averaged total temperature in the absolute frame. This spatial variation can cause significant complications in the experimental determination of the efficiency of the rotor. This phenomenon has been documented and explained fully in a paper by Epstein *et al* (1989). It is due to the potential field of the stator causing an oscillation in time of the circulation around the rotor. This produces a shed vortex sheet which in turn, in the absolute frame of the stator, gives a spatial variation in total temperature which can be explained through the time-averaging of Crocco's theorem. The phenomenon is linear, with the amplitude of the total temperature nonuniformity being proportional to the amplitude of the oscillation in the rotor blade circulation.

This phenomenon will be captured by the steady-state and linear perturbation analysis in a three-step process. This first step is a steady-state combined rotor/stator computation. The second step is the computation of the linear harmonic unsteadiness in the rotor due to the first (and possibly second) circumferential spatial harmonics in the stator inflow plane. The unsteadiness in the rotor frame of reference produces downstream propagating acoustic and vortical disturbances. A circumferential Fourier decomposition shows that some of the modes are stationary in the absolute frame of reference. These modes are then input as boundary conditions for a steady linear perturbation analysis in the stator which will produce the time-averaged spatial variation of total temperature. In this application the second order quadratic effects do not play a significant role.

### 3.3 Losses due to unsteadiness

One of the most important parts of stator/rotor interaction is the potential interaction, the effect of the pressure field about one blade row on a neighboring blade row in relative motion. The potential interaction generates acoustic waves, and with the exception of the situation discussed in the previous example, most of the waves are unsteady in both frames of reference. Associated with these waves is a certain level of acoustic energy, and the question which then arises is whether this acoustic energy is eventually dissipated (converted into thermal energy with an increase in entropy and a decrease in stagnation pressure).

This topic is addressed in a paper by Fritsch (1992) in which it is argued that most of this energy will be lost. The physical mechanism is the unsteady pressure field generating an unsteady Stokes' layer at the bottom of the boundary layer, leading to increased dissipation in the boundary layer. By contrast, an order-of-magnitude analysis comes to the conclusion that in numerical computations the energy is lost in the freestream portion of the flow due to numerical smoothing. A supposition (possibly plausible or possibly just hopeful) is that a numerical computation may still correctly calculate the overall additional loss provided it correctly predicts the rate of generation of the acoustic energy due to the potential interactions.

If this supposition is true, and a nonlinear, time-marching flow calculation including numerical smoothing can indeed predict the increased losses due to this form of unsteadiness, then

the full steady/linear/quadratic analysis in this paper should be equally successful. This is a quadratic effect since the acoustic energy level is proportional to the square of the unsteady flow quantities.

If the supposition is not correct then it will be necessary to extend the theory in this paper to an asymptotic analysis of the Navier-Stokes equations. It will also be necessary to use very much finer computational grids to eliminate the errors due to the numerical smoothing. Of course this will greatly increase the computational cost of such calculations.

## 4 Concluding Remarks

This paper has presented an asymptotic approach toward the calculation of unsteady flows in multistage turbomachinery. The analysis proceeds in three phases. First one performs a steady-state multistage analysis in which the flow is assumed to be steady in each blade row in a frame of reference rotating with the blade row. The stator/rotor interface matching conditions ensure overall conservation of mass momentum and energy across the interface.

In the second phase the unsteadiness in each blade row is treated as a perturbation to the steady flow field. Assuming the perturbation is small it is represented by the linearized unsteady flow equations. The linear stator/rotor interaction is calculated by recognizing that a steady circumferential variation in a stator corresponds to a rotating unsteady disturbance in a rotor, and vice versa. Each circumferential harmonic produces a response of a different frequency. Due to linearity these can be computed independently and superimposed to form the composite unsteady flow.

The third phase calculates the change to the mean flow due to second order consequences of the unsteady flow field. This is achieved through the evaluation of quadratic source terms which are similar in origin to the Reynolds stress terms in the Reynolds averaged Navier-Stokes equations.

Through this process one can calculate the key features of the unsteady flow in turbomachinery, the unsteady forces and moments on blades due to interactions with neighboring rows, as well as the average effects on mass flow and efficiency. The efficiency changes come about as the result of wasted kinetic energy associated with the eventual dissipation of acoustic energy generated by unsteady stator/rotor interaction. A more complete treatment of efficiency prediction would require the application of the entire asymptotic approach to the Navier-Stokes equations. This is an algebraically complicated but otherwise straightforward extension which will be tackled in the future.

This paper does not present any computational results, but clearly this conceptual approach needs to be thoroughly validated by comparison to nonlinear time-marching methods and experimental data. This will be addressed in future work, along with the task of accelerating the numerical computations using techniques such as multigrid. The two reasons at present to believe that there is some merit to this idea are that Adamczyk has already achieved significant improvements using his passage-averaged flow equations, and the alternative approach of nonlinear unsteady multistage calculations requires excessive computation times.

## References

- R. S. Abhari, G. R. Guenette, A. H. Epstein, and M. B. Giles. Comparison of time-resolved turbine rotor blade heat transfer measurements and numerical calculations. ASME Paper 91-GT-268, June 1991.
- J. J. Adamczyk. Model equations for simulating flows in multistage turbomachinery. ASME Paper 85-GT-226, June 1985.
- J. J. Adamczyk, M. L. Celestina, T. A. Beach, and M. Barnett. Simulation of three-dimensional viscous flow within a multistage turbine. ASME Paper 89-GT-152, June 1989.
- J. J. Adamczyk. A mathematical constraint placed upon inter-blade row boundary conditions used in the simulation of multistage turbomachinery flows. AGARD PEP 77th Symposium on CFD Techniques for Propulsion Applications, May 1991.
- G. K. Batchelor. *An Introduction to Fluid Dynamics*. Cambridge University Press, 1967.
- T. L. Butler, O. P. Sharma, H. D. Joslyn, and R. P. Dring. Redistribution of an inlet temperature distortion in an axial flow turbine stage. AIAA Paper 86-1468, 1986.
- Y. S. Chen. 3-D stator-rotor interaction of the SSME. AIAA Paper 88-3095, 1988.
- W. N. Dawes. Towards improved throughflow capability: The use of 3D viscous flow solvers in a multistage environment. ASME Paper 90-GT-18, June 1990.
- J. D. Denton. The calculation of 3D flow through any type of turbomachine blade row. AGARD Lecture Series 140, 1985.
- J. D. Denton. The calculation of three dimensional viscous flow through multistage turbomachines. ASME Paper 90-GT-19, June 1990.
- D. J. Dorney, R. L. Davis, and O. P. Sharma. Two-dimensional inlet temperature profile attenuation in a turbine stage. ASME Paper 91-GT-406, June 1991.
- A. H. Epstein, M. B. Giles, T. Shang, and A. K. Sehra. Blade row interaction effects on compressor measurements. AGARD 74th Specialists Meeting on Unsteady Aerodynamic Phenomena in Turbomachines, Aug 1989.
- J. I. Erdos, E. Alzner, and W. McNally. Numerical Solution of Periodic Transonic Flow Through a Fan Stage. *AIAA Journal*, 15(11):1559-1568, Nov 1977.
- A. Fourmaux. Unsteady flow calculation in cascades. ASME Paper 86-GT-178, 1986.
- G. Fritsch and M. B. Giles. Second-order effects of unsteadiness on the performance of turbomachines. Submitted to the 37th, IGTI Gas Turbine Congress, 1992.
- M. B. Giles. Calculation of unsteady wake/rotor interaction. *AIAA Journal of Propulsion and Power*, 4(4):356-362, July/August 1988.
- M. B. Giles. Numerical methods for unsteady turbomachinery flow. VKI Lecture Series 1989-06, 1989.
- M. B. Giles. Stator/rotor interaction in a transonic turbine. *AIAA Journal of Propulsion and Power*, 6(5), September-October 1990.
- M. B. Giles and R. Haines. Validation of a numerical method for unsteady flow calculations. ASME Paper 91-GT-271, June 1991.
- K. C. Hall. *A Linearized Euler Analysis of Unsteady Flows in Turbomachinery*. PhD thesis, M.I.T., Sept 1987.

K. C. Hall and E. F. Crawley. Calculation of unsteady flows in turbomachinery using the linearized Euler equations. *AIAA Journal*, 27(6):777-787, June 1989.

K. C. Hall and W. S. Clark. Prediction of unsteady aerodynamic loads in cascades using the linearized Euler equations on deforming grids. AIAA Paper 91-3378, June 1991.

L. He and J. D. Denton. Inviscid-viscous coupled solution for unsteady flows through vibrating blades. Part I: Description of the method. ASME Paper 91-GT-125, 1991.

H. P. Hodson. An inviscid blade-to-blade prediction of a wake-generated unsteady flow. ASME Paper 84-GT-43, June 1984.

D. G. Holmes and H. A. Chuang. Two dimensional linearized harmonic Euler flow analysis for flutter and forced response. Sixth International Symposium on Unsteady Aerodynamics, Aeroacoustics and Aeroelasticity of Turbomachines and Propellers, Sept 1991.

A. B. Johnson, M. J. Rigby, M. L. G. Oldfield, and M. B. Giles. Nozzle guide vane shock wave propagation and bifurcation in a transonic turbine rotor. ASME Paper 90-GT-310, June 1990.

J. L. Kerrebrock and A. A. Mikolajczak. Intra-stator transport of rotor wakes and its effect on compressor performance. ASME Paper 70-GT-39, 1970.

T. Korakianitis. On the propagation of viscous wakes and potential flow in axial turbine cascades. ASME Paper 91-GT-373, June 1991.

D. R. Lindquist and M. B. Giles. On the validity of linearized unsteady Euler equations with shock capturing. AIAA Paper 91-1958, 1991.

R. A. Mulac and J. J. Adamczyk. The numerical simulation of a high-speed axial flow compressor. ASME Paper 91-GT-272, June 1991.

R.-H. Ni and F. Sisto. Numerical computation of nonstationary aerodynamics of flat plate cascades in compressible flow. ASME Paper 75-GT-5, 1975.

J. Paulon, Z. Zhang, P. Jia, and J. Meng. Influence of unsteady effects on the measurements in a transonic axial compressor. ASME Paper 91-GT-90, 1991.

M. M. Rai. Navier-Stokes simulations of rotor-stator interaction using patched and overlaid grids. *AIAA Journal of Propulsion and Power*, 3(5):387-396, 1987.

M. M. Rai. Three-dimensional Navier-Stokes simulations of turbine rotor-stator interaction. *AIAA Journal of Propulsion and Power*, 5(3):305-319, May-June 1989.

A. A. Rangwala, N.-K. Madavan, and P. D. Johnson. Application of an unsteady Navier-Stokes solver to transonic turbine design. AIAA Paper 91-2468, 1991.

A. Saxer and M. Giles. Quasi-3D nonreflecting boundary conditions for Euler equation calculations. AIAA Paper 91-1603, June 1991.

H. Schlichting. *Boundary Layer Theory*. McGraw-Hill, 1979.

L. D. Siden. Numerical simulation of unsteady viscous compressible flows applied to blade flutter analysis. ASME Paper 91-GT-203, 1988.

A. Suddhoo, M. Giles, and P. Stow. Simulation of inviscid blade row interaction using a linear and a non-linear method. ISABE Conference, 1991.

### **TASK III: UNSTEADY PHENOMENA AND FLOWFIELD INSTABILITIES IN MULTISTAGE AXIAL COMPRESSORS**

(Investigators: E.M. Greitzer, C.S. Tan, P.P. Silkowski, J.P. Longley,  
N.A. Cumpsty, I.J. Day, D.C. Wisler, H.W. Shin)

#### **Executive Summary**

This progress report describes a combined experimental and theoretical program of research on unsteady flow and instability in multistage axial compressors. The objectives of the program were to define the critical fluid dynamic phenomena associated with the onset of instability in modern, multistage machines and assess those elements that should be incorporated in improved models of this process. The specific research goals included elucidation of newly discovered types of propagating disturbances, having widely disparate wavelengths and waves speeds, which occur prior to rotating stall onset, and definition of the extent to which current unsteady flow models capture the relevant fluid processes of this complex dynamical system. The work is being carried out in collaboration with the General Electric Aircraft Engine Company, with the experiments actually being conducted at the GE Aerodynamics Research Laboratory, on a facility representative of advanced aeroengine compressor geometries.

Two main activities are discussed in the report. The first is unsteady measurements of the blade passage flow field in the first rotor of a multistage compressor, under conditions at which stall occurred naturally as well as under conditions in which the flow was artificially stabilized, so that the behavior at, and even past, the nominal stall point could be addressed. This gives new information concerning the interaction and role of the different wavelength unsteady disturbances. The second is a series of diagnostic experiments with a forced unsteady inlet distortion, which allowed detailed assessment of the concepts that underlie the existing wave dynamic models of compressor response to inlet non-uniformity.

## **1.0 Introduction**

Recent studies of rotating stall inception have led to the definition of two different paths from the essentially axisymmetric flow in the pre-stall state to fully developed rotating stall. The first involves the growth of a small amplitude, long circumferential length scale (of the order of the machine radius) traveling wave into a fully developed rotating stall cell. The initial propagation speed of the traveling wave is close to that of the developed stall cell, and small amplitude traveling waves can exist for a long time (several tens of rotor revolutions) before any operational changes in machine behavior occur. This process is well captured by the models of unsteady flow in multistage machines.

Another, quite different, process has also been observed, however, which involves the circumferential growth of a small circumferential extent disturbance (a few blade pitches) into a mature rotating stall cell in roughly five to ten rotor revolutions. These small extent, or short length scale, phenomena will be referred to here as spikes, primarily because their temporal history appears considerably more "spiky" than the long length scale disturbances. An important factor in the design of the experiments to be discussed was the desire to focus on the different time and length scales associated with the spikes and the long wave disturbances (referred to as LWD's). In particular, the axial locations of probes upstream of the rotor were intended to spatially filter out short length scale disturbances and make the long wavelength disturbances clearer. Also, several rig modifications were used as tools to focus on specific time and length scales, including restaggering the rear three stages, asymmetric tip clearance, and distortion screens.

The basic fluid dynamic questions that were initially addressed in this study were:

- 1) What are the mechanisms of rotating stall inception?
- 2) Is there a repeatable pre-stall event, and if so, is it a long wavelength disturbance (LWD), a short wavelength disturbance (spike), or some combination of the two?
- 3) Can one associate the type of pre-stall events with compressor design parameters?
- 4) At the blade passage length scale how do the various fluid dynamic structures (tip

vortex/leakage jet, blade wakes, and endwall boundary layers) behave with changing operating point and what role do these structures play in the stall inception process?

- 5) How do inlet distortion and changes in tip clearance affect the stall inception process?
- 6) If we are able to artificially stabilize the first stall flow, what is the axisymmetric machine and local flow field behavior in the first stage at these highly loaded conditions, i.e. what, in detail, is the flow field associated with "compressor stall"?

To address these questions, an investigation of a multi-stage compressor flowfield has been conducted involving several different levels of experimentation. Detailed examination of the first stage rotor has been carried out during a series of experiments in which the flow was artificially stabilized by restaggering the rear three stages. This restaggering created a situation in which the behavior of the rear three stages suppressed the growth of long length scale flow disturbances. This enabled the behavior of the first rotor, at flows below that where the rotor would experience stall in a natural environment, to be seen. As will be described, the experiments show that although the stall inception process may begin as a localized event, the evolution into rotating stall is governed by the environment defined by the coupling of the various compression system components. Also, the rotor tip leakage jet appears to be a key feature in the local stall inception process.

As a second facet of the program, diagnostic experiments have been carried out to examine the effect of unsteady inlet distortions on instability onset, i.e. to address the issue of the receptivity of the compressor, considered as a multi-dimensional dynamic system, to inlet disturbances. This set of experiments also allows assessment of wave models of unsteady compressor response that have been developed.

The first experiments showed clearly, perhaps for the first time, that the path to stall can involve the interaction of disturbances of both long and short wavelength perturbations. Understanding the connection between these types of disturbances is a critical new conceptual step in attacking this important problem.

## 2.0 Experimental Facilities

The investigation included theoretical and experimental phases and was a collaborative university-industry effort, involving groups at MIT and General Electric Aircraft Engines. There was also participation from the Whittle Lab, Cambridge, England. The experiments were carried out at the General Electric Aerodynamics Research Laboratory, under the aegis of Dr. D.C. Wisler. The facility used was a large scale, low speed research compressor that presents a model of many aspects of the actual high speed compressor flow field (Fig. 1). The large size minimizes probe blockage and allows for easier access and instrumentation whilst giving correct Reynolds number at low operating speed. A four-stage compressor was used with the NASA/GE Energy Efficient Engine blading. Further information on this facility and the blading can be obtained from Ref [1].

In addition to standard steady state instrumentation, high response pressure transducers and hot wires were used. A radially traversable slant wire, to give three components of velocity, and a total pressure probe were also used at rotor inlet and rotor exit. The bulk of the experiments were carried out with fixed arrays of 40 probes, consisting of 20 hot wires and 20 pressure transducers. At inlet guide vane exit, there were ten reference hot wires at midspan and ten corresponding pressure transducers in the casing. The ten reference locations were circumferentially distributed at eight equally spaced locations to facilitate spatial Fourier analysis. Two closely spaced sensors were also used to allow cross-correlations over various distances, to combat spatial aliasing. Most of the unsteady data was sampled at 10 kHz and low pass filtered at 3 kHz, with several cases sampled at 1 kHz and low pass filtered at 300 Hz.

Complementing the reference probes were ten additional hot wires and ten casing pressure transducers with circumferential distribution identical to the reference probes referred to above. The reference probes were fixed at their locations for all runs as a control, but the test probes were moved to various axial-radial positions. The test probes were used at four axial locations: one half of a radius and one quarter of a radius upstream of rotor inlet, one at rotor inlet, and one at rotor exit, at locations roughly 0.2 chord upstream and downstream of the rotor respectively. At  $R/2$  or



R/4 upstream, the hot wires were at midspan, but at rotor inlet and rotor exit, the hot wires were used at 20% and 80% immersion (tip and hub), as well as at other immersions, as shown in Fig.

2. To focus on small length scale events, experiments were also performed with eight probes equally spaced over three blade pitches.

The baseline build overall compressor characteristic (pressure rise versus axial velocity parameter at constant rotor speed) is displayed in Fig. 3. Figure 4 is the performance of the first stage only. Several points are labeled for future reference. Point A is design and point E is just before rotating stall occurs.

For the restagger, the rear three rotors were closed by  $10^\circ$ . Figure 5 shows the result of the restagger on the overall pressure rise characteristic. The stalling flow coefficient was changed from 0.345 to 0.308. Thus, the purpose of the restagger, which was to extend the stable operating region of the first stage and provide a clearer view of the spikes by suppressing the long length scale disturbances, has been achieved. There is an abrupt change in slope of the overall mismatched characteristic at the stalling  $\phi$  of the baseline build.

Figure 6 displays the first stage characteristic for the baseline and restaggered builds with several operating points labeled for future reference. In the range of flows common to the two builds, the first stage pressure rise characteristic is the same for both. The extended operating region of the first stage characteristic (achieved with the restagger), however, is positively sloped. Stability analysis predicts that a positively sloped compressor stage would exhibit flow instability; here the rear three stages are negatively sloped and the overall compressor has a negative slope and hence is stable.

A second variation from the baseline build was to open the first stage rotor clearance from gap/span = 1.3% to 3.1%. This was done both symmetrically as well as by opening the clearance over a  $120^\circ$  section of the annulus.

### 3.0 Results

#### 3.1 Steady State Blade Row Flow Field Data

The steady state blade row data are presented in two ways: radial profiles, i.e. mass averages over one circumferential pitch at a given radius, and contour or vector format over roughly 1.5 blade pitches.

Figure 7 shows the radial velocity distribution at inlet to the first rotor at various operating points. This should be close to zero if the flow is unstalled. Although the flow angles in the tip region for the extended operating region of the restaggered build were out of calibration range for the slant wire, useful information can still be obtained from the data. In particular, the plot shows that the tip flow field does not deviate from the expected direction until operating point J of the restagger build, which is the baseline stalling flow coefficient. As the flow coefficient decreases further, an increasingly large portion of the tip flow field is out of range for the slant wire.

Figure 8 is a display of the slant wire data at rotor exit at the stable operating point closest to stall in the baseline build. The data has been converted to the relative (rotor) frame and is viewed at a yaw angle of  $55^\circ$  from axial, i.e. an angle aligned with the bulk through flow direction, so the figure represents the cross-plane or secondary flow. The scale vector at the top shows the direction of rotor rotation and the magnitude of blade tip speed,  $U_{tip}$ . Blade wakes, which have strong radial transport, and the tip vortex/leakage jet flow is clearly visible.

Figures 9 and 10 show the throughflow velocity at different flow coefficients with the contour of velocity/ $U_{tip} < 0.45$  shaded. A change in the tip region between points D and K is seen; there appears to be an almost axisymmetric region of low velocity near the tip at point K. Figure 11 shows the axial velocity distribution at 50% immersion (mid-span) at rotor exit for roughly 1.5 pitch at three different flow coefficients, and it is seen that the rotor wakes do not grow much circumferentially in  $\theta$  as  $\phi$  decreases. Figure 12 displays axial velocity profiles for two operating points at rotor exit for the baseline and for a larger first stage tip clearance. An increase of axial flow deficit can be seen near the tip with the larger clearance.

To summarize the steady state data, as the flow ( $\phi$ ) decreases the tip vortex/jet structure

and the rotor wakes do not change qualitatively, but close to stall the rotor leakage jet becomes larger. Furthermore, for the restaggered case, starting at the baseline stall flow coefficient, a region of appreciable radial velocity at rotor inlet grows in radial extent with decreasing flow coefficient. Finally, although the data is not shown here, the larger tip clearance build had a larger axial velocity deficit in the tip region, than the baseline build.

## 4.0 Time-Resolved Data

### 4.1 Baseline Build

Figure 13 shows time traces for eight equally-spaced casing pressure transducers at rotor inlet. Probe numbers increase in the direction of increasing  $\theta$  in the rotor rotation direction, and time is in units of rotor revolutions. The figure displays a situation in which the compressor was set at a stable operating point close to stall and the throttle slowly closed until the machine went into stall. A spike is first visible at  $t \sim 76.5$  on pressure transducer number 5. The growth of the spike, in amplitude and circumferential extent, is seen over the next few rotor revolutions, resulting in a developed stall cell by  $t \sim 82$ . There are no apparent propagating disturbances prior to time  $\sim 76.5$ .

Guidelines have been drawn in Fig. 14, with the slope of these lines representing the speed of propagation of the disturbance around the annulus. The change in slope of these lines indicates the change in the speed of propagation of the disturbance as it decelerates from 70% at inception to 45% as a mature stall cell. No evidence of any long wavelength disturbances above the perturbation levels of  $(\text{perturbation velocity})/U = 0.5\%$ ,  $p'/\rho U^2 = 1\%$  could be found. The data analysis techniques used confirmed the spike's 70% initial speed and subsequent deceleration to 45% with growth in magnitude and circumferential extent.

An example of the data analysis technique used is shown in Fig. 15. At each discrete time, data from eight equally spaced probes were Fourier analyzed and the resulting magnitudes and phases for the various harmonics displayed. The size of the symbols are scaled by the amplitude of the disturbance. No propagating disturbances are visible prior to time  $\cong 77$ , at which point the

disturbance grows rapidly to final size within roughly five rotor revolutions. The continuous change in slope of the phase of the first Fourier harmonic indicates the deceleration of the spike. (The regular pattern seen for times prior to  $t \sim 77$  in harmonic one is attributed to a slight rotor geometry asymmetry.)

Some experiments were conducted with the eight equally spaced test wires alternating between hub and tip, 80% and 20% immersion. Figure 16 displays the results from one of these tests conducted at rotor inlet, which shows the three-dimensional nature of the spike. Between  $t \sim 7$  and  $t \sim 78$ , the spike is seen as an axial deficit traveling in the tip region, with no disturbance visible in the hub wires. Only after the tip deficit has grown appreciably is any disturbance visible at the hub at  $t \sim 78.5$ . The hub disturbance is first seen as a flow increase (partially compensating for the tip blockage), but as the spike grows into a stall cell, a full span deficit eventually occurs.

Time-resolved measurements thus show the baseline build stalled via radial and circumferential growth of an initially small length scale disturbance. The growth occurred in roughly five rotor revolutions and no modal signals were found. The disturbance initial speed of 70% decreased to 45% as it grew into a mature stall cell.

## **5.0 Restaggered Build**

As the throttle was closed for the mismatched build, the following sequence of events occurred. When the flow coefficient decreased to the level at which the baseline encountered rotating stall, spikes would appear and disappear. As the flow was decreased further, to J, more spikes would appear per unit time with the spike width increasing from roughly 2-3 blade pitches to 3-4 blade pitches.

As the flow coefficient was decreased from J, the spike disturbances became more regular; they did not decay after a short appearance, but persisted. Time traces, FFTs, and correlations all showed this. The disturbances traveled at roughly 70%. At operating point N, there were 12 spikes traveling about the annulus at 70%. For any further decrease in flow, one of these would grow into rotating stall in the same fashion as the baseline case. As in the baseline case, the spike

disturbance gives an initial tip axial velocity deficit and a hub velocity increase until the disturbance evolves to cover the full span. The spike disturbance circumferential size at the hub is on the order of one or two pitches.

The disturbances with the restaggered build have similar features to the spike transients for the baseline build. Both appear first at operating point J and travel at a speed of roughly 70%. Both have a radial velocity distribution with a tip deficit and a hub increment in flow. The circumferential size (few pitches) of the disturbances of the restaggered build is comparable to that with the baseline build, early in its growth. The stabilized disturbance with the restaggered build thus resembles the spikes of the baseline build at some time during the five rotor revolution growth period of the latter. It therefore appears that the stabilized disturbances of the restaggered build and the transient disturbance of the baseline build may be the same phenomena, although this has not been proven conclusively. This is important because it suggests that one can use restaggering to enable more accurate flow diagnosis of these events.

## **6.0 Response of Multistage Compressors to Rotating Inlet Flow Distortions**

The second main thrust in this task has been the assessment of the effect of unsteady inlet disturbances on multistage compressor performance and stability. The motivation for the work arises out of two compelling factors concerning operability of gas turbine engines. First is that stability limitations often arise not with uniform flow, but as a result of an inlet non-uniformity, or distortion. Further, distortions encountered in practice usually have significant asymmetry to them, so that the problem of compressor response to circumferential inlet distortion is a real one indeed.

The second aspect is that the instability process is an inherently unsteady one, and the behavior of multistage machines, considered as dynamic systems, is not well understood. The consequence is that it is not scientifically correct to break up the response into smaller, much simpler modules, and study each one separately in the hope that one can somehow learn about the overall behavior. To do so is to ignore the real issues of the dynamic coupling between blade

passages, blade rows, and compressor stages which give rise to the response of interest.

These background facts led us to the set of experiments to be described, which made use of a rotating screen to create an unsteady inlet non-uniformity, which served as a unique diagnostic tool. Although the use of the rotating screen arose primarily for this reason, it can be mentioned that circumferential non-uniformities which can rotate at fixed speed around the compressor annulus can occur in two-spool compression systems, where one of the compressors or the fan could be in rotating stall, subjecting the other to a non-uniform rotating flow pattern.

There is little detailed data concerning the behavior of compressors when subjected to such types of distortions, but experimental results [2], [3] suggest that disturbances which rotate at speeds similar to stall cell propagation speed have the most pronounced effect. This behavior can also be seen in the computations of [4] which linked the phenomena to the resonant response of the compressor, i.e. to a correspondence between the forcing and the natural eigenmodes of the compression system.

The investigation of the effect of rotating flow non-uniformities on multistage compressor performance described here had three central objectives: to obtain information on the overall behavior (surge line changes) as a function of distortion rotation speed; to characterize the unsteady response of the compressor; and to assess present theoretical approaches to compressor stability. The last is particularly important since the existing models make use of rudimentary descriptions of the unsteady flow in the compressor blades, and it is not known to what extent this affects the predictions of overall behavior.

For the present experiments, the General Electric large scale research compressor described earlier was equipped with a drive mechanism which could rotate a distortion screen at speeds between  $\pm 100\%$  rotor speed [5]. The advantage of a screen-generated rotating distortion, rather than one generated by another compressor in rotating stall, is that it allows independent control of the severity of the non-uniformity, the rotation direction and speed and the compressor operating point. The screen was located 1.5 radii upstream of the inlet guide vanes and produced a roughly square wave stagnation pressure distortion of  $120^\circ$  circumferential extent with amplitude

corresponding to  $1.2 \times [\frac{1}{2} \rho (C_{x_{\text{mean}}})^2]$ . This non-uniformity was chosen to give a large change in the compressor stall point with no rotation, based upon predictions of the theoretical model.

Time mean and fast response instrumentation were used to measure the mean overall static pressure rise of the compressor, the unsteady static pressure distribution (both upstream and downstream of the compressor) and the time varying velocity field at various locations. These measurements were processed to analyze both the steady flow redistribution, as seen in the frame of reference of the distortion screen, and the behavior of perturbations which were unsteady in this coordinate system.

In what follows, we shall present the experimental results in close conjunction with theory; this will serve to address the capabilities of the flow models that have been developed.

## 7.0 Theory

The theoretical model used for the predictions and the design of the experiment was an extension of that reported in [4], [6], and [7]. It is a general fluid dynamic stability analysis for the compressor and the associated flowfields. The compressor performance is specified by an axisymmetric pressure rise characteristic with a correction for non-steady effects based on a simple model for the inertia of the fluid within the blade passages. The theory is well documented in [4], [6], and [7], so only the changes necessary for this investigation are commented upon.

For the present situation, the mean (background) flow equations were solved in a coordinate system rotating with the inlet distortion, so the flowfield redistribution may be considered as time invariant. In the engine frame, however, the potential field which causes the upstream redistribution is unsteady, and the stagnation pressure of a fluid particle is not conserved even for an inviscid flow. This introduces an additional term into the equations, but solution of the mean flow can be carried out in the same manner. Once the flow redistribution has been calculated (in the rotating coordinates), the stability of the flowfield is assessed, as in the original form of the theory, by calculation of the growth rates associated with general unsteady perturbations.

## 8.0 Experimental Results and Comparison With Theory

The behavior of the small-amplitude perturbations, which is important in determining the stability of the non-uniform compressor flowfield, is set by the background flow, which is a measure of the compressor's response to the imposed inlet distortion. The theory shows that the velocity field near stall is primarily determined by unsteady flow effects and that these change significantly as the rotation speed of the distortion varies. A study of how screen rotation rate affects the stability boundary of the compression system is thus useful in assessing the importance of the unsteady fluid dynamics and the degree to which the modelling is correct.

Figures 17 through 20 show overall effects of propagation speed of the inlet distortion (rotation rate of the screen) on the onset of flow instability in the multistage compressor. The horizontal axis in the figure is the non-dimensional rotation rate, rotation speed divided by rotor rotation, and the vertical axis is the value of flow coefficient,  $C_x/U$ , at which the instability, i.e. "stall", is encountered. A higher value of this quantity means a decreased stable flow range; the compressor stalls at a higher flow. In the figures, the experimental data are shown by the solid lines, and the calculations by the symbols. There is more than one line in some of the figures because there was a limitation on the mechanical speed of the screen. Data were thus taken at several rotor RPM in order to be able to achieve a higher non-dimensional value of this quantity.

Figure 17a shows the compressor tested by Plumley, as described in [8], while Figure 17b presents this information in more operational terms. In either of the figures, it is seen that counter-rotation has a markedly less severe effect on compressor instability. What is of more interest is the effect on stall margin, for example as measured by the distance between design flow and stall flow. Figure 17b shows that a steady inlet distortion decreases this margin by about twenty-five percent from the uniform flow value. With the rotating distortion, however, this decrease is more than doubled, and the margin decreases to roughly one-third of the uniform flow value.

A somewhat over-simplified explanation for the decrease is that, for the rotation rates at which the large effects are seen, the system is being subjected to disturbances that have a temporal and spatial structure similar to its natural eigenmodes. Because of this "resonance", in the mean



flow as well as in the unsteady perturbations, the system (the compressor) thus responds much more strongly.

The theoretical stability boundaries predicted by the model are also shown for the highest compressor speed. Trends in the predictions can be said to be qualitatively in agreement with the data but they do not indicate the second peak with frequency, nor do they show the difference between counter-rotational and co-rotational distortions. Although a definitive explanation for the differences between these aspects of the theory and experiment has not yet been made, there is an aspect of the model behavior that may be important and will be discussed.

The calculation of the theoretical stability boundary involved a general flowfield disturbance, with no limitations were placed on characteristic length scale nor reduced frequency. However, the waveform predicted for the most unstable disturbance is strongly dependent on the screen rotation speed. For normalized rotation rates of zero or less (counter-rotation), the predicted instabilities have long characteristic length scales and propagate around the annulus at 20-30% of rotor speed in the absolute frame. In the region where the predicted change in the stability limit is greatest, calculated instability waves have a much shorter characteristic length scale, and do not propagate relative to the screen position. These localized disturbances have a high reduced frequency, may not be adequately resolved by the simple model for unsteady flow in the blade passages, and hence may be more stable than the model suggests. If so, this would result in a larger predicted change in the stability boundary than that measured, as is the case.

Figure 18 shows the data for the compressor discussed previously. It can be seen that the variation is considerably less than with the machine of Fig. 17, but the two-peaked structure and the decrease in sensitivity with counter-rotation are still present. (The computations have not yet been done for this compressor build.)

Figures 19 and 20 give different results for two other compressors. Again, the overall picture is one of a significant decrease in stable flow range over a band of rotation rates, but the plots show a qualitatively different type of behavior than Figs. 17 and 18. There is a single hump in the overall plot of stall point versus screen rotating rate, in good agreement with the theoretical

description. In addition, although not shown in the figures, the time-resolved data (with uniform flow) also show qualitatively different behavior in these last two compressors. Long wavelength disturbances can be seen to propagate round the circumference prior to stall.

To summarize the overall experimental results as well as the interaction between theory and experiment, there appears to be a direct link between the overall behavior as regards the distortion response, and the details of the unsteady stall inception process. Current mathematical models of the flow capture the behavior very well in cases in which the long wavelength disturbances exist; for situations in which the shorter length scale disturbances are dominant, the models do show some features of the flow, but the precise degree of applicability is not clear.

## **9.0 Summary and Conclusions**

New fluid dynamic phenomena associated with the stall inception process and the dynamic response of multistage compressors have been identified in the present experimental investigation. The results are thought-provoking in that they impact directly on the development of improved theoretical predictive tools for self-excited as well as forced unsteady motions in compressors. More specifically, we cite the following points that have been made:

- 1) There are two routes to compressor instability, one via the growth of the amplitude of long wavelength disturbances and one in which a short length scale perturbation grows circumferentially, as well as perhaps in amplitude.
- 2) An experiment has been carried out to examine separately the role that each of these disturbances play in multistage machines, by artificially stabilizing the long wavelength disturbances.
- 3) Under conditions in which the long wavelength disturbances were stable, the short wavelength perturbations would appear and propagate, but would not lead to rotating stall.
- 4) The interaction of the two types of perturbations thus appears to be crucial in the stall onset process.
- 5) There is a strong effect of distortion rotation speed and direction on compressor stability.

- 6) A simple theoretical model of unsteady compressor response to rotating distortions shows predictions that are qualitatively similar to the experimental results, for several compressors and quantitatively similar for others. the difference between the two classes appears to be the existence of small amplitude, long wavelength disturbances prior to instability.
- 7) Both the detailed rotor passage results and the information with the rotating inlet distortion point to study of the fluid dynamics of the short wavelength disturbances, both structure and evolution, as an item of extremely high priority for unsteady flows in multistage compressors.

## 10.0 References

1. Wisler, D.C., "Loss Reduction in Axial-Flow Compressors Through Low-Speed Model Testing," ASME Paper 84-GT-184, 1984.
2. Ludwig, G.R., Nenni, J.P. and Arendt, R.H., "Investigation of Rotating Stall in Axial Flow Compressors and the Development of a Prototype Stall Control System", Technical Report USAF-APL-TR-73-45, 1973.
3. Kozarev, L.A. and Federov, R.M., "Aspects of the Appearance and Elimination of Breakdown in an Axial-Flow Compressor in the Presence of a Rotating Non-Uniformity at the Inlet", *Izvestiya vuz Aviatsionnaya Tekhnika*, Vol. 26, No. 1, pp. 33-37 (translated), 1983.
4. Chue, R., Hynes, T.P., Greitzer, E.M., Tan, C.S. and Longley, J.P., "Calculations of Inlet Distortion Induced Compressor Flowfield Instability", *Int. J. Heat and Fluid Flow*, Vol. 10, No. 3, Sept. 1989.
5. Greitzer, E.M., Epstein, A.H., Giles, M.B., McCune, J.E., Tan, C.S., Annual Technical Report on Grant AFOSR-90-0035, "Unsteady Flow Phenomena in Turbomachines," December 1991.
6. Hynes, T.P. and Greitzer, E.M., "A Method for Assessing Effects of Inlet Flow Distortion on Compressor Stability", *ASME J. Turbomachinery*, Vol. 109, pp 371-379, 1987.
7. Longley, J.P., "Measured and Predicted Effects of Inlet Distortion on Axial Compressors", ASME Paper 90-GT-214, Presented at the Gas Turbine and Aeroengine Congress and Exposition, Brussels, Belgium, June 11-14, 1990.
8. Plumley, R.E., "Unsteady Compressor Distortion Response and Compressor Instability," M.S. Thesis, Department of Aeronautics and Astronautics, MIT, 1990.

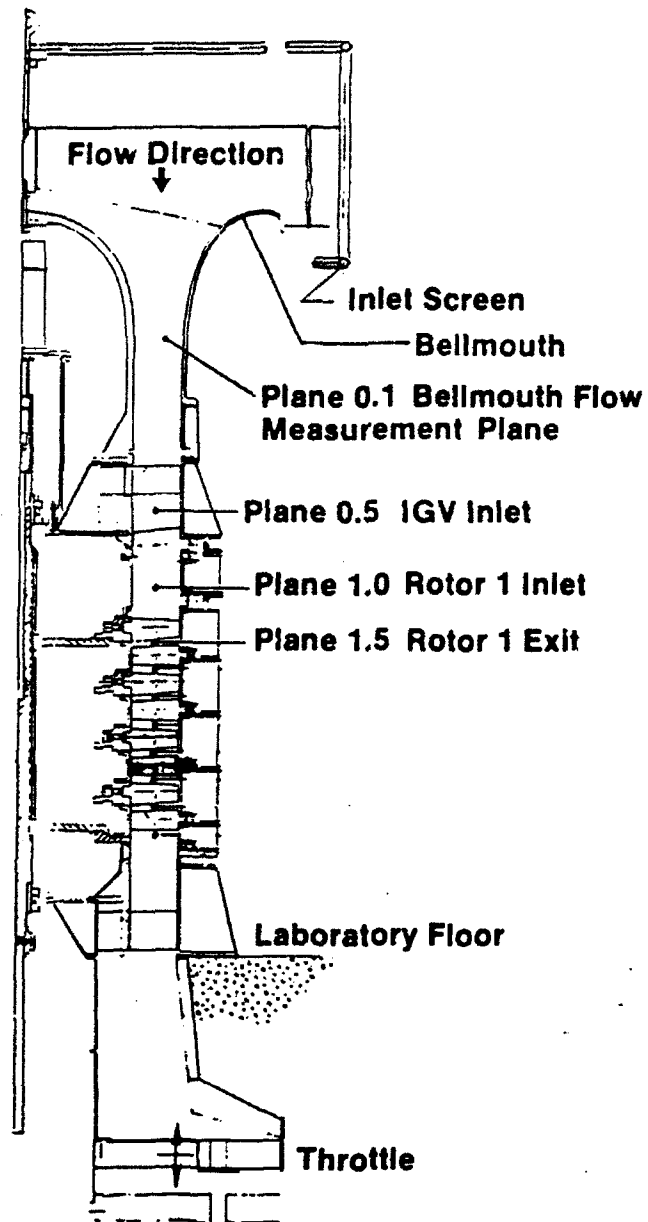


Fig. 1: Cross-section of low speed GE research compressor in 0.7 radius ratio configuration.

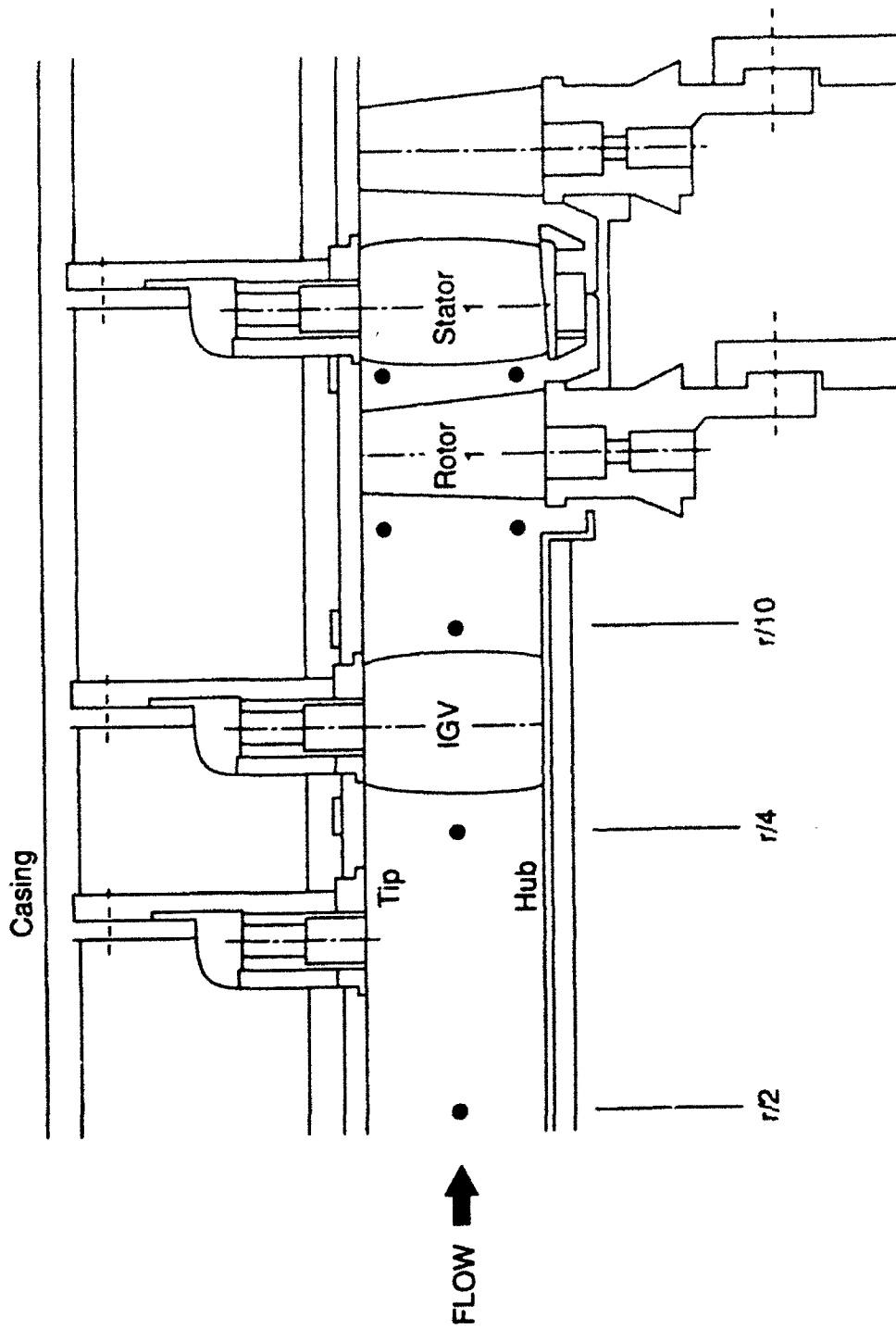


Fig. 2: Expanded view of instrumented region - axial/radial measurement locations.

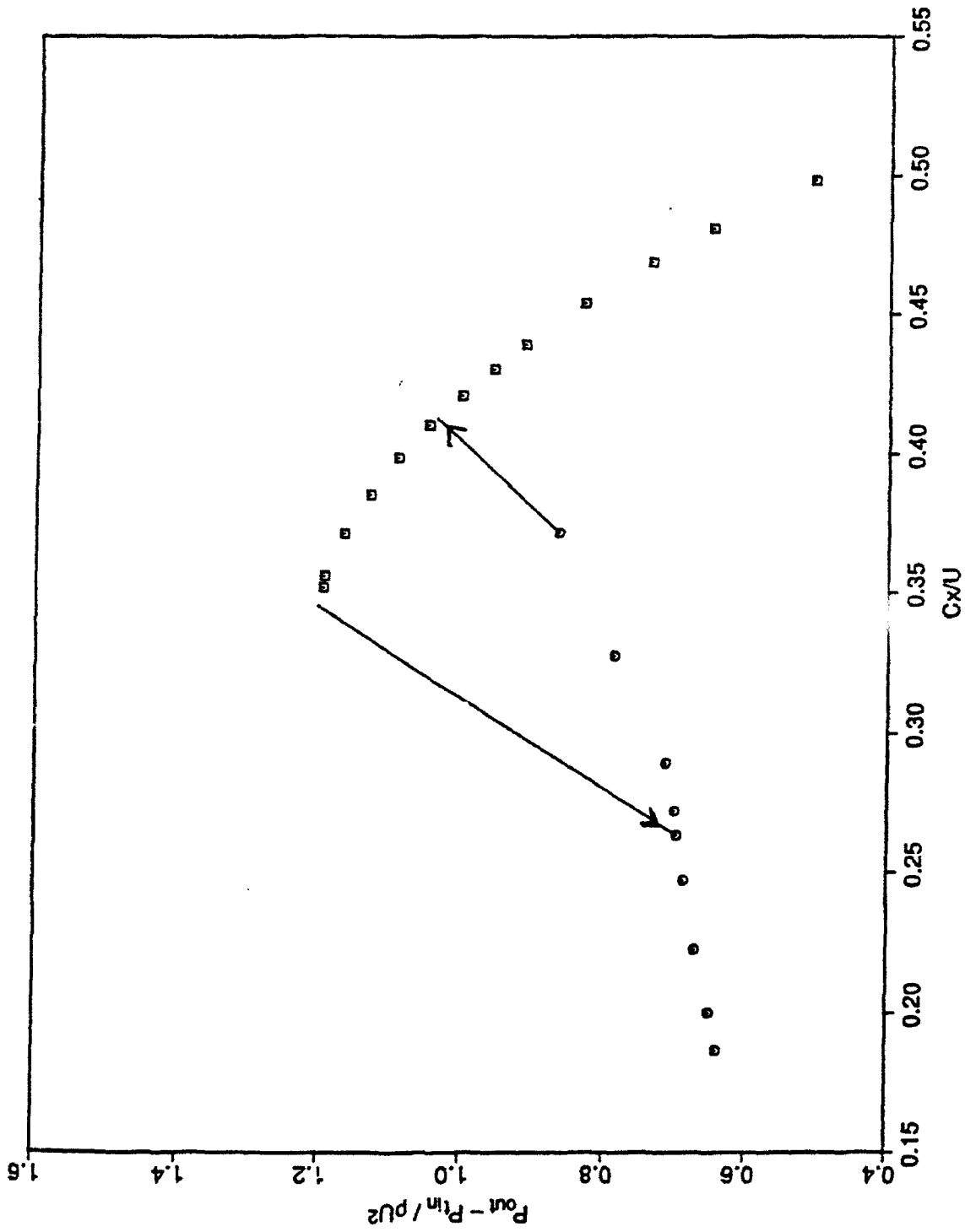


Fig. 3: Baseline build overall characteristic showing stall hysteresis loop.  
Circles denote points in rotating stall.

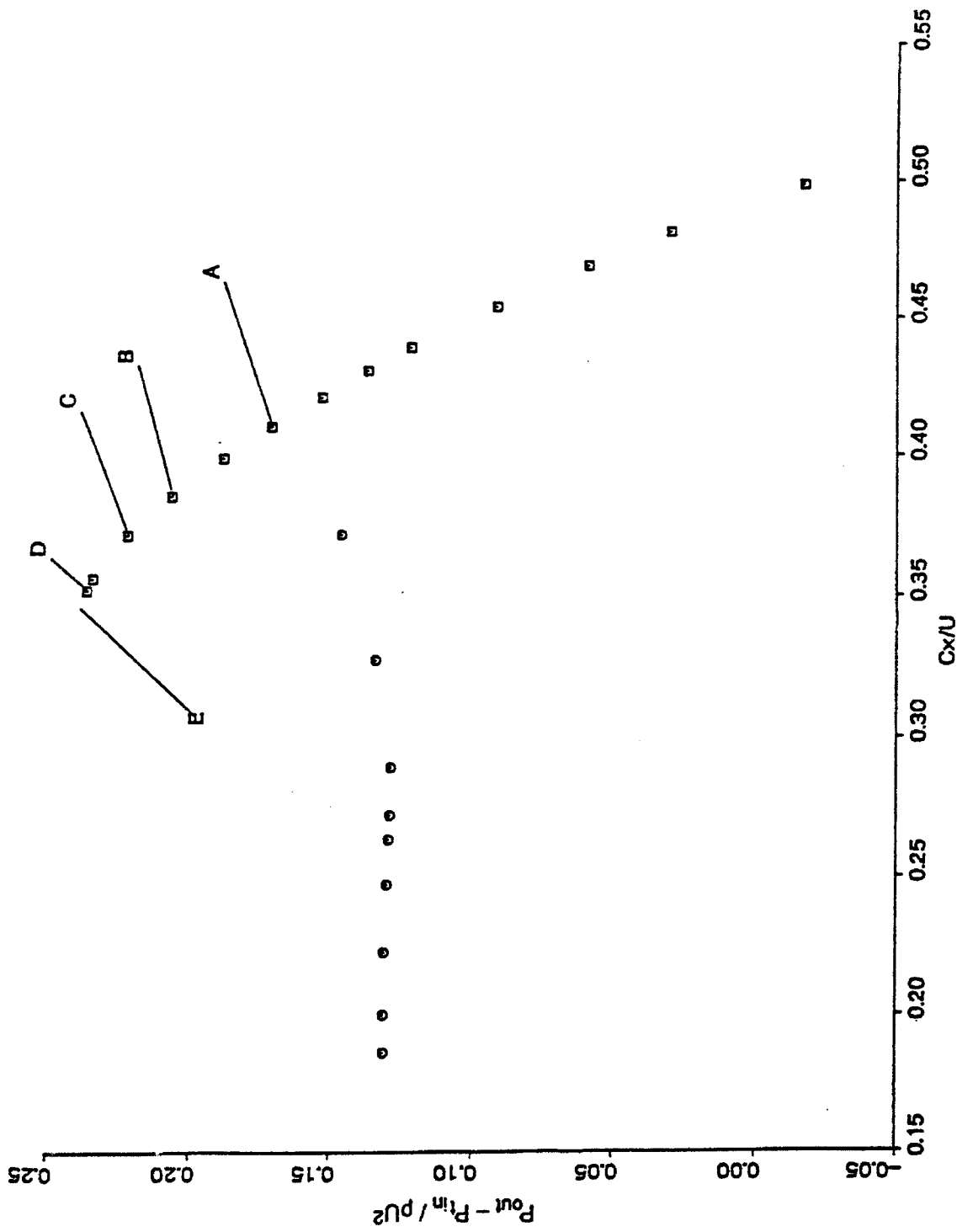


Fig. 4: Stage 1 of baseline build. Circles denote points in rotating stall.

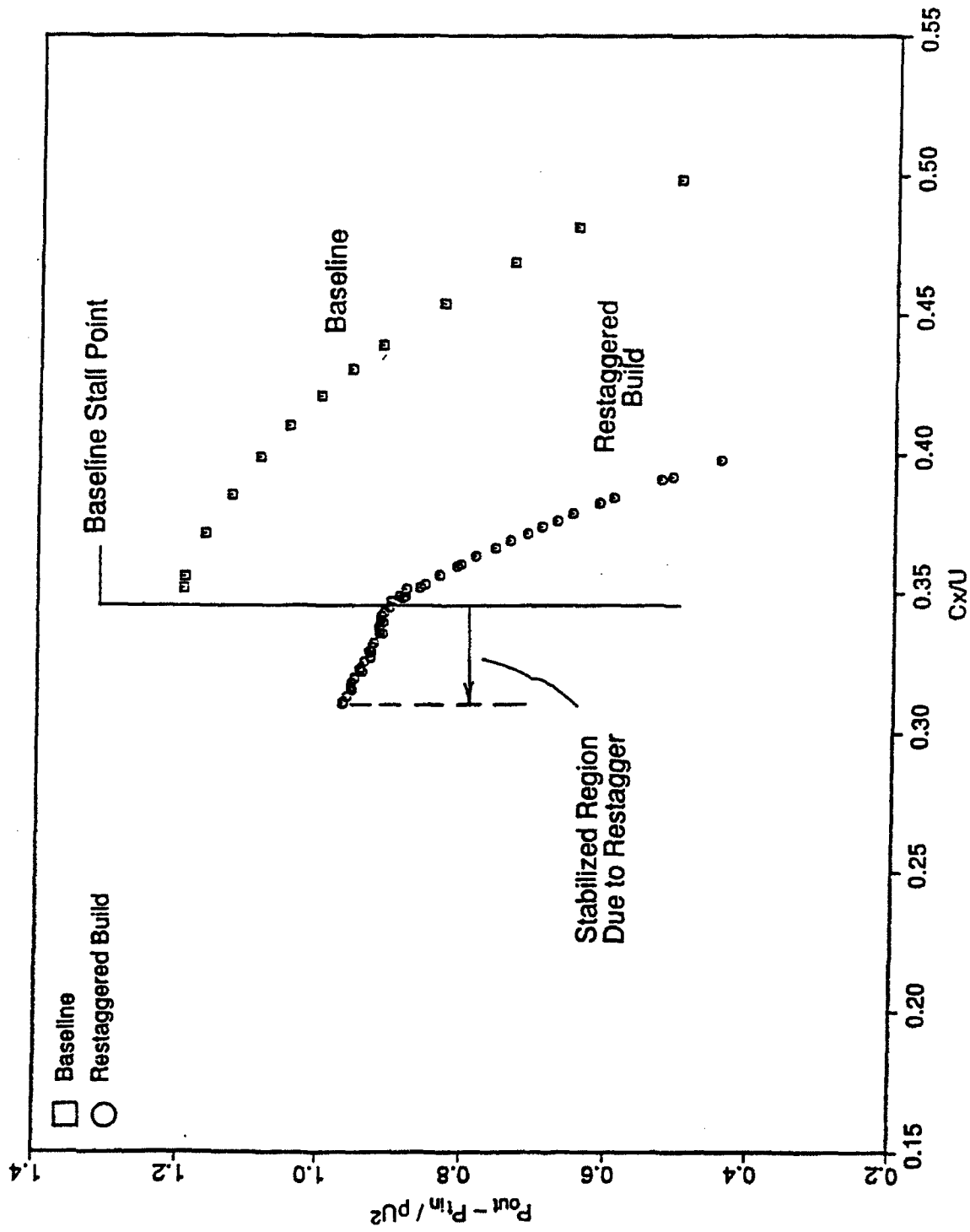


Fig. 5: Shift of overall characteristic due to restagger of rear three rotors by 10°.



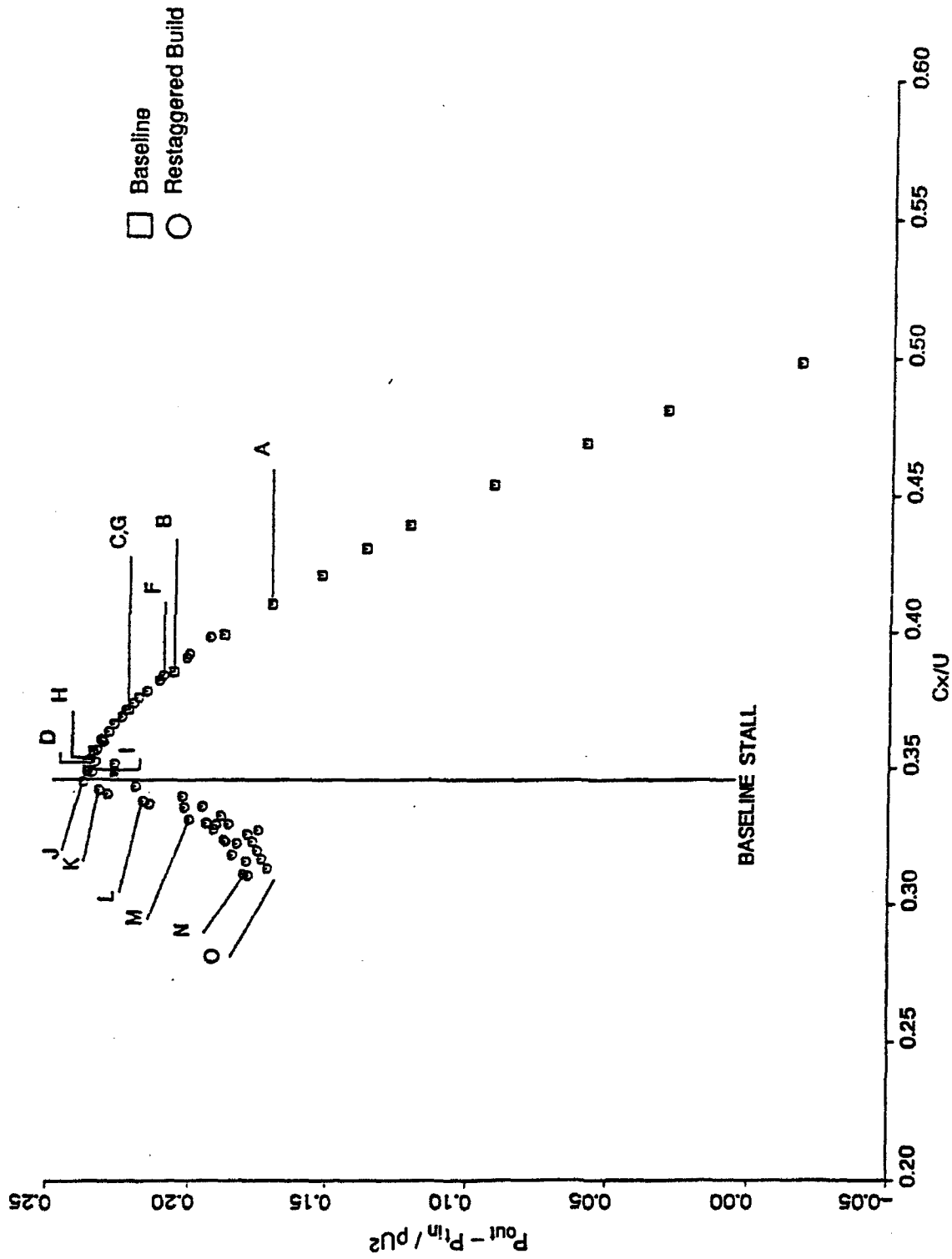


Fig. 6: Stage 1 characteristics for baseline and restaggered builds.

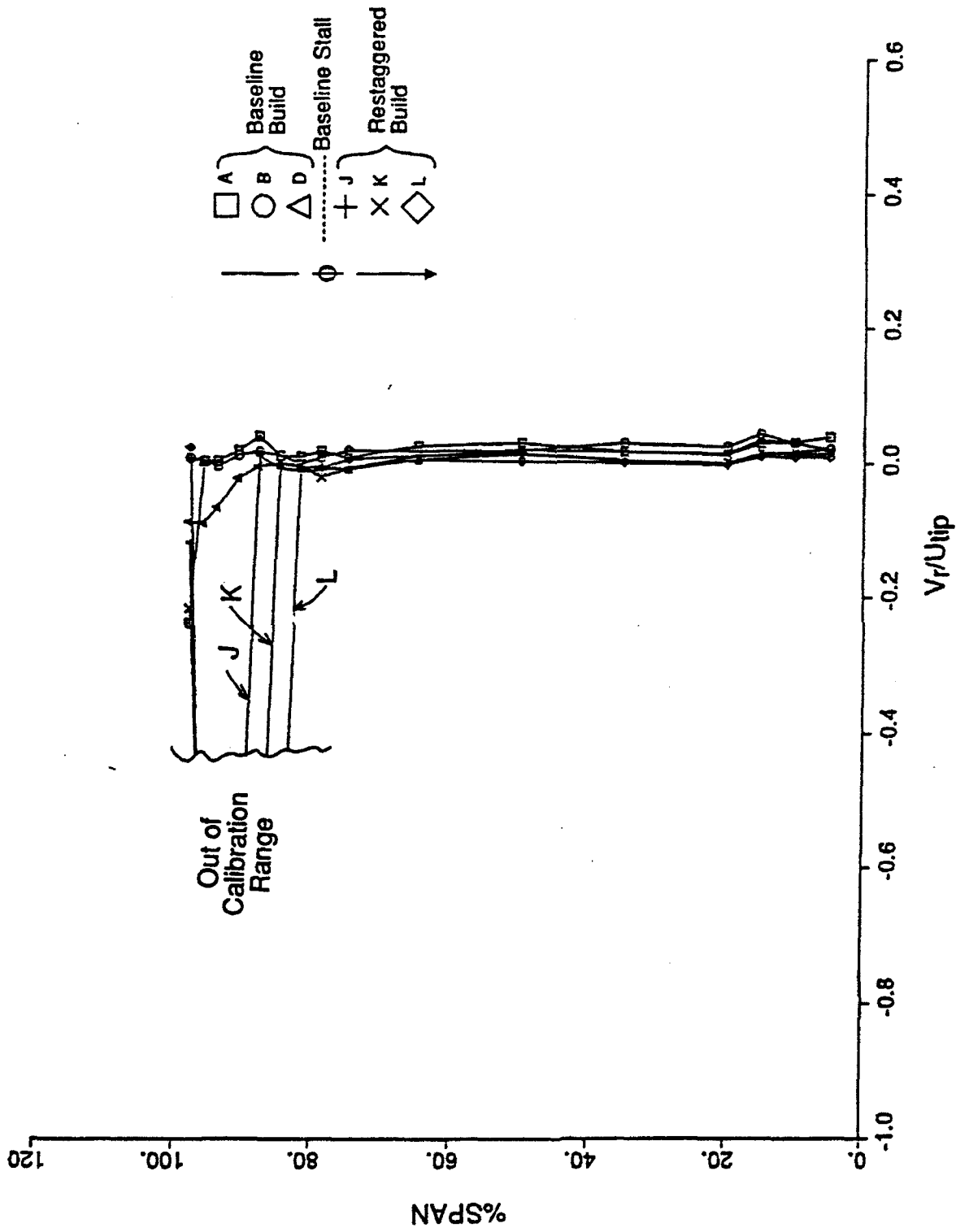


Fig. 7: Radial profiles of circumferentially mass-averaged radial velocity at rotor inlet.

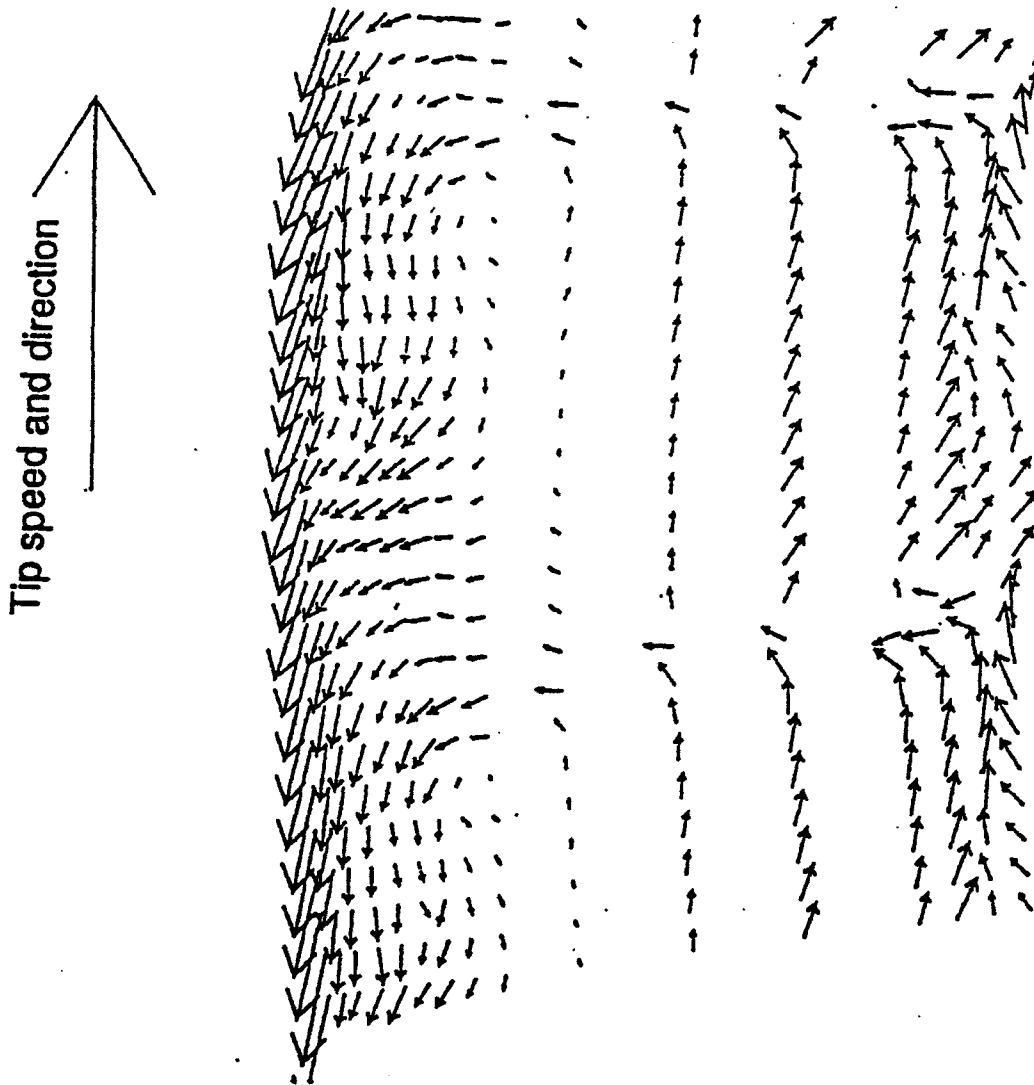


Fig. 8: Secondary flow at rotor exit in the relative frame (yaw = 55° from axial, operating point D, baseline build, near stall).

W/U<sub>tip</sub>

□ 0.3000

○ 0.3500

△ 0.4000

+ 0.4500

× 0.5000

◇ 0.5500

♠ 0.6000

⋈ 0.6500

⌢ 0.7000

Y 0.7500

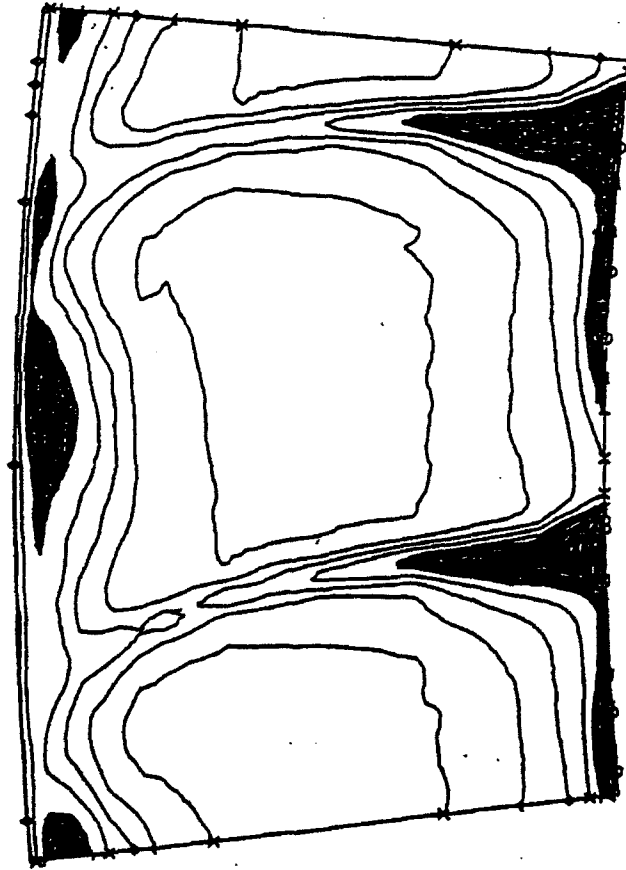


Fig. 9: Throughflow velocity at rotor exit (relative frame, yaw = 55° from axial, operating point D, baseline build, near stall).

W/U<sub>tip</sub>

□ 0.3000

○ 0.3500

△ 0.4000

+ 0.4500

× 0.5000

◇ 0.5500

♠ 0.6000

✕ 0.6500

∇ 0.7000

Y 0.7500

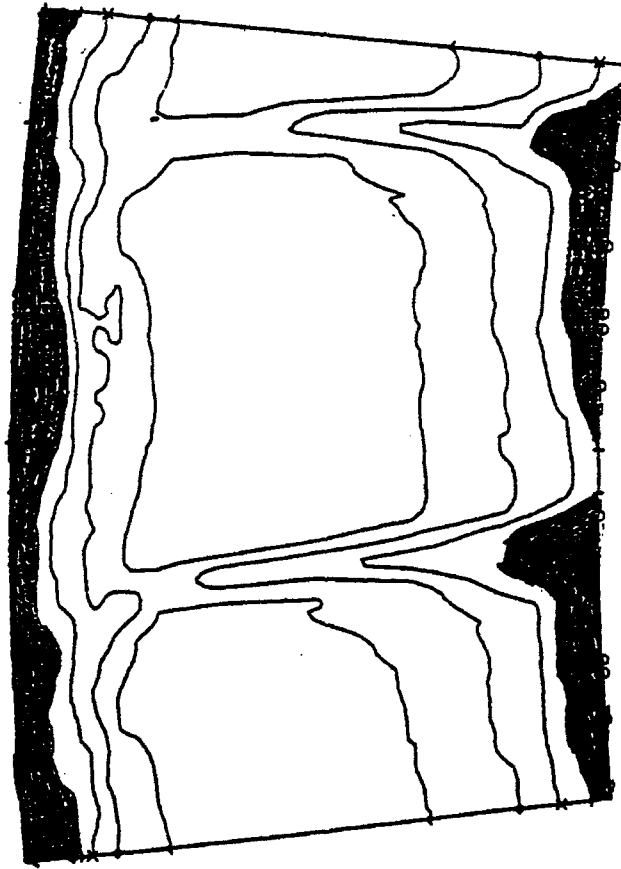


Fig. 10: Throughflow velocity at rotor exit (relative frame, yaw = 55° from axial, operating point K, restaggered build).

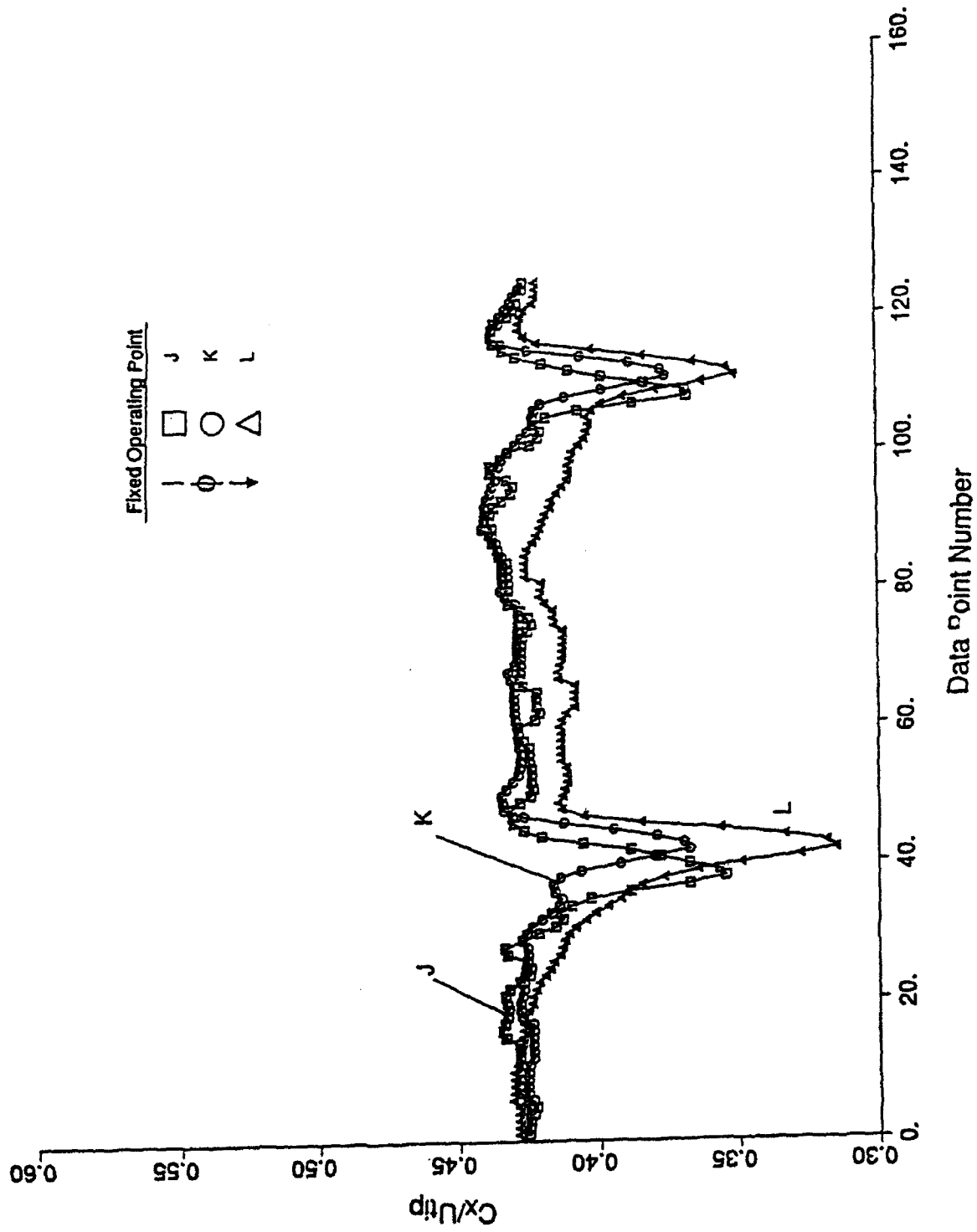


Fig. 11: Axial velocity at midspan of rotor exit, restaggered build.

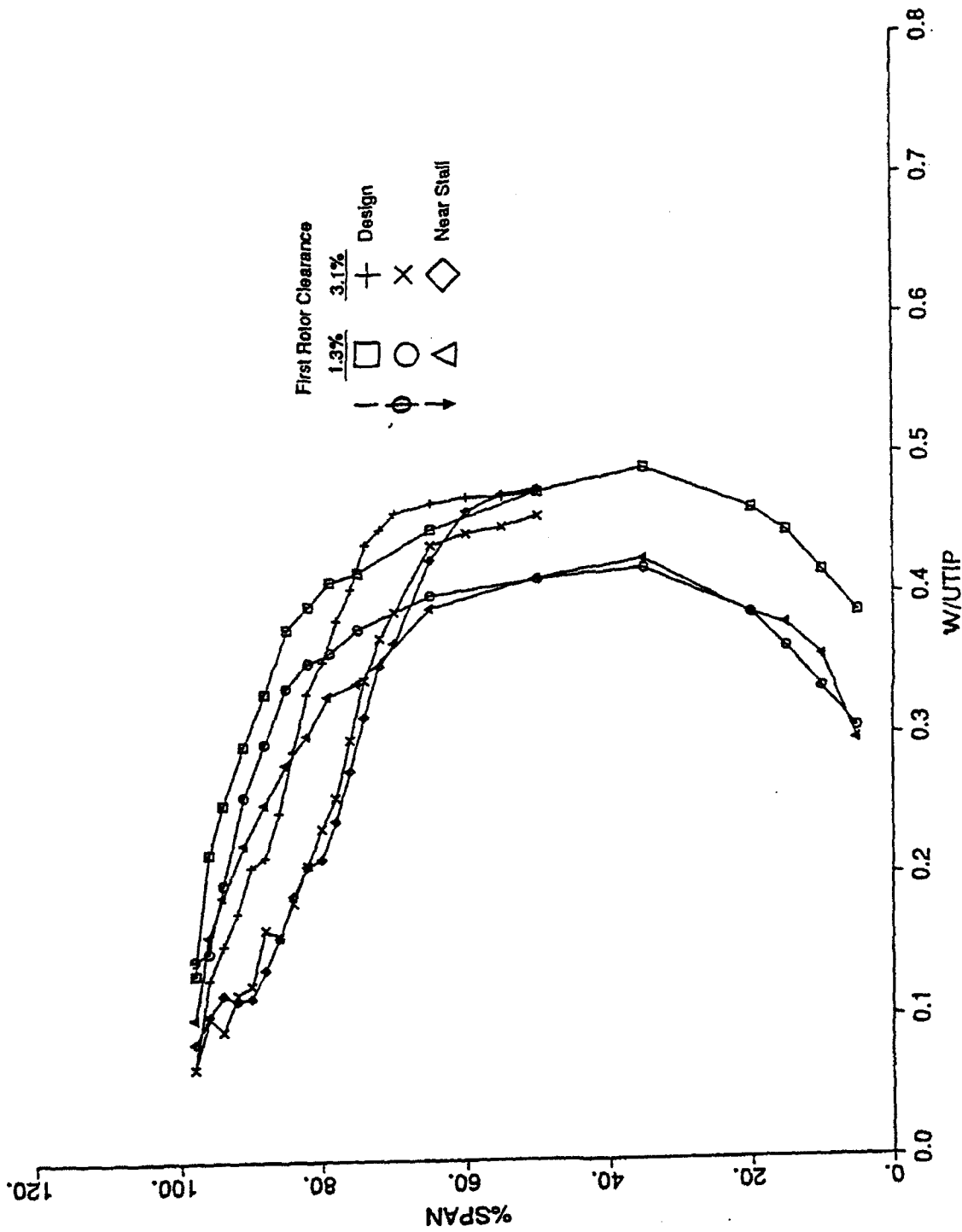


Fig. 12: Axial velocity at rotor exit (pitchwise average).

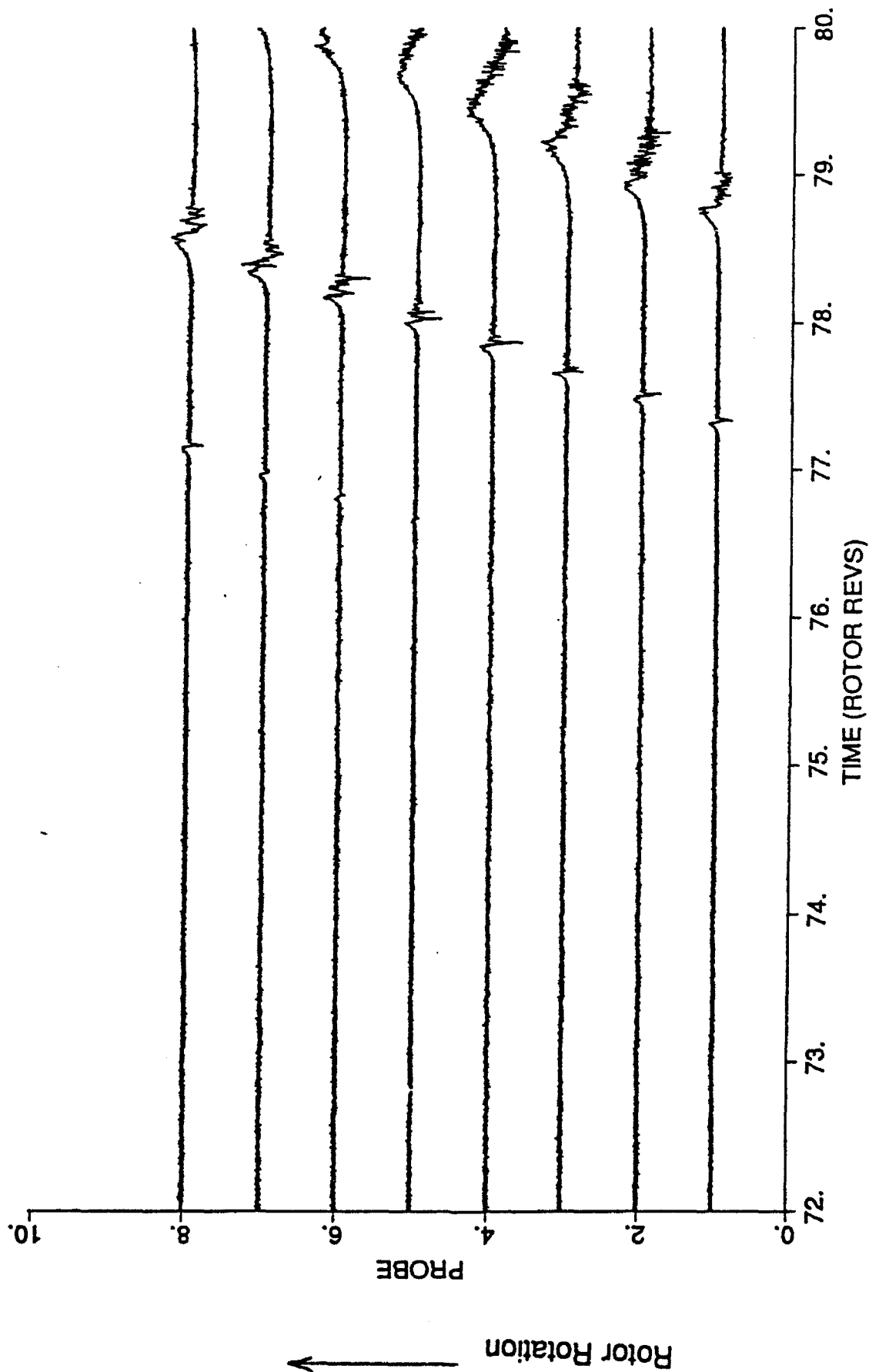


Fig. 13: Pressure at rotor inlet vs. time as the compressor is throttled down into stall  
(8 equally spaced casing transducers, normalized data, baseline build).



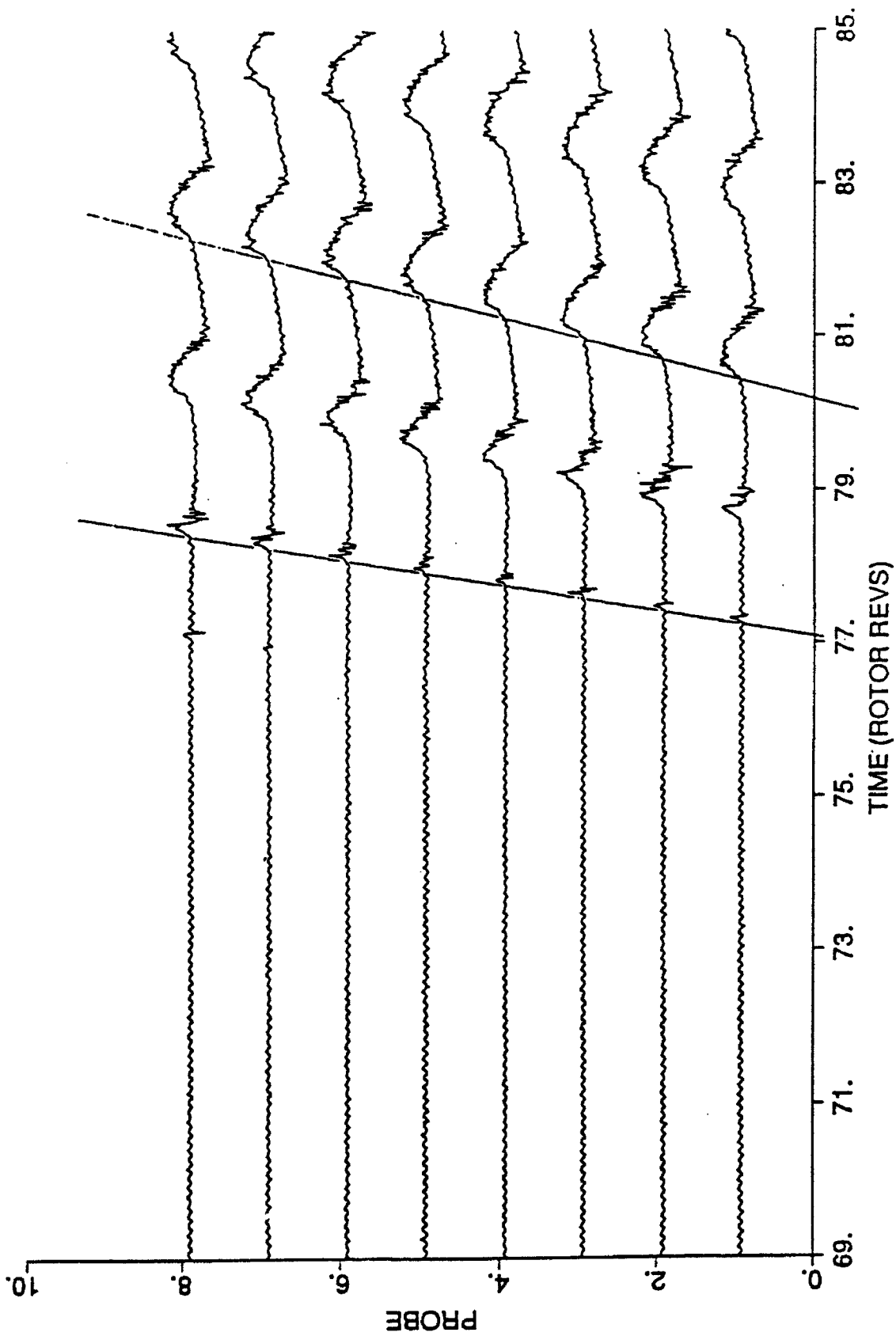


Fig. 14: Pressure at rotor inlet as the throttle is closed (8 equally spaced casing transducers).

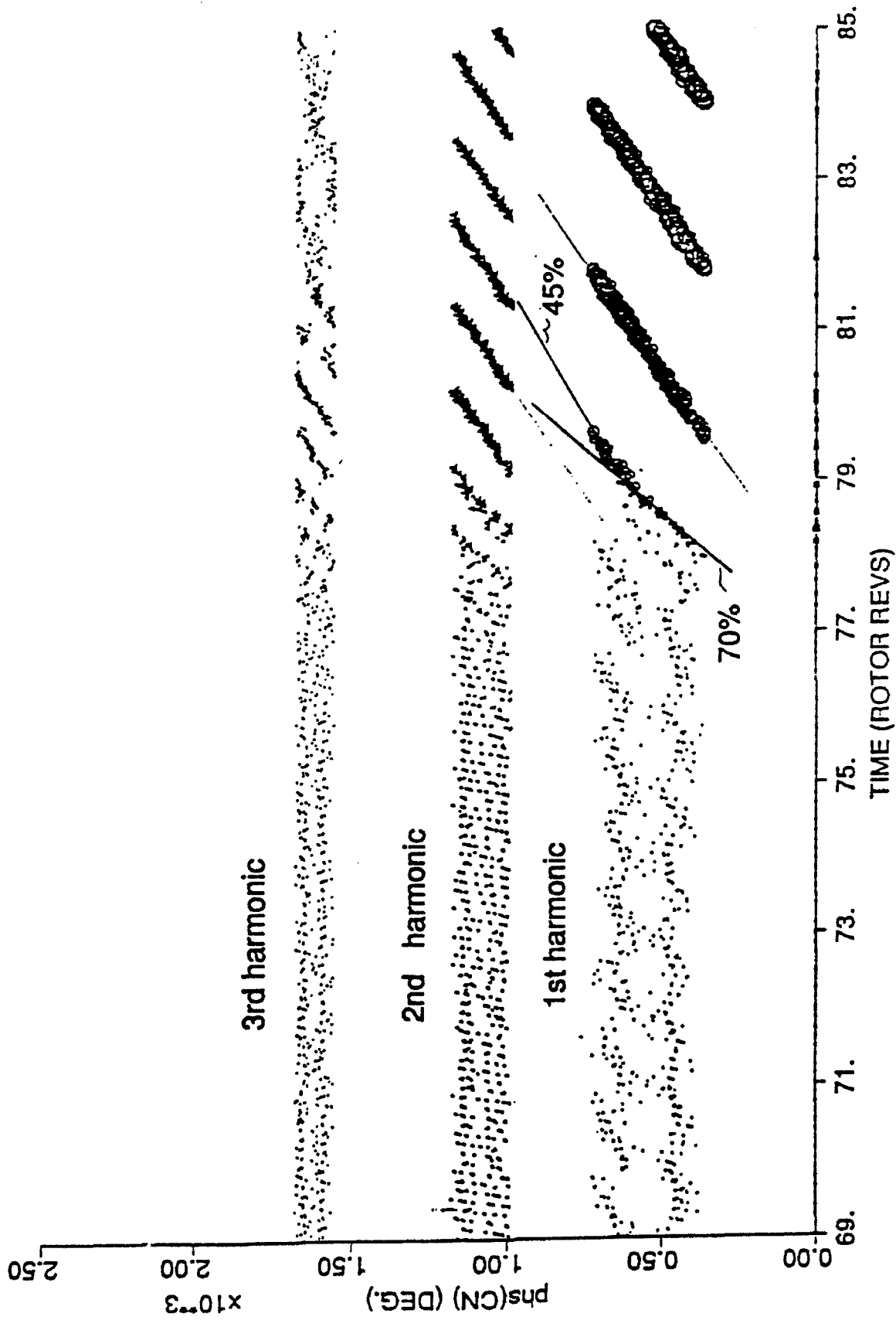


Fig. 15: Phase of spatial Fourier analysis of Fig. 14.

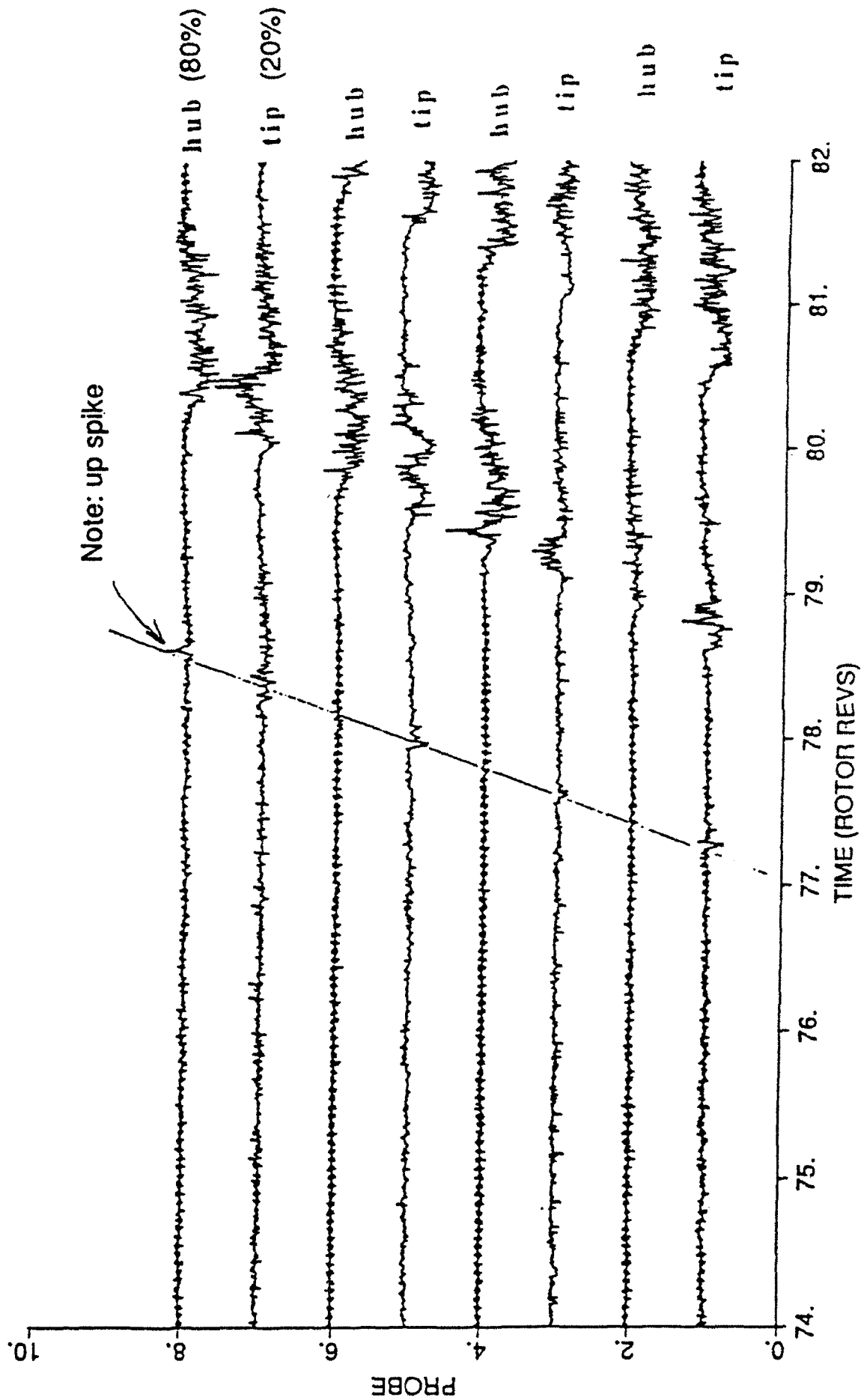


Fig. 16: Alternating hub/tip velocity at rotor inlet vs. time as the compressor is throttled down into stall (8 equally spaced hot wires, normalized data, baseline build).

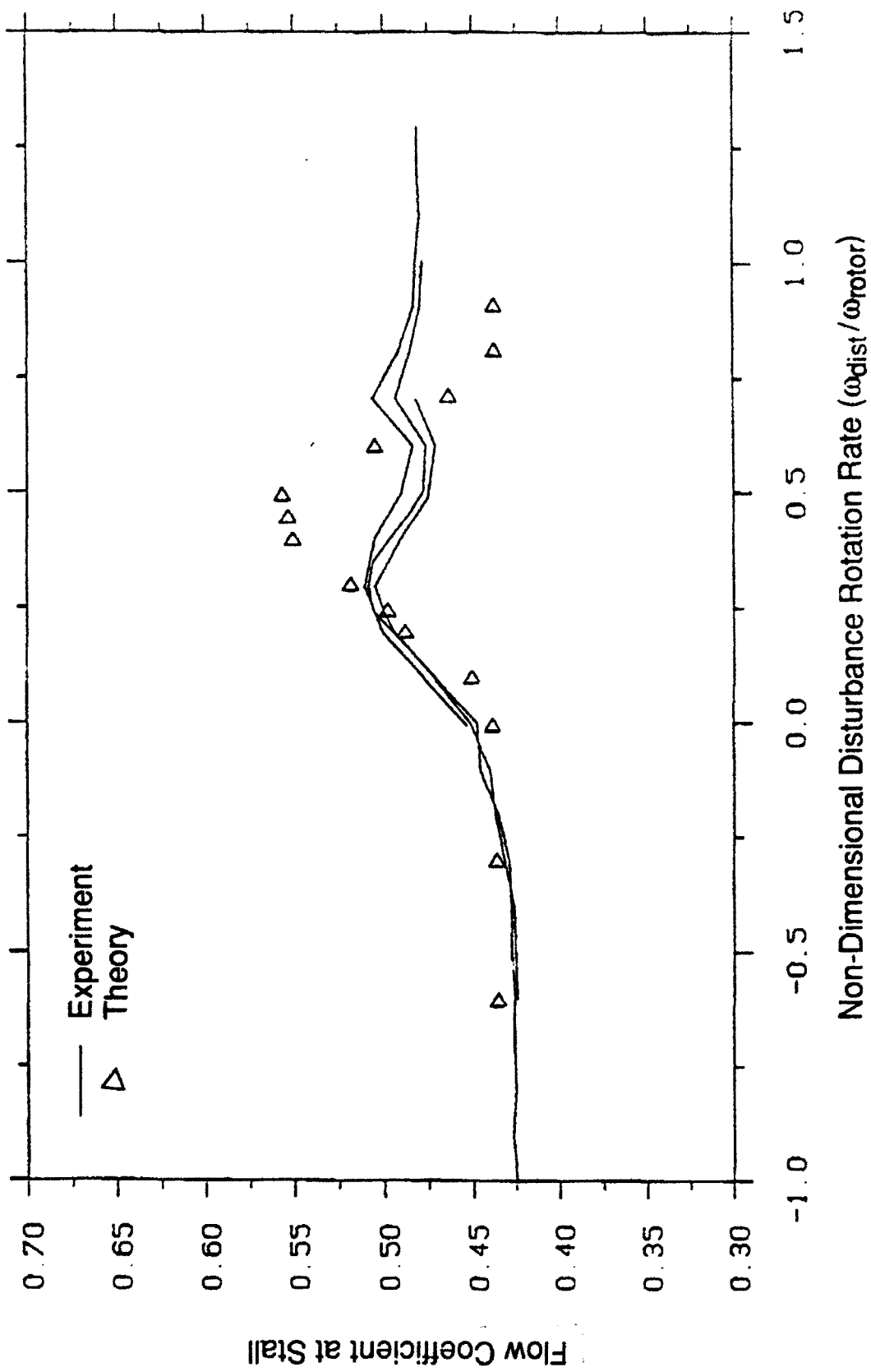


Fig. 17a: Effect of distortion rotation rate on multistage compressor stability (Compressor 1).

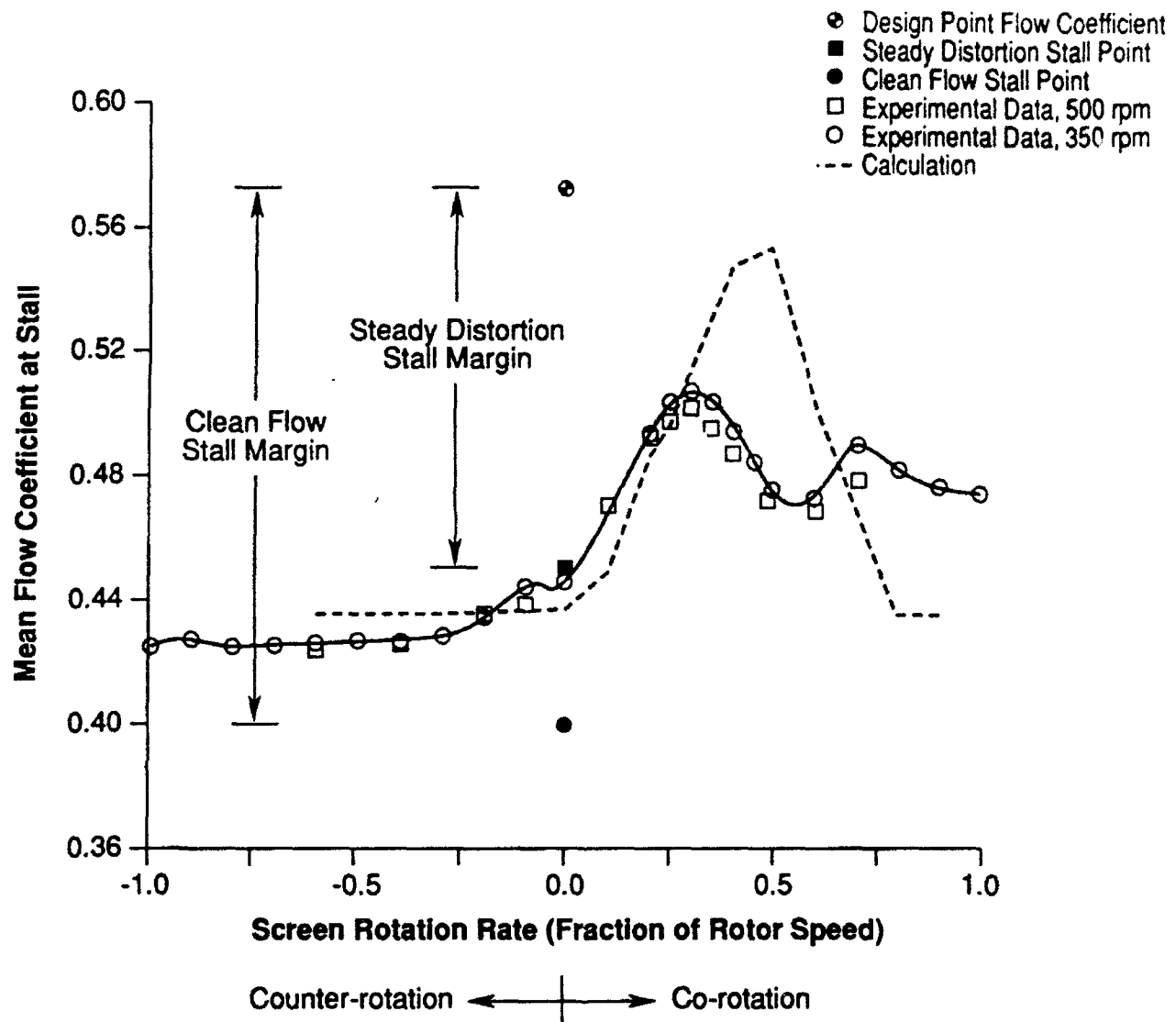


Fig. 17b: Calculated and experimental neutral stability flow coefficients for standard distortion

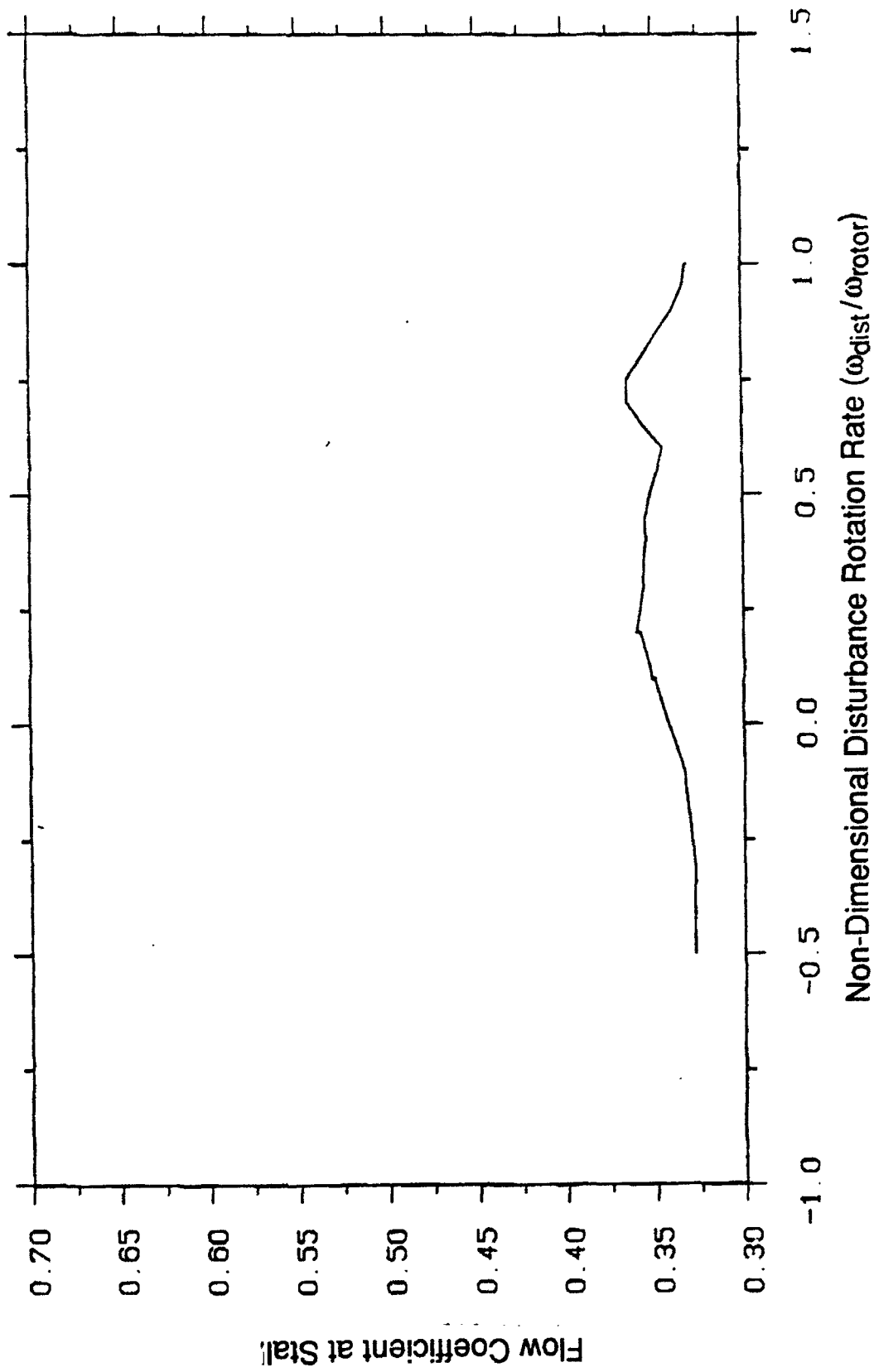


Fig. 18: Effect of distortion rotation rate on multistage compressor stability (Compressor 2).

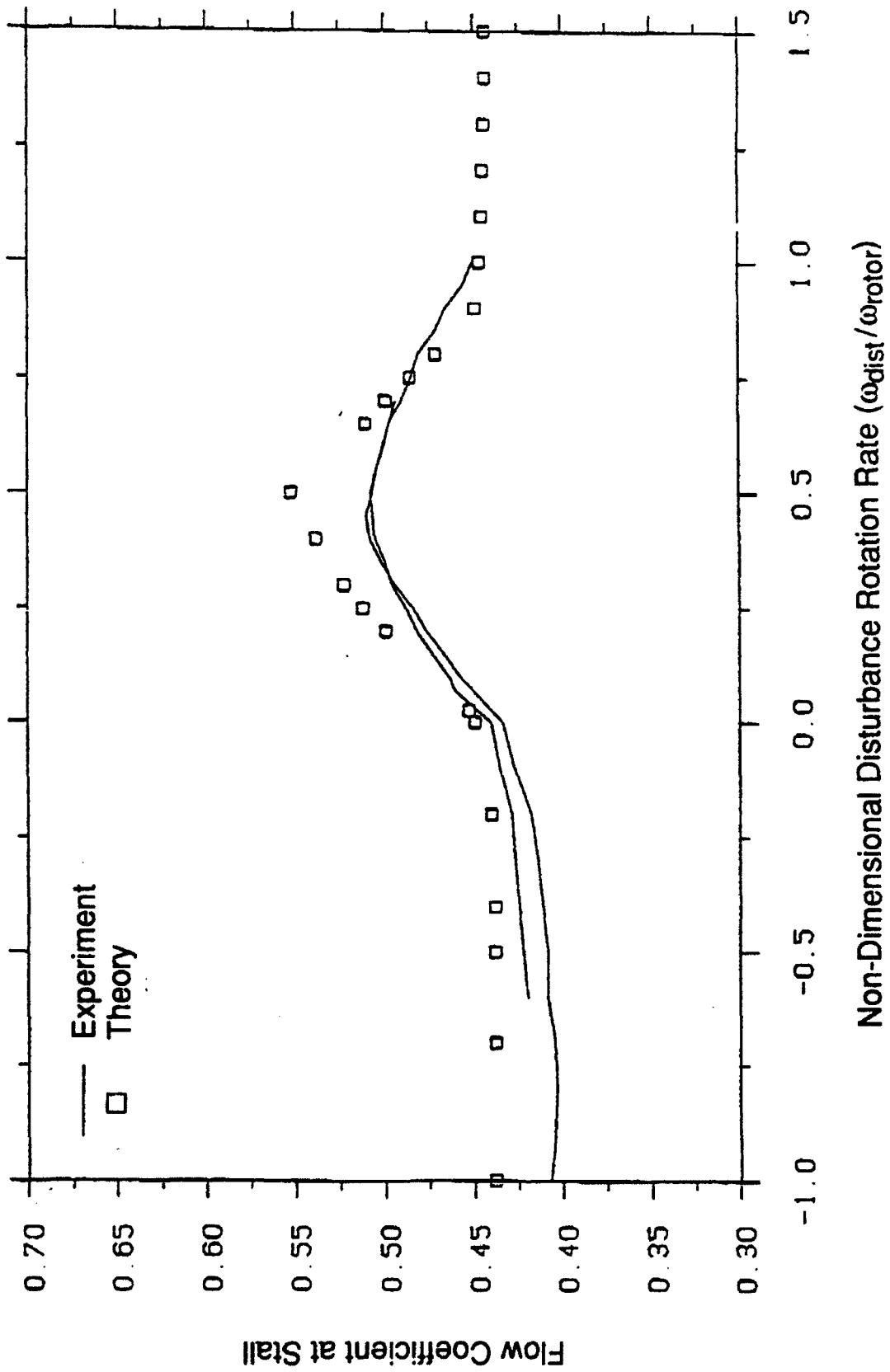


Fig. 19: Effect of distortion rotation rate on multistage compressor stability (Compressor 3).

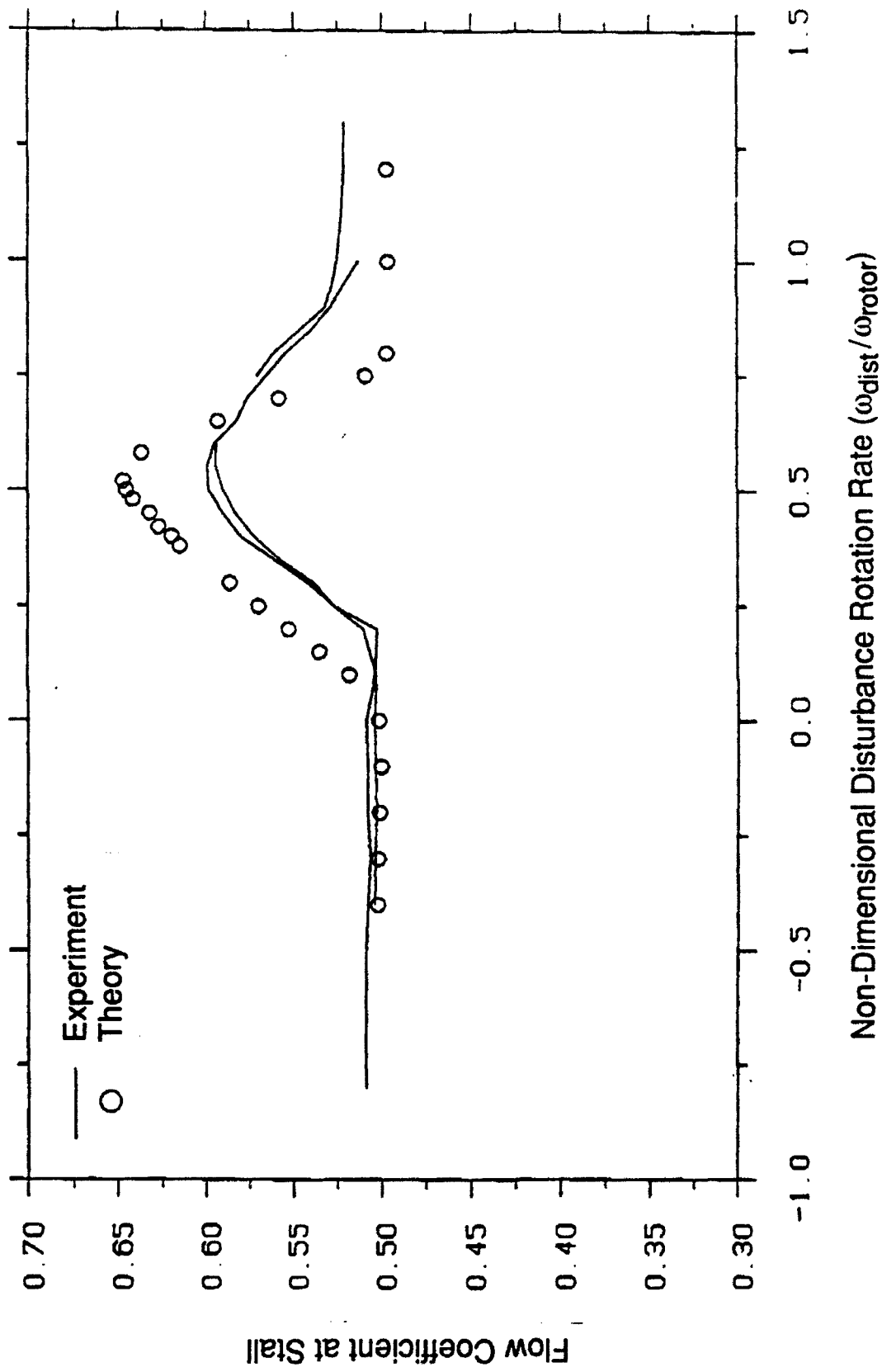


Fig. 20: Effect of distortion rotation rate on multistage compressor stability (Compressor 4).



# **TASK IV: VORTEX WAKE-COMPRESSOR BLADE INTERACTION IN CASCADES: A NEW RAPID METHOD FOR UNSTEADY SEPARATION AND VORTICITY FLUX CALCULATIONS**

(Investigators: J.E. McCune, A. Gioulekas)

## **1.0 Introduction**

In previous progress reports under this grant, we have described the motivation, as applied to bluff airfoils and cascaded blades, for the study of unsteady boundary layer separation in the aerodynamics of turbomachinery. We have also reported the gradual evolution under the program of a useful, much-simplified method for predicting the location and motion of the boundary layer separation points on such blades. This is the key information required to correctly predict the interaction of an airfoil or a blade with its own unsteady vortical wake at reduced frequencies found to be typical of unsteadiness in compressor blade rows, and the consequent prediction of fluid dynamic forces.

This work has now been completed and reported comprehensively in the Ph.D. Thesis of Dr. Alexandros Gioulekas, submitted to the faculty of MIT's Department of Aeronautics and Astronautics, and accepted in May 1992. The title of Gioulekas' thesis suggests its application(s) in the framework of modern aerodynamics, both internal and external: "An Alternative to the Kutta Condition for high Frequency, Separated Flows" (May 1992). A copy of the thesis abstract is attached as an appendix, and the complete thesis is available upon request.

A reproduction (see next section) of the Table of Contents of the thesis further provides a useful overview of the topics covered in this Task over the past few years. It also provides (indirectly) a listing, through Chapter 6 approximately, of the topics addressed in summary form in the earlier progress reports to the AFOSR under this grant.

In this final report, in the sections following the Gioulekas Table of Contents, we focus on our new and more complete results, obtained since the last progress report. The focus during that discussion is on the trends discovered, as a result of this research, for both the mean part (time average) of the blade response and for the variations with reduced frequency of the unsteady part. Some of these trends may appear surprising at first, but have been interpreted successfully by

Gioulekas in his thesis. In addition, some very interesting "rules of thumb" have emerged for the steady (time average) circulation, or turning, that a loaded blade can create in an unsteady flow environment.

## **2.0 Overview of Completed Research**

A brief summary of the research accomplished under this Task is effectively provided by the Table of Contents of Gioulekas' thesis:

### **Table of Contents\***

1	Introduction	14
1.1	Survey of previous work and connection to the present work	14
1.2	Synopsis of the thesis	29
1.3	Overview	32
2	Flow in a boundary layer with a rapidly oscillating free-stream velocity	33
2.1	Assumptions	33
2.2	The division of the flow-field	34
2.3	The non-dimensional form of the equations	41
2.4	The solution	48
2.5	Zero-th order approximation	49
2.6	Second order approximation	51
3	Unsteady separation	59
3.1	Conditions for unsteady separation	59
4	A criterion for predicting unsteady separation	71
4.1	Derivation of the criterion	71
4.2	Nondimensional form of the unsteady separation criterion	79
5	How the interaction between the airfoil and its wake determines the airfoil circulation and the force and moment acting on the airfoil	83
5.1	The circulation	84
5.2	Airfoil in oscillating stream vs. oscillating airfoil in steady stream: what is the difference in the aerodynamic force and moment?	91
5.3	Inertial and airfoil frames of reference	92
5.4	Calculation of the force using the unsteady Bernoulli equation	93
5.4.1	The pressure coefficient	93
5.4.2	The mapping of the physical to the circle plane	95
5.4.3	The force and moment coefficient	96
5.5	Calculation of the force using the impulse	96
5.6	Calculation of the moment using the moment of impulse	100
5.7	The free wake convection	104

---

\* Extracted from Gioulekas' Ph.D. Thesis. The page numbers refer to the thesis, not to this report.

6	The influence of reduced frequency, strength of flow unsteadiness, and ellipse slenderness on unsteady separation	106
6.1	Comparison between theoretical predictions and experiment	106
6.2	The influence of the strength of the unsteadiness on unsteady separation	123
6.3	The influence of the reduced frequency on unsteady separation	129
6.4	The influence of ellipse slenderness on unsteady separation	132
7	A parametric study of the circulation and of the aerodynamic forces acting on an airfoil in unsteady separated flow	143
7.1	How the separation trajectories influence circulation	135
7.2	The time evolution of the aerodynamic forces with varying angle of attack	139
7.3	The influence of the reduced frequency on the aerodynamic forces	145
7.4	The influence of the strength of the flow unsteadiness on the aerodynamic forces	152
8	Conclusions and recommendations for future research	158
8.1	Conclusions	158
8.2	Suggestions for future research	160
A	Why the boundary layer cannot be divided when the reduced frequency is low	168
B	A simplification in the "Stokes equations"	171
C	The nondimensional form of the "Prandtl velocity" distribution	173

- End -

The results discussed in the following sections are selected primarily from Chapters 6 and 7 of the above thesis.

### **3.0 Trajectories of the Upper-Surface Separation Points on Bluff Airfoils or Blades at Angle of Attack**

Application of the generally accepted separation criteria for unsteady boundary layer flow for practical problems involving blade-wake interaction has long been recognized as quite complex. Direct numerical study has been awkward, time consuming and expensive, with results that are both difficult to interpret and to generalize.

But in the research reported in Gioulekas' thesis, and in our earlier progress reports to AFOSR, we have been able to achieve a substantial simplification of this computational task without sacrificing the important physics involved. This is particularly so when the unsteadiness occurs at moderately high "reduced frequencies",  $\omega c/U > 1$ , for reasons originally pointed out

separately by C.C. Lin and by Lighthill. In addition to the simplifications suggested by Lin, we have been able to add an extension of the ideas of Stratford\* to provide an algebraically simple computational criterion for separation, involving only external parameters of the flow, steady or unsteady.

The result is that we can now readily calculate the instantaneous location and motion of the boundary layer separation point(s), without having to go through a complete boundary layer calculation at each time step. This means that when a blade or an airfoil is interacting with its own unsteady wake, the effect of the wake itself, back on the boundary layer that is "feeding" it, can be readily included, and this is a key feature of the results reported here.

The examples included below illustrate the kind of separation trajectories one finds above a slender, bluff airfoil in unsteady flow, and how these depend on some of the key parameters involved. The first cases shown are for an ellipse of slenderness ratio 1:20 at zero mean angle-of-attack. In that case, of course, the separation trajectories on the lower surface of the blade are the mirror image of those shown here. Results for finite mean angle-of-attack are discussed in the following section, in terms of the blades' aerodynamic response, both for the steady and for the unsteady component.

The value of the reduced frequency,  $\omega c/U_\infty$ , in the first case shown for this section, is

$$\lambda^2 \equiv \frac{\omega c}{U_\infty} = 9 ,$$

and results are shown as a function of the strength of the unsteady oscillations, as measured by

$$\varepsilon = \frac{\hat{U}_\infty}{U_\infty} .$$

Here,  $c$  is the airfoil chord and the external flow is  $U_\infty = \bar{U}_\infty + \hat{U}_\infty e^{i(\omega t + \phi)}$ .

Figure 1, extracted from Chapter 6 of the thesis, shows separation point trajectories near the ellipse's trailing edge for  $\varepsilon = 0.01, 0.005, 0.001$ , and 0. The steady flow separation point, as

---

\* An extensive bibliography is provided in Gioulekas' thesis, and has also been made available in earlier AFOSR progress reports. A feature of Gioulekas' thesis, in fact, is the usefulness of his bibliography.

calculated by Howarth (see discussion in previous reports, or in the thesis), is also shown for reference. Each trajectory shown represents the path traversed by the separation point over one period of oscillation.

The figure shows that as the strength or amplitude of unsteadiness decreases from 1% to 0, the trajectories shrink in range and converge on the steady-flow separation point, as would be expected. However, one also readily sees that not all effects are simply "linear" in  $\epsilon$ .

Figure 2 gives corresponding results for fixed  $\epsilon$ , but with varying reduced frequencies, ranging from 9 to 36. At first, these results may seem surprising, because one sees that as the frequency increases at fixed amplitude, the trajectories again converge toward the steady-flow separation location.

This phenomenon is explained by Gioulekas in his thesis. In simple terms, at high frequency the response of the unsteady part of the flow to the wall's resistance is confined to an ever-thinner sheath, analogous to Stokes flow for an oscillating infinite wall. In the limit, this inner sheath becomes decoupled from the "Prandtl-type" boundary layer, which is the part of the flow that responds primarily to the steady part of the wall's resistance, that is, to the mean (time-averaged) flow. Thus, at very high reduced frequencies, the "Stokes layer" and the "Prandtl layer" become decoupled, and in the limit, the boundary layer separation properties are determined completely by the mean flow, precisely because the frequency is high.

#### **4.0 Aerodynamic Response for Loaded Separated Blades**

With the new method made available by his analysis of the problem, and by his corresponding extension of the "Stratford Criterion" to unsteady flow, Gioulekas was able to systematically investigate the aerodynamic response of bluff-edged airfoils over a range of blade slenderness and of mean angle-of-attack.

As we have pointed out in our earlier reports, the new method of rapid location of the separation trajectories plays the same role in determining the blade circulation as does the classical Kutta condition for unseparated, sharp-edged blades or airfoils. It is natural, therefore, to compare

the results Gioulekas obtained with those that would be obtained if the Kutta condition were assumed to apply.

A second benchmark is the circulation that would be obtained in steady flow over the separated bluff airfoil at angle-of-attack, as first obtained by Howarth.

With these limits in mind, Tables 1 and 2 provide useful and revealing summary information to guide our understanding of blade performance in unsteady flow.

In Table 1, the results for an elliptic airfoil of fineness 1:20, at angle-of-attack =  $5^\circ$ , and for an amplitude of unsteadiness  $\epsilon = 0.04$ , are shown for a range of reduced frequencies. Tabulated are the mean (time-averaged) circulation  $\bar{\Gamma}$  developed by the blade, the time-varying circulation  $\hat{\Gamma}$ , and the phase-shift, to be compared with classical unsteady airfoil theory. The values on the left are those that are obtained if the Kutta condition is (arbitrarily) assumed. Those on the right are the responses obtained using the present theory, and are thus based on the more realistic prediction of the instantaneous location and movement of the boundary layer separation point(s).

We note that the values of  $\bar{\Gamma}$  actually achieved by the blade are systematically lower than those it "could" achieve if Kutta applied.

We also note that  $\Gamma_{\text{Howarth}}$ , the steady flow value of circulation obtained by the same airfoil, at the same angle-of-attack, taking into account the separation of the upper-surface boundary layer, would be

$$\Gamma_{\text{Howarth}} = 0.267 \quad ,$$

about 8% less than  $\Gamma_{\text{Kutta}}$ . Based on our observations of the separation trajectories described in Section 3.0, it is clear why, as the frequency increases, the actual  $\bar{\Gamma}$  approaches the lower, separated steady-flow value,  $\Gamma_{\text{Howarth}}$ , for a bluff-edged airfoil.

In any case, the results provide us with useful bounds for the mean circulation obtainable by a bluff-edged blade at angle-of-attack in any unsteady environment:

$$\Gamma_{\text{Howarth}} \leq \bar{\Gamma} \leq \Gamma_{\text{Kutta}} \quad .$$

These bounds can be used, for example, to estimate the maximum loss of mean turning angle that might occur in a blade row as a result of unsteadiness. The higher the frequency, the closer the

lower value is approached. And, at fixed frequency, the thinner the blade, the more closely  $\Gamma_{Kutta}$  can be obtained.

Table 2 serves as one check on the theory, and verifies that, as the blade is chosen thinner and thinner, conditions approach those appropriate to the classical Kutta condition, other parameters being held constant. This is true not only for the mean circulation,  $\bar{\Gamma}$ , but also for the properties of the unsteady component of the blade response. The amplitudes  $\hat{\Gamma}$ , and the phase angles  $\theta_{\Gamma}$ , obtained from the new theory, agree remarkably well, for very thin elliptical blades, with the results of classical thin airfoil theory. Table 2 shows this agreement for the example of an elliptical blade of fineness ratio 1:50, at reduced frequency  $\lambda^2 = 9$ .

Summary conclusions of the kind given in the above two tables were obtained by systematic study of the results obtained for many cases (each for a given set of the above-mentioned parameters) by runs such as are illustrated in Figs. 3 through 5. These figures show how the aerodynamic responses were actually obtained and analyzed, and illustrate only a small sample of the results reported by Gioulekas.

## **5.0 Future and Ongoing Applications**

The extensive results available in Gioulekas' thesis represent a substantial study of the blade-wake interaction effect for driven, or imposed, unsteady oscillations, including realistic treatment of the boundary layer separation properties.

Future work includes application of this technique to the determination of natural-oscillation regimes (analogous to the Karman vortex street behind a cylinder) for thin elliptical blades or airfoils.

The method also has direct application to the dynamic stall problem for airfoils in external flow.

$\lambda^2$	(a) Kutta Condition			(b) Separation		
	$\bar{\Gamma}$	$\hat{\Gamma}$	$\theta_{\Gamma}$	$\bar{\Gamma}$	$\hat{\Gamma}$	$\theta_{\Gamma}$
9	0.288	0.0015	$-50^\circ$	0.279	0.003	$-46^\circ$
18	0.288	0.001	$-52^\circ$	0.272	0.002	$-59^\circ$
36	0.288	0.0005	$-54^\circ$	0.271	0.001	$-65^\circ$

**TABLE 1:** The circulation  $\Gamma(t) = \bar{\Gamma} + \hat{\Gamma} \cos(\omega t + \theta_{\Gamma})$  around an ellipse calculated by: (a) assuming smooth flow at the trailing edge, and (b) using the new separation criterion, as the reduced frequency increases ( $b : a = 1 : 20$ ,  $\alpha = 5^\circ$ ,  $\varepsilon = 0.04$ ). Note that  $\bar{\Gamma} \rightarrow \Gamma_{\text{Howarth}} = 0.267$  as the reduced frequency increases.

Slenderness Ratio	(a) Kutta Condition			(b) Separation		
	$\bar{\Gamma}$	$\hat{\Gamma}$	$\theta_{\Gamma}$	$\bar{\Gamma}$	$\hat{\Gamma}$	$\theta_{\Gamma}$
1:20	0.288	0.0015	$-50^\circ$	0.279	0.003	$-46^\circ$
1:50	0.279	0.002	$-46^\circ$	0.279	0.002	$-46^\circ$

**TABLE 2:** The circulation  $\Gamma(t) = \bar{\Gamma} + \hat{\Gamma} \cos(\omega t + \theta_{\Gamma})$  around an ellipse calculated by: (a) assuming smooth flow at the trailing edge, and (b) using the new separation criterion, as the ellipse becomes slimmer ( $\alpha = 5^\circ$ ,  $\lambda^2 = 9$ ,  $\varepsilon = 0.04$ ).

\* All " $\Gamma$  values" presented here are made dimensionless with  $U_{\infty}c$ , i.e., each number is (circulation)/ $U_{\infty}c$ .



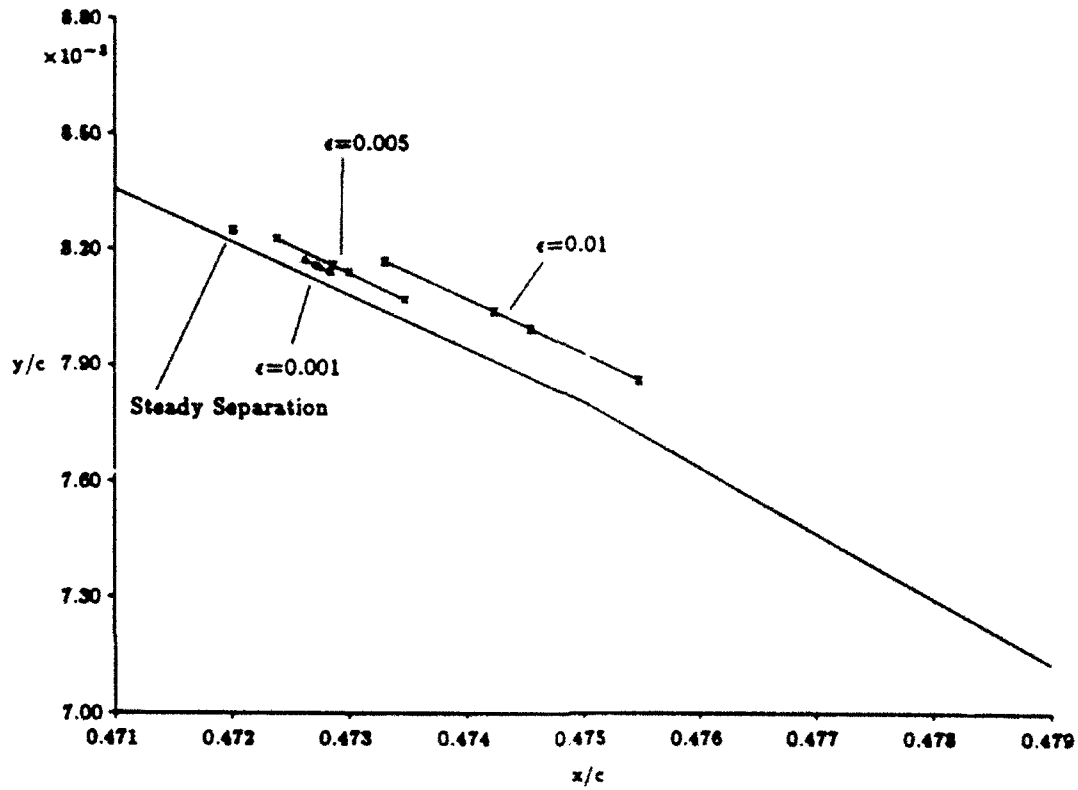


Fig. 1: The separation trajectory for varying strength of flow unsteadiness,  $\epsilon = 0.001, 0.005, 0.01$ , and constant reduced frequency,  $\lambda^2 = 9$ . The separation trajectory shrinks and approaches the location of steady separation as  $\epsilon$  approaches zero.

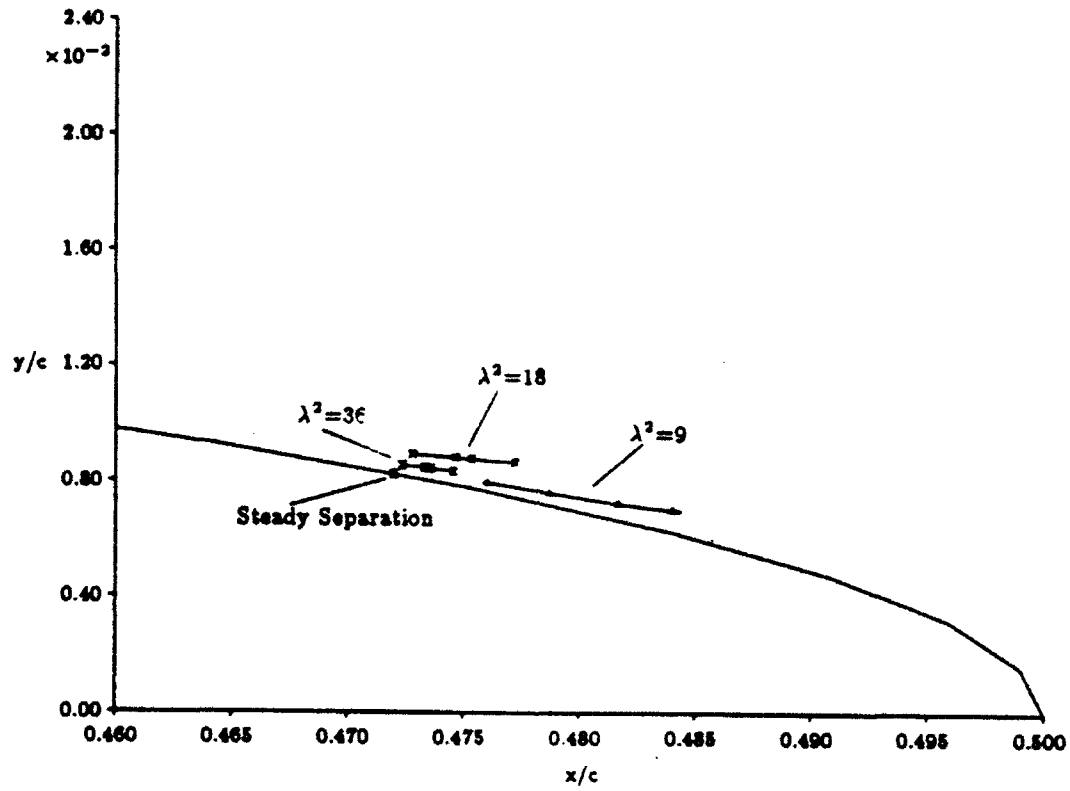


Fig. 2: The separation trajectory for varying reduced frequency,  $\lambda^2 = 9, 18, 36$ , and constant strength of flow unsteadiness,  $\epsilon = 0.04$ . The amplitude of the separation point excursion scales with  $1/\lambda^2$ .

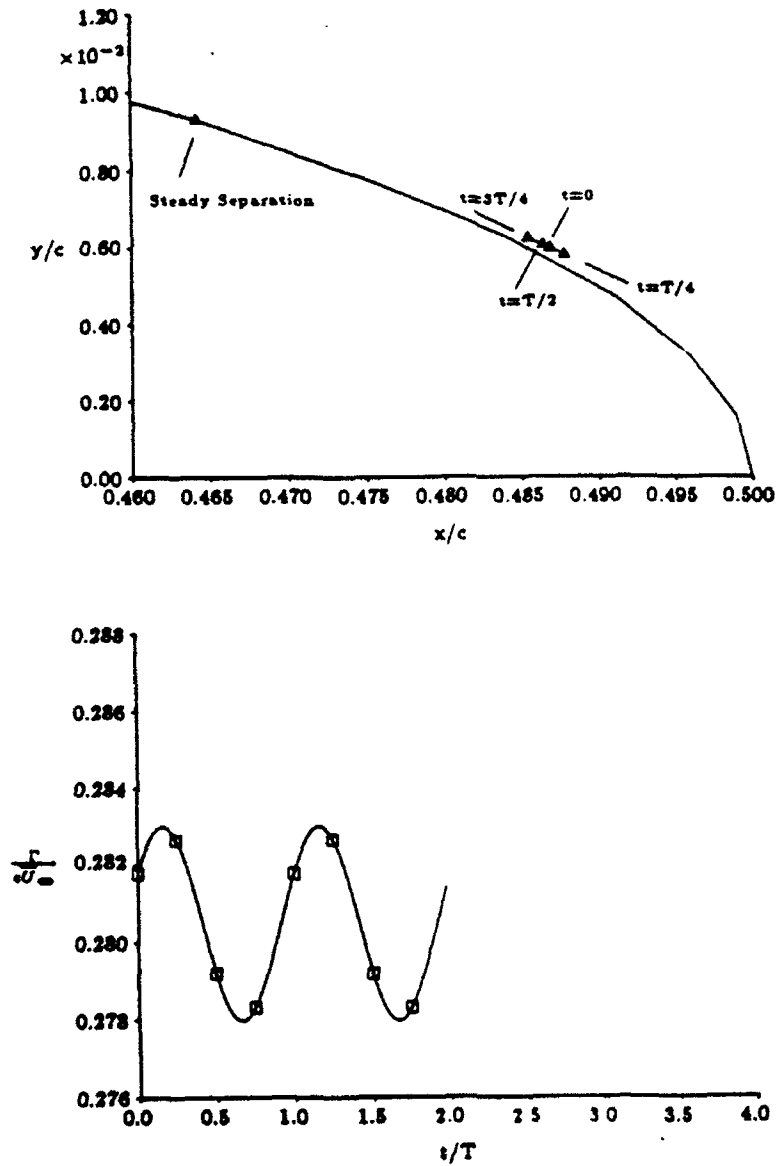


Fig. 3: The stationary points  $t = T/4, /; t = 3T/4$  of the suction-side separation trajectory roughly correspond to the stationary points in  $\Gamma^*(t)$ . The ellipse ( $b/a = 1 : 20$ ) is placed at an angle of attack  $\alpha = 5^\circ$  in a stream oscillating with strength  $\varepsilon = 0.04$  at reduced frequency  $\lambda^2 = 9$ .

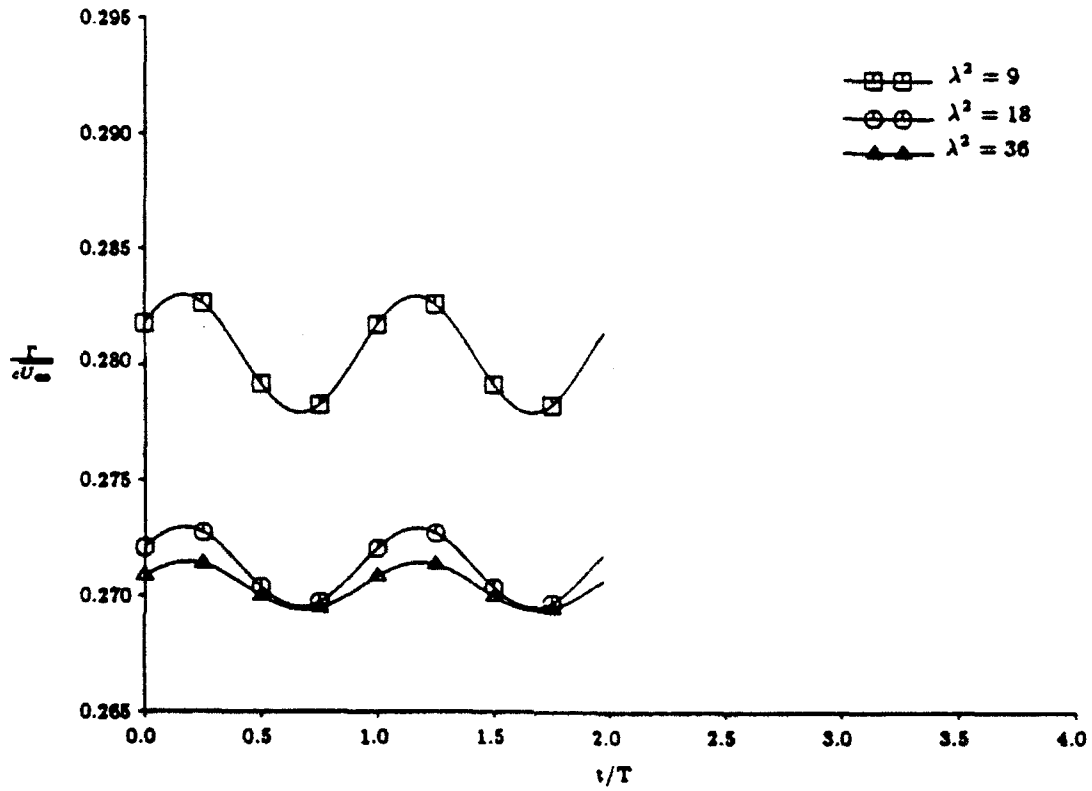


Fig. 4: Time evolution of the non-dimensional circulation for varying reduced frequency ( $\lambda^2 = 9, 18, 36$ ) and constant strength of flow unsteadiness ( $\epsilon = 0.04$ ). The circulation is bracketed by  $\Gamma_{\text{Kutta}} = 0.283$  and  $\Gamma_{\text{Howarth}} = 0.267$ . The ellipse ( $b/a = 1 : 20$ ) is at an angle of attack  $\alpha = 5^\circ$ .

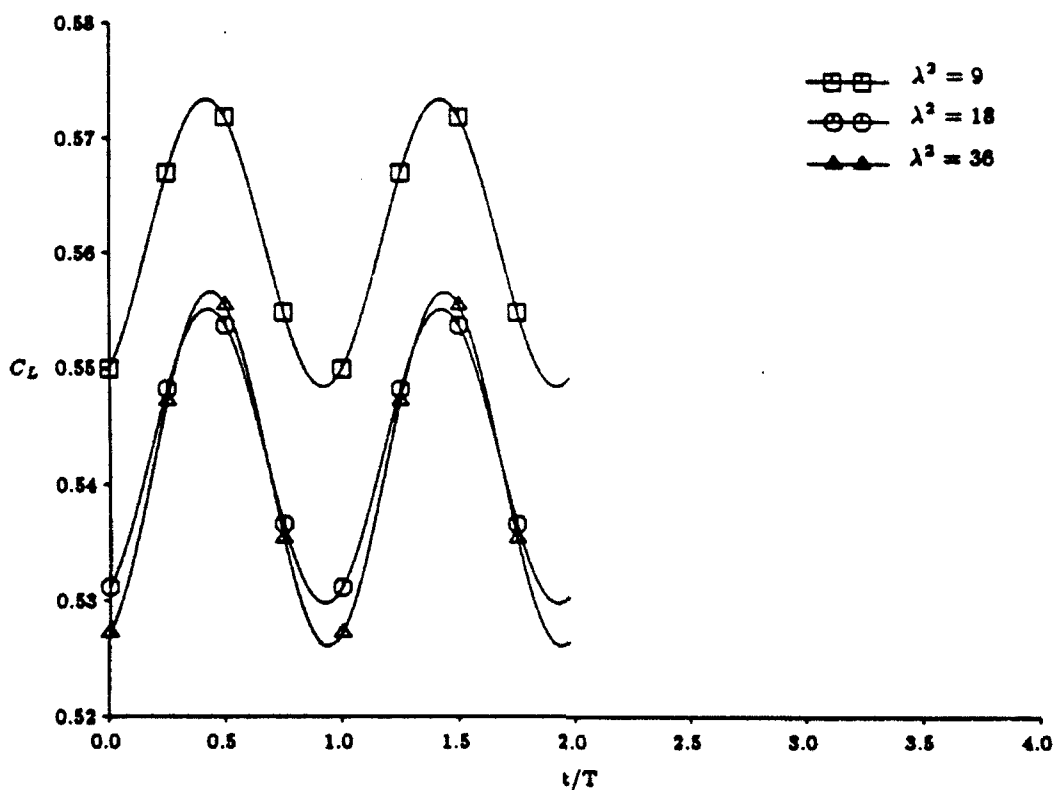


Fig. 5: Time evolution of the lift coefficient for varying reduced frequency ( $\lambda^2 = 9, 18, 36$ ) and constant strength of flow unsteadiness ( $\epsilon = 0.04$ ). The ellipse ( $b/a = 1 : 20$ ) is at an angle of attack  $\alpha = 5^\circ$ .

## APPENDIX IV.1

**An alternative to the Kutta condition  
for high frequency, separated flows**

by

Alexandros Gioulekas

Submitted to the Department of  
Aeronautics and Astronautics  
in partial fulfillment of the  
requirements for the Degree of  
Doctor of Philosophy

**Abstract**

An alternative to the Kutta condition for determining the circulation around a bluff airfoil in unsteady, separated flow is presented. For such flows, there is a need for a practical criterion which would avoid the detailed boundary layer calculations and would predict the time evolution of the airfoil circulation based on the external potential flow only.

This criterion would play for unsteady, separated flows the role that the Kutta condition plays for flows past thin airfoils. It turns out to be a criterion for predicting the location and movement of the "separation points", because they determine the net vorticity flux shed into the wake and thus the rate of change of the airfoil circulation.

The laminar, two-dimensional flow about a bluff airfoil at angle of attack, when the external flow oscillates at a high reduced frequency is considered.

At high frequencies, the vorticity generated as the wall resists the imposed unsteadiness is confined to a thin layer near the blade surface ("Stokes layer") and its contribution to the displacement thickness is proportional to an inverse power of the reduced frequency and thus small. Outside this region, the unsteady part of the boundary layer velocity is approximately the external potential oscillation. Based on this observation and following C.C. Lin, the boundary layer velocity can be divided into two coupled velocity distributions, one predominantly oscillatory ("Stokes velocity") and another predominantly steady ("Prandtl velocity"). The main contributor to the displacement thickness is the latter. Therefore, separation, identified by a dramatic increase in the displacement thickness, can be located by calculating the evolution of the "Prandtl velocity" and finding where the latter bifurcates.

Stratford's ideas, modified to account for unsteadiness in the "Prandtl velocity"

(arising through the coupling of the "Prandtl" to the "Stokes" flow by the no-slip condition on the wall and Reynolds-stress terms in the momentum equation), lead to a criterion for unsteady separation that uses as only inputs parameters of the external flow and avoids a detailed boundary layer calculation.

The airfoil circulation is calculated by an iterative method which calculates how the interaction between the airfoil and its wake affects separation.

An ellipse is adopted as a study case, and results are presented for varying angle of attack, ellipse slenderness, reduced frequency, and strength of unsteadiness. In the limit of a very slender ellipse, the theory recovers the results from the classical unsteady wing theory, which assumes the Kutta condition.

The theory predicts that there exist two limits for the mean value of the circulation. The upper limit is the value of the circulation for which the trailing edge becomes a stagnation point ( $\Gamma_{\text{Kutta}}$ ). The lower limit is the value of the circulation in steady flow ( $\Gamma_{\text{Howarth}}$ ).

The pressure-side "separation point" for all practical purposes can be considered fixed, even at small angles of attack. On the other hand, the "separation point" on the suction-side oscillates with amplitude proportional to the strength of the flow unsteadiness, and inversely proportional to the reduced frequency. When the reduced frequency increases or the strength of flow unsteadiness decreases, the trajectory of this "separation point" shrinks and tends toward the position of steady separation. Since the mean location of the suction-side "separation point" controls the mean value of the circulation, and the amplitude of its excursion determines the amplitude of the oscillatory component of the circulation, the above trends explain how the circulation responds to changes in the flow unsteadiness.

Thesis Supervisor: James E. McCune

Title: Professor of Aeronautics and Astronautics

### 3. AIR FORCE RESEARCH IN AERO PROPULSION TECHNOLOGY (AFRAPT) PROGRAM

The research at MIT is strongly tied in with the AFRAPT Program. The students who have participated in this program during the contract period, the advisors, and the research projects are:

Trainee: Jabin Bell  
 Advisor: Prof. A.H. Epstein  
 Project: Active Control of Jet Engine Surge

Trainee: Aaron Gleixner (finished M.S. Thesis, 8/92)  
 Advisor: Prof. A.H. Epstein  
 Project: Unsteady Phenomena in Transonic Axial Flow Turbines (RR)

Trainee: Martin Graf  
 Advisor: Prof. A.H. Epstein  
 Project: Characterization of Fully Scaled Turbine Blade Boundary Layers

Trainee: Daniel Gysling (finished M.S. Thesis, 8/89; Ph.D. expected, 8/93)  
 Advisor: Prof. J. Dugundji/Prof. E.M. Greitzer/Prof. A.H. Epstein/Prof. J. Kerrebrock  
 Project: Active and Structural Control of Aeromechanical Systems (AFOSR)

Trainee: Dana Lindquist (finished Ph.D. Thesis, 12/91)  
 Advisor: Prof. M.B. Giles  
 Project: Development of Adaptive Procedures for Turbomachinery Flow Computations

Trainee: Knox Millsaps (finished Ph.D. Thesis, 5/92)  
 Advisor: Prof. M. Martinez-Sanchez  
 Project: Rotor Dynamic Instability Due to Alford Forces (NASA MSFC)

Trainee: G. Scott McNulty  
 Advisor: Prof. E.M. Greitzer  
 Project: Self-Adaptive Aeropropulsion Components

Trainee: Taras Palczynski (finished M.S. Thesis, 8/92)  
 Advisor: Prof. M. Martinez-Sanchez  
 Project: Tip Clearance Excited Turbomachine Rotordynamic Instabilities (NASA MSFC)

Trainee: George Pappas (finished M.S. Thesis, 8/90)  
 Advisor: Prof. A.H. Epstein  
 Project: Temperature Distortion Effects on Turbine Heat Transfer (RRI)



Trainee: Peter Silkowski (finished M.S. Thesis, 2/90; left MIT, 8/92)  
Advisor: Prof. E.M. Greitzer/Dr. C.S. Tan/Prof. N.A. Cumpsty (Cambridge University)  
Project: Unsteady Phenomena and Flow Instabilities in Multistage Turbomachines  
(AFOSR)

A more detailed description of the work carried out on these projects is given in Refs. 3.1  
3.2, and 3.3.

### **References**

- 3.1 Greitzer, E.M., Dugundji, J., Epstein, A.H., Giles, M.B., Martinez-Sanchez, M., Tan, C.S.,  
"Air Force Research in Aero Propulsion Technology," Annual Technical Report on Grant  
AFOSR-85-0288, September 1990.
- 3.2 Greitzer, E.M., Dugundji, J., Epstein, A.H., Giles, M.B., Martinez-Sanchez, M., Tan, C.S.,  
"Air Force Research in Aero Propulsion Technology," Annual Technical Report on Grant  
AFOSR-91-0052, September 1991.
- 3.3 Greitzer, E.M., Dugundji, J., Epstein, A.H., Giles, M.B., Martinez-Sanchez, M., Tan, C.S.,  
"Air Force Research in Aero Propulsion Technology," Annual Technical Report on Grant  
AFOSR-91-0052, October 1992.

#### **4. PUBLICATIONS AND PRESENTATIONS (Period 10/91 - 10/92)**

Epstein, A.H., "Unsteady Effects in Turbine Aerodynamics and Heat Transfer," ASEA Brown Boveri Research Laboratory, Baden, Switzerland, October 1992.

Fritsch, G., Giles, M., "Second-Order Effects of Unsteadiness on the Performance of Turbomachines," ASME Paper 92-GT-389, presented at the International Gas Turbine and Aeroengine Congress and Exposition, Cologne, Germany, 1992.

Giles, M.B., "An Approach for Multi-Stage Calculations Incorporating Unsteadiness," ASME Paper 92-GT-282, presented at the International Gas Turbine and Aeroengine Congress and Exposition, Cologne, Germany, 1992.

Giles, M.B., "Current Status of CFD Capability for Unsteady Flow Analysis," presented at NASA Lewis Workshop on "Unsteady Flow in Turbomachines: Potential Benefits, Present Status, Future Research", May 1992.

Greitzer, E.M., Tan, C.S., "Unsteady Flow in Turbomachines: Where's the Beef?", presented at NASA Lewis Workshop on "Unsteady Flow in Turbomachines: Potential Benefits, Present Status, Future Research", May 1992.

Guenette, G.R., Pappas, G., Epstein, A.H., "The Influence of Non-Uniform Spanwise Inlet Temperature on Turbine Rotor Heat Transfer," presented at 80th PEP/AGARD Symposium, Antalya, Turkey, October 1992.

Longley, J.P., Greitzer, E.M., "Inlet Distortion Effects in Aircraft Propulsion System Integration," AGARD Lecture Series 183 on "Steady and Transient Performance Prediction of Gas Turbine Engines," June 1992.

## **5. PROGRAM PERSONNEL**

### **Principal Investigator:**

Edward M. Greitzer  
H.N. Slater Professor of Aeronautics and Astronautics  
Director, Gas Turbine Laboratory

### **Co-Investigators:**

Alan H. Epstein  
Professor of Aeronautics and Astronautics  
Associate Director, Gas Turbine Laboratory

Michael B. Giles  
Associate Professor of Aeronautics and Astronautics

James E. McCune  
Professor of Aeronautics and Astronautics

Choon S. Tan  
Principal Research Engineer

### **Graduate Research Assistants:**

9/89 - 8/92	Peter Silkowski (AFRAPT student)
7/88 - 5/92	Gerd Fritsch
6/88 - 5/92	Alexandros Gioulekas
9/90 - present	Martin Graf (AFRAPT student)
1/92 - present	David Sujudi

## 6. INTERACTIONS

As we have noted previously and as may be inferred from the presentations that were given, there are considerable interactions between Gas Turbine Laboratory personnel and industry and government, as well as with other universities. This occurs in several forms. One of these is collaborative research projects with industry and government laboratories. This creates a direct link with those persons who are actively working in similar areas in other establishments, and aids considerably in helping transfer technology.

A second type of interaction is through presentations and discussions with industry or government agencies. These were listed in Section 4 covering the contract period. It should be noted that only those which involved discussion of the work supported by AFOSR under this grant are given.

The Gas Turbine Laboratory also has an active seminar program which brings speakers from industry and government. The speakers for the past year are listed below; those for previous years have been listed in Refs. [6.1] and [6.2].

Mr. W. Culhane, American Airlines  
"Today's Centralized Fault Detection System, Maximum Information  
Yielding Minimum Value"

Mr. B. Koff, Pratt & Whitney Aircraft  
"Spanning the Globe with Jet Propulsion"

Mr. J. Kuhlberg, Pratt & Whitney Aircraft  
"Jet Engine Controls: Past, Present, and Future"

Dr. D. McCormick, United Technologies Research Center  
"Vortical and Turbulent Structure of Lobed Mixer Free Shear Layers"

Dr. L. Nichols, NASA Lewis Research Center  
"Numerical Propulsion System Simulation"

As mentioned in the description of Task III, there is strong coupling with the Whittle Laboratory at Cambridge University. This laboratory is of comparable size to the Gas Turbine Laboratory and has an excellent and very active group of faculty and students focussed on

turbomachinery research. Another close interaction which spans several of the tasks is with Professor F.E. Marble of Caltech. Marble is the former Head of the Jet Propulsion Center in the Division of Engineering and Applied Sciences, and has worked on a wide range of fluids problems connected to propulsion. He has participated in discussions in the Gas Turbine Laboratory for over a decade, and his physical insight and ability to penetrate to the heart of complex issues have been enormously helpful to us in that time.

E. M. Greitzer spent a month at the Ohio Aerospace Institute as a Lecturer in Residence on Turbomachinery. This included a series of lectures on turbomachinery aerodynamics at NASA Lewis Research Center, as well as lectures and discussions with industry and government laboratories and universities in the Ohio region: General Electric Aircraft Engines, Wright Laboratories, Allison Gas Turbine Division, University of Cincinnati, and Case Western Reserve University.

E.M. Greitzer, C.S. Tan, and M.B. Giles participated in a NASA/industry/university workshop on unsteady flow in turbomachines. The purpose of the workshop was to assess available information on the importance of unsteady flow in practical turbomachines and see whether a consensus existed on the magnitude of the gains to be achieved through better understanding of unsteady flow, and the issues that were central to the potential gains. A further goal was to define and prioritize those fluid dynamic topics in unsteady flow on which attention should be focused. The participants had strong consensus that critical unsteady flow problems, with substantial payoff, exist in the areas of gas turbine engine and compressor stability, and in aeroelasticity in turbomachines. Much of the discussion, therefore, was aimed at the area of greatest uncertainty, the unsteadiness associated with rotor stator interaction, i.e. unsteady flow effects which have a length scale on the order of the blade pitch.

A report on the workshop has been written by J.J. Adamczyk (NASA), A.J. Strazisar (NASA) and E.M. Greitzer (MIT). A summary of this report is given below:

*Summary*  
*NASA Government/Industry/University Workshop on*

**Unsteady Flow in Turbomachines: Potential Benefits, Present Status, Future Research**

On May 20-21, 1992 a workshop was held at NASA Lewis Research Center on the topic of "Unsteady Flow in Turbomachines". The purpose of the meeting was to bring together active workers in the field, from university, industry, and government, to address the following questions:

1. What areas show potential for gas turbine engine performance increase through improved understanding of unsteady flow?
2. What are the magnitude of the gains to be expected?

Associated with the answers to (1) and (2) are several follow-on issues:

3. What is the current state of the art in understanding in the areas defined to be of importance?
4. What topics should be explored further?
5. How does one do this in an appropriate manner (What is the balance of basic and applied research, near term versus long term, etc.)?
6. If C.F.D. codes are to be used to quantify the effects of unsteady flows on aero-performance and surface heat transfer, how should these codes be calibrated?

A. H. Epstein participated in a study of wide breadth carried out by the Aeronautics and Space Engineering Board of the National Research Council. The purpose was to assess the current state of aeronautics in the United States and to help identify the technology advances necessary to meet the challenges of the next several decades. The conclusion of the study are summarized in the report "Aeronautical Technologies for the Twenty-First Century" issued by the ASEP.

E. M. Greitzer participated in an Air Force Scientific Advisory Board Committee to examine failures in titanium components of Air Force aircraft engines.

**References**

- 6.1 Greitzer, E.M., Epstein, A.H., Giles, M.B., McCune, J.E., Tan, C.S., "Unsteady Flow Phenomena in Turbomachines," Annual Technical Report on Grant AFOSR-90-0035, November 1990.
- 6.2 Greitzer, E.M., Epstein, A.H., Giles, M.B., McCune, J.E., Tan, C.S., "Unsteady Flow Phenomena in Turbomachines," Annual Technical Report on Grant AFOSR-90-0035, December 1991.

## **7. DISCOVERIES, INVENTIONS, AND SCIENTIFIC APPLICATIONS**

During the present contract period, there have been no inventions.



## 8. CONCLUDING REMARKS

Several aspects of the multi-investigator program deserve comment. First, one can see explicitly in the research conducted strong technical links with industry and government laboratories. A consequent benefit is the connection with problem areas that are of real interest; this is useful and stimulating to faculty and students alike. A second positive feature is that there are personnel at these organizations who are directly involved in the programs. These people are, within the organizations, the "owners" of the scientific and engineering results that emerge from the research. In this sense, there is much less need for other formal mechanisms for technology transition, since this occurs at the grass roots level.

Another item is the strong coupling between investigators, which has been fostered by this program. We believe this is extremely useful in "cutting edge" aer propulsion research; the problems are not only conceptually difficult, but are also complex. Having several different types of talents focussed on the different areas provides a substantial synergism to the overall program. The multi-investigator aspect of the research program is a powerful resource.